Author:
Blok, Lourens G

Title:
Development of improved fibre reinforced feedstocks for high performance 3D printing

Development of improved fibre reinforced feedstocks for high performance 3D printing

By

LOURENS G. BLOK

Department of Engineering
UNIVERSITY OF BRISTOL

July 2020

Abstract

In the last ten years, much progress has been made combining the field of additive manufacturing (AM) and fibre composite materials. An AM technique such as Fused Filament Fabrication (FFF) allows rapid prototyping of complex parts at a low cost but lacks in mechanical properties to make them applicable as structural components. The addition of reinforcing fibres to thermoplastic filaments has been demonstrated to improve the mechanical properties of 3D printed parts. The fibre architecture plays an important role on the performance and processing of the filament, and in this work a new High Performance Discontinuous Fibre *(HiPerDiF)* filament is presented for an optimal trade-off between performance and processing.

Two existing fibre reinforced filaments for FFF were assessed: short fibre filament and continuous fibre filament. Short fibre filaments have fibres with a length of ~0.1 mm which provide little reinforcing effect but can be processed using a standard 3D printer. Continuous fibre filaments have an order of magnitude higher mechanical properties than short fibre filaments, but they are harder to deposit through corner radii due to the inextensibility of the carbon fibres resulting in a lower quality part.

Aligned discontinuous fibre reinforced composite (ADFRC) tapes were prepared with 3 mm carbon fibres using the *HiPerDiF* fibre alignment method invented at the University of Bristol. Suitable thermoplastic polymer matrix systems were chosen (PLA, ABS, PA, PETG) based on the FFF process requirements. A novel filament forming method has been developed that allows consolidated ADFRC tapes to be formed into a 3D printing filament via a direct extrusion method, utilizing the aligned fibre architecture for better flow behaviour. A thermal and rheological analysis was performed to improve the filament forming method and identify suitable processing windows. Short filament strands were prepared that enabled the first 3D printing trials with the *HiPerDiF* filament.

Performance-wise, the tensile strength and stiffness of the ADFRCs was an order of magnitude higher than available short fibre filament, and comparable to continuous fibre filaments. The processing of the *HiPerDiF* filament showed better deposition quality through corner radii

than continuous fibre filament. This work has demonstrated the hypothesized benefits of aligned fibre reinforced composites for improved 3D printing feedstocks and further work has been identified to improve the filament manufacturing method and quality.

Acknowledgements

To start, I would like to acknowledge the Engineering and Physical Sciences Research Council (EPSRC) for funding the Centre for Doctoral Training in Advanced Composites for Innovation and Science (EP/L016028/1). It has been great to be given the opportunity to explore new manufacturing methods for composite materials

My sincere gratitude goes out to my main supervisors, Dr. Ben Woods, and Dr. Marco Longana, who came up with the idea to combine 3D printing and HiPerDiF.

Ben, king of creativity, thank you for showing me not only the fun but also the importance of creativity in engineering and research. When the fibres got stuck, you had multiple ideas and I thoroughly enjoyed the brainstorming sessions in your office.

Marco, master of fibre alignment, thank you for introducing me into the world of short fibre composites. Aligning fibres in a basement is hard work, but your know-how and dedication to this project kept me going.

I'd like to also thank Dr. HaNa Yu and Prof. Kevin Potter, who's pioneering work on HiPerDiF has been fundamental to where it is today and enabling this research.

My thanks also go out to the support staff at the Bristol Composite Institute for enabling this work to be carried out. This also includes the lab support and workshop, there is something special about the labs in Queen's Building that only you guys know.

Then there are the many chats with my fellow composite PhD students, both in and outside of the labs. A special mention goes out to Rob, Rhys, Arjun, Max, Tom and Beth. Thanks for sharing both the fun times and the hard times, and I am looking forward to looking back at the times we had in Bristol.

Steph, PhDs come with ups and downs, thank you for being the constant encouragement I could come back to at the end of the day.

And lastly, to my parents who have always supported me, taught me the joy of thinking and helped along every step on the way lending a listening ear and giving words of wisdom.

Declaration

I declare that the work in this dissertation was carried out in accordance with the requirements of the University's Regulations and Code of Practice for Research Degree Programmes and that it has not been submitted for any other academic award. Except where indicated by specific reference in the text, the work is the candidate's own work. Work done in collaboration with, or with the assistance of, others, is indicated as such. Any views expressed in the dissertation are those of the author.

SIGNED:

DATE

Table of Contents

List of Figures

List of Tables

Abbreviations

ABS	Acrylonitrile butadiene styrene
ADFRC	Aligned discontinuous fibre reinforced composite
AM	Additive manufacturing
AR	Aspect ratio
ATP	Automated tape placement
CFRP	Carbon fibre reinforced polymer
CoV	Coefficient of variance
CT	Computed tomography
CTE	Coefficient thermal expansion
DMP	Direct metal deposition
DSC	Digital scanning calorimetry
EBM	Electronic beam melting
FDM	Fused deposition modeling
FFF	Fused filament deposition
FRP	Fibre reinforced polymer
HDPE	High density poly-ethylene
HiPerDiF	High Performance Discontinuous Fibre
IFSS	Interfacial shear strength
IR	Infrared
IRD	Isotropic rotary diffusion
LbL	Layer-by-Layer
LDPE	Low density poly-ethylene
LMD	Laser metal deposition
LOM	Laminated object manufacturing
NCF	Non-crimp fabric
PA	Poly amide
PAN	Poly acrylonitrile
PBT	Poly butylene terephthalate
PCL	Poly caprolactone
PCL	Poly carbonate
PDMS	Poly dimethylsiloxane
PEEK	Poly ether ether ketone
PEI	Poly ethylen-imine
PESU	Poly ethersulfone

PETG	Poly ethylene terephthalate glycol
PLA	Poly lactic acid
PP	Poly propylene
PPS	Poly phenylene sulphide
PSU	Poly sulfone
PTFE	Poly tetrafluoroethylene
PVC	Poly vinylchloride
QI	Quasi isotropic
RTM	Resin transfer moulding
SEM	Scanning electron microscopy
SL	Stereolithography
SLM	Selective laser melting
SLS	Selective laser sintering
TGA	Thermo-gravimetric analysis
UD	Uni-directional

Symbols

A	Cross sectional area
$A_{exposed}$	Outer exposed surface area
c_p	Heat capacity
D	Diameter
d_f	Fibre diameter
D_h	Hydraulic diameter
ε	Emissivity
E^*	Flow activation energy
E_{11}	In-plane modulus (parallel to fibre direction)
E_{22}	In-plane modulus (perpendicular to fibre direction)
E_c	Composite modulus
E_c^*	Effective composite modulus
E_f	Fibre modulus
E_m	Matrix modulus
E_t	Rate change of energy
G_{12}	In-plane shear modulus
h	Heat transfer coefficient
h_{air}	Heat transfer coefficient with air
h_{nozzle}	Heat transfer coefficient with nozzle
K	Permeability
k	Thermal conductivity ADFRC
k_f	Thermal conductivity fibre
k_m	Thermal conductivity matrix
L	Flow length
l_c	Critical fibre length
l_f	fibre length
p	Pressure
P	Wetted surface area
Δp	Pressure difference
Q	Volumetric flow rate
q_{cond}	Heat exchange through conduction
q_{env}	Heat exchange with environment
r	Corner radius
R	Gas constant

Re	Reynolds number
R_f	Fibre diameter
t	Time
T	Temperature
t_t	Tape thickness
T_g	Glass transition temperature
T_m	Melt temperature
T_{set}	Set temperature
V	Velocity
ν_{12}	Poisson ratio (in-plane)
V_f	Fibre volume content
V_m	Matrix volume content
w_t	Tape width
α	Nozzle angle
γ	Shear rate
ε	Emissitivity
ζ	Fibre aspect ratio
η	Viscosity
η_0	Fibre misalignment factor
η_1	Fibre efficiency factor
θ	In-plane fibre angle
λ	Shape factor
ϱ	Density
σ	Boltzmann constant
σ_f	Fibre stress
$\sigma_{f,max}$	Maximum fibre stress
$\sigma_{f,u}$,	Ultimate fibre stress
τ	Shear stress
τ_{IFSS}	Interfacial shear strength
ϕ	Out-of-plane fibre angle

Chapter 1
Introduction

1.1 General introduction

In 501 BC, Greek philosopher Heraclitus came up with his famous aphorism *pantha rhei*, which translates to "all flows". He meant this statement as the continuous movement of everything in the universe, often interpreted as "everything flows, and nothing stays". For material scientists, this provides an interesting premise. We try to make our materials strong, stiff and reliable to prevent any unwanted deformation. But Heraclitus teaches us that despite our best efforts, everything will move, including the strongest engineered materials. This can be interpreted by material scientists in two ways. First, during their operative life materials will slowly be degraded by the environment and by usage (i.e. fatigue or damage), and thus they need to be designed to fulfil their function over a required timespan. Secondly, during manufacture, materials "flow" or are shaped into the required geometry at some stage. If you think about this second interpretation and look around you, any object or part you see is made by a manufacturing technique that requires the material to be flowing at some stage to obtain its final shape. Figure 1.1 shows how tree trunks were transported in the early days by moving them downstream with the river flow.

Now in the 21st century, the flow of materials during manufacture is an important field of study. It has a great effect on the costs, quality, and performance of structures. The flow of materials dictates the equipment required to make a part; some materials flow very slowly and require big presses to be forced into shape, other materials can be very thin and flow easily. The flow of materials gives us the geometric tolerances, as shaping actions are required to form it and the accuracy of these may vary. Material flow is also important for the final mechanical properties of the part. Poor understanding of the material movement during manufacture can create inconsistencies or defects and lower its overall performance. All these aspects are related to the flow of material.

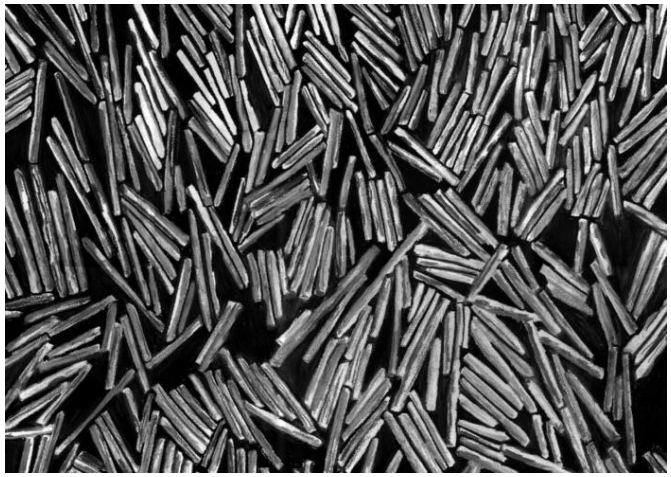

Figure 1.1: Tree trunks flowing down a river to be used as a building material.

High performance materials are often combinations of different materials to give unique properties, generally superior or beneficially different from those of the single constituents. These composite materials benefit from improved mechanical properties and can be tailored for specific purposes. The best-kn own example of this are carbon fibre reinforced polymers (CFRP) which are made from carbon fibres and polymer matrices. They provide high mechanical properties such as strength and stiffness and allow for significant design tailoring by controlling the fibre orientation [1]. Figure 1.2 shows a comparison between the specific strength, stiffness and weight of traditional metals and CFRP composites, where uni-directional (UD) means all fibres are orientated in the same direction and quasi-isotropic (QI) is when the fibres orientations are balanced for all in-plane directions. CFRP clearly outperforms metals compared on a weight basis. This makes fibre composite materials the material of choice where weight matters, such as the aerospace industry. In more recent years, composites are also finding applications in other industries such as automotive, marine and sporting goods for increased performance.

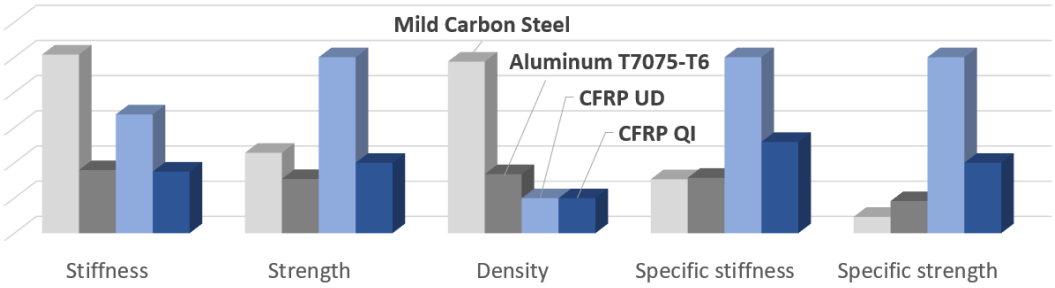

Figure 1.2: Qualitative comparison of metals and CFRP mechanical performance and weight.

The combination of materials, however, also changes the flow or manufacturing process of composites as multiple constituents now need to be simultaneously processed. A fundamental

challenge with fibre reinforced polymers is the combination of the reinforcements with the polymer matrix with good consolidation, maximum control of fibre orientation and at low cost [2]. A wide range of manufacturing methods for composites are available, such as Resin Transfer Moulding (RTM), Automated Tape Placement (ATP) or compression moulding. In general, fibre reinforced polymer (FRP) parts are formed by lay-up of dry or pre-impregnated continuous fibres in the desired shape and consolidated with the matrix through either infusion or final curing of the matrix. For good consolidation, pressure needs to be applied over the entire part surface area which requires expensive equipment and increases manufacturing costs.

In this thesis, an alternative approach to composite manufacture is investigated for fibre reinforced plastic materials using additive manufacture (AM) techniques, and more specifically using fused filament fabrication (FFF). A layer-by-layer (LbL) manufacturing technique such as FFF matches the laminated structure of composite materials. This enables a simple method for composite manufacture with lower production cost and a high degree of automation. Printers capable of printing fibre composite materials are already available, such as the Markforged continuous fibre printers [3], Arevo labs [4], Anisoprint [5] and short fibre reinforced filaments suitable for desktop printers [6]. The higher mechanical properties of fibre reinforced filaments open new applications in both the personal fabrication market and in industry for rapid prototyping of structural parts. Examples of this are 3D printed tooling, 3D printed composite car bodies and recently bike frames [7]–[9]. The fibre orientation in composites parts can be further optimised in each layer, allowing for an increase in design tailorability as reinforcements can be accurately placed during FFF.

Challenges remain for 3D printing of composite materials. Rapid prototyping of fibre reinforced materials using FFF currently faces a trade-off between processing and performance. Continuous fibre printing solutions show good mechanical performance but are limited in design freedom as the inextensible continuous carbon fibres cannot be deposited freely through small steering radii and sharp angles. Filaments with embedded short carbon microfibres (~100 μm) allow for considerably more freedom in where and how the reinforcement is placed, resulting in easier processing of the material and lower void content [10]. Short fibre filaments are made by compounding of the fibres in the matrix with a screw extruder which breaks the brittle carbon fibres. The mechanical properties are low because the 100 μm length fibres in the polymer do not reach their full strength and instead part strength is limited by premature fibre pull-out.

In this thesis, the development of an improved fibre reinforced feedstock for high performance 3D printing is presented. A novel manufacturing method for discontinuous carbon fibre reinforced filament that prevents fibre breakage and preserves a fibre length of 3 mm was designed. This allows for high aspect ratio fibres in the final filament, leading to higher mechanical properties in the final product while maintaining the processing benefits of the original FFF process.

1.2 Description of the project

1.2.1 Project context

This work is based around the High Performance Discontinuous Fibre (HiPerDiF) alignment method [11]. The HiPerDiF method allows for the fabrication of highly aligned discontinuous fibre preforms in a continuous in-line process where the fibre length can be varied between 1 and 12 mm. Figure 1.3 shows a schematic of the fibre alignment process. Fibres are suspended in water at a low concentration and the fibre suspension is sprayed between parallel plates with a small gap between them. Due to the momentum change at the impact with the plate, the fibres align parallel to the plates and fall between them onto a moving mesh conveyor belt. A vacuum is present underneath the belt to remove the water and after drying a continuous tape of discontinuous fibres is obtained [11]. Alignment of the fibres occurs by flow through the spraying nozzle, the momentum change upon impact with the orientation plates and another momentum change when they fall onto the moving mesh belt, yielding highly aligned fibres.

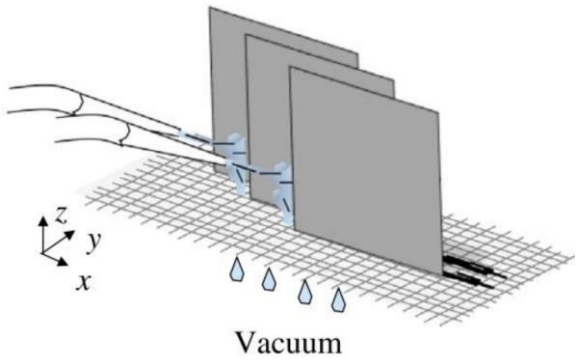

Figure 1.3: Schematic of the HiPerDiF fibre alignment method, fibres suspended in water are sprayed against orientation plates with a vacuum below a moving mesh belt.

The mechanical properties of discontinuous carbon fibre/epoxy composite materials made using this method were close to that of continuous fibre composites. In the original study by Yu *et al.* [11], an autoclave process (7 bar pressure) was used to consolidate aligned 3 mm long carbon fibres with an epoxy film and create 50 mm x 3 mm x 0.2 mm tensile samples. The fibre volume

fraction V_f was 55% and the tensile strength and stiffness were 1509 MPa and 115 GPa, respectively.

The main advantage of aligned discontinuous fibre composites (ADFRCs) is that they provide a balance between performance and processability as illustrated in Figure 1.4. Continuous fibre composites are known for their high specific strength and stiffness, but problems arise during manufacturing related to drapability such as wrinkling and fibre misalignment [12],[13]. Discontinuous fibres need to be aligned first but can then be used as a highly effective reinforcement and may overcome manufacturing problems related to drapability of continuous fibres [12]. A future step for the HiPerDiF project is upscaling and to develop an impregnation/prepreg module to directly create ADFRC prepregs tapes, to be used in state-of-the-art composites automated tape placement (ATP) machines and move towards the optimal trade off region as shown in Figure 1.4.

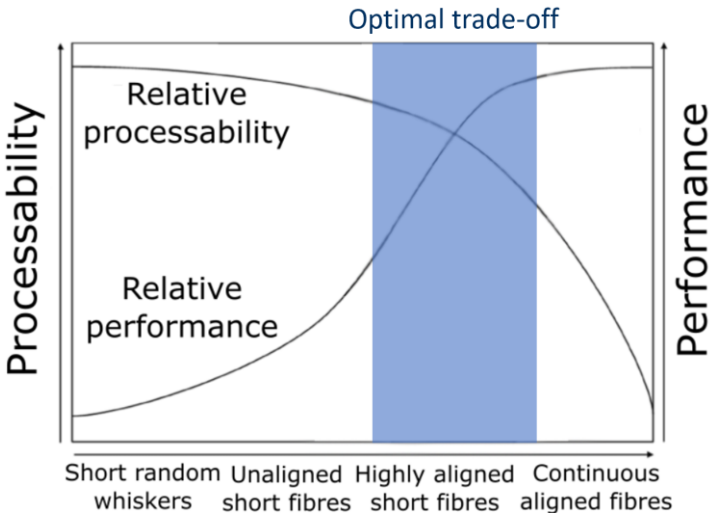

Figure 1.4: Balance between process ability and performance for different fibre architectures showing the optimal trade-off region.

1.2.2 Project aim

This project aims to further increase the relative processability of highly aligned discontinuous fibres by taking aligned fibre preforms from the HiPerDiF process and forming them into a 3D printing filament for fused filament fabrication. This removes the need for expensive manufacturing equipment, and instead enables high-performance composite manufacture using a simple 3D printer. Commercial short fibre reinforced 3D filaments exist, but show only a small gain in mechanical properties as the fibre aspect ratio is too small to utilize the fibre strength in the printed part [14]. In this project, an increase in fibre length in the filament is made possible by using pre-aligned fibres from the HiPerDiF machine, circumventing problems with fibre breakage during filament manufacture and clogging during printing.

To successfully develop an improved fibre reinforced feedstock for 3D printing, called HiPerDiF filament, the following research challenges are addressed:

1. To understand the current limitations of state-of-the-art fibre reinforced 3D printing methods and identify important processing parameters for FFF that enable successful extrusion of fibre reinforced filaments.
2. To identify suitable matrix systems and consolidate the matrix with dry carbon fibre preforms from the HiPerDiF process to be further developed into a filament.
3. To design a continuous manufacturing method for HiPerDiF filament as the nature of the FFF process requires the feedstock material to be spooled. This process must avoid fibre breakage as that would reduce the mechanical performance of the material.
4. To investigate the 3D printing performance of the improved HiPerDiF filament and compare it to the state-of-the-art 3D printing methods.

1.3 Novelty statement

The work presented here is the first demonstration of 3D printing of a filament reinforced with discontinuous carbon fibres with fibre length above 1 mm. Previous work on composite 3D printing has focused on continuous fibre filament and short fibre (~100 μm) filaments, with both already having been commercialised. The potential benefits of aligned discontinuous fibre composites have been hypothesised but no research has been published to date assessing both their performance and the processing experimentally. This work presents the first automated manufacturing method for HiPerDiF aligned discontinuous fibre thermoplastic composites using an additive manufacturing technique. Within this overarching novelty are a series of novel developments and achievements:

- The first benchmarking study is performed directly comparing 3D printing of continuous fibre filaments and short fibre filaments. The advantages and shortcomings of both techniques are clearly identified, highlighting a gap that may be filled with an improved discontinuous fibre reinforced filament.
- An analysis of the FFF process has been coupled to relevant matrix material properties, resulting in a matrix selection methodology for the development of

new fibre reinforced filaments. This methodology can be applied in future case studies to select suitable matrices for FFF given different constraints.

- A new consolidation method has been developed to manufacture HiPerDiF ADFRC composites with thermoplastic matrices. A double belt press module allowed continuous manufacture of thermoplastic ADFRC tapes which have the added benefit of being usable as a pre-preg tape for tape laying processes in the future.
- The mechanical performance of HiPerDiF ADFRCs with new thermoplastic matrices has been assessed, showing that near-continuous fibre performance is achievable with thermoplastic composites using aligned 3 mm carbon fibre reinforcements.
- An extensive experimental study on the flow of thermoplastic ADFRC tapes with high aspect ratio fibres through converging channels is presented. It is shown ADFRC tapes can be directly extruded given correct process conditions. Their cross-sectional shape can be changed, and this technique may be used as a novel manufacturing method for improved fibre reinforced filaments where fibre fracture is avoided.
- The first 3D printing trials were performed with a HiPerDiF filament reinforced with 3 mm carbon fibres, showing this filament has processing benefits over continuous fibre filament whilst having near continuous fibre mechanical performance.

The findings of this work have a significant impact on the following areas of composite materials and additive manufacturing:

- It opens a new method for high-strength composite 3D printing for the masses, using low-cost 3D printers. The HiPerDiF filament can be 3D printed on standard desktop 3D printers with only small adaptations required.
- The improved processing characteristics of HiPerDiF filament over continuous fibre filaments can lead to higher quality 3D printed structures and allow rapid prototyping of composite structural elements.
- It can reduce the costs associated with composite materials as HiPerDiF filament provides a cheaper manufacturing method with low capital investment.

- The HiPerDiF filament lends itself for use of reclaimed or recycled fibres, increasing the sustainability of composite materials by having a new re-use application for carbon fibres reclaimed from scrap or end-of-life material.

1.4 Thesis outline

The thesis starts with a review on the state-of-the-art of composite 3D printing in Chapter 2. It contains an extended introduction to introduce the relevant concepts for discontinuous fibre composites. A benchmarking study on fibre reinforced printing is presented here that compares the performance and processing of continuous fibre and short fibre filaments.

The work continues with the development of improved discontinuous fibre filaments which follows the path depicted in Figure 1.5. First, ADFRC tapes were prepared using the HiPerDiF dry fibre preforms and thermoplastic matrices which is presented in Chapter 3. It contains a matrix selection process that was performed to find suitable candidate polymers for the ADFRCs to be further developed into a filament for FFF. Four different matrices were selected, and tensile testing was performed on the different types of ADFRC tapes.

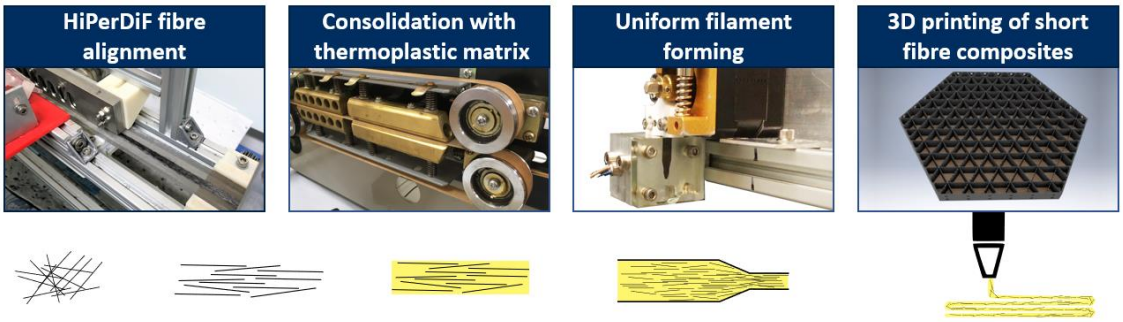

Figure 1.5: The main filament development of this work consist of fabrication of ADFRC tapes, reshaping of the tapes into a uniform filament and 3D printing studies of the filament.

Chapter 4 contains the studies performed on reshaping the ADFRC tapes into a uniform filament. The flow of the fibre-matrix melt through converging dies was studied and the effect of various processing conditions was investigated. A thermal analysis was performed to predict the temperature profiles and viscosity profiles during extrusions that helped identify suitable processing windows for forming the ADFRC tapes.

Chapter 5 contains the 3D printing studies of the improved HiPerDiF filament. Short filament strands were prepared, and the extrusion behaviour and deposition behaviour were investigated at different temperatures and extrusion speeds. The effect of printing height was also included, and a comparison was made between the quality of the printed parts with respect to continuous fibre filament and short fibre filament.

The main conclusions drawn from this work are presented in Chapter 6, where the main findings of each section are highlighted. With all findings combined, it is shown how HiPerDiF filament can improve current fibre reinforced printing methods and future work is then identified for the further development of the filament.

Chapter 2
State-of-the-art of composite 3D printing

The contents of this chapter are based around the following peer reviewed journal paper:

L. G. Blok, M. L. Longana, H. Yu., and B. K. S. Woods., "An investigation into 3D printing of fibre reinforced thermoplastic composites," Addit. Manuf., vol. 22, pp. 176–186, 2018.

And a conference paper:

L.G. Blok, B.K.S. Woods, H. Yu, M. Longana, and K. Potter, "3D Printed Composites– Benchmarking The State-Of-The-Art"," in 21st International Conference on Composite Materials, 2017, pp. 1–9.

An introduction to composite materials and manufacturing methods is first given in section 2.1 to provide the composites manufacturing context on which this project is built. Section 2.2 details the state-of-the-art of composite 3D printing with a detailed analysis of the FFF process and the effect of fibre reinforcement. A contribution to the state-of-the-art is then made in section 2.3 in the form of benchmarking experiments that provide a direct comparison between different composite 3D printing methods. The chapter finishes with discussion and conclusions in section 2.4 on the current state of fibre reinforced 3D printing which highlights a significant gap between what is desired and what is available, which directly motivates development of a new 3D printing filament using longer aligned discontinuous fibres.

2.1 Introduction

As mentioned in the thesis introduction, fibre reinforced carbon fibre composites have high mechanical properties with a relatively low density compared to other engineering materials. However, challenges remain on how to combine the fibres and polymer matrix together with good consolidation, high volume fraction (V_f) and at low cost. Before the specific manufacturing challenges are introduced and advantages and disadvantages of additive manufacturing for composites are discussed, a brief overview of fibre composites is given in this section, with particular attention paid to the aspects which will influence the work carried out here.

2.1.1 Polymeric matrices

In a composite material, the polymer matrix holds the fibres together, allows for load transfer into them, and protects them from environmental exposure. Polymers are very large molecules that consist of many repeating units or monomers [15]. Different types of repeating units are used to give the bulk polymer different properties such as density, mechanical performance, environmental stability and thermal stability. These properties are dictated by the molecular structure of the repeating units, how the monomers are formed into a polymer chain and how the polymer chains connect with each other.

From an engineering perspective, polymers can broadly be divided into two categories; thermosets and thermoplastics. Thermosetting polymers consist of long polymer chains which are cross-linked by atomic bonds, creating a rigid and large reticulated network of polymer chains. Thermosetting polymers start as a resin of unlinked molecules with a low viscosity, allowing easy flow into and around the fibres. The cross-linking formation, called curing, can be started by the addition or the activation of hardeners through application of heat, light or other stimuli. Typical thermosetting resins are epoxies and polyester. When heated, the thermoset polymer cannot be melted, but some softening can take place for weakly cross-linked thermosets.

Thermoplastic polymers consist of long polymer chains which are entangled with each other and held in place by secondary bonds such as Van der Waals forces and hydrogen bonds [1]. When thermoplastics are heated, these secondary bonds easily break, allowing movement of the polymer chains. The bulk material then softens and can flow. Compared to thermosets, thermoplastics at processing conditions typically have a higher viscosity and need higher processing temperatures. When cooled, the polymer chains are locked in place by secondary bonds again and the material solidifies keeping its new shape. This process can be repeated which allows thermoplastics to be reused (reshaped or recycled). Typical thermoplastics include Polypropylene (PP), Acrylonitrile butadiene styrene (ABS), Polyamides (PA) and higher performance Polyether ether ketone (PEEK) and Polyethylenimine (PEI).

The entanglement of the polymer chains can have structured and/or unstructured regions. A completely disordered entangled polymer is known as an amorphous polymer, while semi-crystalline polymers have structured regions, typically with lamellar shape, in them. The degree of crystallinity, expressed in percentage, is how much of the polymer has a structured region which usually varies from 10 to 80%. Crystallinity generally improves the mechanical properties and changes the processing characteristics of thermoplastics.

With increasing temperature, amorphous polymers exhibit a transition from a hard, solid material to a soft, rubbery state which is known as the glass transition temperature T_g (Figure 2.1). Amorphous polymers do not exhibit a melting point and gradually soften, becoming a highly viscous liquid at higher temperature. Semi-crystalline polymers exhibit a similar softening at T_g, with another sudden change at the melt temperature T_m, which is paired with a large reduction in viscosity. Thermoset polymers, unlike thermoplastics, do not melt but instead simply degrade at higher temperatures.

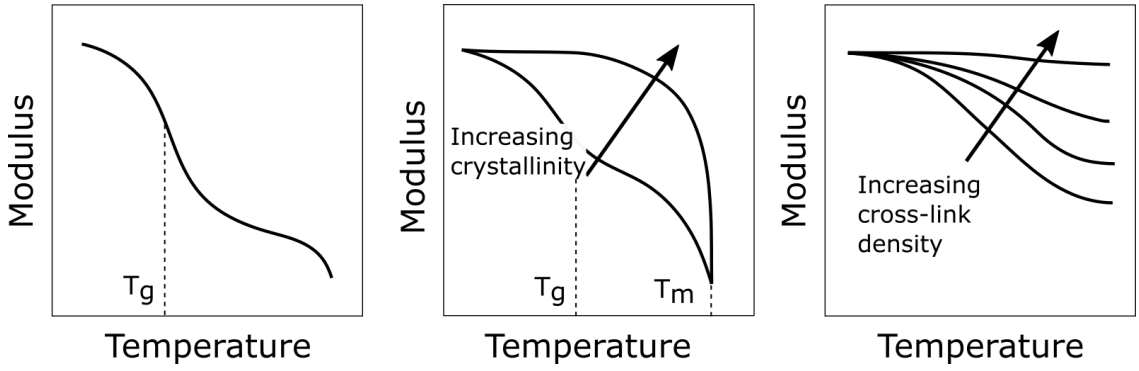

(a) amorphous **(b)** semi-crystalline **(c)** thermoset

Figure 2.1: Modulus versus temperature showing softening behaviour of (a) amorphous thermoplastics, (b) semi-crystalline thermoplastics and (c) thermoset polymers adapted from [1].

The selection of polymer for the matrix of a composite therefore determines what processing or repairing methods and recycling opportunities are available and is therefore a fundamental aspect of all composite development. Thermoset polymers cannot be reshaped and thus are a single-use material. The fibres in a thermoset composite can be recycled, but to do this the matrix needs to be removed which is typically via thermal decomposition (pyrolysis). Pyrolysis is a high energy process that also degrades the fibres. Thermoplastic polymers are readily reshaped during or after processing and can be dissolved to reclaim the fibres and allow re-use of the polymer as recently demonstrated by Tapper et al. [16], [17]. In this thesis, solely the use of thermoplastics is studied as it enables fused filament fabrication of composite materials.

2.1.2 Fibre reinforcements

Various fibre types and architectures may be used as reinforcement in the polymer matrix. The most common fibre types are carbon, glass and Kevlar fibres which present different strength, stiffness, ductility, cost and density (see Figure 2.2). Carbon fibres are known for their high modulus and high performance relative to their density but are also the most expensive. They are made by carbonisation of specific polymeric fibres, typically Polyacrylonitrile (PAN) or pitch, at high temperatures (up to 2000 °C) in inert atmospheres. This creates a fibre that consists

of graphite crystals with the basal planes aligned with the fibre axis. Typical fibre diameters are 7-10 μm and they are very inert. After fabrication, a carbon fibre is typically coated with a specific sizing to improve the bonding to the matrix material.

Glass fibres are the cheapest reinforcing fibres but with a higher density and lower stiffness than carbon fibres. A glass fibre mainly consists of silica (>50% SiO_2), but other oxides can be added to tailor the processing and performance. On a molecular level, the silicon oxide and other additives form an amorphous three-dimensional network. To manufacture a glass fibre, a glass melt is first prepared and through several extrusion steps they are drawn into filaments.

Kevlar fibres are polymeric fibres with a backbone that consists of aromatic rings and N-H and C=O groups, resulting in many inter-molecular hydrogen bonds. They are known for very high specific properties and are commonly used for applications where a high ductility is important.

In this work, carbon fibres are considered as they exhibit the highest specific mechanical properties and the proposed filaments would create a new high value use for recycled carbon fibres, which are currently mostly disposed of in landfill.

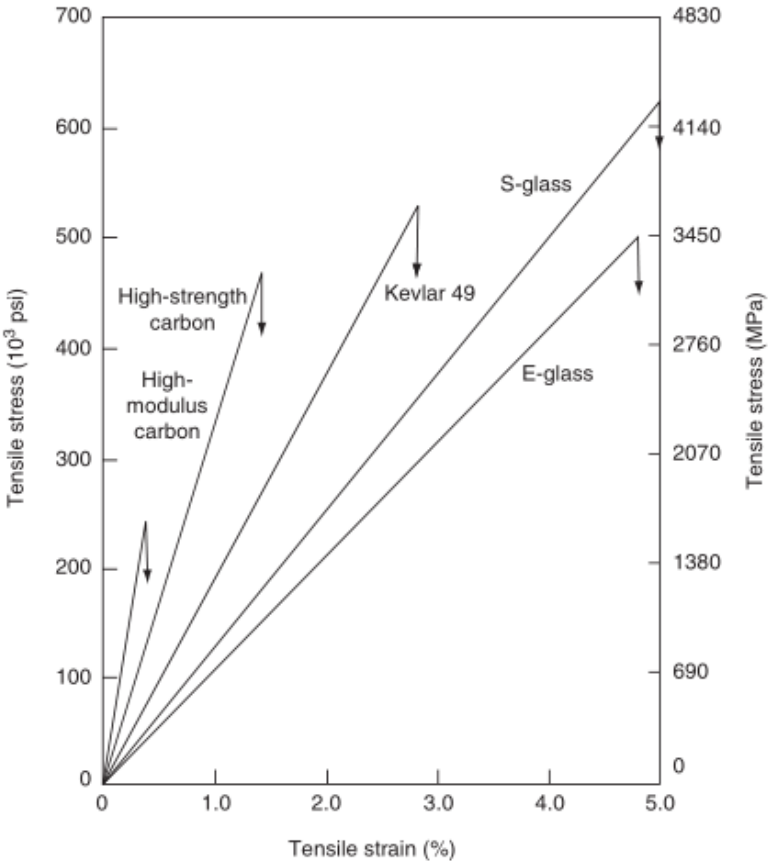

Figure 2.2: Typical tensile stress-strain curves for different fibre types [1].

Carbon fibre reinforcements currently come in a wide variety of architectures, some of which are shown in Figure 2.3. The raw carbon fibres are supplied in the form of 'tows', which are continuous bundles of long fibres, with the tows typically wound around spools. The tows can then be formed into uni-directional (UD) tapes, woven fabrics or non-crimp fabrics (NCF). UD tapes, where all the fibres are orientated in one direction, give the highest performance in the principal fibre direction while woven fabrics have two main principal directions. Non-crimp fabrics are UD layers that are stacked on top of each other (in varying orientations) and sown together. The shaping of the fibres into desired geometries is a large field of study of composites. Continuous fibres cannot easily be steered as they are inextensible along their length, complicating the placement of UD tapes onto complex, curved shapes. Woven fabrics can more easily be shaped (sheared) into more complex shapes, and significant research activity has gone into the development of draping simulations to predict required shearing motions and resulting changes in fibre directions due to forming of the fabric [18], [19] – with a view towards the development of part geometries and fibre preforms that can be more easily manufactured.

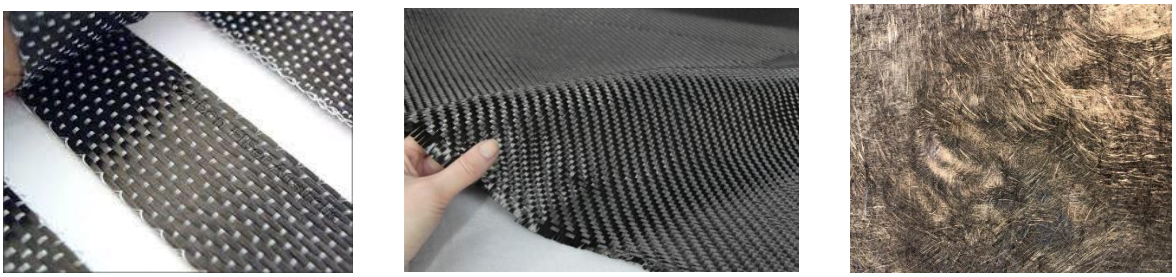

Figure 2.3: Different fibre architectures; (a) UD tape and (b) woven fabric and (c) non-woven mat.

Short fibre composites are easier to mould but typically lack control of fibre orientation and have a limited fibre volume fraction due to low fibre packing ratios. The most common architecture is a random nonwoven mat. Novel alignment techniques can enable high fibre content and control of orientation such as the HiPerDiF method [11]. Such aligned discontinuous fibre reinforced composites ADFRC have the benefit of better formability over continuous fibre architectures. During forming or tape placement, discontinuous fibres may move relative between each other while continuous fibres are constrained by their inextensibility have a limit degree of freedom to move.

2.1.3 Fibre - matrix coupling

The fibre-matrix interface quality is crucial for the performance of the resulting composite material as any inconsistencies, defects or voids can significantly affect the resulting mechanical properties. On the manufacturing side, the challenge is how the fibre reinforcement can be fully

wetted and impregnated with the viscous thermoplastic matrix. An advantage of thermoplastics is that they can be reshaped and softened which allows thermoforming and injection moulding techniques. However, the high viscosity of thermoplastics requires high temperatures, high moulding pressures and it limits the matrix infiltration length. The interface between the thermoplastic matrix and carbon fibres must be considered both mechanically and chemically to allow for good load transfer between the fibres and the matrix.

The flow of a polymer matrix through the fibre preform is often described mathematically as fluid flow through a porous medium using Darcy's law (Equation (2.1) [20]. It shows the flow rate per unit area (Q/A) is proportional to the fibre bed permeability (K) and the applied pressure (ΔP) divided by the fluid viscosity (η) and the flow length (L). Any of these parameters can be changed to improve the flow of the matrix to fully wet the fibres and improve the quality of the consolidated product.

$$\frac{Q}{A} = \frac{K\Delta P}{\eta L} \tag{2.1}$$

Increasing the temperature generally makes the polymer less viscous and easier to flow. Increasing the pressure forces the polymer matrix between the fibres and increasing time allows the matrix flow (which moves at a certain velocity depending on the other parameters) to cover larger distances to more fully impregnate the fibre preform. Lastly, the flow or infiltration length can be reduced by changing the stacking structure of the fibres and the matrix before consolidation [21],[22]. For example, thin fibre preforms can be used or polymer fibres can be distributed with the reinforcement fibres (hybridisation) to reduce the flow length required for full fibre wetting.

Typical manufacturing methods for high performance continuous carbon fibre reinforced thermoplastics are prepreg based, where the fibre tape or fabric is pre-impregnated with a thermoplastic matrix. The fabrication of thermoplastic prepreg can be done using solvent based methods or using hot-melt impregnation [20]. Any residual solvent may reduce the composite performance, while hot-melt impregnation is difficult because of the high temperatures and pressures involved. Powder based methods or comingled fibre prepreg are alternative methods to manufacture thermoplastic carbon fibre prepreg [20], [22], [23].

A thermoplastic carbon fibre prepreg may be used in thermo-forming operations, automated tape laying (ATL) techniques or filament winding. All three processes require heat to soften the matrix during forming/placement and pressure for consolidation to obtain good impregnation of the matrix in the fibre reinforcement. Typical problems during these processes relate

to the formability of the continuous fibre material on the required geometry, similar to thermoset prepreg material systems, such as wrinkling, bridging or buckling of continuous fibres. Replacing continuous fibres with discontinuous ones would allow for some of the underlying driving physics behind some of these manufacturing issues to be mitigated [12].

Fibre-reinforced thermoplastic composites may also be produced by extrusion or pultrusion techniques. In pultrusion, continuous carbon fibres are pulled through an impregnation station where the molten thermoplastic matrix is injected, after which the impregnated fibres are pulled through a cooling die to obtain the final shape. Extrusion techniques allow (often discontinuous) fibres to be mixed with a thermoplastic resin and extruded through a shaping mould by either a screw extruder or ram extruder. Extrusion manufacturing is similar to fused filament fabrication discussed further on, where extruded material is directly used to build up a part. A challenge for extrusion techniques is how to prevent fibre breakage, as the brittle carbon fibres easily fracture in high shear flows and by the rotating extrusion screw.

Having established how fibre architecture and polymer type influence the available manufacturing methods, it is now worth discussing the importance of compatibility between the fibre and the matrix. The chemical interface between the fibres and matrix is important to maximise the reinforcing effect of the fibres, by maximising load transfer and preventing premature interface failure. Carbon fibres intrinsically have a poor interfacial adhesion with polymers (both thermoset and thermoplastic) due to their hydrophobicity and chemical inertness [24]. For thermoset composite materials, the resin cures around the fibres and new chemical bonds are made. Special fibre coatings, or *sizings* which are typically based on a similar polymer as the resin, may be used to improve the fibre-resin adhesion or compatibility [25]. In general, carbon fibres surrounded by thermoplastic matrices have lower interfacial properties than with thermoset matrices due to weak physical interactions between the polymer and the fibre [24],[26]. For thermoplastic composite materials, the matrix cools down around the fibres during manufacture, but no new chemical bonds are made.

The interface between thermoplastic polymers and carbon fibres depends on the fibre surface microstructure, functional groups in the polymer chain, possible sizings and the surface energy. Figure 2.4 shows two Scanning Electron Microscope (SEM) images of thermoplastic resin drops on carbon fibres with very different levels of matrix wetting, indicating different surface energies between the fibre and polymer as the contact angle differs greatly. Somewhat surprisingly, studies have shown that the removal of existing thermoset optimised sizing from carbon

fibres has improved the interfacial performance with high temperature thermoplastics [27]. This may be attributed to degradation of the thermoset sizing due to higher temperatures [25]. Improvements on the interfacial properties between carbon fibres and thermoplastic have been reported by tailored surface treatments and coatings [25], [28], [29].

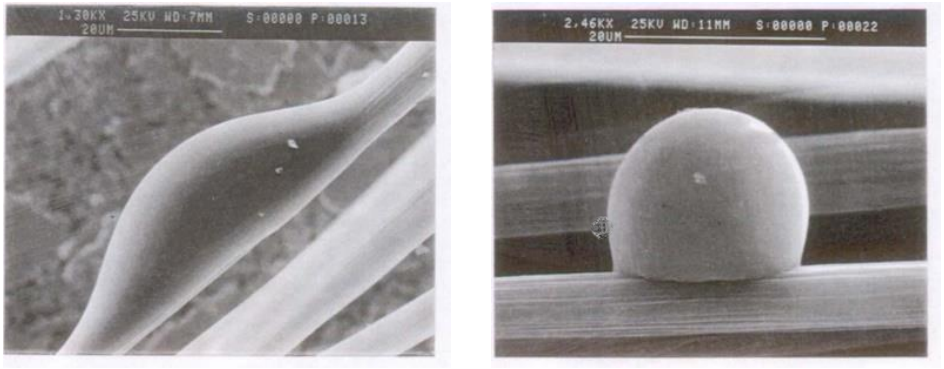

(a) (b)

Figure 2.4: SEM micrograph of (a) PEEK polymer and (b) PEI polymer droplet on carbon fibre [21].

2.1.4 Fibre - matrix interface analysis

This section presents a simple stress-based, analytical derivation of the mechanics of the fibre-matrix interface as a way of establishing the key driving parameters in the performance of these interfaces, and the way in which they scale with fibre geometry. It is these physics which drive the performance benefits of moving from the very short fibre reinforcements used in other work to the beyond critical length fibres used within this work.

When a fibre reinforced polymer material is loaded, the polymer matrix distributes the load between the fibres. The fibres have a much higher stiffness than the matrix which means they will carry most of the loading. On a micromechanical level, each fibre is loaded through shear stress transfer by the matrix. For the reinforcement to have maximum effect, interfacial failure must be prevented before fibre failure as this would limit the maximum attainable strength of the composite material. The failure load of a fibre typically cannot be changed, as it depends on the fibre type and its cross-sectional area which normally is fixed. The interfacial failure load between the fibre and the matrix can be changed by increasing the area through which shear transfer takes place. Larger diameter fibres can be used (but typically this is a fixed property) or the fibre length can be increased. For very short fibres, the interface will fail before the fibre as there is not enough surface area available to load the fibre. The fibre length which is needed for fibre fracture to occur at the same point as interfacial failure is known as the critical fibre length. Above this length, the fibre is loaded such that it fails before the interface.

The load transfer between the fibres and the matrix can be analysed by assuming a perfect bond between the fibre and polymer matrix. There must exist a shear stress between the polymer matrix and the carbon fibre as their moduli are different. For an infinitesimal segment of the fibre as shown in Figure 2.5, the force equilibrium gives a relation between the stress in the fibre σ_f and the shear stress τ at the interface as shown in Equation (2.2). This can be simplified to Equation (2.3).

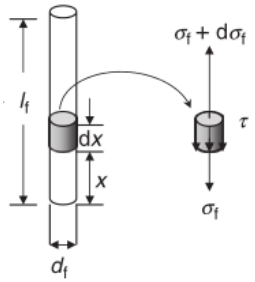

Figure 2.5: Stress analysis of small fibre segment loaded through shear [1].

$$\left(\frac{\pi}{4}d_f^2\right)(\sigma_f + d\sigma_f) - \left(\frac{\pi}{4}d_f^2\right)(\sigma_f) - (\pi d_f d_x)\tau = 0 \tag{2.2}$$

$$\frac{d\sigma_f}{dx} = \frac{4\tau}{d_f} \tag{2.3}$$

Using the same symbols as in Figure 2.5, the stress σ_f in the fibre can be determined by integrating Equation (2.3) over the length x as shown in Equation (2.4). Assuming there is no stress at the fibre ends (i.e. $\sigma_f = 0$) and the interfacial shear stress is constant, Equation (2.5) is obtained.

$$\sigma_f = \frac{4}{d_f}\int_0^x \tau dx \tag{2.4}$$

$$\sigma_f = \frac{4\tau}{d_f}x \tag{2.5}$$

Equation (2.5) shows that the stress increases linearly from the fibre end to a maximum stress at the centre of the fibre. For a fibre with length l_f, the maximum stress in the fibre $\sigma_{f,max}$ can be found at $x=l_f/2$ by Equation (2.6). The critical fibre length l_c is the length at which the maximum stress in the fibre is equal to the ultimate fibre stress $\sigma_{f,u}$, causing fibre fracture, which is given in Equation (2.7). It shows that l_c will increases with the ultimate fibre stress $\sigma_{f,u}$ (i.e. a stronger fibre has to be longer to become fully loaded) and with fibre diameter (as failure load of a fibre scales with d_f^2 and the shear transfer with the matrix scales with d_f). A higher interfacial shear strength (IFSS) τ_{IFSS} decreases the critical fibre length, which shows that a stronger interface means shorter fibres may be used to obtain fibre failure as expected.

$$\sigma_{f,max} = \frac{4\tau_{IFSS}}{d_f}\frac{l_f}{2} \tag{2.6}$$

$$l_c = \frac{\sigma_{f,u}}{2\tau_{IFSS}} d_f \tag{2.7}$$

More advanced models based on shear lag theory have been developed, taking into account the relative deformation of the fibres and resin to better predict the shear stress transfer, but the concept of a critical fibre length for discontinuous fibres is well understood [30]–[32]. From literature, the critical fibre length of carbon fibres in thermoplastic matrices is expected to be about 1 mm [33]–[36], but strongly depends on the exact matrix and fibre type used. Generally, composites with fibre lengths at l_c will have a lower performance than those made with continuous fibres as the fibres are loaded less efficiently due to lower stresses at the fibre ends. The average fibre stress can be calculated using Equation (2.8) below, where l_f is the fibre length.

$$\bar{\sigma_f} = \sigma_{f,u}\left(1 - \frac{l_c}{2l_f}\right) \tag{2.8}$$

As the fibre length increases in discontinuous fibre composites, strength approaches continuous fibre performance. For example, at a fibre length l_f three times the critical fibre length ($3 \cdot l_c$), 83% of the continuous fibre composite strength can theoretically be obtained.

2.1.5 Concluding remarks

An overview on polymers, fibres and fibre reinforced polymer matrix composites has been presented. Various fibre architectures are available that give different control of fibre orientation and determines possible manufacturing methods and constraints. Continuous fibre composites are known for the highest mechanical performance, but a problem is the placement of the continuous fibres into complex geometries. An analysis was presented that showed discontinuous fibres can reach similar performance levels as their continuous fibre counterparts if the fibres are sufficiently long, while benefiting from more processing freedom.

The polymer matrix type influences the available manufacturing methods and potential recycling opportunities. Thermoplastics may be reshaped and re-melted but have a higher viscosity than thermoset resins which makes consolidation more difficult. Thermoplastic processing methods allow direct fabrication of objects using additive manufacturing (AM). The combination of AM and fibre reinforcements is a recent development for composites materials that is discussed in the next section.

2.2 Review of state-of-art on composite 3D printing

Additive manufacturing techniques, such as FFF, commonly known as 3D printing, have an underappreciated similarity to those of traditional composite materials, as both are inherently based on stacking a series of discrete layers. In both processes, the lay-up orientation plays an important role to tailor the properties of the manufactured part. It is therefore reasonable to suggest that successful adaptation of 3D printing technologies to composite materials could enable a simple composite manufacturing method with lower production cost and a high degree of automation. As reinforcements can be accurately placed, the laminated structure of composite parts can be further optimised in each layer, allowing for an increase in design freedom and mechanical performance.

While still a relatively undeveloped avenue of research, in the last five years several commercial applications for fibre reinforced 3D printing have become available. One of the first commercial 3D printers capable of processing continuous fibre reinforced composite materials were developed by MarkForged [3]. The Mark One and Mark Two printers developed by MarkForged print continuous carbon fibre reinforced PA with mechanical properties an order of magnitude higher than typical polymer 3D printers, and open new applications in both the personal fabrication market and in the manufacture of lightweight parts for industry. Other continuous fibre 3D printing methods are being developed by Arevo Labs, Anisoprint and 9T labs amongst others [4], [37], [38]. Several short fibre reinforced filament are commercially available for use on standard desktop 3D printers with different matrices [39]–[41] that result in more rigid 3D printed parts. Another notable composite additive manufacturing technique is the Big Area Additive Manufacturing at the Oak Ridge National Laboratory [42]. Instead of a filament, it uses a screw extruder to extrude pelletized material (including carbon fibre reinforced polymers) for large scale additive manufacturing.

Significant challenges remain for 3D printing of CFRPs. In addition to some process specific limitations with the MarkForged printers, which will be discussed in further detail below, there are more fundamental issues which need addressing. For example, there are currently only a few different materials available for fibre reinforced 3D printing, which limits application areas and design flexibility. The addition of (short) fibres to the printing filament increases the stiffness of the part but the strength increase is still limited as fibre pull out may occur before fibre break-

age. Furthermore, current printing techniques and material options lead to the creation of significant voids in the finished parts, which have a negative impact on the obtainable strength of composites [43].

Here, a review is presented on the body of knowledge of 3D printing of fibre composites using the FFF technique, followed by a detailed consideration of the processing parameters which dictate the final part quality. The aim is to identify to what extent FFF may be used as a composite manufacturing method, considering along the way what progress has been made and what challenges remain. Following this, an experimental characterisation of two of the best currently available methods of composite 3D printing (continuous fibre printing and short fibre printing) is presented to benchmark the state-of-the-art. Comparisons were made between the two methods in terms of mechanical properties, part quality and printing versatility.

2.2.1 Additive manufacturing techniques

A wide range of additive manufacturing (AM) techniques exist, with new methods constantly being invented and commercialised. The ISO/ASTM52900-15 standard defines seven AM categories, as shown in Figure 2.6. A brief overview is given here with the advantages and disadvantages of most common AM techniques with respect to their potential to be used to print composite materials. As the main focus of this section is the ability of these methods to make composite materials, the reader is referred to the comprehensive review paper by Stansbury and Idacavage for a more thorough overview of additive manufacturing methods [44].

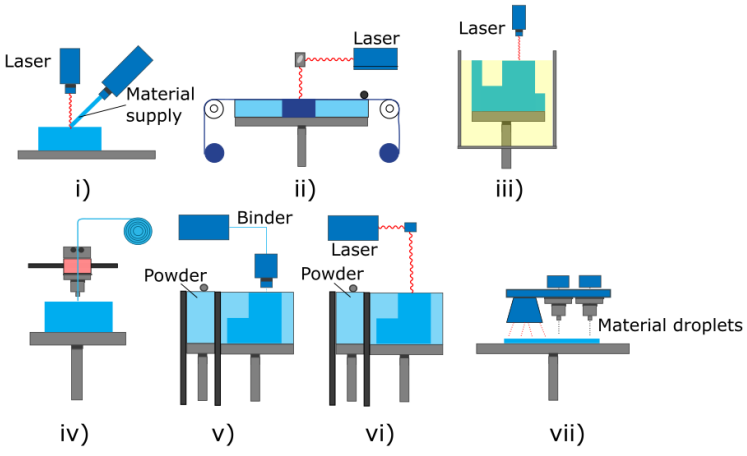

Figure 2.6: Seven categories of AM: i) Directed Energy Deposition, ii) Sheet lamination, iii) Vat photopolymerization, iv) Material extrusion, v) Binder jetting, vi) Powder bed fusion vii) Material jetting.

Directed Energy Deposition (a.k.a Direct metal deposition – DMP, Laser Metal Deposition - LMD): a laser is used to locally melt a metallic material, and material is fed into the melt pool to locally deposit new material. This material is thus fusion bonded together, which

results in good adhesion and mechanical properties. A downside of this technique is that support structures are required, and careful control is needed of the laser, powder and metallic substrate and typically only one material is used.

Sheet lamination (a.k.a. Laminated Object Manufacturing – LOM): uses a layer of paper/plastic/metal which covers the printing bed or layers below. The top layer is then cut to the required shape by a laser and fused together to the material below with heat and pressure applied by a hot roller. The part is built up by repeating this process and the sheet theoretically may be reinforced with fibres, but the method allows little control of the fibre orientation.

Vat photopolymerization (a.k.a. Stereolithography – SLA/SL): uses a laser to cure a liquid photopolymer resin. This can be done with high accuracy (up to 10 μm). The resin needs to be photo-curable, limiting flexibility in material selection. The method is not deemed ideal for printing composites as a reinforcement would have to be suspended in the liquid resin and fibre orientation would be hard to control. The presence of the fibres may also negatively affect the photopolymerization process. For complex geometries, the design may require support structures which need to be removed in a post-processing stage. Warpage may also occur as the material goes through a phase change (liquid to solid).

Material extrusion (a.k.a. Fused Filament Fabrication – FFF, Fused Deposition Modeling – FDM): extrusion of a thermoplastic material by melting and depositing material layer by layer. Different thermoplastics can be used depending on the requirements and fibre reinforced filament can also be used. Adhesion between layers can be poor as material solidifies layer by layer. Features which overhang beyond a critical overhang angle (~45°) require supports. Accuracy can be high (100μm), but production speed is limited by melting and cooling of the thermoplastic material.

Binder jetting: uses a liquid binder to bond powder particles together, distributing new layers of powder on top of each other to build up the part. Curing may be done between each layer or as a post-processing stage to improve bonding of the powder particles. Different binders may be used with different powders, creating a variety of composite materials, but little control of orientation is possible within this process.

Powder bed fusion (a.k.a. Selective Laser Sintering – SLS, Selective Laser Melting – SLM, Electronic Beam Melting – EBM): uses a laser or electron beam to melt/sinter powdered materials. A layer of powder is locally melted/sintered after which a new layer of powder is added and the process is repeated. This allows complex structures to be made and does not

require support structures. Typically, polyamides are used but other polymers used in SLS include polypropylene, polycarbonate and Polyether ether ketones (PEEK) [45], [46]. The resulting part, however, is usually relatively porous. Fibre reinforcements can be added up to 50wt% but typically have very short fibre lengths of about 50 μm and it has been reported to result in more isotropic material properties [45], [47]–[52], [48], [49] .

Material jetting: similar to material extrusion but with droplets instead of a continuous filament. Droplets are jetted onto the printing bed/previous layers and may be charged to improve uniformity and deposition accuracy. Different materials can be used but only droplets can be deposited, limiting the use of stiff reinforcements.

2.2.2 Material extrusion processes

Material extrusion-based 3D printing techniques, such as FFF and FDM, are manufacturing processes where a solid thermoplastic material is extruded through a hot nozzle. The viscous material solidifies on the build plate which allows build-up of a part with dimensional accuracies typically in the order of 100 μm [53]. The most commonly used thermoplastics for this process are acrylonitrile butadiene styrene (ABS) and polylactic acid (PLA), with typical bulk strengths between 30–100 MPa and elastic moduli in the range of 1.3–3.6 GPa [54]. Mechanical properties of 3D printed parts, however, can deviate significantly from the material bulk properties due to the specifics of how a structure is formed on the meso-scale during printing [55].

To maximise the mechanical performance of printed parts, the key elements of the printing process and how they affect final print quality must be understood (Figure 2.7). Turner et al. [53], [56] provide an extensive review on FFF process modelling, including the flow and thermal dynamics of the melt, the extrusion process and the bonding process between successive layers of material. Temperature, viscosity and surface energy of the melt play an important role in how the material flows through the nozzle and more importantly, how the final interface between the beads is formed.

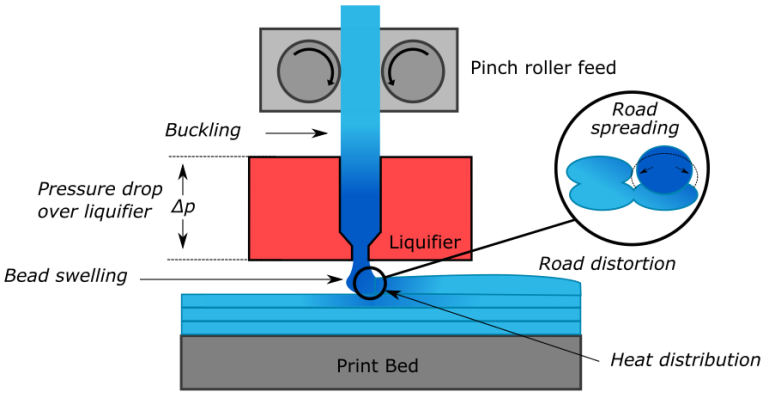

Figure 2.7: Key elements of the FDM process, adapted from [56].

One of the major process variables is the raster angle, as illustrated in Figure 2.8, which is the angle between the global *x*-axis and the dominant material axis (1-axis). This leads to different properties across the principal material directions [57]–[59], similar to the orthotropic behaviour of fibre composites. This allows for design tailoring, but stiffness can be 11% lower and tensile strength up to 50% lower in the weaker 2- and 3- directions compared to the bulk properties, as the interface between printed tracks can be weak [60],[61].

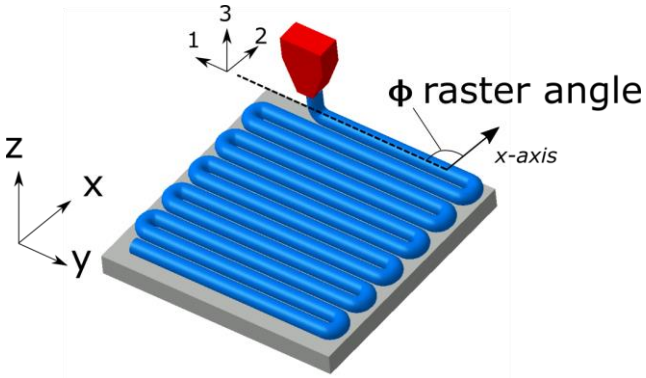

Figure 2.8: Example of meso-structure of 3D printed parts with raster angle.

Important features on the mesoscale are the contact area between the printed tracks and the minimization of the overall void content, as they can have a large effect on the printed part strength. Different printing patterns can be used to increase area of contact between the printed tracks and minimize the void content as shown in Figure 2.9. Several studies analysed the void density in 3D printed parts, both analytically and experimentally, with changing the gap size between tracks [55], [62]. A small overlap between the tracks gave the best results, with a void density of ~5% in the 1-3 plane and 27% in the 2-3 plane. Micrographs taken of 3D printed structures typically show a clear meso-structure with diamond or triangular shaped interbead voids, as shown in Figure 2.9.

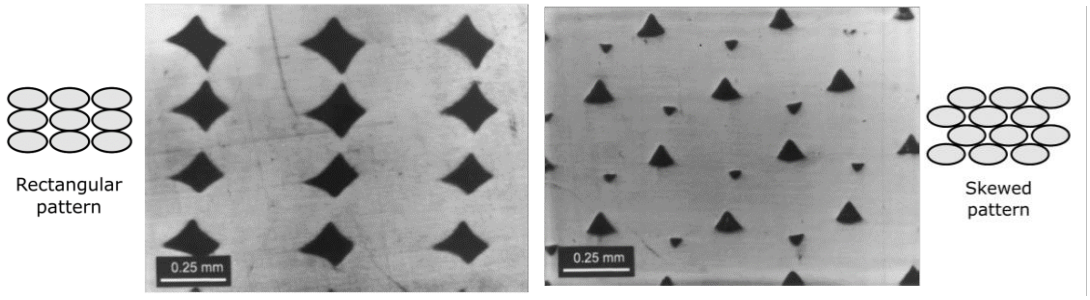

(a) **(b)**

Figure 2.9: Micrographs and schematics of two different meso-structures, a) rectangular and b) skewed, showing typical triangular void formation [55].

On a molecular level, good chemical bonding between the polymer chains inside of adjacent beads is required for effective load transfer to obtain a high strength part [43],[63]. After extrusion, the hot, viscous thermoplastic material bonds with surrounding material through a mechanism known as polymer sintering. After contact, the newly deposited polymeric material coalesces with the previously deposited material in a process driven by surface tension and viscous flow for polymers above their glass and melt temperatures [43].

The amount of initial surface contact and the distribution of heat between two adjacent beads leads to the formation of a neck (Figure 2.10) as absorptive equilibrium is reached (a lower state of overall energy by minimizing surface area). This process is inhibited by the viscosity of the material. During neck formation, diffusion of the polymer chains occurs while the viscosity of the material increases as it cools down, slowing down the neck formation and diffusion process [56]. No external pressure is applied and the bond strength between printed tracks is determined by how well the polymer chains are entangled across the boundary [64], [65].

Reptation theory, as introduced by de Gennes in 1971, describes the thermal motion of polymer chains as snake-like Brownian motion. This can be used to predict the reptation time, a characteristic time for the polymer chains to have completely moved to a new position [66],[67]. The reptation time is an important characteristic time that relates to the level of (new) entanglement across an interface and can be used to predict the bond strength [65], [67].

This polymer sintering process is therefore sensitive to the viscosity (temperature dependent), thermal conductivity and heat capacity of the material, as well as the cooling rate (determined in part by the external environment). A higher temperature leads to better flow of the polymer melt and a higher mobility of the polymer chains, improving the polymer sintering and diffusion process. Similarly, a higher thermal conductivity would improve heat distribution, aiding the chemical bonding between filaments as previously deposited material heats up to improve the

sintering process. At too high temperatures, however, the polymer may degrade, and dimensional accuracy may decrease because of the increased flow.

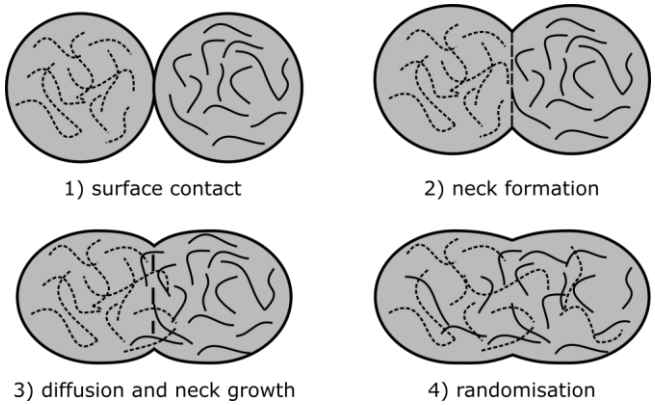

Figure 2.10: Schematic overview of the polymer sintering process, adapted from [56].

Multiple attempts have been made to numerically model the polymer sintering process based on heat transfer calculations. Early work by Yardimci *et al.* [63], [68] presented different modelling approaches to capture the heat transfer between printed beads, but did not look at the polymer flow dynamics. Bellehumeur *et al.* [64] used a model based on a polymer sintering model described by Pokluda *et al.* [69]. This approach performed an energy balance between surface tension and viscous dissipation [69], but with the extension of temperature dependent surface tension and viscosity. Although they did not model molecular diffusion, they found that the extruded material cools too quickly for complete bonding. They also report that the convective heat transfer coefficient has a large effect on the bond formation and neck growth, where less heat transfer leads to better neck formation. However, they modelled isothermal polymer sintering and did not consider the heat transfer from the hot extruded material to the surrounding material. Bellini [70] performed extensive modelling of the entire FDM process with ceramic filled filament using four different numerical simulations focusing on; the liquefier, the nozzle contraction, deposition on the printing bed and on stacked layers. This enabled tracking of the material temperature, swelling and filling as a function of various printing parameters. It was found that the higher thermal conductivity of the filled material increased heat transfer from the liquefier to the printed material and improved the flow behaviour.

To conclude, Figure 2.11 summarises the discussed printing and material parameters that influence the print quality, mapped to the different stages of the printing process. Overall, the key to high quality parts is to obtain good surface contact and temperature conditions for optimal polymer sintering. The viscosity and surface tension of the material are important parameters, as they dictate the flow characteristics which are mainly dependent on temperature. Therefore, the

heat conductivity and capacity are important, as they affect how heat is distributed and the temperature profiles of the printed tracks. Qualitatively, the main sintering process is well understood and several studies focused on the effect of some of these parameters [71]–[73]. Of further interest is how the addition of fibre reinforcement to the feedstock will affect these parameters which is discussed below.

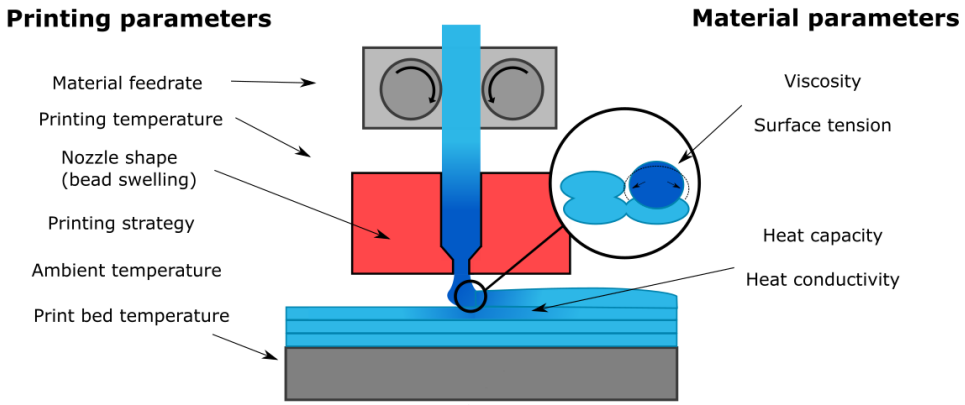

Figure 2.11: Main parameters for good surface contact and temperature conditions to enable optimal polymer sintering conditions.

2.2.3 Reinforced filaments for material extrusion

The FFF process can be utilized to print CFRPs by adding fibres into the thermoplastic filament. Besides the obvious motivation of increasing mechanical properties, the reinforcement may also be used to add extra functionality to the material such as higher heat conductivity, electroconductivity or biocompatibility. Kalsoom *et al.* [74] and Wang *et al.* [75] recently provided a general overview of 3D printable composite materials; this work instead provides a more detailed focus on the engineering aspects of FFF as a composite manufacturing method. The use of fibre reinforcements in 3D printing filaments for FFF is a topic of on-going research with both advancements in scientific literature as well as in commercial products, e.g. the MarkForged printers and the numerous reinforced thermoplastic filaments available on the market [3], [76]–[83].

Table 2.1 shows an overview of the different studies performed to date on printing of reinforced filaments, showing the different methodologies and resulting relevant mechanical properties. Most studies report on the use of very short carbon fibres (~0.1 mm) which are mixed with a thermoplastic polymer and then typically screw extruded to create the filament used in traditional FFF printers. This increases the strength and stiffness of the printed material by around 65%, but this level of performance remains low compared to CFRP materials made with traditional composite manufacturing methods (e.g. pre-preg/autoclave, resin infusion, etc). High

shear mixing leads to fibre breakage, reducing their length in the filament and consequently lowering the strength of the printed part [84].

Commercial short fibre reinforced filaments makers were contacted who typically fabricate their filaments using this screw extrusion method. Typical fibre content of commercially available fibre reinforced filaments varies between 10 to 20%, with reported tensile strength values from the datasheets in the order of 55 MPa and a tensile modulus of ~4 GPa [40], [41], [87]–[91]. This confirms the fibres in commercially available short fibre reinforced filaments are too short to reach their full strength.

Table 2.1: Overview of studies on printing of reinforced filaments.

Study	Matrix	Reinforcement	Amount of reinforcement	Manufacturing technique	Result	Other
Ning *et al.* [85]	ABS	Carbon fibre powder (L=100 µm, 150 µm and Φ = 7.2 µm)	3-15 wt%	Mixing in blender, followed by double extrusion	Strength from 34 MPa to 42 MPa, stiffness from 2 GPa to 2.5 GPa, decrease in toughness, yield strength and ductility.	An increase in void content increase from 3% to 9% was recorded for 10 wt% specimens
Tekinalp *et al.* [77]	ABS	Short carbon fibres (L = 3.2 mm, after 0.26mm mixing)	10,20,30,40 wt%	Mixing with torque rheometer, followed by plunger extrusion	Strength from 35 MPa to 65 MPa. Stiffness from 2 GPa to 14 GPa	For 40 wt% some nozzle clogging. Good fibre orientation for printed parts. Void content 16-27%.
Matsuzaki *et al.* [78]	PLA	Continuous carbon fibres and jute fibres	V_f of 6.5%	Pre-heating fibres and adding it to thermoplastic filament	Strength from 40 MPa to 185 MPa, modulus from 4 GPa to 20 GPa, with a decrease in maximum	Fibres poorly distributed at the outside of the filament due to manufacturing technique, voids reported but not quantified
Shofner *et al.* [79]	ABS	Vapor grown carbon nanofibers L=100 µm and Φ=0.1 µm)	10 wt%	Sizing added to nanofibers, banbury mixing, compression moulding, granulation, screw extrusion	Strength from 26.9 MPa to 37.4 MPa and stiffness from 0.49 GPa to 0.79 GPa.	Poor adhesion between fibres and resin found by SEM pictures. Good alignment.
Mahajan and Cormier [80]	Epoxy resin	Short carbon fibres (L=100 µm, Φ=7.2 µm)	15 wt%	Mixing of epoxy resin and fibres, and printing via syringes	Strength from 46MPa to 65 MPa and modulus from 2.8GPa to 4.05 GPa.	FFT analysis was used to obtain the fibre orientation. It was found through design of experiments that fibre content, translation speed and nozzle diameter had a significant effect, while fibre length and printing pressure were less important.
Peng *et al.* [81]	Epoxy resin	Short glass fibres (L= 0.8 mm, Φ= 10 µm)	8 wt%	Mixing of epoxy resin and fibres and printing via syringes	Flexural modulus increase from 4.2 to 6.3 GPa and flexural modulus from 91 MPa to 109 MPa from unaligned to aligned fibres.	Similar to Mahajan and Cormier [80], writing speed was found to have a significant impact on fibre orientation.
Yang et al. [86]	ABS	Continuous carbon fibre	10 wt%	In-situ impregnation of continuous fibre through melt pool of matrix before printing	Flexural strength of 7127 MPa and flexural modulus of 7.72 GPa	Very low interlaminar shear strength of 2.81 MPa.
Lewicki et al. [83]	Epoxy resin, modified for fast curing	Carbon fibres (L=300 and 600µm and Φ = 6 µm)	V_f of 8%	Direct Ink Writing, mixing of resin with reinforcements using centrifugal mixer and printing using 3ml syringe	Strength of 172 MPa and stiffness from 2 GPa to 5.5 GPa.	15 wt% silica nanoparticles were added to the resin such that it behaves as a thixotropic, non-Newtonian fluid which improved flow of the fibres.

The porosity of 3D printed short fibre composite parts has also been investigated. Three types of voids are identified by Ning *et al.* [76] as shown in Figure 2.12 which were; (1) gas bubbles in the matrix, (2) interbead voids between the printed tracks and (3) fibre pull-out. They found that the overall porosity initially decreased with the addition of fibres, but at fibre contents above 10 wt% the porosity increased to almost 10%. The authors did not distinguish between inter-

bead void content and voids created from fibre-pull out. Tekinalp *et al.* [77] found a reduction of inter-bead voids with the addition of fibres, which was attributed to a decrease in die swell and increase in thermal conductivity, which helps the surrounding beads to soften and improve polymer sintering. However, voids were found around the fibres indicating incomplete wetting, and the number of these voids increased with higher fibre contents. This was attributed to a weak fibre-matrix interface and partially independent movement of the fibres and matrix during extrusion. Lastly, Zhang *et al.* [92] found an increase in porosity with the addition of fibres to ABS filament which shows the effect of reinforcement on the porosity is not fully understood.

Bellini [70] found from numerical studies that the increased thermal conductivity caused by reinforcement (roughly a factor of 7 higher than unreinforced material) improves heat transfer from the liquefier to the printed material, improving overall flow. The addition of fibres to the printing filament reduces die swell, as reported in three different studies [70],[77],[79],. The addition of fibres may be used to alter the thermal energy transfer between printed beads during deposition and the flow and the swelling behaviour of the material when leaving the nozzle.

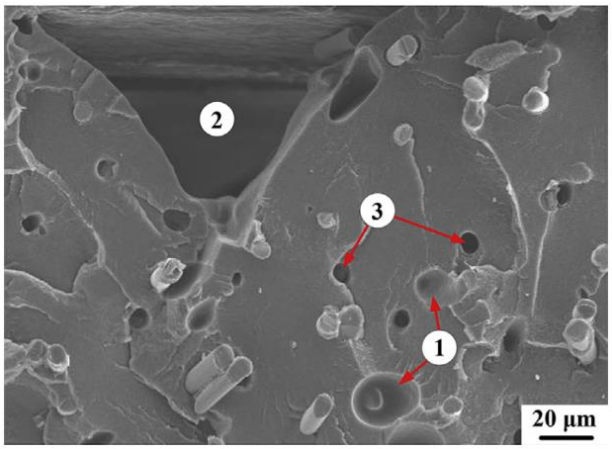

Figure 2.12: Different categories of porosity in 3D printed carbon fibre composites, (1) gas bubbles (2) inter-bead voids and (3) fibre pull-out [76].

Another promising, albeit less common, approach to 3D printing composites is to use filaments reinforced with continuous fibres. MarkForged has developed a printer which deposits continuous fibres (carbon, glass or Kevlar) in a Poly-amide (PA, Nylon) matrix. The manufacture reports strength and stiffness of printed parts with carbon fibres of 700 MPa and 50 GPa respectively [3]. A ~0.4mm diameter continuous fibre/Nylon filament is fed through a heated nozzle and, after it is initially anchored to the printing bed, dragged along the print bed to build up the current print layer, with the continuous fibre filament being cut with a mechanical shear as needed to terminate layers or features. As it is printed, the fibre reinforced filament is transformed from

an initially round cross-section to a rectangular one, with a significant amount of compression and flattening occurring to improve in-fill and inter-laminar bonding. This process, and its limitations are discussed further in the experimental section (section 2.3.1.1).

Yang *et al.* [86] developed a novel composite extrusion head, where dry carbon fibre is fed through a melt pool of ABS. This increased in-plane mechanical properties by a factor of 2-5, but a limiting factor was the interlaminar shear properties of the printed part. Matsuzaki *et al.* [78] printed continuous fibres (straight carbon fibres or twisted jute fibre yarns) by feeding them through a nozzle simultaneously with a thermoplastic filament (PLA) which acts as a matrix. They reported a strength and stiffness of 195 MPa and 10.5 GPa respectively which may be attributed to a low V_f of 6.6%. This technique also showed a non-uniform fibre distribution as the fibres were not pre-impregnated in the matrix.

From the review of the composite 3D printing technology presented above, two main printing methods approaches can be identified: the printing of short (0.1 mm) fibres with traditional material extrusion based printing methods and continuous fibre printing with a custom printing head and technique. Despite multiple studies available on both methods, there does not seem to be a clear consensus how these two methods compare in terms of printing versatility, print quality and mechanical properties. To better understand the two methods and how they compare, both will now be evaluated in terms of mechanical properties and printing characteristics in a direct comparison test using the best currently commercially available examples of each approach before drawing final conclusions on how FFF may be used to manufacture cost-effective, high quality parts with good mechanical performance.

2.3 Benchmarking study on the state-of-the-art of composite 3D printing

A direct contribution to the state-of-the-art of composite 3D printing was made by benchmarking a continuous fibre printing method and short fibre printing method. The findings of this benchmarking study are presented here to give a direct comparison on the two main composite 3D printing methods. The part quality and mechanical performance of 3D printed composite parts manufactured using two different printing methods were investigated. Continuous carbon fibre/PA 3D printed parts were made using the Mark Forged MarkOne printer and discontinuous carbon 'microfibre' reinforced PA parts were made using a standard desktop 3D printer. Various experiments were performed to quantify key mechanical properties, including

the most detailed set of mechanical tests on the MarkOne printed parts reported to date, and optical microscopy was used to examine the quality of the parts.

2.3.1 Printing set-ups

2.3.1.1 MarkOne continuous fibre printer

The MarkOne printer is a proprietary 3D printer which can deposit a filament made of continuous fibres embedded in a PA matrix. The printer has two printing nozzles as shown in Figure 2.13, one to deposit pure PA filament, and one for fibre reinforced PA filament. Due to confidentiality issues, the exact fibre and matrix type is unknown but it is reported the matrix is a PA-6 blend [93], [94]. The unreinforced PA nozzle is crucial for the overall integrity and quality of the prints, as the fibre filament cannot be used for the outer layers of the parts (top, bottom, sides). For more complex shapes and thin features there often are large regions which the fibre filament is not able to fill, which instead are filled with the unreinforced PA. The PA filament and PA/fibre filament are fed through Teflon Bowden tubes which run between the drive motors and the nozzles, as highlighted Figure 2.13.

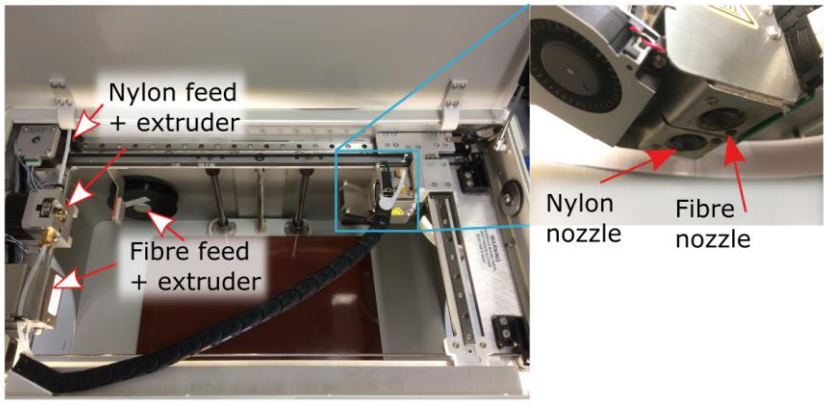

Figure 2.13: Overview of the MarkOne Printer with the dual nozzle system to print PA filament and fibre filament.

To print an object, a proprietary slicing software must be used. This software is "closed source" and does not allow for user adjustment of key printing parameters such as temperature, nozzle movement or extrusion speed. This limits the printing capabilities as the printing settings cannot be fully customized. For the deposition of carbon fibres, only a circumferential fill pattern is possible which fills the shape from the outside inward in a spiralling motion. This means the fibre is always orientated along the outer perimeter of the part. The tightest corner radius allowed by the software is 0.6 mm which was determined from the deposition path in a sharp angle.

A 3D object is sliced into layers with a layer height of 0.125 mm for carbon fibre reinforced layers. The bottom and top layers are always printed with the 100% triangular fill PA filament, as well as the outer periphery for each layer. This is presumably done to avoid exposed fibres on the outer surface and to take advantage of the higher quality surface finish and accuracy available from the unreinforced PA. While this feature exists for sensible reasons, it has the negative effect of lowering the overall fibre volume fraction for the part - and thus the maximum achievable mechanical properties. Printing is done at 260 °C with at an estimated speed of 6.90 cm^3/hr for the PA layers and 2.39 cm^3/hr for the carbon fibre layers. A significant downside of PA is that it is sensitive to water absorption, which plasticizes the matrix and can lead to a decrease in strength of up to 33% [95].

To provide a reliable and useful benchmark of the MarkOne printer, the most extensive suite of mechanical tests and printing trials reported to date were performed. The tensile, flexural and shear response of the printed material have been measured. To get around the limitations in fibre orientation caused by the circumferential fill pattern, the tensile specimens were printed in an "oval racetrack" shape to allow for two unidirectional 0° specimens to be extracted from each print, as shown in Figure 2.14a. The dimensions of the tensile specimens were 250 mm×15 mm×1 mm, sized in accordance to ASTM standard D3039 [96], where the bottom and top layers of 0.125 mm thickness were 100% triangular fill PA as discussed above. The volume fraction of these specimens was $V_f \approx 27\%$, estimated using optical microscopy as shown in section 2.3.2.1. Glass fibre tabs with a length of 25 mm were bonded to the specimen using an epoxy adhesive and the tensile test was carried out at constant displacement rate of 2 mm/min in a servo-hydraulic test machine. Strain measurements were obtained from a video extensometer (IMETRUM, UK) over a gauge length of 100 mm, and the load was obtained from a 25 kN load cell (Instron).

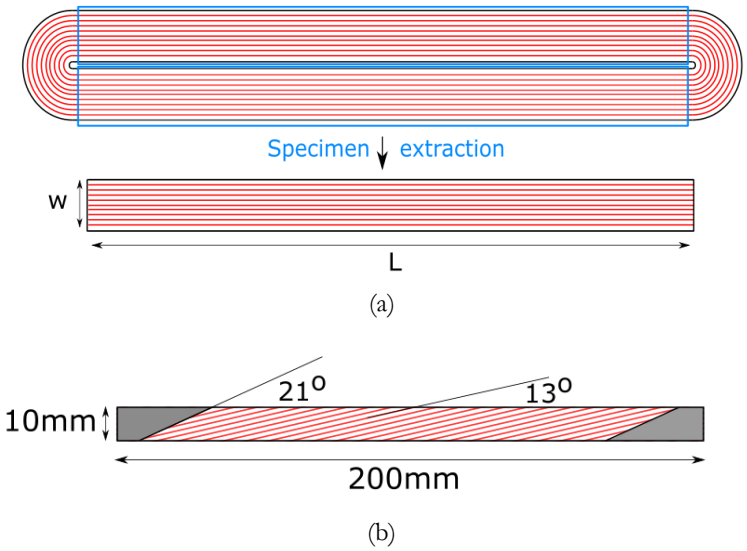

Figure 2.14: Print schematic of (a) unidirectional tensile and flexural specimens and specimen extraction and (b) shear specimens, showing carbon fibre path.

A three-point bend fixture was used to obtain the flexural properties of the printed composite material with a support rod radius of 4 mm and a support length of 128 mm according to the ASTM D7264 standard [97]. The flexural specimens were manufactured in a similar approach as the tensile specimens, with outer dimensions of 160 mm×11 mm×4 mm and all fibres orientated in the 0° orientation. A constant displacement rate of 1 mm/min was used and the force and displacement were directly measured from the machine with a 1 kN load cell.

To obtain the shear properties, the methodology proposed by Sun and Chung [98] was used for uniaxial off-axis testing with oblique end-tabs, as a ±45° specimen could not be printed. The oblique end tabs help create a uniform state of stress from which the shear properties can be obtained. The required oblique angle is a function of the chosen off-axis angle of the fibres and the properties of the composite, which were estimated from the results of the previous tests to be E_{11} = 50 GPa, E_{22} = 0.38 GPa, G_{12} = 3.9 GPa and ν_{12} = 0.3. A 1 mm thick plate was printed to extract the shear samples. The sample dimensions were 200 mm x 10 mm x 1 mm, with the fibres orientated at 13°. The required angle for the oblique end-tabs for a uniform state of stress was 21° [98], as shown in Figure 2.14b. The specimen was tested using an electrical-mechanical tensile test machine with a 10 kN load cell and full field strain measurements were obtained from a 5MP LaVision DIC system.

Lastly, to assess the printing performance of the MarkOne printer and the quality of the continuous fibres deposited, benchmark parts were printed in the form of a 40×40 mm square, a 30°-60°-90° triangle (85×50 mm) and a circle with a diameter of 40 mm. Defects in printed

parts due to the different geometry conditions were investigated using visual inspection and optical microscopy on the printed samples.

2.3.1.2 Short carbon fibre PA filament

Short fibre reinforced PA parts were printed using a Lulzbot TAZ 6 printer and a PA filament which was reinforced with chopped carbon fibres. The material was acquired from Fiberforce Italy (under the brand name Nylforce) and has 6 wt% carbon fibres added to the 3.00 mm diameter filament [40]. In comparison to the Mark One, an open-source printer allows far more control of the material deposition strategy, such as printing tracks, extrusion rate and printing temperature. Tensile and flexural properties are reported in the manufacturer's datasheet [40]. To fully characterize this printing technique and the material, tensile, flexural and shear specimens were printed to determine the mechanical properties. Similarly, optical microscopy was used to investigate the quality of these specimens.

Tensile specimens were printed in dog-bone shapes according to the ASTM D638 [99], using a 0.4 mm nozzle diameter, 0.2 mm layer height and a printing temperature of 260°C as recommended by the filament manufacturer. A 0° fill pattern was used such that the gauge section of the dog-bone specimens consists of tracks aligned in the 0° direction as shown in Figure 2.15. The flexural specimens were printed as rectangles with dimensions 168 mm x 13 mm x 4 mm to match the ASTM D7264 standard for three point bending [97] with a support length of 128 mm. Shear samples were printed based on the ASTM D3518 standard for in-plane shear of composites, with the geometry of a dogbone and a $[\pm 45]_{8s}$ layup. The x- and y- strain components were measured at the gauge section using a video extensometer to obtain the shear modulus and strength. To assess the printing performance with the carbon fibre/PA filament, similar benchmark parts to the MarkOne benchmark parts were printed to investigate the corner radii and quality.

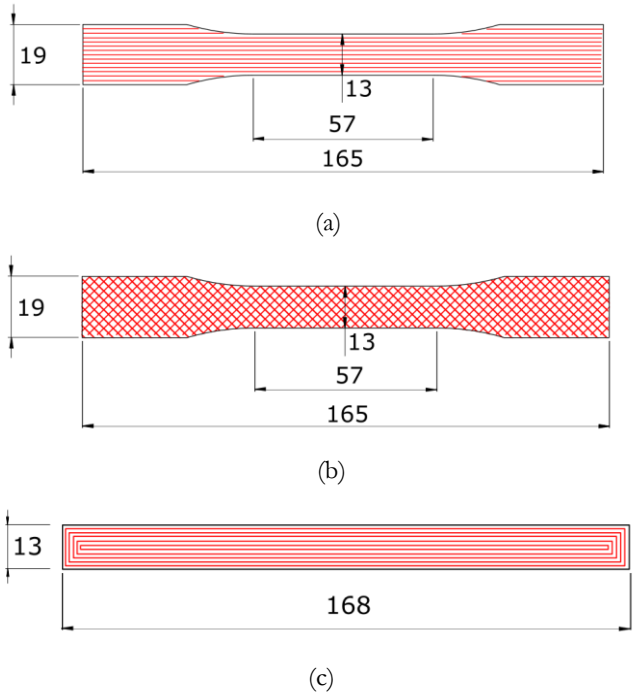

Figure 2.15: Test samples showing (a) tensile dog-bone, (b) shear and (c) flexural specimen printing fill patterns and specimen dimensions.

2.3.2 Performance and processing characterisation of printing methods

2.3.2.1 MarkOne continuous fibre printer

The results of the tensile tests on the specimens printed by the MarkOne printer are shown in Figure 2.16a. Four composite samples were tested which show an average strength and stiffness of 986 MPa (±8.3%) and 62.5 GPa (±4.9%) respectively, which are higher than reported by MarkForged [3]. During the test, characteristic high frequency fibre fracture sounds were heard at a low stress of 200 MPa, after which no fracture was heard before failure. In Figure 2.16a, a slight stiffening effect can be seen where the slope increases at higher strains. This may indicate early fibre fracture of possibly wrinkled fibres, followed by relaxation of most the fibres which leads to better alignment at higher load levels.

The results of the flexural tests are shown in Figure 2.16b. The flexural modulus and strength of the carbon specimens are 41.6 GPa (±4.3%) and 485 MPa (±1.0%) respectively. The flexural strength is lower than the tensile strength which indicates there may be issues with the quality of the printing, as a higher flexural strength is expected for high quality fibre composites [100]. A compressive failure was found for these specimens relating to a poor fibre/matrix interface and/or a high void content as failure initiators.

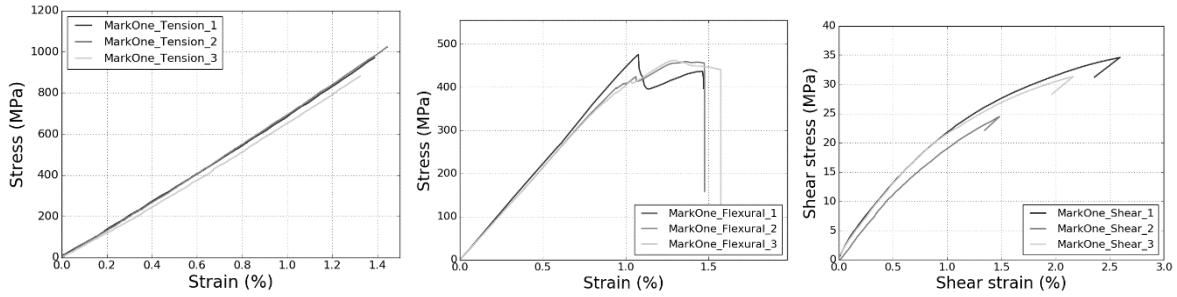

(a) Tensile (b) Flexural (c) Shear

Figure 2.16: Stress-strain graphs for (a) tensile, (b) flexural and (c) shear test results of MarkOne continuous fibre printed specimens.

The shear response of the off-axis unidirectional specimens is shown in Figure 2.16c. The modulus has been determined from the initial linear part of the curve defined between a shear strain of 0.1% and 0.3%. The average shear modulus was found to be 2.26 GPa (±4.9%) and is lower than the predicted value of 3.9 GPa. The predicted value was used to determine the oblique end-test tab angle to obtain a uniform stress state. The difference may influence the results as a non-uniform state of stress occurs which can lead to premature failure. The maximum shear stress was 31.16 MPa (± 15.8%) where it must be noted that specimen 2 failed near the tab, which may explain its lower shear stress.

The printing quality of the MarkOne can be seen in Figure 2.17 with the printing of various generic shapes. The MarkOne printer prints the carbon fibres as a continuous path which spirals from the outside contour to the inside. For more complex geometries, this causes large fibreless areas as shown in the triangular part. These fibreless areas can be up to 2.5 mm x 1 mm, which are recognized by the printing software and are partially filled with pure PA, but this leads to a local weakness in the part. For a simpler shape, such as a square, a similar effect is present in the corner regions on a smaller scale (1.5 mm x 0.3 mm) but the areas are not filled with PA here which leads to voids. For the circular shape, the fibres neatly follow the outside contour with some small gaps with a width of roughly 0.05 mm. The minimal corner radii *r* was determined from the inner circular shape which was ~1.4 mm.

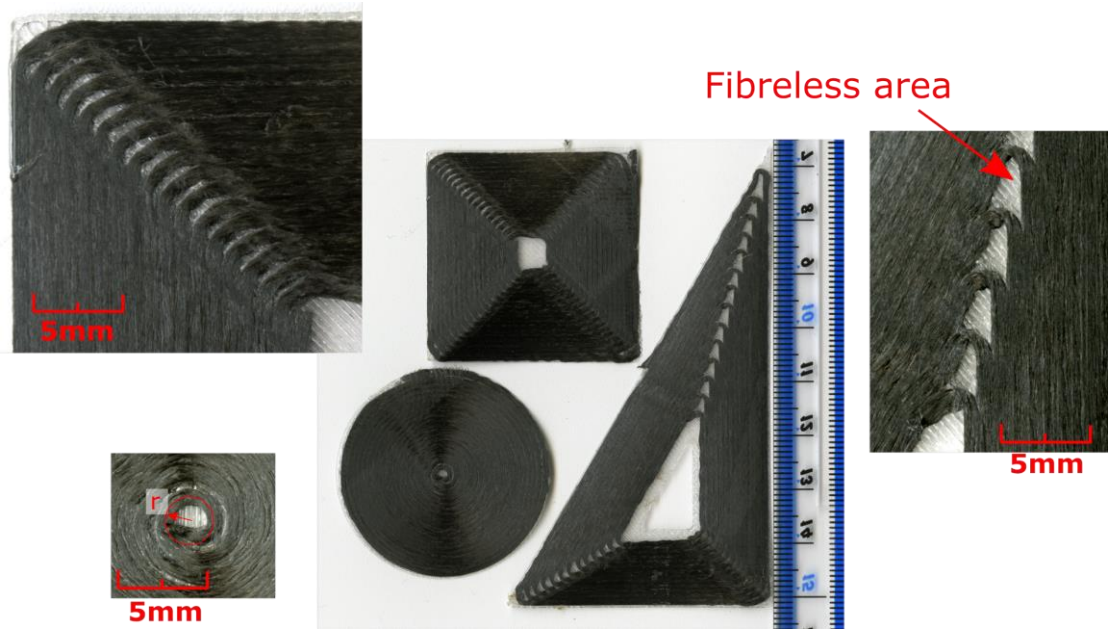

Figure 2.17: Benchmark prints for MarkOne printer with detail of corner radii.

Optical microscopy was performed to further asses the printing quality of the MarkOne printer. Figure 2.18 shows the unprinted fibre reinforced filament, which has a nominal diameter of 400 μm. The carbon fibres seem to be localised in three bands and some voids can be seen as dark spots. The V_f in the filament was estimated over the single cross section using ImageJ software with a greyscale threshold and was found to be 20%.

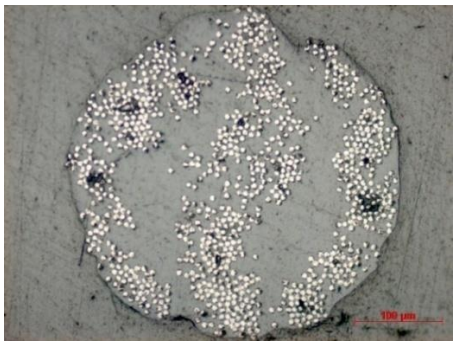

Figure 2.18: Cross section of the MarkForged carbon fibre filament.

Figure 2.19 is a micrograph of the cross section of one of the flexural test specimens showing the multiple stacked layers through the thickness of the part. Within each layer distinct regions of polymer, fibres, and voids can be seen. The fibre volume content was estimated for to be 27% over the cross section, which is higher than in the filament which is attributed to possible non-uniformity of the filament over its length. During the printing process, additional voids may be created as the filament is non-uniform, forming airgaps between printed tracks as visible in the cross section. A void content of 7-11% was estimated from the micrograph using ImageJ and a

greyscale threshold for the darker void regions. A non-even distribution of fibres can also be seen in the printed tracks.

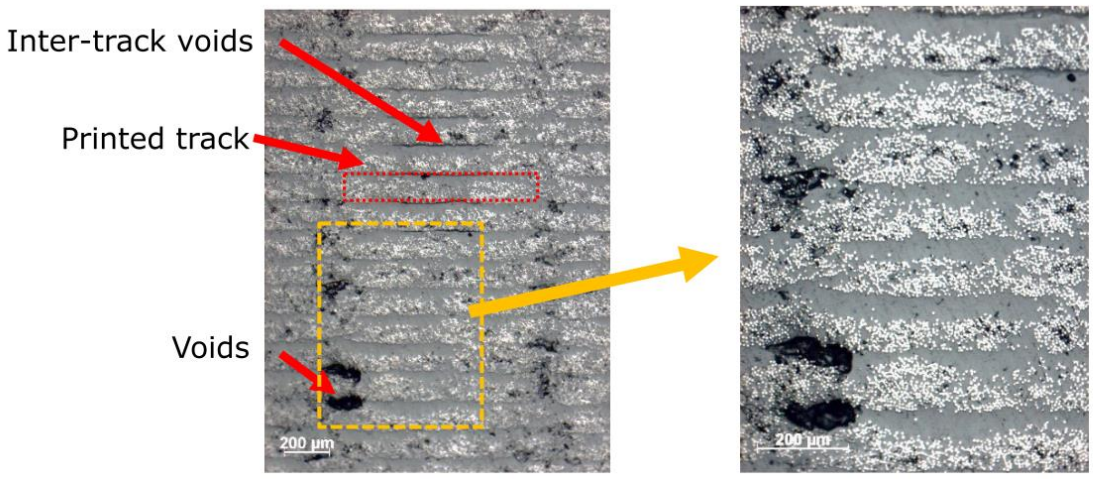

(a) (b)

Figure 2.19: Cross section of printed MarkForged part showing structure from 3D printing tracks and distribution of voids.

2.3.2.2 Short carbon fibre PA filament

The result of the tensile tests and flexural tests on the short carbon fibre PA filaments are shown in Figure 2.20. The average tensile strength and stiffness are 33.5 MPa (±2.7%) and 1.85 GPa (±6.1%) respectively. The properties are lower than the bulk properties of PA [101], showing that the fibres do not reach their ultimate strengths. The flexural strength and stiffness were found to be 55.3 MPa (±3.4%) and 3.0 GPa (±4.1%) respectively. For the reinforced carbon fibre PA filament, the flexural strength is higher than the tensile strength. This is expected for a high quality composite part [100]. It must be considered, however, that 3D printed parts typically have a relatively large void content which can have different effect on the apparent tensile and flexural properties. The difference between tensile and flexural properties is thus not a direct indication of a high-quality composite part.

The shear results are shown in Figure 2.20c. The shear strength and modulus were found to be 19.02 MPa and 0.31 GPa, respectively. One comment here is that the test method was developed for continuous fibre reinforced ±45° layers, while the short carbon fibre PA part behaved more like a plastic part, with a large amount of plastic deformation. This large deformation may cause fibre scissoring (rotation of the fibres in the specimen). The ASTM D3518 standard advises to discard data above 5% shear strain [102]. The modulus may be obtained from this test as it falls within the measurement region, however, the maximum shear stress value may be influenced by excessive fibre rotation.

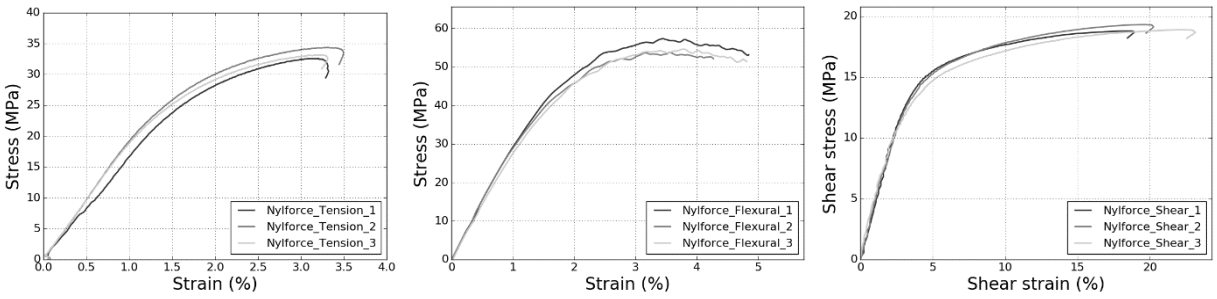

(a) (b) (c)

Figure 2.20: Experimental (a) tensile , (b) flexural and (c) shear test results of carbon microfibre reinforced PA.

Figure 2.21 shows the micrographs of parts printed with short carbon fibre reinforced PA filament. The printed part (Figure 2.21a) shows characteristic triangular voids between the printed tracks from the FFF process. Using ImageJ software and a greyscale threshold, the total void content in the 1-3 plane was estimated at 3.5%, with mainly triangular voids from the printing process.

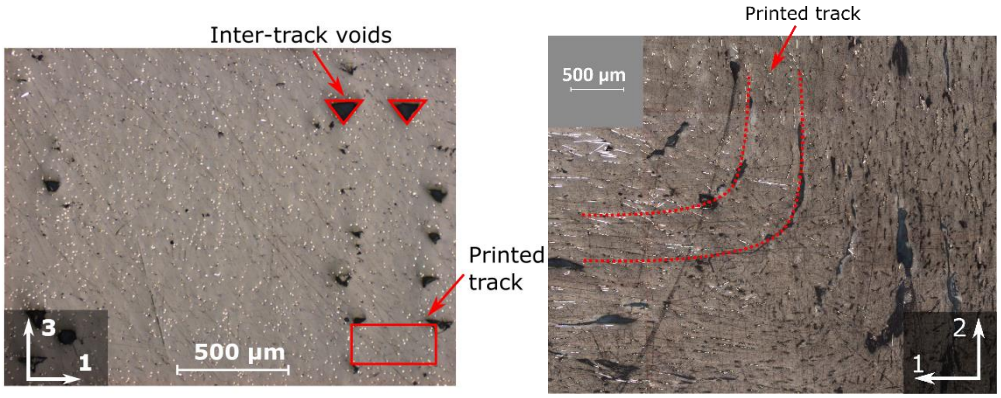

(a) (b)

Figure 2.21: Microstructure of 3D printed short fibre PA showing (a) cross section and (b) top view of corner.

Figure 2.21b shows a 90° corner region of a printed part, showing the change in orientation of the fibres. The fibres show up as light stripes that are horizontal in the left region and vertical in the top region. It also shows that considerable fibre pull-out has occurred during cutting and polishing of the sample as multiple dark area in the fibre direction can be identified with the same width of the fibres – indicating a low fibre-matrix adhesion. Some voids are present, but the gap between the printed tracks is much smaller compared to the continuous fibre filament (Figure 2.17).

2.3.3 Comparison of continuous fibre printing and short fibre printing

Figure 2.22 shows SEM micrographs of the failure surfaces under tension of the continuous fibre 3D printed sample and the short fibre 3D printed part. For the continuous fibre part, fibre fracture is clearly present with a multitude of fibres sticking out of the matrix. The fracture surface

was relatively non-even, with varying levels of depth which could be an indication that the load distribution between printed tracks is not completely even. The fracture surface of the short fibre part clearly shows the typical structure of a 3D printed part with inter-bead voids between the printed tracks. Overall, the fracture surface shows signs of plastic deformation of the matrix, with some fibres left in the matrix and fibre pull-out.

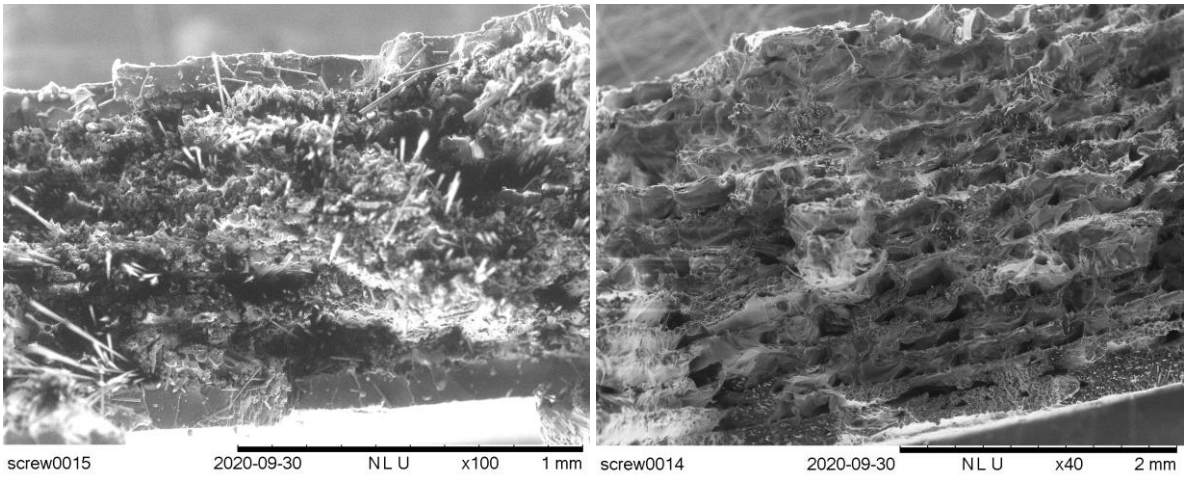

(a) Continuous fibre part **(b) Short fibre part**

Figure 2.22: SEM micrographs of tensile fracture surfaces of (a) continuous fibre and (b) short fibre reinforced part.

Table 2.1 shows a comparison of the printing methods, where the mechanical properties have been normalised by ratio to a V_f of 15%. The porosity was determined via microscopy and image analysis with gray scale thresholds using ImageJ. The tensile strength and stiffness of the continuous fibre 3D printed samples were roughly an order of magnitude larger than those of the short fibre reinforced samples. This can be attributed to the fact that the short fibres are not loaded up to their full capa

The flexural properties of the continuous fibre parts were lower than the tensile properties, indicating quality issues [100]. The flexural properties of the short fibre 3D printed parts were higher than its tensile properties, but still a factor 3 lower compared to the continuous fibre printing method. The shear properties of both printing methods are closer together, with the short fibre parts showing a relatively high shear strength. Together with the lower porosity, it shows that the short fibre printing method produces a higher quality part than the continuous fibre printing method.

Table 2.2: Comparison printing methods with normalised mechanical properties to a V_f of 15%.

	Short fibre printing method		**Continuous fibre printing method**	
Brand name	Nylforce		MarkForged	
Fibre volume content	6%		27%	
Porosity determined via microscopy	1.1%		9%	
	Measured	*Normalised*	*Measured*	*Normalised*
Tensile modulus [GPa]	1.85	4.6	62.5	46.9
Tensile strength [MPa]	33.5	83.8	968	726.0
Flexural modulus [GPa]	3	7.5	41.6	31.2
Flexural strength [MPa]	55.3	138.3	485	363.8
Shear modulus [GPa]	0.31	0.8	2.26	1.7
Shear strength [MPa]	19	47.5	31.16	23.4

2.4 Discussion and conclusions

This chapter started with an overview of fibre reinforced polymer composites which highlighted the effects of polymer type and fibre architecture on performance and processing. Thermoplastics can be reshaped and can be used in processes such as FFF for direct manufacture of 3D objects, but their relatively high viscosity makes consolidation harder. The potential benefit of discontinuous fibres over continuous fibre was introduced as they are easier to form and can have high mechanical properties when sufficient fibre length is maintained during manufacture. This trade-off between fibre architecture vs. performance and processing was also found in additive manufacturing of composites.

From the current body of work on composite 3D printing it must be concluded that the quality of 3D printed composites is still low compared to traditional aerospace grade composite materials, as literature and this study showed void contents in the order of 10% are not uncommon for 3D printed parts. Multiple studies reported on an increase in mechanical properties from unreinforced to reinforced filament, but to be used as a structural material the absolute strength and stiffness must increase as well as the consistency and quality of manufactured parts.

The coupled thermo-fluid-mechanics of the material extrusion 3D printing process has been carefully laid out to allow for the identification of physics-based approaches to improving the quality of 3D printed composite parts. The basic extrusion process is well documented, but the literature lacks a coherent understanding of how different printing parameters affect final part quality.

The ideal properties for a 3D printing filament are summed up in Table 2.3 and categorized into processing and performance properties. The flow properties of the polymer are important for the polymer sintering process, which ideally consists of a low melt viscosity and high surface

energy. The thermal properties of a 3D printing filament dictate the thermal energy history of the printed tracks, where it is important that the extruded material and the surrounding material reach a high enough temperature and maintain that temperature for long enough to enable bonding between adjacent tracks. A higher heat capacity means the material needs more heat input to increase its temperature but can also store more heat once it leaves the liquefier, while a high conductivity is required to transfer the heat to the surrounding material. After sintering, the material cools down which may induce residual stresses, so ideally the material has a low melt/glass transition temperature, which is a conflicting requirement with a high operating temperature. The desired mechanical properties of the polymer are a high stiffness and strength, and good interfacial strength when reinforcing fibres are used.

Table 2.3: Overview of desired properties for a fibre reinforced 3D printing filament.

Processing properties	Melt viscosity	Low melt viscosity for easy flow of the polymer
	Surface energy	High surface energy to improve polymer sintering process
	Melt temperature	Low melt temperature for lower residual stresses
	Heat capacity	High heat capacity to better retain temperature after printing
	Heat conductivity	High heat conductivity to transfer heat through the printed part
Mechanical performance properties	Stiffness/strength	High stiffness and strength for overall mechanical performance
	Interfacial strength	Good interfacial strength with reinforcing fibres
	Operating temperature	High operating temperature before becoming glassy

Studies indicated that the addition of fibres to the filament may improve the heat transfer between printed tracks, leading to a better sintering process and reducing void content. However, fibres also increase the viscosity of the melt which has a negative effect on the sintering process as some studies reported a higher void content with fibres. The net-effect of fibre reinforcements on the quality of the FFF process will be dependent on both the heat transfer mechanism and flow behaviour of the fibre-polymer melt.

Another important aspect for the printing of composite materials is the use of short versus continuous fibres. Currently, a limited number of commercial products are available for both, but rigorous, comparative material testing with detailed consideration of defects (through optical microscopy) has until now not been available in the public domain. The performance of two of the most advanced solutions currently available have been benchmarked with mechanical testing and optical microscopy.

Printing of short fibre (~0.1 mm) reinforced PA filament was performed using a standard open-source FFF printer and a MarkOne 3D printer was used to print continuous carbon fibre / PA composite specimens. The tensile strength and stiffness of the continuous fibre printed parts were 986 MPa and 64 GPa respectively, which is more than an order of magnitude higher

than the short fibre reinforced PA printed parts (33 MPa and 1.9 GPa) although still significantly lower than unidirectional composites made with traditional manufacturing methods (strength/stiffness on the order of 1500 MPa/135 GPa). A disadvantage of the continuous fibre printing method, however, are process limitations such as a minimal deposition length and minimal corner radii. This gives limited control over the placement of the fibre and the creation of voids when printing more complex shapes. Short fibre printing allows for considerably more freedom in where and how the reinforcement is placed, resulting in easier processing of the material and lower void content. The mechanical properties are relatively low as the matrix or fibre-matrix interface fails before the fibres.

The results agree with the known trade-off between processing and performance as shown in Figure 1.4. To further optimize fibre reinforced 3D printing materials, highly aligned discontinuous fibres with fibres above the critical fibre length may provide a good trade-off between processing and performance. For carbon fibre in a PA matrix, the critical fibre length is roughly 0.5 mm [33]. Increasing the fibre length therefore may be a way forward to a composite 3D printing filament with the advantages of the original FFF process and the ability to compete with continuous fibre mechanical performance. This may enable new applications for high performance 3D printed parts suitable for medical, aerospace, sport and rapid prototyping applications.

Chapter 3

Fabrication and characterisation of ADFRCs

The contents of this chapter are based around the following peer reviewed journal paper:

L. G. Blok, M. L. Longana, and B. K. S. Woods., "Fabrication and Characterisation of Aligned Discontinuous Carbon Fibre Reinforced Thermoplastics as Feedstock Material for Fused Filament Fabrication," Materials, vol. 13 (20), 2020

And a conference paper:

L. G. Blok, H. Yu, M. L. Longana, and B. K. S. Woods, "Development of discontinuous fibre reinforced thermoplastic feedstocks for high performance 3D printing." 18th European Conference on Composite Materials, ECCM 2018, Athens, Greece, 2018.

In this chapter, the development of a consolidation module for making aligned discontinuous fibre reinforced composite (ADFRC) tapes, and characterisation of their material properties are presented. A brief introduction on the benefits of ADFRCs is first given in section 3.1. Then, in section 3.2, an extensive down-selection process is used to identify suitable thermoplastic matrices for FFF, along with material characterisation. Section 3.3 discusses the manufacturing and testing methodology of the ADFRC tapes and the corresponding results are shown in section 3.4. The chapter is concluded with a discussion on the ADFRC performance and comparisons to existing 3D printing filaments.

3.1 Introduction

The first two chapters introduced the benefits of carbon fibre reinforced plastics, identified challenges limiting wider commercial uptake of composite materials and benchmarked the state-of-the-art in fibre reinforced 3D printing. Composite materials are well known for their high specific mechanical properties, however, the manufacturing of these composite materials is expensive due to high equipment, consumables, and labour costs [2]. These costs creates significant barriers to the adoption of composite materials, and therefore cheaper manufacturing methods are a key enabling technology for more widespread use of CFRP [103], [104]. It was shown that the fibre architecture directly influences the performance and processing of fibre reinforced composites. Aligned discontinuous fibre reinforced composite (ADFRC) tapes are expected to have

an improved formability which may simplify manufacturing methods and allows uptake of recycled discontinuous fibres to further reduce costs [16]. They also have the potential to achieve mechanical performance comparable to continuous fibre reinforced composites, given sufficient fibre length and a high level of alignment, while mitigating many of the manufacturing difficulties associated with continuous fibres, e.g. wrinkling, bridging and corner radii constraints.

Here, ADFRC tapes are developed and investigated as precursors for a novel 3D printing filament and their mechanical performance is assessed. Careful selection of the fibre length and matrix system allows for retention of most of the mechanical performance of a continuous fibre solution, without the need for cumbersome and restrictive fibre cutting and laydown procedures within the additive manufacturing process. This process may enable a low-cost and automated method for composite manufacture where rapid prototyping and a high degree of automation are required. Existing additive manufacturing processes have been covered in section 2.1.1.

A dedicated matrix selection process was performed to find the polymer matrices best suited for fibre reinforced FFF manufacturing. Relevant process parameters for FFF were derived and data from different polymers were compared to yield four candidate matrices; ABS, PLA, PA and PETG. A double belt hot-press was made to consolidate the fibres with thermoplastic films and using the four matrices, ADFRC thermoplastic tapes were fabricated. Tensile test samples were prepared to give an expected performance level of the 3D printing filament before the ADFRC tapes were shaped into a uniform filament.

3.2 Materials

3.2.1 Matrix selection process

Depending on the application and manufacturing method, different thermoplastic polymers may be selected for the matrix of composite materials. Here, the focus is on extrusion based additive manufacture such as FFF. FFF is strongly influenced by rheological and thermal phenomena during printing which can be influenced in part by the printing settings, but which are ultimately governed by intrinsic material properties. During the FFF process, the material heats up, flows out of the nozzle and solidifies again after being extruded. Multiple studies have investigated heat transfer and extrusion problems in 3D printing [56], [64], [105]–[107].

Analysis of the FFF process has identified the main properties that are important for 3D printing with fibre reinforced filaments as explained in Chapter 2 (repeated in Figure 3.1) [14].

They can be divided into printing parameters and material parameters. In this chapter, the material parameters are of interest for the matrix selection process which includes viscosity, surface tension, heat capacity and heat conductivity.

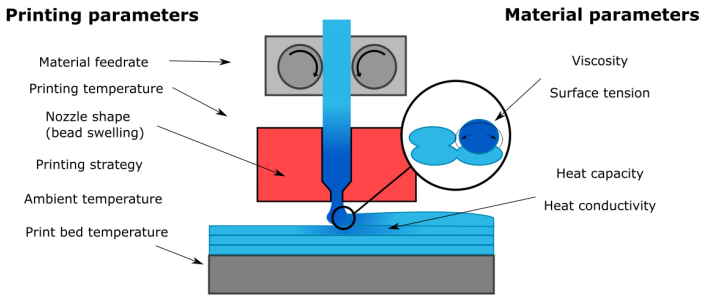

Figure 3.1: Main parameters for good surface contact and temperature conditions to enable optimal polymer sintering conditions.

The addition of fibres in the 3D printing process changes several parameters. They increase the viscosity of the bulk material in molten state [108] and they increase the heat capacity and heat conductivity [109], [110]. This changes the temperature profile during and after deposition which also affects the polymer viscosity and bonding process between printed tracks. To successfully implement discontinuous fibres with a length above the critical fibre length as a reinforcement in 3D printing filament, a matrix with good intrinsic processing characteristics is preferred. A material selection process was performed to find the most suitable matrices for fibre reinforced 3D printing by collecting information from material databases and literature. The goal was to find matrix systems that will aid the development of a 3D printing filament with discontinuous fibres. Therefore, good processability of the polymer was considered most important. Several selection criteria were identified and used, from general properties to thermal and processing properties. Table 3.1 shows the full comparison of different plastics.

Table 3.1: Comparison chart for suitability of different polymer for fibre reinforced 3D printing.

	Explanation	PA	PLA	ABS	PETG	PP	PCL	PC	LDPE	HDPE	PVC	PBT	PEI	PEEK	PPS	PSU	PESU
Other names	Commercial and/or full name	Polyamide (Nylon)	Poly lactic acid	Acrylonitrile butadiene styrene	Poly ethylene terephthalate glycol	Poly propylene	Poly caprolactone	Poly carbonate	Low-density poly ethylene	High-density poly ethylene	Poly vinyl chloride	Poly butylene terephthalate	*Polyetherimide* (Ultem)	Poly ether ether ketone	Poly phenylene sulfide	Polysulfone	Polyether-sulfone
Structure	Can be important to derive adhesion to fibres																
Strength / stiffness	Mechanical properties	0.94-1.18 GPa 38.6-48.2 MPa [104]	2.3-2.6 GPa 38-68 MPa [104]	2.2-2.9 GPa 29.6-44.1 MPa [104]	2.01-2.11 GPa 47.9-52.9 MPa [104]	1.34-1.59 GPa 32.9 -36.4 MPa [104]	0.390-0.44 GPa 21.1-38.5 MPa [104]	2.32-2.44 GPa 59.1-65.2MPa [104]	0.17-0.28 GPa 8.96-14.5MPa [104]	1.07-1.09 GPa 26.2-31 MPa [104]	2.48-3.3 GPa 41.4-52.7 MPa [104]	1.93-3 GPa 56.5-60 MPa [104]	2.89-3.04 GPa 73.5-81.1 MPa [104]	3.79-3.95 GPa 87-95 MPa [104]	3.23-3.39 GPa, 64-67.2 MPa [104]	2.62-2.76 GPa, 94-104 MPa [104]	2.76-2.9 GPa, 85.4-94.1 MPa [104]
Density	Density	1060 - 1080 kg/m³ [104]	1110 - 1210 kg/m³ [104]	1020 - 1080 kg/m3 [104]	1260-1280 kg/m3 [104]	899-908 kg/m³ [104]	1140 - 1150 kg/m³ [104]	1190-1210 kg/m³ [104]	914-932 kg/m³ [104]	952-965 kg/m³ [104]	1300-1490 kg/m³ [104]	1300-1380 kg/m³ [104]	1260 – 1280 kg/m³ [104]	1300 -1320 kg/m³ [104]	1340-1360 kg/m³ [104]	1230-1250 kg/m³ [104]	1360-1380 kg/m³ [104]
Costs	Lower cost better	2.35 – 2.53 GBP / kg [104]	2.34 – 3.01 GBP / kg [104]	1.82-2.15 GBP/kg [104]	1.98-2.06 GBP/kg [1]	1.1 -1.14 GBP/kg [104]	5.73-8.32 GBP/kg [104]	2.57 – 2.75 GBP/kg [104]	1.32 – 1.35 GBP/kg [104]	1.22-1.25 GBP/kg [104]	1.06-1.21 GBP / kg[104]	1.98-2.06 GBP / kg [104]	13.4 GBP / kg [104]	75 GBP/kg [104]	4.83 – 5.23 GBP/kg [104]	7.53 – 10.9 GBP/kg [104]	8.73-9.26 GBP/kg [104]
Glass transition temperature	High glass transition temperature for usage.	~60 °C [104]	52 - 82.6°C [104]	88 - 120°C [104]	81 - 91°C [104]	-14 - 6°C [104]	-72, -59°C [104]	142-158°C [104]	-125, -90°C [104]	-125, -90°C [104]	80-88°C [104]	22-43°C [104]	215-217°C [104]	143-157°C [104]	81-97°C [104]	186 -192 °C [104]	210-235 °C [104]
Processing temperature	Lower processing temperature is easier / cheaper	220 - 327°C [104]	170 - 210°C [104]	177 - 260°C [104]	249 - 288°C [104]	203 - 250°C [104]	106-133 °C [104]	205-298°C [104]	121-232°C [104]	177-274°C [104]	177-199°C [104]	184-274°C [104]	309-430°C [104]	349-399°C [104]	257-338°C [104]	273 - 360°C [104]	295 - 391°C [104]
Coefficient thermal expansion (CTE)	Low thermal expansion to prevent warpage.	141-147 µstrain/°C [104]	126 – 145 µstrain/°C [104]	128-234 µstrain/°C [104]	120-123 µstrain/°C [104]	81.1 – 109 µstrain/°C [104]	158-172 µstrain/°C [104]	120-125 µstrain/°C [104]	180-396 µstrain/°C [104]	106-198 µstrain°C [104]	90-180 µstrain/°C [104]	108-171 µstrain/°C [104]	84.6 - 101 µstrain/°C [104]	50-60 µstrain/°C [104]	48.6-88.2 µstrain/°C [104]	54.7 -56.9 µstrain/°C [104]	54.7 – 56.9 µstrain/°C [104]
Thermal conductivity	High thermal conductivity, easy to heat up and redistribute heat for polymer sintering	0.24-0.32 W/m°C [104]	0.13-0.16 W/m°C [104]	0.266-0.335 W/m°C [104]	0.257-0.267W/m°C [104]	0.205-0.214 W/m°C [104]	0.17-0.18 W/m°C [104]	0.193 – 0.218 W/m°C [104]	0.322 – 0.348 W/m°C [104]	0.461-0.502 W/m°C [104]	0.147-0.209 W/m°C [104]	0.274-0.285 W/m°C [104]	0.123 – 0.13 W/m°C [104]	0.24-0.26 Wm/°C [104]	0.23-0.29 Wm/°C [104]	0.277 -0.288 Wm/°C [104]	0.291 - 0303 Wm/°C [104]
Specific heat capacity	Higher is better, more heat can be added in the system when extruding	1.65e3-1.71e3 J/kg°C [104]	1.18e3-1.21e3 J/kg°C [104]	1.39e3-1.41e3 J/kg °C [104]	1.47e3-1.53e3 J/kgC [104]	1.66e3 – 1.7e3 J/kg°C [104]	1.42e3-1.5e3 J/kg°C [104]	1.15e3-1.25e3 J/kg°C [104]	1.84e3-1.92e3 J/kg°C [104]	1.75e3-1.81e3 J/kg°C [104]	1e3-1.1e3 J/kg°C [104]	1.42e3-1.48e3 J/kg°C [104]	1.47e3-1.53e3 J/kg°C [104]	1.34e3 J/kg°C [104]	1.41e3-1.47e3 J/kg°C [104]	1.5e3 - 1.53e3 J/kg°C [104]	1.4e3 - 1.45e3 J/kg°C [104]
Crystallinity	Lower is better, want to print viscous and better bonding [105]	Semi - crystalline	Semi -crystalline	Amorphous	Amorphous	Semi -crystalline	Semi -crystalline	Amorphous	Semi -crystalline	High level of crystallinity	Semi -crystalline	Semi-crystalline	Amorphous	Semi -crystalline	Semi -crystalline	Amorphous	Amorphous
Shrinkage	Low shrinkage from melt to prevent warpage	1.2-1.8 % [104]	0.3-0.4% [104]	0.4 – 0.7% [104]	0.2-0.5% [104]	1.4-1.95% [104]	0.15-0.7% [104]	0.5-0.7% [104]	1.5 – 5% [104]	1.5-4% [104]	0.2-0.6% [104]	0.9-2.2% [104]	0.5%-0.7%[104]	1-1.21% [104]	0.6%-1.4% [104]	0.5%-0.7% [104]	0.7%-1% [104]
Molding pressure	Used as it is related to viscosity	6.88 - 172 (89.44) MPa	55 - 100 (77.5) MPa	55 -172 (113.5) MPa	6.88 - 138 (72.44) MPa	18 - 115 (66.5) MPa	50 – 52 (51) MPa	55 – 138 (96.5) MPa	34.3 - 103 (68.65) MPa	82 – 103 (92.5) MPa	68.8 - 275 (171.9) MPa	27.5 - 68.8 (48.15) MPa	69 - 138 (103.5) MPa	68.8 - 138 (103.4) MPa	13.8 - 20.6 (17.2) MPa	34.4-138 (86.2) MPa [104]	41.3 – 138 (89.7) MPa [104]
Printing capability	Check proven 3D printing capability	Higher printing temperature than PLA/ABS, needs to be dry.	Good printing characteristics.	Good printing characteristics.	Good printing characteristics.	Hard to print. Warping problems due to high crystallinity.	Seems good, multiple reports on 3D printing of PCL.	Printing demonstrated, quite high temperatures.	Can be used for printing, but quite hard only stick to itself and stringy and warps.	Can be used for printing, but quite hard only stick to itself and stringy and warps.	Good printing demonstrated but safety and health issues.	Often used as additive for better printing, not available in filament itself.	Good, high performance 3D printing material.	Been demonstrated, high temperatures though.	Printing demonstrated, again high temperatures.	Printing filament on the market	Printing filament on the market
Interfacial properties w. carbon fibre	Better interface properties for both mechanical performance and consolidation	IFSS of 19.3 MPa [33]	IFSS of 11-19 MPa [106]	Less than PA6, as PA6 improves adhesion [107]	Less than Nylon; carbon PETG filament has a lower strength than carbon Nylon filament [39]	Poor based on molecular structure	Strength reported of 1000 MPa (with nanodiamonds)[108]	IFSS of 20 MPa [109]	No studies found, expected low from molecular structure	No studies found, expected low from molecular structure	No studies found, expected low from molecular structure	Paper used coupling agent which was needed for interfacial adhesion [110]	IFSS of 100 MPa [111]	Similar to epoxy, IFSS around 80 MPa [112]	IFSS of around 40 MPa [113]	IFSS of around 50 MPa [114]	IFSS of around 50 MPa [114]

Relative performance: Good Medium Poor

From a product engineering perspective, the costs, density, stiffness and strength were considered. A lower density results in a lower overall weight and lower material costs are beneficial to reduce development costs and final filament costs. As the mechanical properties of the finite product are mainly driven by the reinforcement fibres, the strength and stiffness of the matrix itself are less important. Mechanical properties such as fracture toughness or brittleness of the polymer may be considered for specific performance requirements but for this initial selection these properties are left out.

The thermal properties of the matrix are important to consider in the material trade-off as they influence the FFF process. Ideally the matrix material should have a low processing temperature to reduce energy costs and a high usage temperature, however, these are conflicting requirements. For the trade-off, it was decided to consider the glass transition temperature T_g and the processing temperature.

The glass transition temperature is a property of both semi-crystalline and amorphous polymers that relates to softening of the polymer. Above the glass transition temperature polymers lose their rigidity are not suitable for structural use.

For processing, the polymers must be in a molten state, which requires a temperature above the glass transition temperature. For semi-crystalline polymers, the melt temperature may be used as an indicator for the processing temperature. Amorphous polymers, however, do not have a distinct melt temperature and instead increasingly soften above their T_g. To compare both semi-crystalline and amorphous polymers, the well-documented processing temperature is used. This is a relevant material characteristic which gives a good comparison of the average processing temperature required for different types of polymers.

The specific heat capacity and thermal conductivity are included in the trade-off as they influence the heating and associated softening of the material. If the material has a high specific heat capacity and high thermal conductivity, more heat initially must be added to soften the polymer. The benefit of this is that more heat can be distributed after deposition between the printed tracks to improve the polymer sintering process [112]. Having a high specific heat capacity and thermal conductivity is therefore beneficial to the FFF process. Upon cooling, the material shrinks which creates residual stresses and therefore a low coefficient of thermal expansion (CTE) is preferred.

Several processing characteristics of the polymers are also compared. The linear shrinkage expressed as % of the material from melt processing conditions to final cooled part is compared

as a metric for minimising residual stresses. This is different than the CTE as other effects (such as crystallisation) may influence shrinkage [52].

The crystallinity of the polymer is an important parameter for 3D printing that influences the melt behaviour of the material. FFF works best with polymers that are amorphous, despite their lower mechanical performance, as they have no distinct melting point and increasingly soften (lower viscosity) with increasing temperature. This means the polymer sintering process happens over a longer time when cooling down [112].

The polymer sintering process is related to material flow and the reptation time, which is the time required to create a fully welded, entangled interface. Reptation theory, as explained in section 2.2.2, predicts that the reptation time is dependent on temperature and the molecular mass of the polymer. Material flow is related to viscosity, which is a function of temperature and shear rate (process dependent) and the molecular weight as well. These properties cannot be readily compared between polymers, but a simplification is possible to obtain an alternative comparison that is related to these properties. The average moulding pressure is a well-documented property that depends on the processing temperature, viscosity and molecular weight of the polymer. A higher moulding pressure means the polymer, at its processing conditions, flows less easily and thus would have a higher viscosity and longer reptation time. Although no external pressure is applied in the FFF process, the extrusion process is pressure driven and the moulding pressure gives a relative comparison between polymer viscosities which is confirmed later by rheological testing of the candidate polymers.

The last set of properties that are compared are the printing performance and the interfacial properties with carbon fibres. Some materials already have proven to be processable by FFF while others are less commonly used. In the development of an improved fibre reinforced 3D printing filament, a successful printable material is preferred. Likewise, the interfacial properties with carbon fibres plays an important role to maximise the reinforcing effect of the fibres.

The properties discussed above are compared for sixteen thermoplastic matrices, ranging from commodity polymers such as polypropylene and polyamides to high end polymers such as *Polyethylen-imine* (PEI) and *Poly ether ether ketone* (PEEK). Common 3D printing materials were also considered such as *Acrylonitrile butadiene styrene* (ABS), *Poly lactic acid* (PLA) and *Poly ethylene terephthalate glycol* (PETG). An overview of the polymers considered, and their relevant properties are shown in Table 3.1. Each of these polymers is now considered in turn, highlighting key aspects that affect their use in the present application.

From the common 3D printing polymers, PLA has the lowest thermal conductivity and specific heat capacity but exhibits good processing temperatures and has a low shrinkage [111]. PLA is a semi-crystalline material and one of the most used 3D printing thermoplastic filaments on the commercial market [44]. The ease with which this material can be printed can be attributed in part to its low shrinkage and good rheological behaviour over a wide temperature range, as seen from its relatively low molding pressure.

ABS is another widely used thermoplastic filament which has better thermal conductivity properties than PLA, but it is expected to have a higher viscosity which negatively affects bonding [111]. ABS, however, is an amorphous polymer which is advantageous for 3D printing [14], [112]. It is known that ABS is best printed in a closed, heated environment as it is sensitive to temperature variations and warping as it has a relatively high CTE [122].

PETG shows very similar properties as ABS, with a lower viscosity and lower shrinkage which explains its growing popularity as a 3D printing feedstock in recent years [111].

There are different types of PA (PA-66 and PA-6, PA-11, PA-12, etc.) and it is commonly known as Nylon. In general, PA shows average properties in all criteria [111]. It has good resistance against oils and common solvents and has good impact resistance and low friction properties. It is mainly used in the transportation sector for non-structural and electronics parts, and is also common in the consumer goods sector. It is known to degrade at higher temperatures and to absorb moisture [123]. It less commonly used as a 3D printing material than ABS, PETG or PLA.

Most commodity polymers show a very low glass transition temperature and are expected to have low interfacial properties with carbon fibres based on their molecular structures. *Polypropylene* (PP) is a much used material for general plastic parts and moulding as it is cheap, and resistant to heat and impacts [123]. Despite having a low expected processing viscosity, polypropylene has a relatively high shrinkage and is known to warp during 3D printing. Moreover, the interfacial properties with carbon fibres are expected to be low [124].

Low density poly-ethylene (LDPE) and *High density poly-ethylene* (HDPE) are two low cost plastic materials that have lower mechanical properties than PP. They are used for cheap consumables such as plastic bags and bottles. They have a high crystallinity and print trials have shown they are hard to print [125]. Another downside of PE are the lower interfacial properties with carbon fibres expected from their molecular structure.

Polycaprolactone (PCL) is a bio-degradable polymer with a very low melt temperature. Despite the good processing properties such as low viscosity and shrinkage, the low melt temperature of PCL (~55 °C) makes processing harder as solidification increases processing times [111]. It also has a very low T_g and low mechanical properties and therefore is not commonly used for structural parts.

Polycarbonate (PC) has better mechanical properties than the other commodity polymers and is known for its high impact strength [123]. It shows overall good properties for 3D printing. It has a relatively high processing temperature and a high viscosity, and it is an amorphous polymer which is advantageous for 3D printing.

Polyvinylchloride (PVC) is another low-cost polymer with a lower processing temperature than PC. It has a high viscosity but low shrinkage [111]. They are mainly used for plastic piping for several applications. Processing of PVC is harder as it release toxins when heated and has several health and safety issues [123].

The higher end polymers in general show better interfacial properties with carbon fibres but require higher processing temperatures and are more expensive.

Poly butylene terephthalate (PBT) is a semi-crystalline engineering thermoplastic with relatively low cost. It has a relatively high shrinkage but a low expected viscosity [111]. It is often added to filaments to improve the printing quality but is not currently available on the market as filament.

Polyetherimide (PEI) is common high-end 3D printing material also known as Ultem [126] [127]. It is an amorphous polymer with a very low shrinkage and good interfacial properties with carbon fibre [111]. It has a relatively high processing temperature and high viscosity, but additives may be used to improve the flow properties [126] [127].

Poly-ether-etherketone (PEEK) is a high-performance engineering thermoplastic used in structural applications [123]. Carbon fibre pre-preg tape are available to be used for autoclave processing and recently have been used in Laser Assisted Automated Tape Placement for direct manufacturing of aerospace grade parts [128]–[130]. It has been used in both SLS and FFF processes [50], [52], [131]. The material trade-off shows it has a high processing temperature, high viscosity, and a higher shrinkage than PEI which makes it less suitable for FFF 3D printing applications [111].

Poly phenylene sulphide (PPS) is a cheaper high-performance semi-crystalline thermoplastic. It has good mechanical properties and due to its low viscosity it is a preferred choice for high performance carbon fibre thermoplastic composites [132]. For 3D printing applications it has

the disadvantage that it has a relatively high processing temperature and shrinkage compared to other materials.

*Polysulfone (*PSU) and *polyethersulfone (*PESU) are relatively new high performance amorphous polymers used in 3D printing [133]. They have a high glass transition temperature and can be used up to 250 °C [123], [134] with good mechanical properties. The downside is a relatively high viscosity and processing temperature but low shrinkage.

A material selection was performed using weighted scores for the different criteria. The aim was to find matrices which are best for carbon fibre reinforced FFF, and as such the criteria relating to processability were more important than the performance-based criteria at this stage. The best candidate matrices were used to manufacture ADFRCs within the available lab facilities. This meant the processing temperature and costs were important from a practical point of view, and for processing the moulding pressure (directly related to the viscosity of the material as will be shown in section 3.2.2) was important. All other properties had equal weighing except for the density, crystallinity and strength/stiffness which had a lower importance for this study as they relate more to the performance of the final composite, while the focus was on FFF processing. The final trade-off with the criteria, weightings and scores are shown in Table 3.2.

Table 3.2: Trade-off study of polymer matrices for ADFRCs suitable for 3D printing.

Criteria	Weighting (%)	ABS	PETG	PLA	PBT	PCL	PSU	PESU	PA	LDPE	PP	PC	PEI	PVC	PPS	PEEK	HDPE
Processing temperature	12.5	3	2	3	3	3	1	1	2	3	3	1	1	3	1	1	2
Molding pressure	12.5	1	2	2	3	3	1	1	2	3	3	1	1	1	1	1	1
Costs	10.0	3	3	3	3	2	2	2	3	3	3	3	2	3	2	1	3
Glass transition temperature	7.5	2	2	2	2	1	3	3	2	1	1	3	3	2	2	3	1
Coefficient thermal expansion (CTE)	7.5	2	2	2	2	1	3	3	2	1	3	2	2	2	3	3	2
Thermal conductivity	7.5	2	2	1	2	1	3	3	2	3	1	2	2	2	2	2	3
Shrinkage	7.5	3	3	3	1	3	3	3	2	2	2	3	3	3	2	2	2
Printing capability	7.5	3	3	3	2	3	3	3	2	2	2	2	3	2	2	2	2
Interfacial properties w. carbon fibre	7.5	2	2	2	2	3	3	3	3	1	1	3	3	1	3	3	1
Specific heat capacity	7.5	2	2	1	2	2	2	2	2	3	2	1	2	1	2	2	3
Density	5.0	3	2	3	2	3	2	2	3	1	1	3	2	2	2	2	1
Crystallinity	5.0	3	3	2	2	2	3	3	2	2	2	3	3	2	2	2	1
Strength / stiffness	2.5	3	3	3	3	1	3	3	2	1	2	3	3	3	3	3	2
	TOTAL SCORE (/100):	79.2	77.5	76.7	76.7	75.8	75.8	75.8	74.2	73.3	71.7	70.8	70.8	68.3	64.2	63.3	62.5

The most suitable polymer for 3D printing from this selection is ABS, followed by PETG and PLA. This is not necessarily a surprising result, as these are the three most popular 3D printing filaments currently on the market, although it was also not a forgone conclusion given the consideration of criteria and weightings driven by use of fibres within the FFF process. PBT also scores highly, but it is not commonly used as 3D printing feedstock and so availability may be an issue in the short to medium term. PCL has good temperature and moulding pressure characteristics that gives it a good score for 3D printing, despite its low mechanical properties and low usage temperature. The polysulfones (PSU, PESU) scored high and are indeed an upcoming 3D printing material, especially when temperature constraints would be removed. Polyamide was ranked 8th in this study, with overall medium properties. LDPE and PP have better processing

temperature and expected lower viscosities than PA, but they have lower thermal properties and low interfacial properties with carbon fibre which makes them less attractive for fibre reinforced 3D printing feedstock. PC and PEI have good mechanical properties and good thermal properties but require higher processing temperatures and moulding pressures which makes them less attractive to use in the filament development phase. The same holds for PPS and PEEK. PVC is attractive because it has a low processing temperature but scores low on the expected viscosity and interfacial properties. Finally, HDPE is the least attractive for 3D printing in this trade off as it is a crystalline material which has relatively high processing temperature and expected high viscosity.

A sensitivity study was performed on the selection shown in Table 3.2 using MATLAB ver 2019b, where the importance ratios and scores were changed randomly by ±2% and ±1 respectively over multiple runs (>1000) to see how sensitive the polymer rankings were to variance in the scores. The results are shown in Figure 3.2, which shows the ranking order based on the average scores across the sensitivity study along with the standard deviation of each polymer's score. Here we see the top five choices are the same as in the single study shown above. The gradual drop in scores and the overlaps seen within the variance ranges of adjacent polymers implies that it would be prudent to consider more than just the top ranked choice.

Based on this study, ABS, PETG, PLA were chosen for further consideration as they are the three best performing matrices from the selection. PA, while not a very strong performer in this study, will also be considered moving forward as it provides a useful benchmark against existing fibre reinforced 3D printing options, as discussed in Chapter 2.

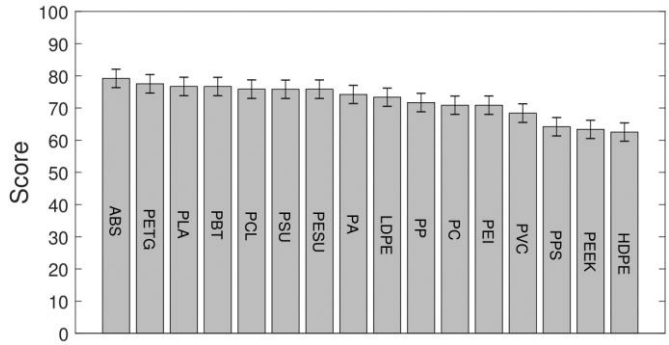

Figure 3.2: Sensitivity study on the ranking of the different polymers.

3.2.2 Matrix analysis

The selected polymers were characterized by Digital Scanning Calorimetry (DSC), Thermo-Gravimetric Analysis (TGA) and shear rheology. The four different polymers were acquired as 3D printing filament from 3D4Makers [135] and MarkForged [3]. The DSC results are shown in

Figure 3.3 which show the melt temperatures of the semi-crystalline polymers PA and PLA, being 148.6 °C and 194.7°C. The amorphous polymers ABS and PETG do not melt and no endothermic peaks show up in the DSC curves for these two polymers.

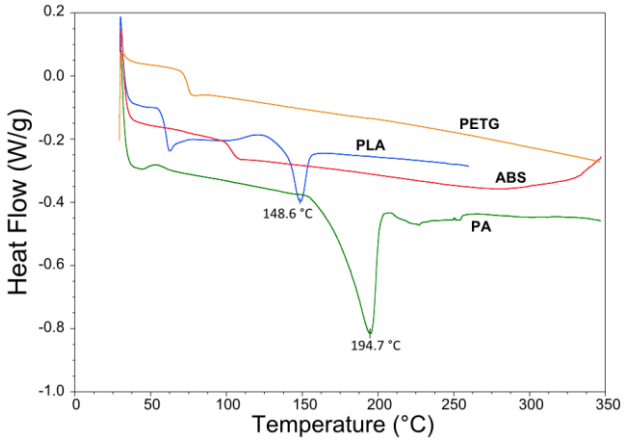

Figure 3.3: Digital Scanning Calorimetry (DSC) results of PA, PLA, PETG and ABS.

TGA was performed under oxidative atmosphere to identify whether the polymer exhibits any mass loss at higher temperature which may indicate degradation. The samples weighed between 8-10 mg and were heated to 300 °C at a rate of 10°C/min, under air atmosphere and a gas flow rate of 50 mL/min. The results are shown in Figure 3.4. From the four candidate polymers, only PA showed a mass loss starting from roughly 100 °C and at 300 °C lost 7% of its mass. This indicates possible degradation at higher temperature as expected for PA and/or may be related to water absorption of PA which it is prone to do. The other candidate polymers (ABS, PETG, PLA) lost less than 1% of their mass at the end of the test.

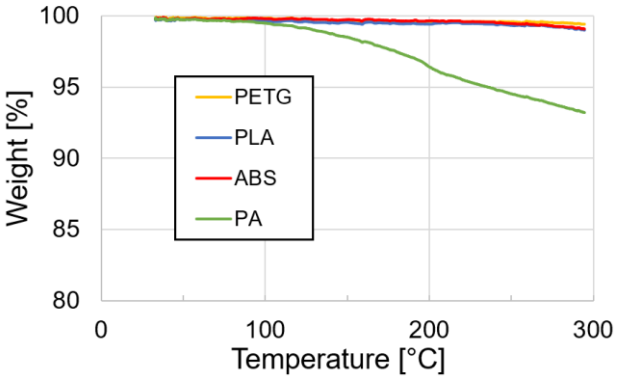

Figure 3.4: TGA data of the four different candidate polymers.

Lastly, rheological testing was performed on the candidate polymers. A TA Instruments parallel plate rotational rheometer was used, with a 25 mm diameter plates and a shearing gap of 0.6 mm. The samples were prepared as 3D printed disks with a diameter of 20 mm and a thickness of 1.1 mm, such that the entire gap was filled when the parallel plates were lowered to the shearing gap of 0.6 mm. Any excess material was removed after squeezing of the disks as shown

in Figure 3.5. Oscillatory measurements were performed at 1 rad/s, 10 rad/s and 100 rad/s at temperatures up to 300 °C.

Figure 3.5: Shear rheology sample preparation showing the excess material and 0.6 mm gap.

Figure 3.6 shows the complex viscosity of the candidate polymers. All samples clearly show a reduction in viscosity for increasing temperatures as expected. Shear thinning can also be observed, which was most pronounced for ABS as the viscosity reduced by an order of magnitude for a strain rate of 100 rad/s compared to 1 rad/s. For the other polymers, the effect of shear thinning was less pronounced. Comparing the difference in viscosities to the predicted trends from the documented moulding pressures, one can see that ABS (113.5 MPa) indeed has the highest viscosity, followed by PA (89.42 MPa) and with PLA (77.5 MPa) and PETG (72.44 MPa) having a similar viscosity range. This confirms that the moulding pressure can be used as a relative comparison for the polymer viscosity.

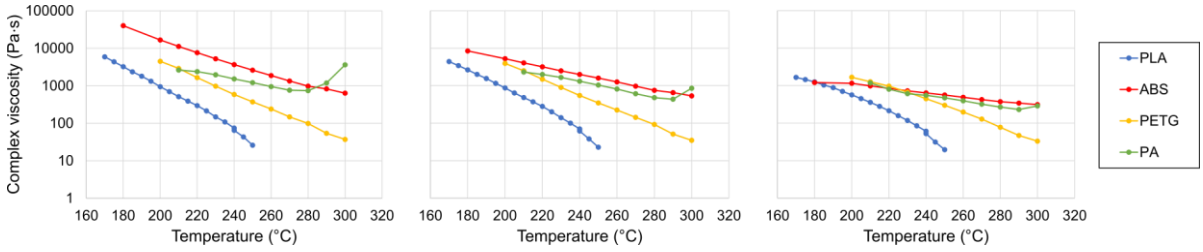

(a) 1 rad/s (b) 10 rad/s (c) 100 rad/s

Figure 3.6: Complex viscosity measurements at different strain rates for the candidate polymers.

3.2.3 Fibre reinforcement

The aim of this work is to make a thermoplastic composite tape with aligned discontinuous fibres where the full strength of carbon fibres is reached. This requires the fibre length to be above a critical length such that fibre failure occurs before interfacial failure as explained section 2.1.4. For PA and PLA, the interfacial shear strength (IFSS) was found in literature [33], [113]. The critical fibre length was estimated using Equation (2.7) and found to be 0.78 mm and 0.8-

1.38 mm, respectively. This provides a rough estimate of the critical fibre length, which will be dependent on the exact polymer composition, fibre type and sizing.

It was chosen to use 3 mm carbon fibres to ensure the critical length was exceeded. Toho Tenax C124 fibres were used which have been used with the HiPerDiF fibre alignment method before [11], [16], [136], [137]. These fibres have a water-soluble sizing which allows them to disperse well in water which aids the HiPerDiF fibre alignment process. Because the sizing is water-soluble, some loss of the sizing is expected during the HiPerDiF process. The properties of the fibres are shown in Table 3.3 below.

Table 3.3: Toho Tenax C124 carbon fibre properties.

Cut length	Density	Filament diameter	Tensile strength	Tensile modulus
3 mm	1820 kg/m³	7 µm	4344 MPa	225 GPa

3.3 Method

3.3.1 Composite manufacture

The HiPerDiF fibre alignment process as explained in the introduction was used to create aligned 3 mm carbon fibre preforms, which were then coupled with the thermoplastic films. For this work, fibre preform tapes with a width of 5 mm and aerial weight of 60 g/m² were prepared. The four candidate polymers were used as matrix for the ADFRCs; ABS, PLA, PETG and PA. These materials were acquired as 3D printing filament from 3D4Makers [135] and MarkForged [3] and 3D printed into films with a 0.125 mm thickness for film impregnation. For the consolidation process, film impregnation was used where a sandwich of a single aligned dry fibre preform between two polymeric matrix films was fed through a custom double-belt hot press, as shown in Figure 3.7 and Figure 3.8.

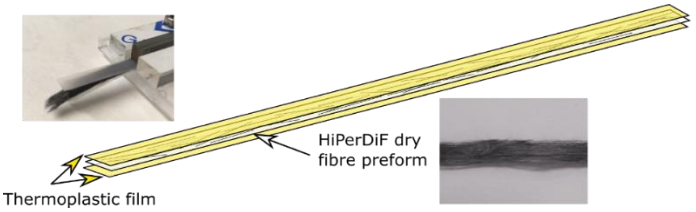

Figure 3.7: Preform before consolidation showing aligned 3mm fibres sandwiched between polymer films.

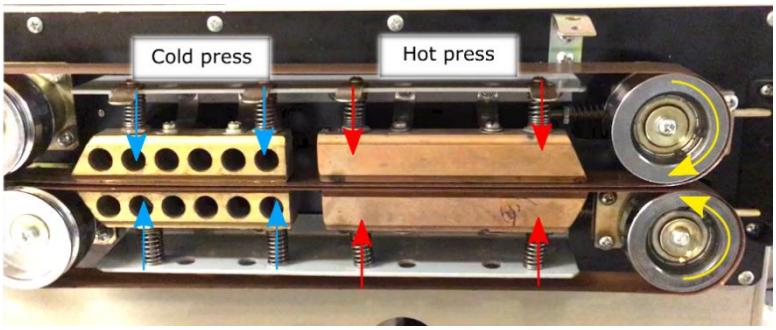

Figure 3.8: Pre-pregging module for consolidation of the fibres with the matrix.

In the double belt hot press, pressure and heat were applied to consolidate the fibres and the matrix into a composite material. The consolidation module consists of two glass fibre reinforced PTFE belts, a hot press and a cold press. As explained in section 2.1.3, Darcy's law gives a relation between pressure p, time t, viscosity η, permeability K and flow rate for consolidation. Equation (2.1) can be rewritten as Equation (3.1) to give a direct relationship between the time t and the flow length with different processing conditions.

$$t = \frac{L^2 \eta}{2K\Delta p} \tag{3.1}$$

The permeability of the fibre bed depends on the packing structure, volume fraction and fibre dimensions. The permeability is approximated using Gebart's derivation for the perpendicular permeability of uni-directional reinforcement [138]. Quadratic/rectangular packing as shown in Equation (3.2) and Equation (3.3), where R_f is the fibre diameter. The lowest permeability of the two was used to predict the infiltration length L for the HiPerDiF aligned fibre preform. Although the fibres may be not be perfectly aligned and have different packing structures, any misaligned fibres will make a more porous preform that increases permeability such that the conservative case is considered. The lowest permeability was found to be $7.9 \cdot 10^{-12}$ m^2 using a fibre volume fraction of 12.5 % and fibre radius of 3.5 µm.

$$K_{\perp,hex} = \frac{16}{9\pi\sqrt{6}}\left(\sqrt{\frac{V_{f,max}}{V_f}} - 1\right)^{\frac{5}{2}} R_f^2 \quad \text{with } V_{f,max} = \frac{\pi}{2\sqrt{3}} \tag{3.2}$$

$$K_{\perp,quad} = \frac{16}{9\pi\sqrt{2}}\left(\sqrt{\frac{V_{f,max}}{V_f}} - 1\right)^{\frac{5}{2}} R_f^2 \quad \text{with } V_{f,max} = \frac{\pi}{4} \tag{3.3}$$

A Tekscan pressure mapping system was used to determine the applied consolidation pressure. Because the hot plates are spring loaded, the total compressive force depends on the thickness of the material. A thin film tactile pressure sensor (0.1 mm) was enveloped between two sheets of paper to obtain a total thickness of 0.2 mm for force measurements, equivalent to the average ADFRC tape thickness. The total compressive force was 49.1 N over the entire hot plate

area (100 mm x 10 mm). During consolidation, that force is applied onto the tape which has a width of 5 mm, and this results in an average consolidation pressure of 0.098 N/mm² or roughly 1 bar.

The measured tape thickness was ~0.2 mm and this correlates to a processing time of 25 seconds for a viscosity of 1000 Pa·s (rough average of all polymers from rheological testing at low strain rate) and 1 bar of consolidation pressure. The belt speed was changed to have a 25 second consolidation stage to obtain good impregnation for all specimens which were visually inspected. The dry fibre preforms, polymer films and offcuts were weighed before and directly after processing, from which the fibre volume fraction V_f was estimated. After processing, the ADFRCs were trimmed to 100 mm length and 4 mm width to create uniform tensile test specimens.

Different processing temperatures were investigated for the different matrix systems as shown in Table 3.4. These temperatures were chosen to be the lower and upper bounds of the recommend processing temperatures according to CES Edupak [111]. The PA upper processing temperature was based on the manufacturer recommended printing temperature of 260 °C [3]. For the lower processing temperature, a value of 200°C was selected to minimise potential degradation of the matrix.

Table 3.4: Processing conditions for each ADFRC with a different thermoplastic matrix.

Material	**T_{low}**	**T_{high}**
PLA	170 °C	210 °C
PA	200 °C	260 °C
ABS	177 °C	260 °C
PETG	249 °C	288 °C

3.3.2 Mechanical testing

Tensile testing was performed on samples with dimensions of 100 mm x 4 mm x 0.2 mm. For each configuration, three samples were tested. The ADFRCs were taped to a paper tab as shown in Figure 3.9 and clamped between two mechanical grips of an electromechanical Shimadzu test machine equipped with a 1 kN load cell. The specimen was loaded at a displacement rate of 1 mm/min and a video extensometer by iMetrum was used to measure the strain during testing.

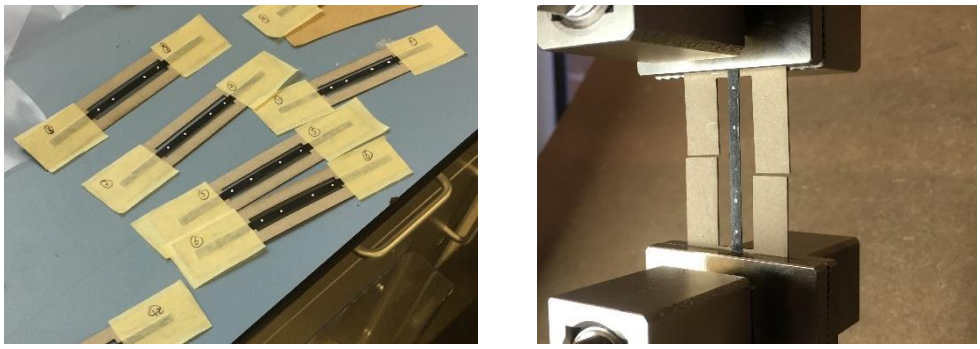

(a) (b)

Figure 3.9: Tensile test samples during a) preparation and (b) loaded in tensile test machine.

3.4 Results

3.4.1 Mechanical testing

The tensile response of the four different ADFRCs can be seen below in Figure 3.10, where all stress-strain curves are shown for the different specimens. In general, all specimens showed a linear stress-strain curve until failure. This shows the reinforcing effect of the discontinuous fibres, as plastic deformation was prevented, and the maximum elongation was limited to about 1.1%. Overall, the best performing specimens had a strength of around 300 MPa and a stiffness on the order of 23 GPa, which included the PETG, PLA and ABS specimens.

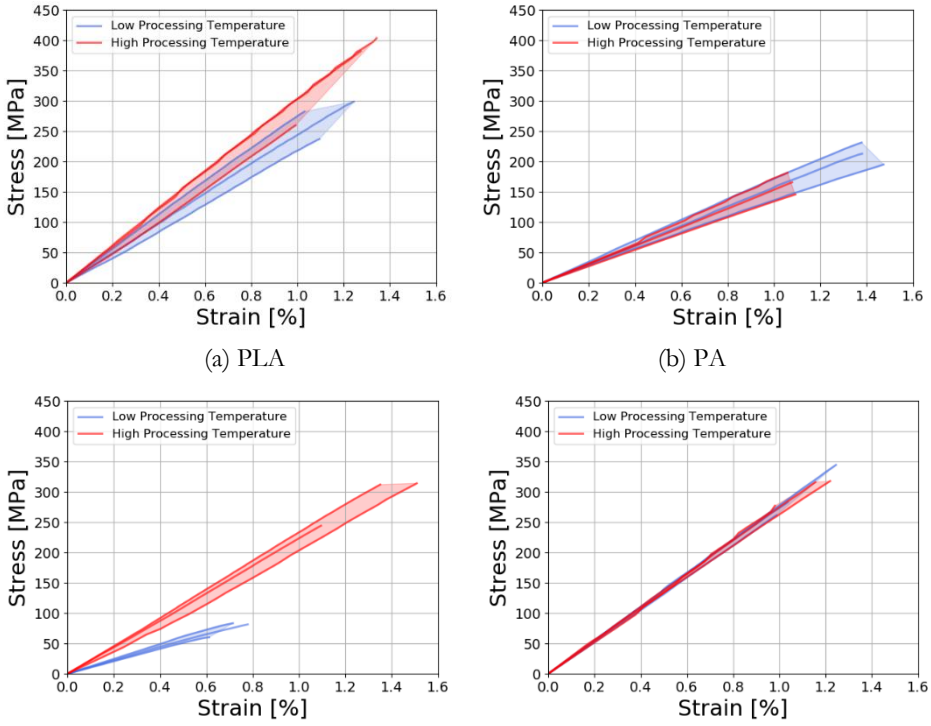

(a) PLA (b) PA

(c) ABS (d) PETG

Figure 3.10: Stress-strain curves of ADFRCs at low processing temperature and high processing temperature.

The PLA specimens (Figure 3.10a) showed a small increase in strength and stiffness for the higher processing temperatures as consolidation may have improved due to the lower viscosity

during processing. The ABS specimens (Figure 3.10b) showed a large increase in performance at higher processing temperatures, which was caused by poor consolidation at the low processing temperatures. At 177°C, ABS has the highest viscosity of the polymers tested which meant the polymer did not fully impregnate the specimen, which was confirmed via visual inspection. For the PA specimens (Figure 3.10c) the strength decreased somewhat at higher processing temperatures which may be caused by degradation of the matrix as confirmed by TGA testing presented in section 3.2.2. The PETG specimens (Figure 3.10d) showed the lowest variation and little change between processing temperatures. Table 3.5 shows average test results with coefficient of variance (CoV) for the different tensile properties.

Table 3.5: Tensile test results of showing modulus, stress and strain at break and coefficient of variance (CoV).

Material	Temperature	Modulus [GPa]	CoV [%]	Stress [MPa]	CoV [%]	Failure strain [%]	CoV [%]
PLA	Low	24.15	16.71	274.68	11.39	1.12	9.76
	High	28.00	13.69	351.54	22.64	1.20	15.45
PA	Low	15.71	10.67	215.83	8.45	1.41	3.85
	High	14.95	8.23	166.79	10.98	1.08	1.58
ABS	Low	11.24	8.63	76.76	17.08	0.70	11.93
	High	21.04	10.23	294.73	13.40	1.32	15.84
PETG	Low	27.12	3.05	300.49	14.61	1.09	12.54
	High	25.94	6.30	309.36	7.76	1.12	11.05

A comparison of the strength of stiffness of each ADFRCs is shown in Figure 3.11, which also shows the standard deviation of each three specimens tested. The increase in performance of the ABS specimens at higher processing temperatures can clearly be seen here, as well as the lower overall performance of the PA specimens. For reference, the tensile properties of the MarkForged continuous fibre PA filament are also shown, normalised from a V_f of 20% to a V_f of 12.5% by ratio.

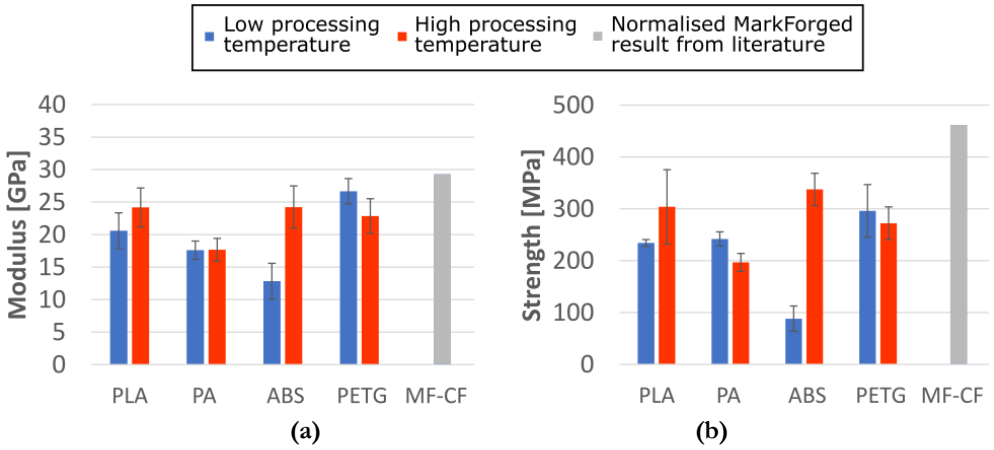

Figure 3.11: Tensile test results of ADFRCs processed at different temperatures as measured compared to MarkForged continuous fibre (MF-CF) printed parts normalized by ratio to a V_f of 12.5% [14].

3.4.2 Microstructural analysis

Two different micrograph studies were performed, using optical microscopy and scanning electron microscopy (SEM) for fracture surface analysis. Figure 3.12 shows representative cross sections of the four different ADFRCs at low and high processing temperatures. The PA ADFRCs show a dark region around the fibres which is attributed to polishing artefacts caused by the low modulus of PA and the poor adherence to the carbon fibres.

The PLA and ABS specimens showed a clear reduction in void content from a low processing temperature to a high processing temperature. The low temperature processed ABS specimen showed poor consolidation as two distinct resin films with dry fibres in the middle could be observed. For the PETG specimens, similar quality was observed for the low and high processing temperatures. Small darker regions near the fibres can be seen that show fibre fracture in the specimen, which is also present to some extent in the other specimens.

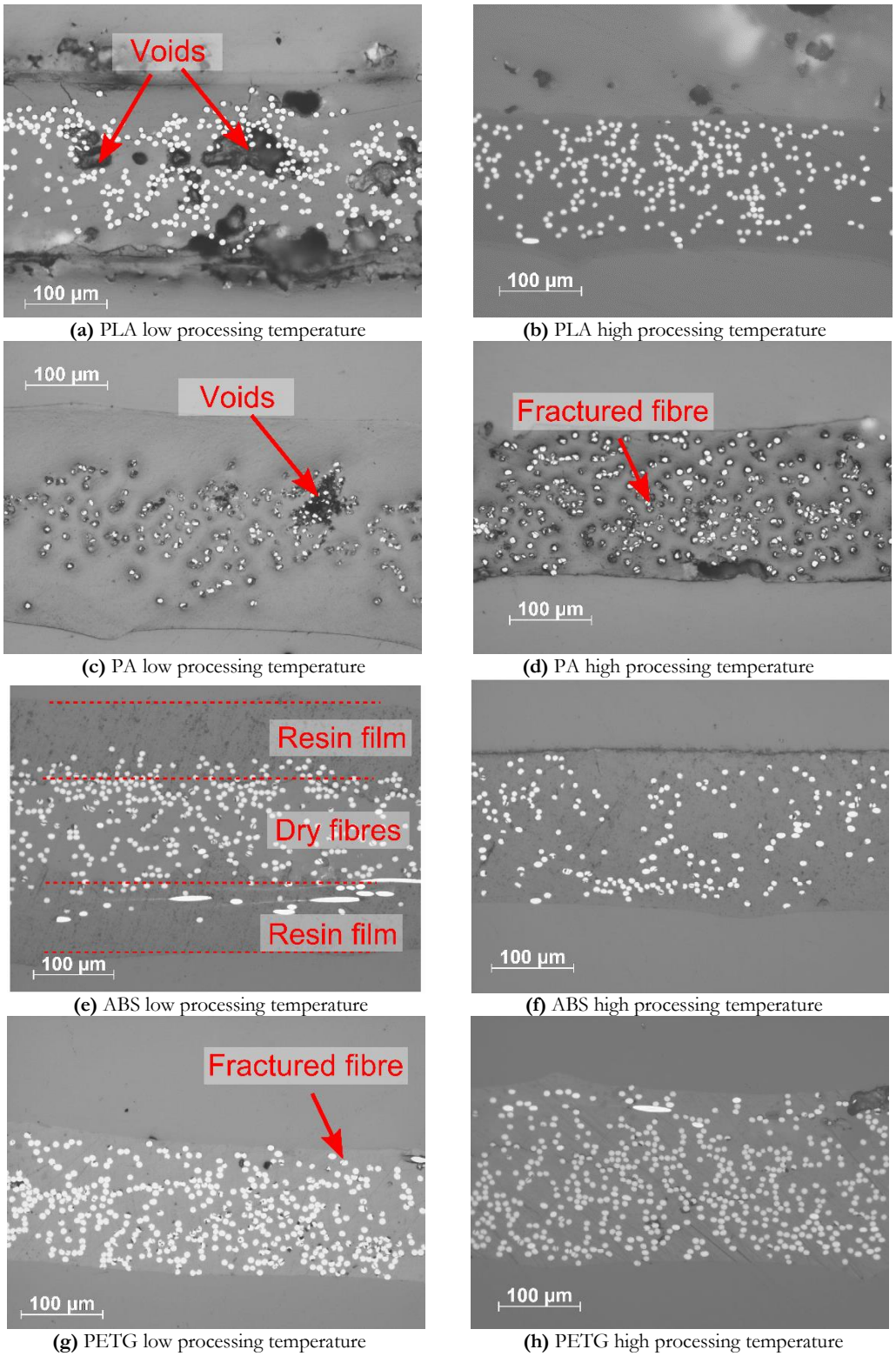

(a) PLA low processing temperature
(b) PLA high processing temperature
(c) PA low processing temperature
(d) PA high processing temperature
(e) ABS low processing temperature
(f) ABS high processing temperature
(g) PETG low processing temperature
(h) PETG high processing temperature

Figure 3.12: Optical micrographs of different ADFRPs, left low processing temperatures and right high processing temperatures.

Figure 3.13 shows the fracture surfaces obtained from SEM of four different ADFRCs, all processed at higher processing temperatures. The PA specimen clearly shows more plastic deformation of the matrix compared to the other specimens. The serrated and rough fibre ends indicate fibre fracture occurred. Some fibre-pull out appears to be also present which as clear

circular holes in the resin are visible. Overall, little matrix residue was found on the fibres which shows the fibre-matrix interface is poor.

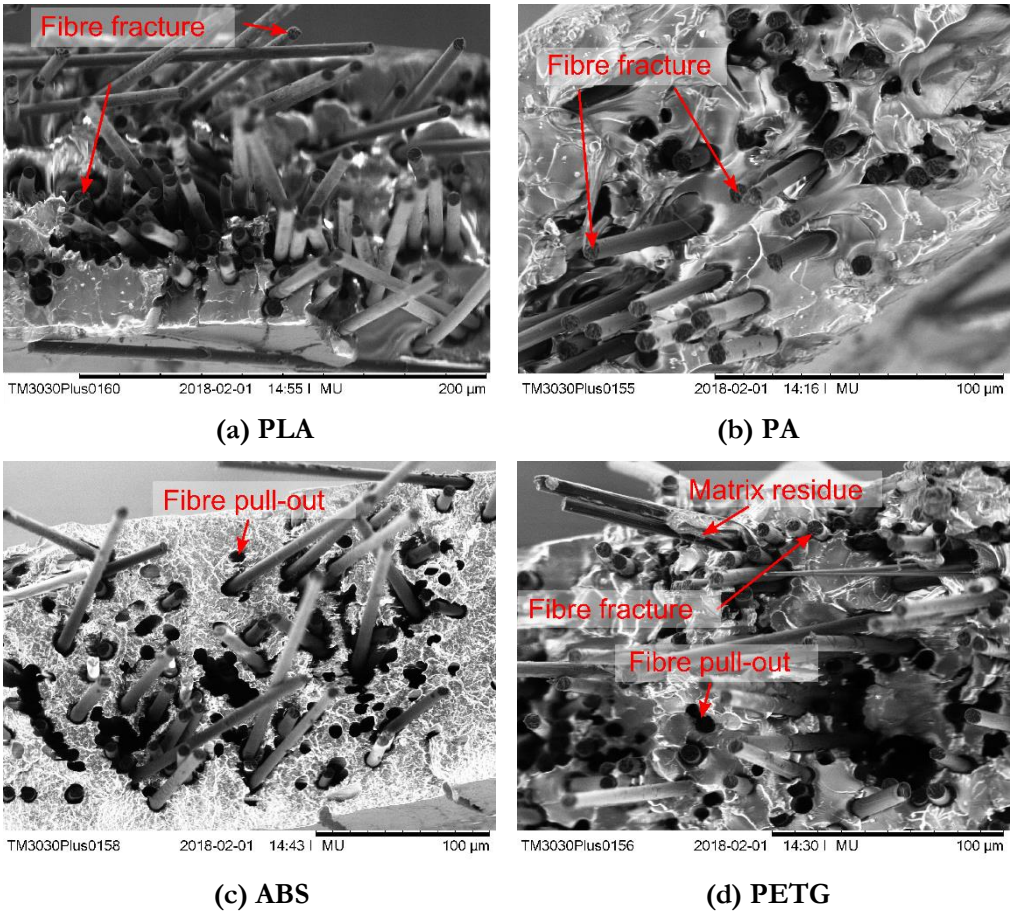

Figure 3.13: SEM micrographs of fracture surfaces of different ADFRCs, all for higher processing temperatures

3.5 Discussion

A matrix selection for fibre reinforced FFF was presented based on consideration of a wide range of criteria that influence the mechanical behaviour and process dynamics. In this work, the goal was to select polymers that are suitable for future fibre reinforced FFF processing and as such the processing temperatures and the polymer viscosity were more important at this stage than performance criteria such as crystallinity and strength/stiffness. A substitute for polymer viscosity was used (the documented average moulding pressure) which allowed comparison of different polymers. Rheological testing of the candidate polymers showed similar trends between their relative viscosities and documented moulding pressure, confirming this can be used as a relative comparison between polymers.

The study highlighted ABS, PLA, and PETG as the most promising polymers for future FFF use. Other polymers have been identified which can be suitable for fibre reinforced 3D printing such as PBT. This process may therefore be used for future identification of suitable 3D

printing materials, where the criteria and weightings may be changed depending on temperature and cost restrictions and performance optimisation. The performance of the fibre reinforced thermoplastic composites was investigated by the manufacture of ADFRC tapes.

ADFRC tapes were manufactured using a custom-built consolidation module. A flow analysis through Darcy's law indicated enough pressure was applied to impregnate the fibres within 25 seconds. However, some voids were found on the specimens and further improvement may be possible by increasing the pressure and/or time of consolidation. The flow of the polymer may also affect the fibre alignment as the fibres are not fixed in place. An improvement could be made by preventing any side flow through redesign of the consolidation station.

The reinforcing effect of the fibres was clearly present as the strength increased by a factor 7.5 from ~40 MPa for the pure polymer to 300 MPa of the ADFRCs. The measured average failure strength of 300 MPa was lower than the theoretical continuous fibre composite strength (~580 MPa) based on a rule of mixtures analysis of fibre strength and fibre volume fraction. The same holds for the predicted composite stiffness of roughly 30 GPa compared to the measured stiffness of ~23 GPa. This may be attributed to uneven fibre distribution, fibre misalignment and the discontinuous fibres not being fully loaded as explained by shear lag theory [139].

A better prediction of the ADFRC modulus is given by Equation (3.4), where the composite modulus E_c is calculated as a function of the fibre modulus and content (E_f, V_f), matrix modulus and content (E_m, V_m) and the fibre misalignment factor η_0 and fibre efficiency factor η_1 [11]. The fibre efficiency factor η_1 relates to the fibres not being completely loaded as explained in section 2.1.4. It can be calculated using the analysis presented by Cox [140]. It is dependent on the fibre length l_f and diameter d_f and a constant a relating to the matrix modulus E_m, fibre modulus E_f and fibre volume content V_f as shown in Equation (3.5) and (3.6). Substituting the known values for the carbon fibres and PLA matrix, with a V_f of 12% gives $\eta_1 = 0.970$.

$$E_c = \eta_0 \eta_1 V_f E_f + V_m E_m \tag{3.4}$$

$$\eta_1 = 1 - \frac{\tanh(a l_f / d_f)}{a l_f / d_f} \tag{3.5}$$

$$a = \sqrt{-\frac{3E_m}{2E_f ln(V_f)}} \tag{3.6}$$

For η_0, the fibre orientations need to be known which are estimated using ellipse fitting which is the most widely used technique to obtain fibre orientations from micrographs [141]. The orientation of a single fibre in 3D space can be described by two angles, θ and ϕ, as shown in Figure 3.14. For a composite cross section, each fibre will be represented by an ellipse, and its

major axis *a* and minor axis *b* will change direction and magnitude depending on the fibre orientation. The fibre orientation angles θ and ϕ and can obtained using Equation (3.7) and (3.8), where θ is the in-plane angle the fibre makes with the 1-2 plane and ϕ is the out-of-plane angle.

$$\theta = \cos^{-1}(b/a) \tag{3.7}$$

$$\phi = \gamma \tag{3.8}$$

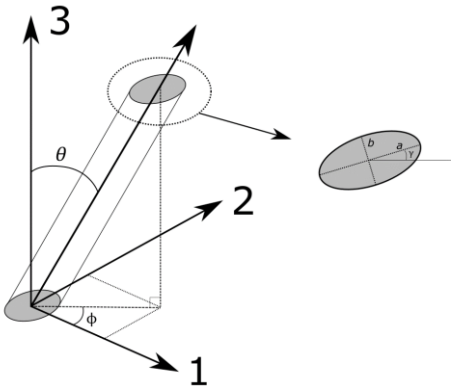

Figure 3.14: Definition of fibre orientation expressed as angles (θ,ϕ)

Ellipse fitting was performed via the ParticleSizer script for ImageJ [142]. Figure 3.15 shows the ellipse fitting for an example cross section of the PLA ADFRC with the accompanying in-plane fibre distribution. As the micrograph cross section can be misaligned with respect to the fibre tape, the mean fibre orientation was calculated and used to centre the fibre orientation distribution around 0°. The fibre orientations fall between ±20°, with 37% of the fibres bounded between ±5°, which is lower than expected from previous HiPerDiF results.

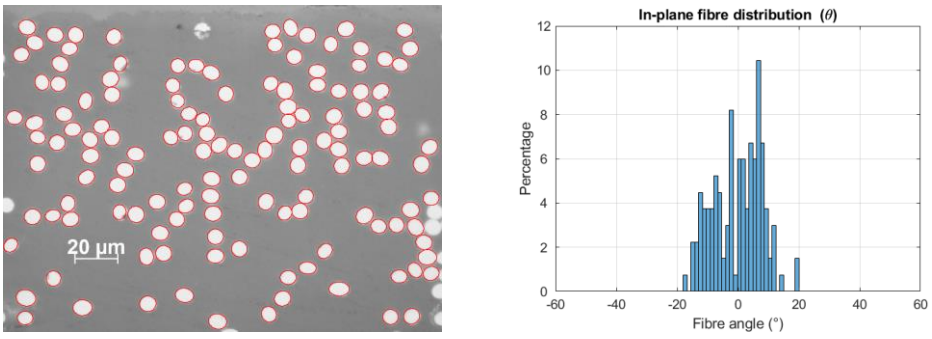

(a) (b)

Figure 3.15: Fibre orientation analysis showing (a) ellipse fitting performed on PLA cross section and (b) resulting in-plane fibre distribution.

The fibre misalignment factor η_0 is calculated using an analogue to classical laminate theory, by representing each fibre as a lamina with an angle *θ*. The modulus for each lamina can be calculated using Equation (3.9), where E_{11} is the composite modulus along the fibre direction, E_{22} is the composite modulus perpendicular to the fibre direction , G_{12} is the in-plane shear modulus and ν_{12} is the in-plane Poisson ratio. These properties are estimated by rule of mixtures using a V_f of 12.5% and the fibre and matrix properties. The effective composite modulus E_c^* with

different fibre orientations can then be calculated using Equation (3.10), and the fibre misalignment factor is defined as the ratio between E_c and E_0 as shown in Equation (3.11).

$$\frac{1}{E_\theta} = \frac{\cos^4\theta}{E_{11}} + \left(\frac{1}{G_{12}} - \frac{2\nu_{12}}{E_{11}}\right)\sin^2\theta\cos^2\theta + \frac{\sin^4\theta}{E_{22}} \tag{3.9}$$

$$E_{c^*} = \sum_{k=1}^{n} \frac{E_{\theta,k}}{n} \tag{3.10}$$

$$\eta_0 = \frac{E_c^*}{E_\theta} \tag{3.11}$$

The fibre misalignment factor η_0 was found to be 0.874 and this results in a predicted stiffness of 25.36 GPa for the PLA sample, which is within one standard deviation from the best performing samples. An increase in mechanical performance may therefore be possible by increasing the level of fibre alignment.

The stress-strain curves exhibited a linear trend with a maximum strain of ~1.1% which indicates fibre fracture was obtained for these specimens. The SEM micrographs showed a combination of fibre fracture (serrated fibre ends), together with some fibre pull-out. One can see that little matrix residue was left on the fibres which indicated a generally poor interfacial adhesion between the thermoplastic matrices and the carbon fibres.

The use of fibres significantly beyond the critical length has in large part made up for deficiencies of the interface through the simple addition of interface area. In concurrent work, closed-loop recycling of thermoplastic matrix composites was investigated which showed an increase in strength over multiple recycling loops which shows an increase in strength may be possible by optimizing the fibre-matrix interface [16], [17] .

The ABS samples showed a large increase in mechanical properties at higher processing temperatures. This was confirmed by the poor impregnation of the ABS samples at lower temperatures as seen in Figure 3.12c. ABS was expected to be the best performing and processable material from the material selection and has the highest average stiffness of 25 GPa.

The PA matrix ADFCR clearly showed local ductile deformation of the matrix on the SEM micrograph and it showed the lowest performance of the four tested materials. This sample was fabricated to compare it to the MarkForged continuous fibre printer, which prints a carbon fibre - PA composite with a V_f of 20% and a tensile stiffness and strength of 50 GPa and 700 MPa respectively. The ADFRC PA composites in this study had a V_f of a 12.5% and showed a stiffness and strength of 17.3 GPa and 239 MPa. In this study, the strength and stiffness reduced at higher

processing temperature which could be due to oxidation of the matrix as TGA analysis confirmed. El-Mazry [143] identified that during oxidation of PA, main chain scission occurred which reduces the average molar mass and affects the level of entanglement.

From the matrix selection process, PLA, PET and ABS were expected to perform better than PA as ADFRC matrix. The results confirm this, where the highest mechanical performance was obtained with PLA, PETG and ABS matrices with strength and stiffness in the order of 300 MPa and 23 GPa. The highest measured strength was 407 MPa and the highest measured modulus was 30.9 GPa for a PLA sample for a relatively low fibre content of 12.5%. This is a factor 8 increase in strength compared to available short fibre thermoplastic filament with similar matrices [76], [77], [90], [91].

3.6 Conclusions

Aligned discontinuous fibre reinforced composites (ADFRCs) were investigated as a feedstock material for automated composites manufacture using extrusion based additive manufacturing. The hypothesized advantage of ADFRCs is that they can provide near continuous fibre composite performance but have better processing characteristics as the discontinuous fibres can be more freely deposited. Aligned 3 mm long carbon fibres were used which is well above the average reported critical fibre length of ~1 mm for carbon fibres in thermoplastic matrices. A matrix selection was performed based on the process characteristics of fused filament fabrication which yielded four candidate thermoplastic matrices (ABS, PLA, PETG and PA). An in-house developed continuous consolidation module was used to manufacture composite tape with a V_f of 12.5%, which were then subjected to a tensile test. Tensile stiffnesses and strengths up to 30 GPa and 400 MPa respectively were recorded with failure strains in the order of 1.1%. Compared to currently available short fibre thermoplastic filaments, the strength of the ADFRCs was an order of magnitude higher. Fracture surface analysis revealed a combination of fibre fracture and fibre pull out. Little matrix residue was found on the fibres which indicates the interfacial properties may be improved. Overall, the measured strength was lower than theoretically predicted. This may be attributed to an uneven fibre distribution, misalignment and incomplete load-transfer, and therefore better understanding of the flow properties of the matrices and fibre-matrix interface may improve consolidation and the mechanical properties.

This chapter demonstrated the performance of ADFRCs and that they can compete with their continuous fibre counterpart. The next chapter of this thesis focuses on investigating the flow properties of the ADFRCs and how the fibres behave in a thermoplastic melt. This will

allow extrusion based additive manufacture of these ADFRCs, enabling a low-cost manufacturing method for high performance materials.

Chapter 4
Filament forming

The contents of this chapter are based around the following two conference presentations:

L. G. Blok, M. L. Longana, and B. K. S. Woods., "Development of short fibre reinforced thermoplastic feedstocks for high performance 3D printing," 11th International Conference on Manufacturing of Advanced Composites (ICMAC 2018), Nottingham, UK, 11-12 July 2018

And:

L. G. Blok, H. Yu, M. L. Longana, and B. K. S. Woods, "Flow Behaviour of Aligned Discontinuous Fibre Reinforced Thermoplastics for Additive Manufacturing Applications." Euromech colloquium 602: Composite Manufacturing Processes - Analyses, Modelling and Simulations, Lyon, France, 13-15 March 2019.

In this chapter, the work on forming the aligned discontinuous fibre reinforced composite (ADFRC) tapes into a uniform, circular filament is discussed. First, the challenge of forming the ADFRC tape into a circular filament using a continuous process is presented in the introduction. Five different concepts for reshaping the ADFRC tape into a circular cross section filament were proposed and evaluated. An extrusion based method was chosen and the required background information on the flow of short fibre thermoplastic polymers is given in section 4.2, which highlights the multi-physical aspects involved, including the importance of thermal and rheological behaviour of the ADFRC tape. The methodology of the filament forming process is given in section 4.3, which shows the development of a convergent nozzle based extrusion forming process for ADFRC tapes using a direct feeding mechanism of the tape to avoid fibre breakage. Different extrusion studies were performed to converge on successful processing methods to directly extrude the ADFRC tapes through custom dies. Initial extrusion tests were performed to demonstrate the extrusion concept and give a better understanding of the flow behaviour of ADFRCs. The results of this initial extrusion study are presented in section 4.4. A numerical thermal analysis of nozzle behaviour was written and validated against the experimental set-up presented in section 4.5. The results of the thermal analysis and the initial extrusion tests were

used to design a second set of extrusion tests which are presented in section 4.6, leading to successfully achieving continuous extrusion. The discussion and conclusions on the overall filament forming process are presented in section 4.8.

4.1 Introduction

4.1.1 Filament forming criteria

The main question considered in this chapter is how the ADFRC tape can be reshaped into a circular filament, with a continuous process that allows for the creation of filament spools. The advantage of starting with ADFRC tapes is that the consolidation has been performed at a previous stage, which makes the material easier to handle and only a reshaping action is required. A filament with a circular cross section is required for fused filament fabrication (FFF) such that the material can be freely deposited in any direction. The reshaping process will require the application of heat to allow the fibres and polymer matrix to flow and be shaped into the required geometry. It is therefore clear that several physical aspects will play a role in reshaping the filament such as thermal behaviour, rheological properties and interactions of the fibres with the flow and between themselves.

The required change in cross-section is schematically shown in Figure 4.1, where the dimensions of the tape (5 mm x 0.2 mm) and those of a circular filament with an equivalent cross sectional area (1.12 mm diameter) are given. The filament diameter is a relevant parameter for the FFF process as it relates to the spooling capability, nozzle sizes, printing resolution, track widths and height. Unreinforced thermoplastic filaments for desktop 3D printers typically have a diameter of 1.75 mm or 3 mm and they are used with a nozzle with a ~0.3 mm outlet diameter. A fibre reinforced filament with a similar diameter as standard pure thermoplastic filament may not spool properly as it has a much higher stiffness. A filament with a small diameter filament may require alterations to a standard printing head and reduce production rates as less material is deposited in each printed track. The nominal filament size shown here is both a direct result of the size of the tapes, and a reasonable trade-off between production rate and spoolability.

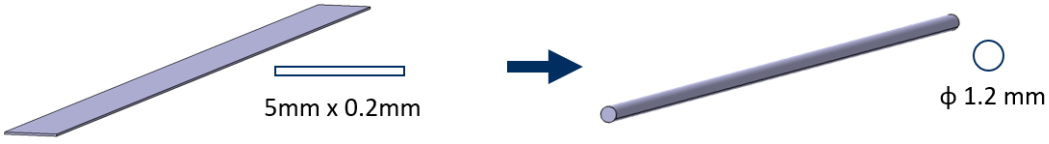

Figure 4.1: The highly aligned fibre reinforced polymer tape needs to be reshaped into a circular filament.

Standard manufacturing processes for 3D printing filaments are based on screw extruders, where a molten polymer is extruded through a die and spooled onto a roll. Using a similar process

for fibre reinforced polymers causes the brittle carbon fibres to fracture due to the high shear rates involved and interactions between the fibres and the extrusion screw [144]. This decreases the average fibre length in the filament and reduces the performance of the printed part. Alternative manufacturing methods therefore need to be designed to form a uniform circular filament without breaking the carbon fibres. The ability to start with ADFRC tapes, where the fibres are pre-aligned in the same direction, is a benefit here as it helps prevent problems with fibre jamming according to the literature review presented in section 4.2.

Three main criteria for potential filament forming methods have been established. They are (1) a high dimensional control, (2) low risk and (3) low complexity of the process. A high dimensional control is needed as this directly influences the quality of the printed part. Any inconsistencies in filament diameter leads to irregular 3D printed path width and/or height and can cause voids between printed tracks which become weak points in the printed part. Risk in a filament forming concept relates to whether or not similar methods exist and have been studied before. Processing of high aspect ratio fibres in polymer melt can cause fibre jamming and an assessment on the risk for different concepts is made. This is based on existing literature, looking at similar processes and considering the characteristics of the different concepts. The complexity of concepts is also considered as this relates to the ability to engineer it in the project time frame within the budget constraints. An overview of the filament forming concepts considered is presented next before more detail is given on the method chosen.

4.1.2 Filament forming concepts

The filament forming process of transforming the ADFRC tape into a uniform filament can be done in multiple ways. At the start of this work, five methods were conceptualised which are shown in Table 4.1. All methods require heating of the preform to soften the thermoplastic matrix and allow the tape to be reshaped.

Table 4.1: Different filament forming methods with advantages/disadvantages.

Method	Twisting and heating	Conical shaping	Direct-Extrusion	Roll moulding	Induction heating and pull
Concept		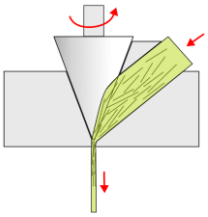	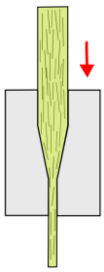	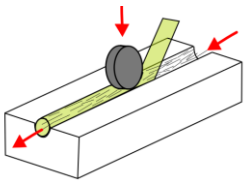	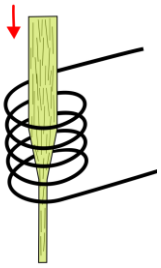
Complexity	High	High	Low	Medium	Low
Risk	High	High	Low	Medium	Medium
Dimensional control	Very low	Medium	High	Medium	Medium

The twisting-heating method is based on twisting the preform into a helical shape and pulling it, such that the formed helix folds on itself. This process requires intimate contact of the tape with itself to start the polymer sintering process. It is considered a relatively complex method as it requires both a twisting action and a pulling action with the requirement of intimate contact. No information has been found on using a similar process before and therefore the risk is high. It is also expected to have a low dimensional control. The twisting/folding action depends on local stiffness properties of the tape and a uniform temperature is required which may be hard to obtain when twisting the tape.

The conical shaping method relies on a rotating conical tip which twists and rolls the AD-FRC tape. The angle of the conical tip, rotation speed, tape feed speed and inlet angle of the tape can be changed to improve the reshaping method. The tape will be in contact with the conical tip and with the inlet region which means it is possible to heat the tape through conduction and/or frictional forces. The direct contact between the molten polymer and the rotating conical tip with surrounding guides means a build-up of polymer is possible and tight tolerances need to be maintained to prevent gaps where the polymer or fibres may get stuck. Depending on the set-up, the fibres may experience a considerable force as they are moved along the conical cone which can cause them to break. No previous implementation of such a conical shaping method has been found before and therefore it would need to be developed from the start, so the risk is high. The complexity is high as small tolerances are needed for this set-up as discussed above. As the cone angles, speed and tape feed rate can be changed, some dimensional control is expected

to be possible but given the asymmetric rotation action with respect to the tape this may not lead to a completely uniform filament.

The direct-extrusion method is a proven method that allows for high dimensional control as the feed rates and the channel geometry can be changed. It is widely used in common filament production using a screw extruder. In this concept, the screw extruder is replaced with a direct tape feeder and careful design of the channel is required to enable continuous extrusion and prevent fibre jamming. The complexity is relatively low as only a simple convergent nozzle/channel needs to be manufactured, and it is a proven method for extrusion as some studies have investigated this before which are discussed later. The filament dimensions can be controlled by controlling the nozzle dimensions, feed rate, the geometry and the temperature.

The roll moulding method for direct filament creation is an integrated solution for use directly on the HiPerDiF machine. The idea of this concept is that the dry fibre preform of the HiPerDiF machine is transported by a belt into a custom consolidation module that has the shape of the filament. A resin powder or film must be added, and the filament can then be made by consolidating the resin and fibres together under a roller. It is more complex than the extrusion method as it needs to be integrated with the HiPerDiF machine and the dimensional control is medium as some post processing may be required on the moulded rod. The consolidation of rods with a circular cross-section is harder than consolidation of the ADFRC tapes as the impregnation length of the resin will be higher.

Lastly, an induction heating and pull mechanism was considered which is based on heating the preform under a slight tension such that it shapes into a filament. It is similar to the twist-heat method but without the creation of a helix. Upon heating and applying tension, the tape may stretch and break before it forms itself into a circular filament which gives this method a higher risk. As only the feed in and feed out rate and temperature can be controlled, and not the shape of the output, this unproven concept was expected to have poor dimensional control.

With all of these factors taken together, it was decided to develop an extrusion-based method as it seems to be the most proven method for filament manufacture. It allows to further study the fibre orientation in thermoplastic flows with longer, aligned fibres and it is similar with the 3D printing process itself which allows translation of lessons learned. The roll moulding method may also be a good filament forming technique, but it was not pursued due to perceived higher process risk and the requirement for direct modification of the HiPerDiF machine, which would have impacted other concurrent research activities.

4.2 Background information

The flow of short fibre reinforced polymers is an important topic for injection moulding, extrusion and compression moulding techniques of short fibre composites [145]–[147]. The fibres affect the bulk fluid properties while the fluid flow affects the fibre orientation. Some of the earliest work on this topic dates back to Einstein who modelled the increase in viscosity due to the addition of spheres in a fluid [148]. Jeffery [149] built up on that work to predict the fibre orientation of a single fibre suspended in a fluid. Since then, studies have evolved to include simulations of multiple fibres in polymer flows and predicting the fibre orientation state [150]–[153]. An overview on fluid analysis and (short fibre) polymer rheology is first presented here to explain the relevant physical aspects and then more detail is given on flow-induced alignment which is important for reshaping the tape into a circular filament.

4.2.1 Basics of channel flow

Rheology is the field of study that looks at how fluids flow and deform under various conditions. The main property of interest here is viscosity, which is the resistance of a fluid to flow. Viscosity relates to the internal friction in the fluid and can change depending on the flow conditions, temperature or material composition. The flow of a fluid can be visualised by streamlines, which depict the path followed by a fluid particle over time as shown in Figure 4.2. The velocity of the fluid between adjacent streamlines can be different, so a fluid can be thought of as shearing layers. The friction between the shearing layers causes an internal shear stress τ which is dependent on the viscosity of the fluid η and the velocity difference (dV/dx) as shown in Equation (4.1)

$$\tau = -\eta \frac{dV}{dx} \tag{4.1}$$

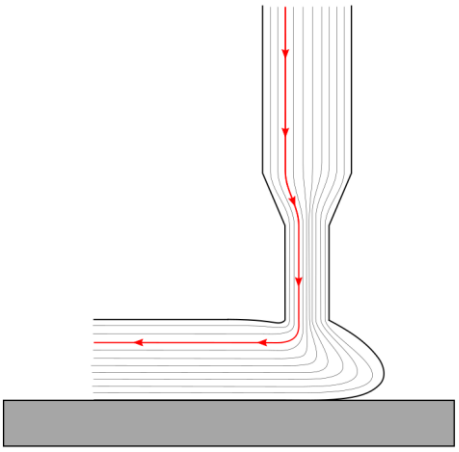

Figure 4.2: Schematic of streamlines of a polymer fluid during 3D printing.

Another aspect of fluid flow is whether the streamlines are constant over time or fluctuate. For a laminar flow, the streamlines are constant which means there is a steady flow without mixing between adjacent layers. When lateral mixing takes place and the streamlines change over time, the flow is called turbulent. A turbulent flow generally leads to more internal friction. The transition between laminar and turbulent flow is characterised by the Reynolds number as defined in Equation (4.2). The Reynolds number is the ratio of inertial forces (density ϱ, velocity V and a characteristic length L) and the viscous forces, characterised by the dynamic viscosity η. This non-dimensional number is used to capture the importance of viscosity effects, and for fluid flow in pipes the transition from laminar only to laminar and turbulent flow occurs around a value of 2000. For the polymeric flows considered in this thesis, the Reynolds number is much smaller than 2000 and laminar flow can therefore be assumed.

$$\mathrm{Re} = \frac{\rho V L}{\eta} \tag{4.2}$$

A brief analysis of laminar flow through a 2D channel flow is performed to help understand the main flow parameters. Figure 4.3 shows the velocity profile through a 2D channel. For simplicity, it is assumed that the fluid velocity at the wall is zero (no-slip boundary condition). A typical velocity profile **V** is then parabolic with the maximum velocity in the centre of the channel.

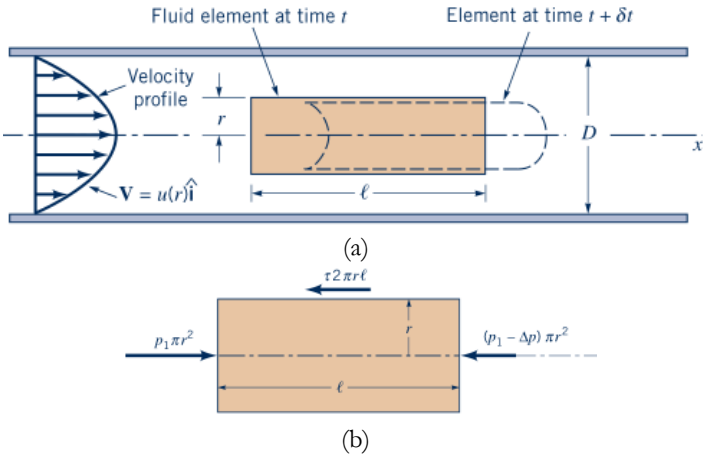

Figure 4.3: Fluid flow through a channel with (a) velocity profile and (b) fluid element [154].

The fluid element shown in Figure 4.3b experiences a pressure force and an internal shear force. For the fluid element we can write the force balance as Equation (4.3) and simplify it to Equation (4.4), which relates the pressure difference Δp in the fluid to the shear stress τ from the viscous forces in the fluid. It shows that a pressure drop must be present due to the shear stress τ. The shear stress τ is caused by shearing of the fluid as explained earlier. For a Newtonian fluid, the shear stress is linearly dependent on the velocity gradient (or shear rate $\dot{\gamma}$) as shown in Equation (4.5) where the dynamic viscosity η is a constant. For thermoplastic polymers the dynamic

viscosity η is not constant and depends on the shear rate and the temperature as will be discussed later.

$$(p_1)\pi r^2 - (p_1 - \Delta p)\pi r^2 - (\tau)2\pi r l = 0 \tag{4.3}$$

$$\frac{\Delta p}{l} = \frac{2\tau}{r} \tag{4.4}$$

$$\tau = \eta \frac{dV}{dr} = \eta\dot{\gamma} \tag{4.5}$$

The above equations can be further integrated for a circular pipe to yield Equation (4.6), which is a variant of the Darcy-Weisbach equation [154] . This equation shows that a certain pressure is required to force a fluid with viscosity η over a length *L* through a pipe with diameter *D* with an average velocity *V*. Increasing the flow length, the viscosity or the velocity of the fluid increases the required driving pressure while increasing the diameter will lower the driving pressure. These will be relevant parameters for the channel flow considered in filament forming process.

$$\Delta p = \frac{32V\eta L}{D^2} \tag{4.6}$$

Another consideration for the flow through a channel is how the fluid behaves near the wall surface. The analysis presented above assumed a no-slip boundary condition and only the internal friction of the fluid was considered to estimate the pressure drop in the flow. In theory, the surface type and quality should not affect the flow as for a laminar flow the fluid velocity at the wall is zero, so no friction force can be present. This assumption, however, has been much debated in scientific literature [155]-[156] and exceptions to this rule include polymeric flows and confined channel flow [157].

Surface friction can be attributed to two main factors; Coulomb friction and hydrodynamic friction [158]. Coulomb friction relates to direct contact between the solid fibres and the mould surface, and hydrodynamic friction relates to a thin surface boundary layer at the mould surface. Microscopically, hydrodynamic friction can be explained by deformation theory and adhesion theory [159]. Deformation theory relates to the surface roughness which causes flow irregularities at the mould surface as illustrated in Figure 4.4 and resulting in a net loss in energy. Adhesion theory predicts the polymer melt interacts with the mould surface through adhesive forces such as Van der Waals forces or electrostatic forces [160].

For both hydrodynamic and adhesive friction, the surface roughness plays an important role as it enlarges the surface contact area. Murtagh et al. [161] studied the surface friction of

continuous fibre thermoplastic polymers using a friction sled and found surface friction also increased with increasing temperature and higher shear velocities, while release agents could almost half the friction coefficient. For the ADFRC flow through a channel considered here, surface type, coating and roughness must be considered as relevant variables as they can affect the surface friction.

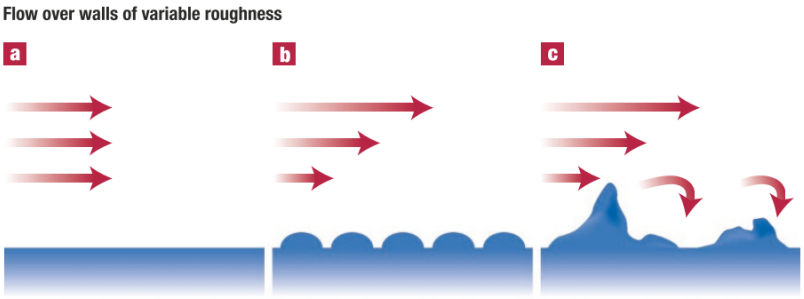

Figure 4.4: Flow over (a) smooth surface, (b) and (c) rough surface causing flow irregularities [156].

4.2.2 Basics of polymer rheology

Polymer rheology is the study of how polymers flow. Chapter 2 introduced two types of thermoplastic polymers, amorphous and semi-crystalline polymers. When amorphous polymers are heated above their glass transition temperature T_g, the mobility of the entangled chains increases, allowing the polymer chains to slide and enabling the bulk material to flow. Semi-crystalline polymers have crystalline regions in their structure, i.e. areas where the molecules are packed in a regular fashion, which act as reinforcement. At temperatures above their T_g they soften but keep some rigidity. Above their melt temperature T_m the crystalline regions lose their structural organisation, which makes it much easier for the polymers chains to move and the material to flow.

Both amorphous and semi-crystalline polymers above their glass transition temperature behave like visco-elastic fluids. A viscous material, as mentioned above, can be thought of as shearing layers and any force applied to this material causes it to flow over time. An elastic material deforms when a force is applied and returns to its original shape when the force is removed. Polymers have both an elastic and a viscous response to an applied load which is caused by a combination of sliding and stretching of the polymer chains. The amount of viscous and elastic behaviour changes depending on the polymer composition and temperature. The elastic part directly affects die-swell, which is recovery of the elastic energy when the material flows out of a contraction and increases in size. For material extrusion of the ADFRC tapes, the viscous part of the polymer melt is of most interest to obtain a continuous flow to reshape the tape, but die-swell may be important to consider in order to achieve tight geometric tolerances.

At low shear rates (close to zero), the viscosity of polymers is relatively constant which is known as the zero-shear viscosity. At higher shear rates, their viscosity decreases as shown in Figure 4.5 which is known as shear-thinning. The zero-shear viscosity of a polymer melt depends on the polymer type, molecular entanglement and average molecular weight. A higher molecular weight means the polymer has longer chains, and this leads to an increase in viscosity. The zero-shear viscosity can be used as a measure for the average molecular weight of a polymeric material. At higher shear rates, the polymer chains (regardless whether they are long or short) align and this leads to a reduction in viscosity and therefore the relative difference in viscosity between polymers with different molecular weights also reduces as Figure 4.5 shows.

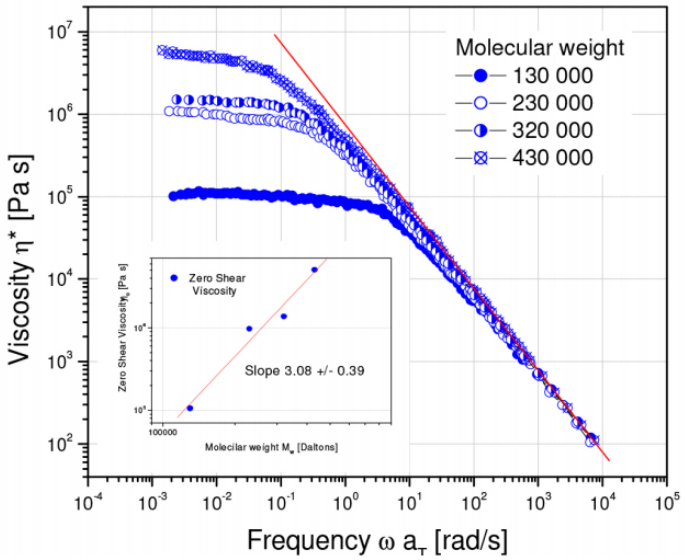

Figure 4.5: Viscosity dependence on shear rate for different molecular weight styrene-butadiene rubbers [162].

Temperature has a large effect on the viscosity of the polymer. At higher temperatures, there is an increase in polymer chain mobility and therefore movement between them is easier. This translates to a lower viscosity and the reduction in viscosity is typically described using an Arrhenius equation as shown in Equation (4.7) [163].

$$\eta(T) = A \cdot e^{\frac{E^*}{RT}} \tag{4.7}$$

In Equation (4.7), η is the viscosity, R is the gas constant, A is a fitting constant and E^* is the flow activation energy and there typically is an exponential decrease in polymer viscosity with respect to temperature. Although this model does not consider the physics within the polymer of entangled chains sliding, it is effective in predicting the bulk polymer viscosity as a function of temperature. The rheological testing of the candidate polymers shown in section 3.2.2 also

showed a similar trend between polymer viscosity and temperature and this data is later used for the extrusion tests of the ADFRCs.

4.2.3 Rheology of fibre filled polymers

Several flow phenomena of particle filled polymer melts are well-established, but the ability to simulate, predict and control long fibres in flow is still an ongoing field of study. This section aims to review the main knowledge on this topic, discuss the flow behaviour of fibre filled polymers and give an overview of some of the latest literature on predicting and controlling fibre orientation in fluid flows. Of specific interest is the ability of highly aligned fibres to flow through contractions as it directly relates to the filament forming challenge.

As mentioned in the introduction of this chapter, some of the earliest work on the topic of fluid suspensions was performed by Einstein and it was continued by Jeffery [148], [149]. Einstein investigated the increase in viscosity due to the addition of spherical particulates to a fluid while Jeffery modelled the orientation of a single fibre in a fluid flow. These two early approaches directly illustrate the complexity involved in the rheology of fibre filled polymers. The fibres change the bulk viscous properties, while the viscous forces in the fluid change the fibre orientation. These effects occur simultaneously and as will be shown, they influence each other. First, the change in viscosity due to the addition of fillers is discussed and then the fibre orientation effects are presented.

4.2.3.1 Effect of particulates on flow behaviour of a fluid

The flow of a fluid with suspended particles is dictated by a complex interaction between the fluid, the particles and the flow boundaries and conditions. The particle volume fraction Φ, their shape and their distribution have an important role in determining the rheology of the particle suspensions. Suspensions typically have a strong non-Newtonian behaviour as particles can form structured groups or layers, changing the bulk flow behaviour [164]. This makes it hard to link theoretical predictions with practical applications [165]. Despite the complexity involved, much research has been devoted to understanding the flow of particle suspensions both on a numerical and an experimental side. Here, the main work is reviewed, and some generalisations are made to explain the flow behaviour of filled suspensions.

Early work focused on suspensions with spherical particles. Einstein predicted the increase in viscosity of suspensions with spherical particles by considering the hydrodynamics surrounding the particle [148]. His approach was to model the flow of a fluid around a single sphere, and from this derive the effective increase in viscosity. By relating the relative size of the sphere in a

unit cell to the volume fraction a relationship between fibre volume content and relative viscosity increase was obtained. Others extended on this work, such as Batchelor who considered the Brownian motion of the particles and Krieger & Dougherty who included the interaction between spherical particles [166], [167].

A review on the rheology of suspensions is given by Stickel and Powell [168] which highlights the importance of particle interactions and the non-Newtonian behaviour (shear rate dependence) on the flow. The increase in viscosity can be described by the relative viscosity η_r which is defined as the ratio between the viscosity of the fluid with and without particles. Figure 4.6 shows η_r for different particulate fractions Φ, where Φ_m is the maximum particulate fraction. The relative increase in viscosity η_r tends to go to infinity as the ratio Φ/Φ_m approaches unity as this would be a completely filled fluid. The simple models by Einstein and Batchelor only predict the relative increase in viscosity (η_r) accurately at relatively low particle concentrations and the interaction between particles becomes dominant when $\Phi/\Phi_m > 0.4$.

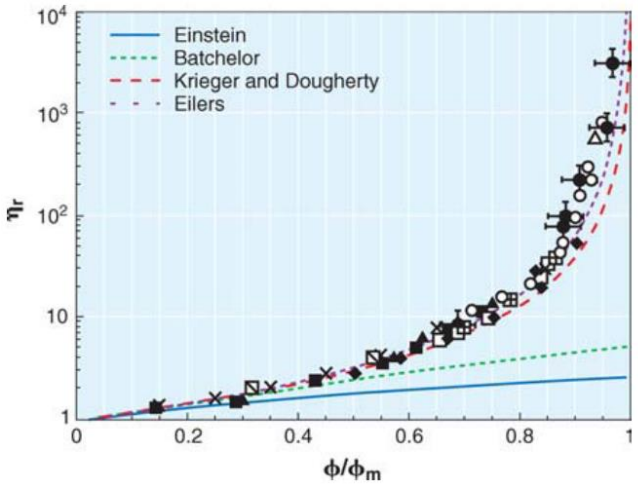

Figure 4.6: Relative viscosity η_r versus particulate concentration for different models and data points from experimental studies [168].

The two main aspects that cause an increase in viscosity of particle suspensions are the (constricted) internal hydrodynamics and the motion of particles. Interactions between particles lead to a further increase in effective viscosity as kinetic energy of the flow is dissipated through particle collisions [169]. The effect of particle interaction on the flow of the suspensions depends on the likelihood of interaction, which is mainly determined by the shear rate, particle concentration and particle shape.

Pabst et al. discuss the effect of particle shape on the rheology of suspensions [108]. Elongated particles with a high aspect ratio, such as fibres, behave differently in a fluid than spheres

as their orientation needs to be taken into account. The likelihood of interactions between particles also changes as a fibre is spread out over a larger distance in space. Typically, three concentrations regions are defined with respect to the density of fibres in suspensions: dilute, semi-concentrated and concentrated. In a dilute concentration, fibres can freely rotate without interacting with other fibres. This means the interparticle spacing must be larger than the fibre length. This is expressed by Equation (4.8) where V_f is the fibre volume concentration and r is the fibre aspect ratio [146]. In semi-concentrated regimes, defined by Equation (4.9), the spacing between fibres is less than the fibre length but hydrodynamic effects still prevail. For the concentrated regime, defined by Equation (4.10), the spacing between fibres is in the order of magnitude of their diameter and the interaction between particles becomes important.

$$V_f < \frac{1}{r^2}, \text{ dilute} \tag{4.8}$$

$$\frac{1}{r^2} < V_f < \frac{1}{r}, \text{ semi-concentrated} \tag{4.9}$$

$$\frac{1}{r} < V_f, \text{ concentrated} \tag{4.10}$$

Figure 4.7 shows the different concentration regimes plotted for fibre aspect ratio versus fibre volume fraction. The ADFRCs considered in this research work are located within the concentrated regime region, which means that the fibre interactions during flow are relevant for the flow behaviour.

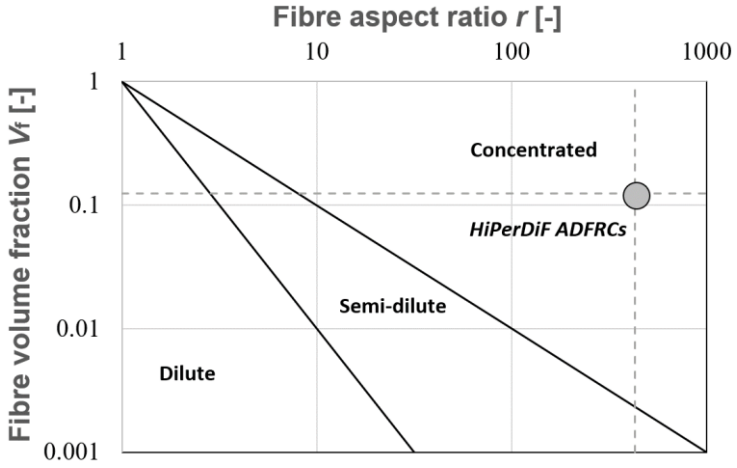

Figure 4.7: Different concentration regimes for fibre suspensions highlighting the location of the ADFRCs considered.

As presented in section 2.4, the orientation of a single fibre in 3D space can be described by two angles, θ and ϕ, as shown in Figure 4.8. These angles are related to the fibre unit vector **p** by Equations (4.11) to (4.13).

$$p_1 = \sin\theta \cos\phi \tag{4.11}$$

$$p_2 = \sin\theta \cos\phi \tag{4.12}$$

$$p_3 = \sin\theta \tag{4.13}$$

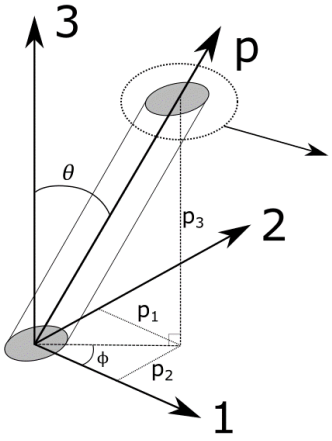

Figure 4.8: Definition of fibre orientation expressed as angles (θ,ϕ) or vector **p.**

For the HiPerDiF ADFRCs with a V_f of 12%, a 5 mm x 0.2 mm cross section has about 3000 fibres. Different descriptions exist to describe the orientation of multiple fibres. The most straightforward approach is to use a probability distribution function that expresses the probability to find a fibre within a certain angle range. Although some detail of the orientation of individual fibres is lost, it gives a clear overview of the mean and spread of fibre orientations.

The orientation of a fibre in flow was first described by Jeffery [149]. He solved the flow field around an ellipsoid particle and found that a single fibre in shear flow re-orientates periodically. This hydrodynamic approach showed that a fibre generally aligns itself with the flow direction, but it is always slowly rotating. After a characteristic time, the fibre rotational speed increases and it rapidly rotates by 180° and then rotates slowly again when aligned with the flow direction. This behaviour is known as Jeffery's orbit and different orbits with respect to θ and φ are possible depending on the initial orientation state of the fibre and flow conditions.

For concentrated suspensions, however, fibres are not able to freely rotate without colliding with other fibres. In general, interactions between fibres are difficult to model [170]. For a concentrated suspension, multiple fibre interactions may take place simultaneously which makes the problem more complex to solve. Different approaches have been used to model and understand the fibre orientation in concentrated suspensions. Folgar & Tucker modelled the evolution of fibre orientation in concentrated regimes using a statistical approach with the probability density function description of fibre orientation [170]. They assumed that, statistically, the flow has a similar effect on the fibre orientation as Jeffery's model, but with the introduction of a diffusive

interaction term based on the premises that fibre interaction causes randomisation of the alignment. The assumption here is that collisions cause a random change in fibre orientation. This diffusive term depends on the shear rate of the flow and includes a fitting constant.

Others have continued Folgar's & Tucker's model, also known as the isotropic rotary diffusion (IRD) model, to improve the fibre orientation predictions as it has been shown to over-predict the rate at which fibres orientate. The IRD model ignored any directional bias to the orientation change which likely is the case for aligned suspensions [170]. Studies have indicated that the diffusion term in the IRD model was lower for more aligned suspensions [171], [172]. More recently, Phelps and Tucker [173] introduced an anisotropic rotary diffusion model to better predict the orientation suspensions with longer fibres up to 10 mm in length. Their model showed improved predictions for injection moulding simulations but relied on five phenomenological parameters that required empirical fitting.

The flow regimes of suspensions with slender fibres through narrow gaps were studied by Tucker [174]. He identified four different flow regimes, depending on the initial anisotropy of the material, the out-of-plane fibre distribution and the slenderness of the gap. For highly anisotropic suspensions and a 'flat' or mainly planar fibre orientation, plug flow is predicted which may be simplified to a 2D problem. Mezher et al. [175] more recently performed direct numerical simulation to compare the Folgar-Tucker model for confined and unconfined shear flows. They found that the Folgar-Tucker model works well for unconfined shear flow but for strongly confined flows improvements are needed with respect to the diffusion coefficient. In a confined shear flow, fibres do align along the shearing direction but slower than predicted by the widely used Folgar-Tucker model. The effect of pre-alignment was not studied in this case.

A different approach to studying fibres in flow is to model the interaction between fibres using slender body theory, where the forces on a single fibre are more explicitly considered. For a single fibre in a shear flow, the hydrodynamic forces acting upon it can be resolved and coupled to beam bending equations. Du Roure et al. [176] recently reviewed the dynamics of flexible fibres in flows. Fibres typically exhibit three main types of motion in flow; tumbling, buckling or snaking behaviour. This depends on the elastic properties of the fibre (flexular stiffness) and the intensity of the flow (viscosity and shear rate). Another analysis approach for fibres in flow are bead models, representing the fibres by a series of beads connected by linear springs and using kinematic constraints to predict the bending and/or buckling behaviour of the fibres. Alternatively, particle based methods may be used to model individual fibres in flow [177].

From the studies presented on fibre orientation above, the generic flow behaviour of fibre suspensions can be summarised. In general, fibres will orientate with the flow direction although some re-orientation may be possible through fibre interactions. Jeffery's original model predicts that fibres periodically re-orientate, but for concentrated suspensions there is a tendency for fibres to become more aligned with the flow due to physical constraints [146]. Hydrodynamic forces act on the fibres and bending or buckling instabilities may be present depending on the shear rate and fibre stiffness. Although considerable work has been done on the theory behind orientation of fibres in flows, there is limited work on applying this theory to experimental studies with aligned fibre suspensions which is presented next.

4.2.3.2 Flow induced fibre alignment

Some experimental studies on flow-induced alignment of fibres have been performed with similarity to the extrusion problem for filament forming. Some of the earliest work was performed by Bell [178], who investigated the fibre alignment in flows with a V_f of 50%, where fibre interactions play an important role for the flow behaviour, as shown in Figure 4.7. Pre-orientated glass fibre pellets were used with a length of 3.175 mm in an epoxy resin with a viscosity of 1000 Pa·s, which was forced through a rheometer tube going from a diameter of 12.7 mm to 3 mm with an angled constriction ranging from 15° to 40°. Pressure was applied via a plunger and plug flow was observed. Above the constriction the fibres aligned perpendicular to the flow direction while in the constriction, the glass fibres became orientated with the flow direction and remained orientated after the constriction. Experiments were also performed with random orientated fibres instead of pre-orientated pellets, but this led to fibre jamming in the constriction. For successful filament forming without fibre breakage, precursors with pre-oriented fibres may therefore be required to prevent nozzle jamming – a finding which is highly relevant to the current work.

Murty and Modlen [179] investigated the alignment of short glass fibres (3, 6, 12 mm) in glycerine with 0.001% - 0.010% fibre volume content. The viscosity of the carrier medium ranged between 10 – 500 Pa·s. Their experimental set-up consisted of a Perspex square tube section with a 10 mm x 10 mm internal cross section. A converging section was made by inserting blocks with a 60° angle leading into 5.5 mm or 0.6 mm slit widths. In general, similar results as Bell were found where the orientation of fibres increased in the constriction. The influence of various fibre concentrations, lengths, and viscosities was investigated. They found that the viscosity of the carrier medium must be larger than a certain critical viscosity, otherwise fibre jamming and segregation occurred. The critical viscosity to have continuous alignment and prevent jamming was

dependent on fibre length and volume fraction. This is closely related to the filament forming process, for which a range of matrix viscosities can be investigated.

More recently, Lewicki et al. [83] reported on a direct ink writing technique for 3D printing of carbon fibre polymers. The resin was a bisphenol-F epoxy oligomer and 0.6 mm long carbon fibres were used. Colloidal silica was added to the resin to increase the viscosity of the suspension which allows the fibres to be better transported and aligned during extrusion which further indicates there may be a minimum viscosity for extruding the ADFRCs.

4.3 Methodology

An extrusion-based method was selected to form the ADFRC tape into a uniform filament. The literature on polymer flow and fibre suspensions has been reviewed which highlighted the multi-physical aspects involved in extruding ADFRCs (rheology, thermal and fibre interactions). In this section, the translation of that information into a practical extrusion method preventing fibre breakage is detailed as several steps were necessary to make extrusion of the ADFRCs possible. First, an overview is given of the relevant process parameters for extrusion and how they are incorporated in the study. Several extrusion trials have been performed to converge on a suitable processing window and their rationale is presented here. Finally, the hardware design of the physical extrusion set-up is presented before subsequent sections show the extrusion results and the analysis work that was performed in support of this process development.

4.3.1 Overview

The review of literature on fibre-polymer flow showed the main parameters that may influence the extrusion of the ADFRC tapes. From a simple flow perspective (section 4.2.1), the channel geometry will influence the pressure required to force the ADFRC through the die. The surface or coating of the surface may also influence the driving pressure required as surface friction may be present for polymer flow in a confined channel. The polymer viscosity is important as it relates to the internal friction in the suspensions and it depends on the polymer type, the shear rate and the temperature. The addition of fibres complicates the extrusion as interactions between fibres are expected to increase the viscosity and fibre jamming, fibre bending and/or fibre buckling may occur. Based on the Bell [178] and Murty and Modlen [179] studies, the alignment of fibres is expected to play an important role in the extrudability of the ADFRCs and a lower threshold for viscosity may be present

Figure 4.9 shows a schematic of the filament forming process with the expected temperature profile of the tape. The main parameters that influence the extrusion process are divided into process parameters, material parameters and geometric parameters. The process parameters that can directly be controlled are the temperature of the extrusion head (T_{set}) and the extrusion speed v. As the tape is fed through the channel, it heats up and the temperature profile will depend on the process parameters and on the thermal properties of the tape. The temperature profile directly affects the polymer viscosity. The polymer viscosity depends on the polymer type but is also dependent on the temperature and shear rate (dictated by extrusion speed). The fibre alignment is another material parameter that is expected to affect the extrusion, as misaligned fibres may cause fibre jamming which must be prevented. Lastly, the geometry of the channel and the channel surface can be changed to tailor the flow conditions.

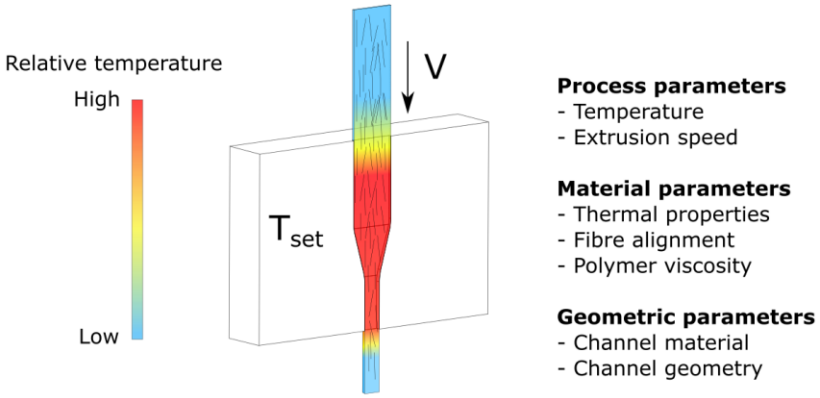

Figure 4.9: Relevant parameters for filament forming process of ADFRC tape extrusion through converging channel.

Some limitations may exist for the filament forming process that prevent successful extrusion. These are expected to be related to fibre jamming and can be dependent on the geometric parameters (i.e. maximum contraction ratio), polymer viscosity (i.e. too high or low viscosity) and fibre alignment of the tape. A multi-stage filament forming process, that gradually forms the ADFRC tape into a filament, may be required, as shown in Figure 4.10. In this thesis, extrusion studies are performed on the first stage to shape the 5 mm x 0.2 mm tape into a rectangle with a lower aspect ratio whilst keeping the same cross-sectional area. A sudden and severe change in cross sectional area would impose more stress on the tape and increase the likelihood of fibre jamming. In this chapter, the first extrusion step is considered as it is the most difficult because the wetted perimeter is largest which can increase possible surface friction as identified for polymer composite flow in section 4.2. Rectangular channels were designed, as they could be easily machined as a groove from a block of material. A top plate was used as a cover and this allowed easy removal of the sample to investigate the fibre orientation.

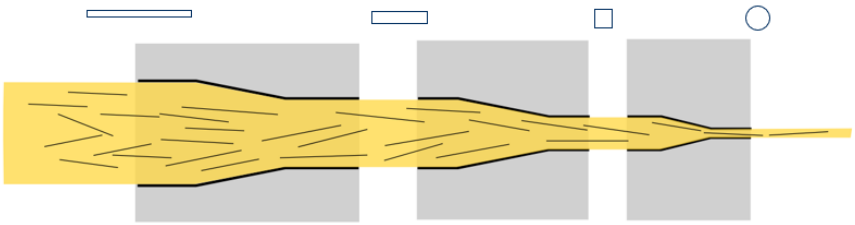

Figure 4.10: Multi-stage filament forming process with several converging ducts.

Five main parameters are considered for the channel configuration as shown in Figure 4.11. The inlet length can be changed to influence the amount of heating before the contraction. A longer inlet would give the tape more time to heat up such that the tape has the right viscosity in the contraction where most of the deformation is expected to occur. The contraction angle is a variable that can be changed to have a more gradual converging flow and change the level of constraint on the fluid. The outlet width is important as it determines the change in aspect ratio, going from a 5 mm x 0.2 mm tape to a cross section with a lower aspect ratio. Finally, the outlet length can be changed which affects the die swell. The amount of die swell depends on the shear stress at the wall, the outlet geometry and outlet length [180]. A longer outlet typically reduces the die swell as it increases the time the melt can dissipate any residual stress imposed on the nozzle. The downside of a longer outlet is that it increases the overall pressure drop over the nozzle as the length and wetted surface is increased.

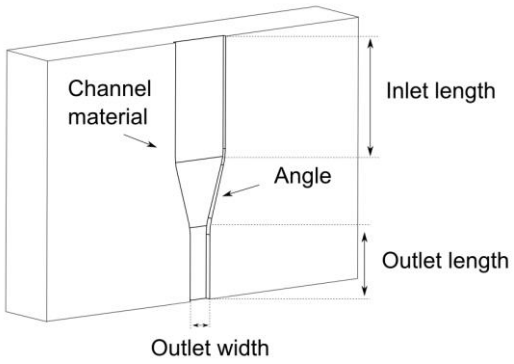

Figure 4.11: Schematic of the direct extrusion channel with five main parameters.

With the main parameters identified, different extrusion studies were performed to investigate their influence on the extrusion process. These included different outlet width, angles and inlet lengths as well as different temperatures, extrusion speeds and polymer types. The different extrusion studies are presented in the next section.

4.3.2 Extrusion studies

The main purpose of this work was to find a suitable method that enables continuous extrusion of the ADFRCs into a printable filament. Many parameters were identified in the previous

section that can influence the extrusion behaviour. Several studies were performed to both narrow down the most promising part of the design space and to quantify the impact of varying individual parameters. An overview of the different set of studies is shown in Table 4.2. The initial studies were done with channels that had an angle of 15° which was chosen to be similar to the successful studies performed by Bell with a piston-die system [178]. An inlet length of 10 mm was used to allow the tape to heat up during extrusion. In later iterations, different angles and inlet lengths were tested to improve the filament forming process as these were found to play an important role in enabling continuous extrusion of the tapes. The first extrusion study helped identify potential improvements to be made to the experimental set-up which were incorporated in the second extrusion study. The second extrusion study investigated the effect of different channel surface coatings and a temperature sweep was performed to cover different viscosity ranges for the different materials. A thermal analysis was performed after the second extrusion study and this led to the final set-up. The third extrusion study was performed with PTFE nozzles to reduce surface friction and continuous extrusion was obtained in this last study.

Table 4.2: Extrusion channel parameter variation of different studies

Geometric parameter	First extrusion study	Second extrusion study	Third extrusion study
Inlet length	10 mm	10 mm	1, 3, 5 mm
Angle	15°	15°	7.5°, 10°, 15°
Outlet length	10 mm	2, 4, 9 mm	2.5 mm
Outlet width	1 mm	1, 2, 3 mm	2.5 mm
Channel material	Aluminium, with top glass plate and using silicone release agent.	Aluminium, with top glass plate and using silicone release agent.	PTFE

For the first and second extrusion study, the channels were machined from 30 mm x 30 mm aluminium blocks. A cartridge heating element was directly mounted into the aluminium block and a glass plate was used to cover the channel as shown in Figure 4.12. This allowed to visually monitor the flow during extrusion. The downside of this method is that the ADFRC tape is in contact with two different surfaces and may therefore experience different heating rates and friction forces. Both the aluminium block and glass plate were coated with a release agent to reduce the friction. The through-thickness temperature variation of the thin ADFRC tape was expected to be minimal as the thermal analysis will show in section 4.5.

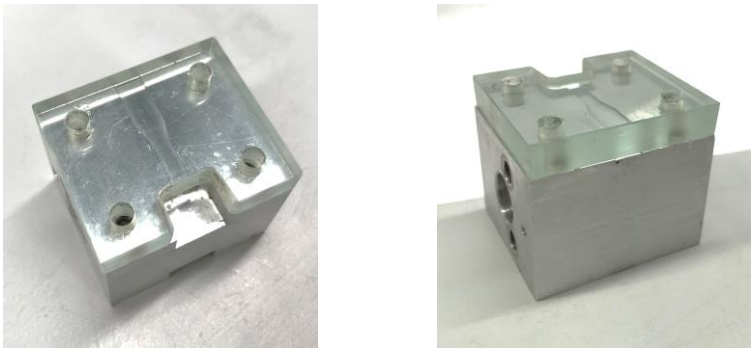

(a) (b)

Figure 4.12: Extrusion die with aluminium channel with glass plate (a) top view and (b) inlet view.

The first extrusion study was an attempt to directly extrude the tape into a 1 mm x 1 mm square and obtain a general idea of the flow and extrusion behaviour. The tape was manually fed into the channel and the flow was monitored visually. These trials were unsuccessful as the flow halted before the ADFRC exited the channel as shown in Figure 4.13.

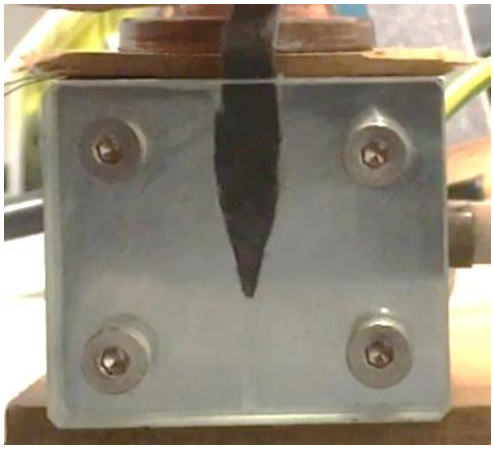

Figure 4.13: Early un-successful filament forming trials using V0 nozzle, tape folding and the inlet and fibre jamming prevented extrusion.

This first extrusion study helped to improve the extrusion set-up through several changes. Manually feeding of the ADFRCs tapes prevented a constant feed rate and the tape was unsupported before entering the channel. This made it difficult to transfer the driving force through the tape as it folded prematurely above the inlet. It gave a quick indication of the extrusion behaviour, but to improve the process a tape-feeding mechanism was made.

Figure 4.14 shows the tape-feeding mechanism to control the extrusion speed of the tape which also guides the tape before it enters the channel. A stepper motor was used to drive a 12 mm diameter roller covered with a heat shrunk polymer sleeve (final outer diameter 13 mm) to grip the tape, with the tape being pushed against the drive roller by a sprung compression wheel (13 mm diameter). The stepper motor driver and software was calibrated to calculate the required rotation speed for a desired extrusion speed. *Polytetrafluoroethylene* (PTFE) guides were machined

to directly guide and support the tape from the drive rollers to the channel inlet and prevent premature buckling of the tape during extrusion. The stepper motor / guide assembly was mounted on an aluminium frame using a custom bracket to allow for *y*- and *x*- offset control (insuring proper alignment) as per the coordinate axis shown in Figure 4.14. The extrusion channel was mounted on the side of the aluminium frame with a heat break in between to prevent the aluminium extrusion and stepper motor from heating up.

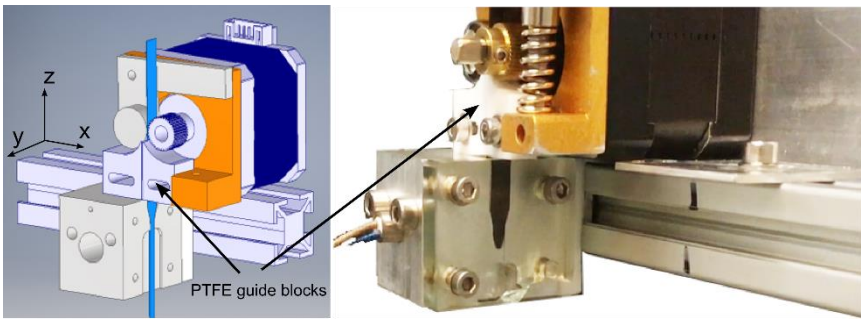

Figure 4.14: Tape feeding mechanism for the filament forming set-up.

At a later stage, the tape feeding mechanism was changed to have smaller extrusion blocks. This reduced the heating power requirements and improved the turnaround time for each experiment. A custom frame was made to position the extrusion head above the channel as shown in Figure 4.15.

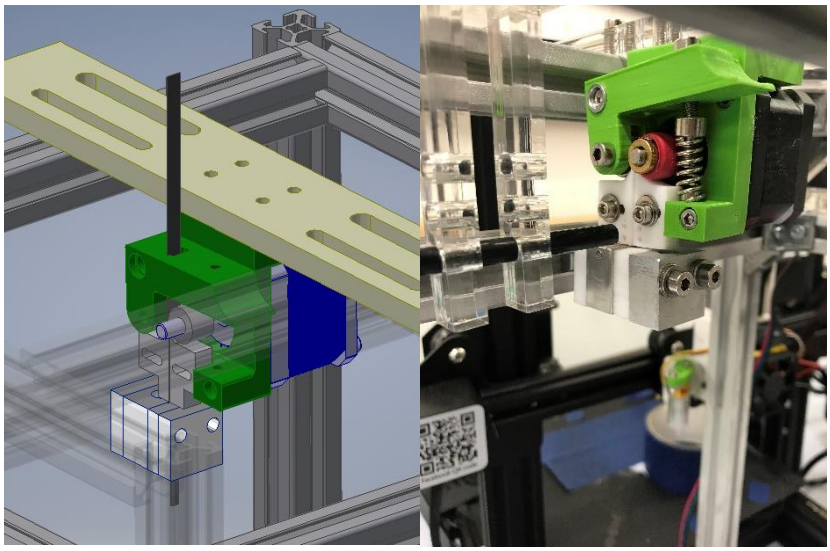

Figure 4.15: Extrusion assembly for final extrusion tests.

The first extrusion study also showed that a channel outlet cross section of 1 mm x 1 mm with an outlet length of 10 mm gave too much of a constriction on the flow. The ADFRCs tape could not be directly extruded into this new cross section. For the second extrusion study, the

tape-feeding mechanism was used and new channels with different outlet widths were manufactured. These led to more successful extrusion of the ADFRCs and allowed studying different process parameter as will be discussed in the next section.

4.4 Second filament forming trials

The second filament forming trials were performed to methodically find a suitable combination of processing variables to allow continuous extrusion. The aim of this work was to reduce the total number of parameters to be considered. As discussed in section 4.3.1, there are multiple parameters that influence the extrusion process, these include temperature settings, speed settings, material type and geometric parameters. To reduce the size of the experimental matrix required to fully explore the relationships between variables, some parameters were fixed. The channel outlet was set to 3 mm, and the experiments explored different coatings, temperature settings, polymers types and extrusion speeds. The 3 mm outlet width was used as it requires significantly less reshaping of the material (than the previous 1 mm outlet), while still being a meaningful step towards the desired final shape – in line with the multi-stage process shown in Figure 4.10.

4.4.1 Effect of coating

A coating may be used to improve the flow of polymer melt through the channel by reducing friction and preventing polymer build-up on the surface. Different coatings are available that provide a non-stick surface and simplify the release of polymer material. For the extrusion process, ideally a long-lasting coating should be used to promote flow of the material while being able to cope with the abrasive nature of the polymer fibre suspension. Two coating methods were used for these trials:

1. **Frekote 770-NC**

   A lab-standard solvent based release agent with high slip properties and thermal stability up to 400 °C. The Frekote coating series are based on polydimethylsiloxane (PDMS) [181].

2. **Electrolube DAS Silicone Mould Release**

   A silicone lubricant with high temperature stability and the capability to prevent surfaces from bonding

The first extrusion tests were performed with the Frekote 770-NC coating as it is very commonly used in composites manufacture and is readily available. A PLA polymer ADFRC

tape was extruded at a temperature of 230 °C and with an extrusion speed of 14 mm/s. These extrusion settings were chosen to match the rheological testing done, where PLA has a relatively low viscosity at that temperature which was expected to improve extrusion. The extrusion speed of 14 mm/s matches a shear rate of 100 rad/s at which rheological testing was performed. The wall shear rate $\dot{\gamma}$ was approximated using the calculation for a circular channel shown in Equation (4.14). Here Q is the volumetric flow rate and D is the channel diameter. The channel diameter was assumed to be 1.13 mm, which gives the same cross-sectional area of the ADFRC tape of 5 mm x 0.2 mm (1 mm^2). This assumption was later updated using the hydraulic diameter of the rectangular cross section which is presented in section 4.5.5.2.

$$\dot{\gamma} = \frac{32Q}{\pi D^3} \tag{4.14}$$

Figure 4.16 shows the extrusion of a PLA ADFRC with an extrusion speed of 14 mm/s at a temperature of 230 °C, using the Frekote 770-NC coating. The tape halted before it reached the exit of the nozzle and a wavy pattern appeared which looks like wrinkling of the tape inside the channel. This behaviour resembles micro-buckling of the tape and may indicate that there is too much backpressure for successful extrusion, and this causes the fibres to buckle. A high backpressure may be caused by several factors which include friction with the walls, a too high viscosity of the suspension or too aggressive a change in cross section.

A similar extrusion was performed changing the coating on the channel to the silicone mould release agent. The extrusion temperature and speed were kept the same at 230 °C and 14 mm/s to observe the effective difference of friction during extrusion. Figure 4.17 shows the extrusion behaviour with silicone mould release agent, where extrusion improved as roughly 9 mm of the ADFRC tape exited the channel. The micro-buckling effect, clearly observed in the Frekote 770-NC extrusion, seems to be less pronounced in the silicone mould release.

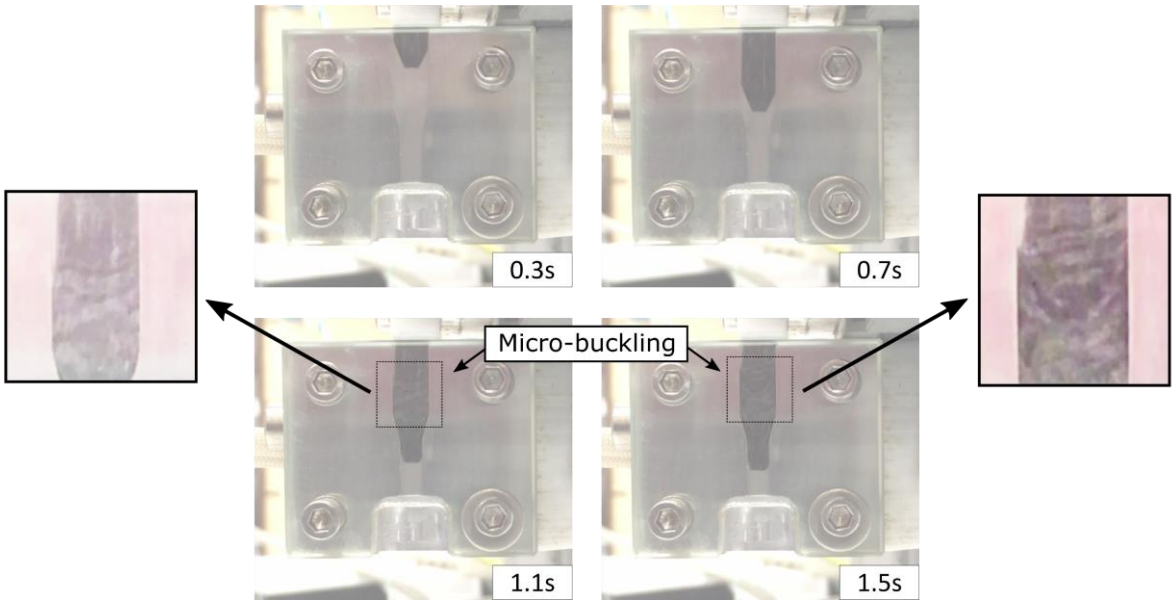

Figure 4.16: Filament forming with V1 nozzle (3 mm outlet) and Frekote 770-NC coating showing unsuccessful forming.

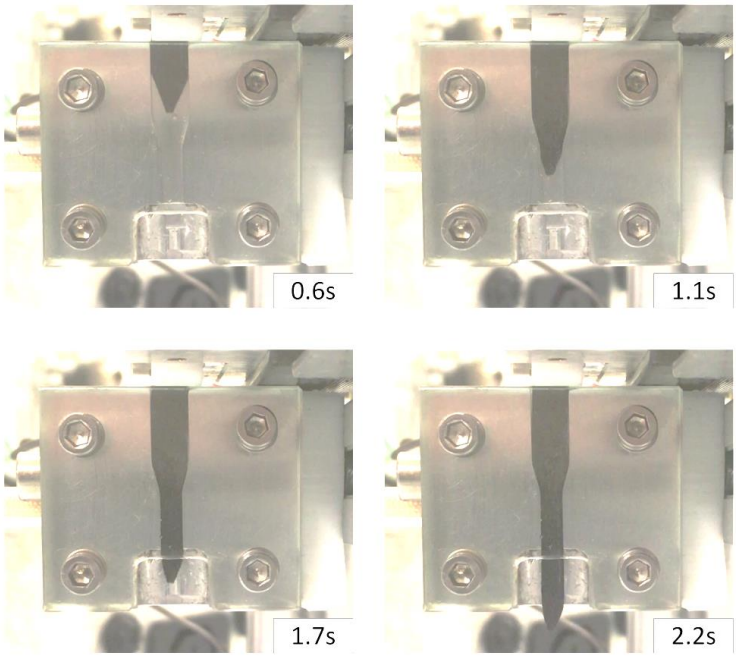

Figure 4.17: Filament forming with V1 nozzle (3mm outlet) with silicone mould release lubricant.

The difference in extrusion performance due to different coatings shows that the surface of the channel does influence the extrusion behaviour of ADFRCs. Theoretically, a perfect viscous material has a no-slip boundary condition but as discussed in section 4.2, surface friction was expected to affect extrusion behaviour role. As the ADFRC tape enters the channel it is expected to still be solid with a sliding surface and then exhibits a visco-elastic behaviour as it gradually heats up and this changes the frictional behaviour. It was decided to continue with the

silicone mould release as it provided a better extrusion performance than the Frekote 770-NC release agent.

4.4.2 Rheological properties sweep

To further understand the effect of viscosity on the extrusion performance of the ADFRCs tapes, a series of extrusions with different temperatures was done matching the rheological conditions tested earlier (section 3.2). The rheometry results are shown Figure 4.18 again for the 100 rad/s shear rate. Using the rheological data, one can match the effective viscosity between different polymers and selectively choose processing temperature so the polymers have similar viscosities. It was decided to do an initial rheology sweep using PLA as it has the biggest variation in viscosity with temperature, varying from ~1600 Pa·s to 20 Pa·s. Furthermore, PLA has the advantage that extrusion tests can be done at a relatively low temperature compared to the other polymers. A sweep was done at five different temperatures (170 °C, 190 °C, 210 °C, 230 °C and 250 °C) using PLA ADFRC tapes to cover a wide range of matrix viscosities. The results of this are presented in this section.

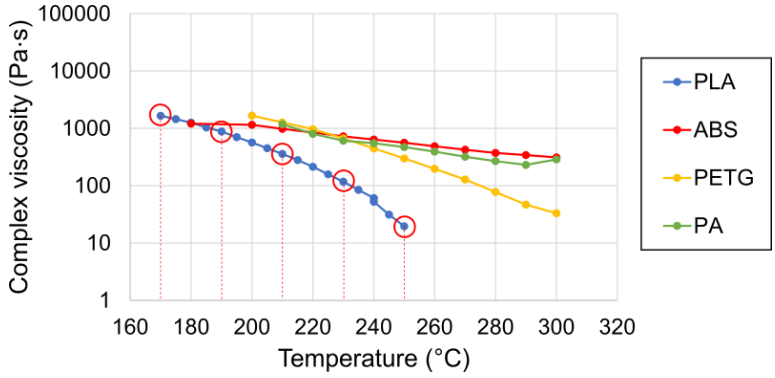

Figure 4.18: Complex viscosity measurements for different candidate polymers at strain rate of 100 rad/s.

Figure 4.19 shows the extrusion of a PLA ADFRC tape at 170 °C and a speed of 14 mm/s. The temperature corresponds with a matrix viscosity of ~1600 Pa·s. In the contraction region (which the tape is in after ~0.9s), some reshaping of the tape occurs but the flow halted, preventing further extrusion. Figure 4.20 shows the same set-up but with the channel temperature set at 190 °C where the matrix viscosity should be ~880 Pa·s. A slight improvement in extrusion length can be seen together with more reshaping than at 170 °C but the flow halted again before the tape was extruded through the entire channel.

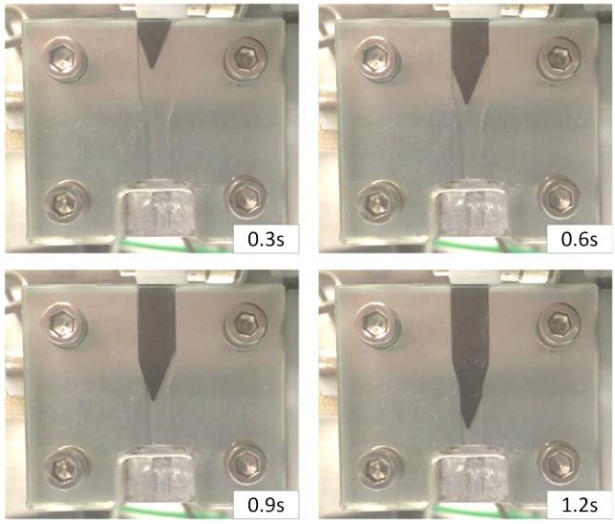

Figure 4.19: Extrusion of PLA ADFRC at 170 °C-14 mm/s and silicone lubricant.

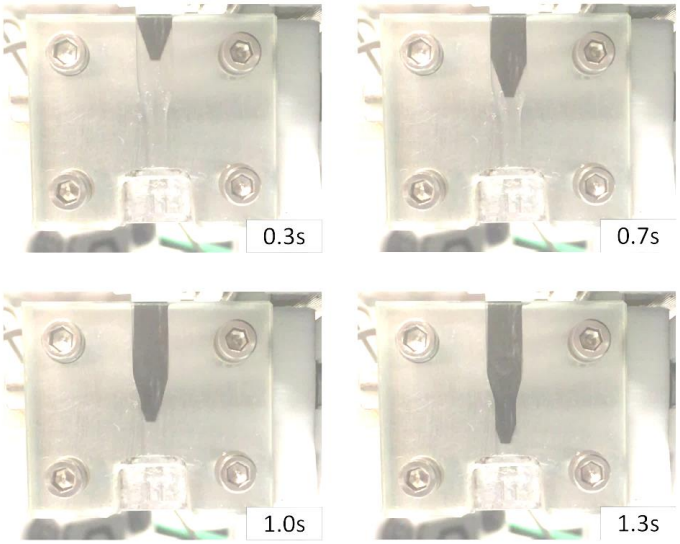

Figure 4.20: Extrusion of PLA ADFRC at 190 °C-14 mm/s and silicone lubricant.

Figure 4.21 shows the extrusion of a PLA ADFRC tape at a channel temperature of 210 °C. An extrusion speed of 14 mm/s was used again, and the matrix viscosity was expected to be around 360 Pa·s for these conditions. An improvement in extrusion can be seen compared to the lower temperature extrusions as around 10 mm of the tape exited the channel. After roughly 10 mm of extrusion, the flow halted again which prevented continuous extrusion, but the tape clearly reshaped through the channel and some extrusion was obtained.

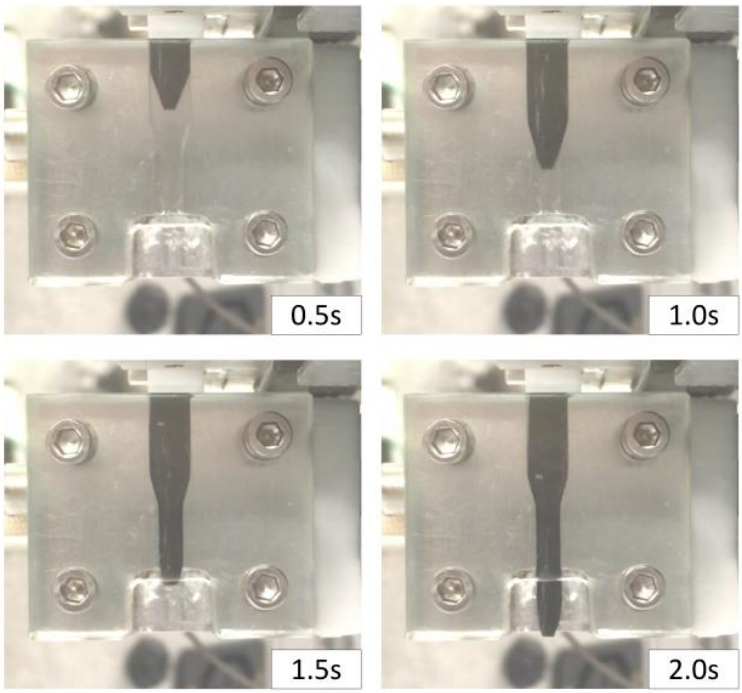

Figure 4.21: Extrusion of PLA ADFRC at 210 °C-14 mm/s with silicone lubricant.

Two more extrusion trials with ADFRC PLA tapes were performed at 230 °C and 250 °C (Figure 4.22 and Figure 4.23) at an extrusion speed of 14 mm/s. Small improvements over the extrusion done at 210 °C were seen but the flow halted again after around 10 mm of extrusion through the channel. In Figure 4.23 it can be seen that the tape did not fill the complete width of the channel. The flow halted suddenly after some initial extrusion, without much side flow happening in the inlet channel.

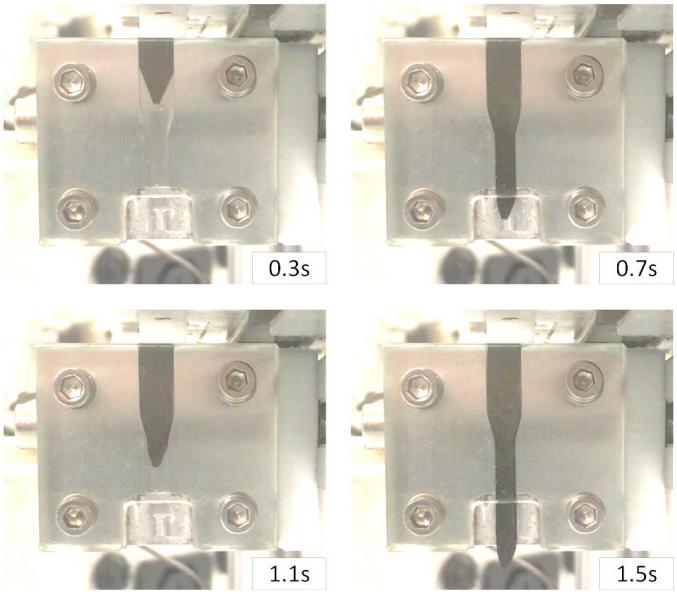

Figure 4.22: Extrusion of PLA ADFRC at 230 °C-14 mm/s with silicone lubricant.

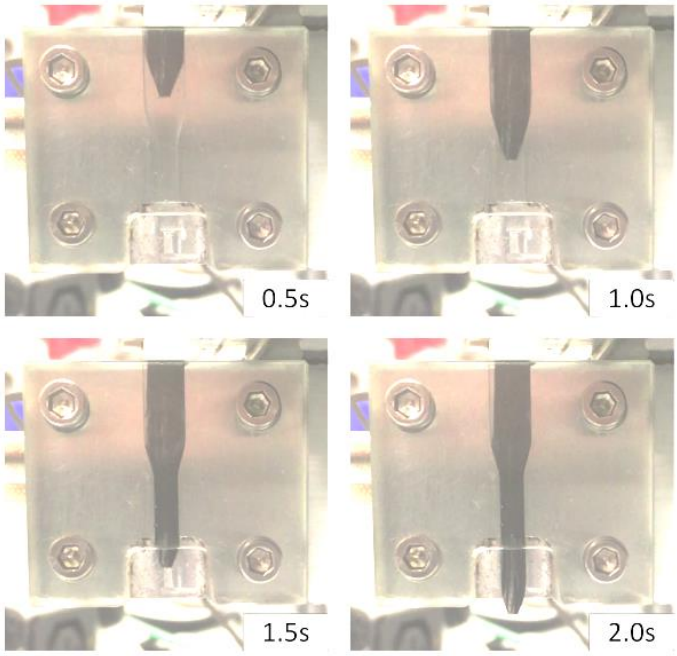

Figure 4.23: Extrusion of PLA ADFRC at 250 °C-14 mm/s with silicone lubricant.

The extrusion trials presented above covered a wide range of polymer viscosities, which were simply assumed to be coupled to the polymer type and channel temperature. This simplification allows easy comparison of extrusion settings, but it ignores that the polymer viscosity varies with extrusion speed and polymer type and that there will also be a certain viscosity profile across the channel due to temperature and flow condition variations. Before the first conclusions can be drawn on the extrusion behaviour, further trials were performed at different extrusion speeds and with different matrices. This also helps to reduce the full experimental matrix and focus future extrusions around a single polymer system.

4.4.3 Extrusion speed

The rheology sweep study using PLA ADFRCs has shown that lowering the matrix viscosity improved the extrusion behaviour of the ADFRC tapes. At temperatures above 210 °C the extrusion behaviour improved with some material extruding through the entire die. At this temperature setting, the viscosity of PLA was expected to be around 360 Pa·s at 100 rad/s. The polymer viscosity is also dependent on the extrusion speed, which influences both the heating rate and the strain rate.

The effect of extrusion speed was investigated to see the combined effect of higher shear rate and different heating dynamics. The extrusion speed was doubled, and this led to an improvement of the overall extrusion length. Figure 4.24 shows the extrusion of a PLA ADFRC at a speed of 28 mm/s and a temperature of 210 °C which increased the extrusion length to roughly

17 mm. Some fibre micro-buckling can be observed in the contraction of the channel. After 17 mm of extrusion the flow suddenly stopped as in previous trials.

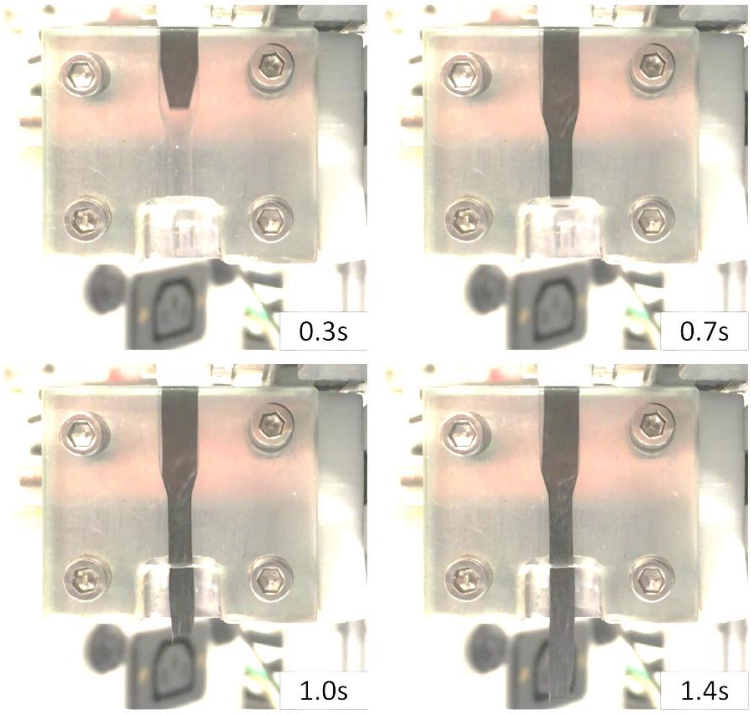

Figure 4.24: Extrusion of a PLA ADFRCs at a temperature of 210°C and s extrusion speed of 28 mm/s.

The extrusion speed clearly has an influence on the extrusion process and can be used to changes the temperature and viscosity profile of the tape during extrusion. Another variable to be considered for the viscosity profile is the polymer type, which is presented next.

4.4.4 Polymer type

The rheology sweep on PLA ADFRCs has shown that lowering the matrix viscosity improved the extrusion behaviour of the ADFRC tapes. At higher extrusion speeds, the extrusion improved which may be attributed to the lower viscosity of the matrix but other effects may also play a role such as heating of the tape or dynamic flow effects. For the PLA ADFRCs there seemed to be a threshold temperature of 210 °C, above which the extrusion behaviour improved with some material extruding through the entire die. At this temperature setting, the viscosity of PLA was expected to be around 360 Pa·s at 100 rad/s.

The effect of different matrices was investigated by extrusion tests on ABS, PETG and PA ADFRCs. For each material, an extrusion temperature was selected that matches the viscosity of PLA at 210 °C. This allows to compare the different matrices at a similar viscosity range to find what effect the matrix type has on the extrusion behaviour.

Figure 4.25 shows the extrusion of the PA ADFRC at 265 °C and an extrusion speed of 28 mm/s. At these process conditions, PA and PLA should have a similar viscosity. Both PA and PLA are semi-crystalline polymers and compared to the PLA ADFRCs, the extrusion of PA ADFRC was less successful, with an extrusion length of about 6 mm. Fibre folding or micro buckling can be observed in the inlet section at 0.9 s when the flow halted. Some squeeze flow at the inlet section was observed where the ADFRC tape was compressed but no material was extruded through the channel anymore.

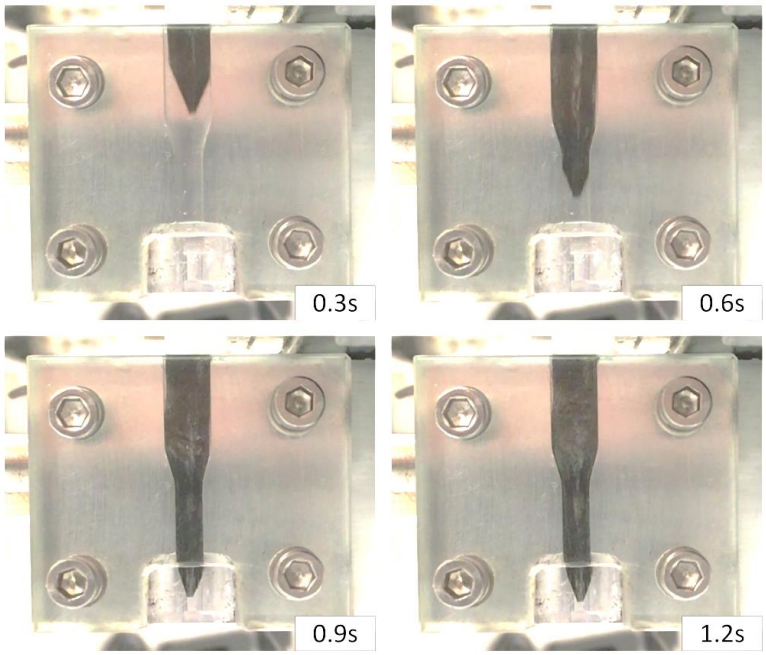

Figure 4.25: Extrusion of a PA ADFRCs at a temperature of 265 °C and an extrusion speed of 28 mm/s.

Figure 4.26 shows the extrusion of an ABS ADFRC at 285 °C and 28 mm/s, which matches the viscosity of the PLA ADFRC at 210 °C. Around 15 mm of material exited the channel which is less than that achieved with the PLA ADFRC. ABS is an amorphous polymer which means it exhibits gradual softening above its T_g, therefore it may influence the extrusion behaviour as the material does not exhibit a sudden drop in viscosity. After 1.3s of extrusion, the wavy pattern indicating micro buckling can clearly be observed at the inlet channel. This means there is too much pressure on the tape to extrude it, and compression causes micro buckling in the tape.

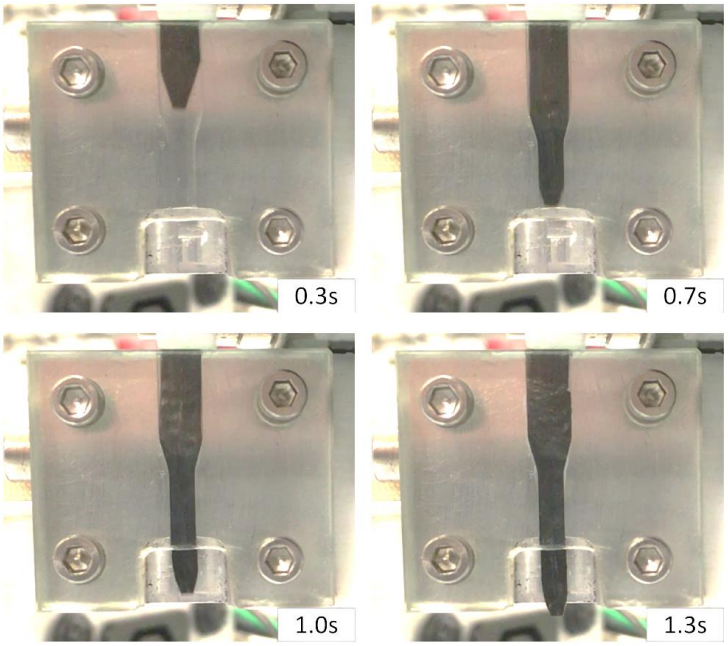

Figure 4.26: Extrusion of an ABS ADFRC tape at 285 °C-28 mm/s with silicone lubricant as coating.

The last polymer, PETG, is another amorphous polymer and an extrusion trial was performed such that it had a similar processing viscosity as the PLA ADFRCs at 210 °C. Figure 4.27 shows the extrusion of the PETG ADFRC tape at 240 °C and 28 mm/s where the flow halted before any material exited the channel. Similar to the ABS ADFRC, micro-buckling can be observed in the inlet channel. This means there is considerable back pressure for extrusion and the driving force from the extruder went into folding of the tape instead of continuous flow.

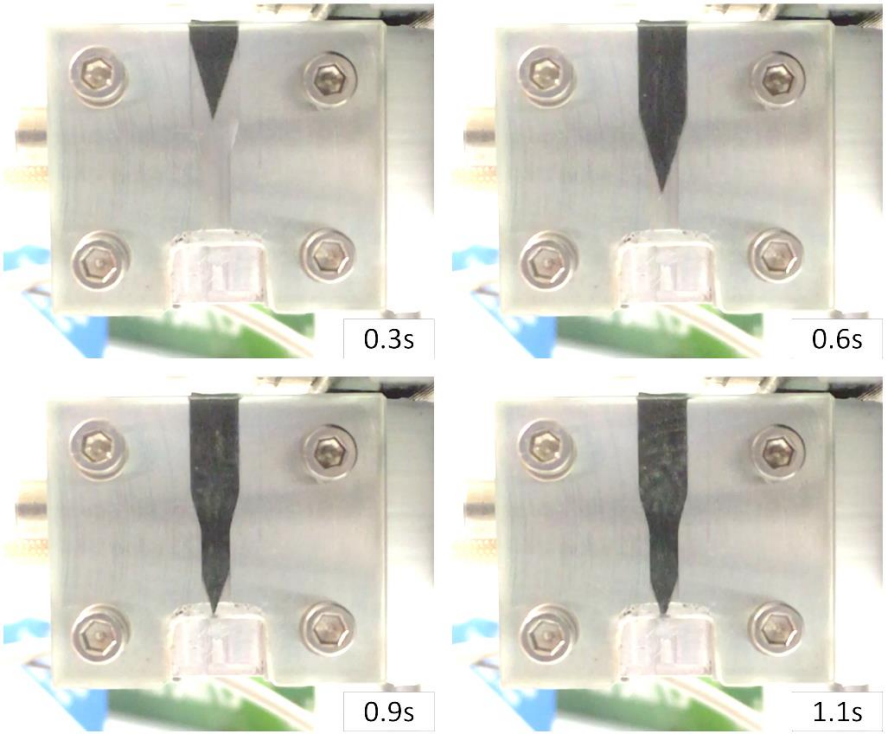

Figure 4.27: Extrusion of a PETG ADFRC tape at 240 °C-28 mm/s with silicone lubricant as coating.

The polymer extrusion tests showed that semi-crystalline polymers extruded better than amorphous polymers, where the extrusion settings were such that the polymers were in a similar viscosity range. Reasons for this are discussed in section 4.4.5. For the amorphous polymers (ABS and PETG), micro-buckling was clearly observed in the inlet channel indicating an overall higher back pressure to force the ADFRC tape through the channel. The PA matrix showed similar performance as PLA which are both semi-crystalline polymers that are expected to show a more sudden drop in viscosity once they reach a temperature above their melt temperature.

4.4.5 Early filament forming trials conclusions

The early filament forming trials were performed to find a processing window that enables extrusion of ADFRC tapes and to better investigate the relevant parameters for this process. Continuous ADFRC tape extrusion was not obtained, and the average extrusion length was around 10 mm before the flow halted. The cause of unsuccessful flow needs to be better understood. The effects of coating, temperature, speed, and matrix type were investigated and improvements in extrusion lengths were obtained.

From the coating studies, it was clear that silicone mould release improved the extrusion as the initial attempts with a Frekote coating yielded unsuccessful extrusions, with the ADFRC tape not extruding past the end of the channel. This shows that surface friction plays a role for the ADFRC extrusion. The silicone mould release coating provided better lubrication but is less hard-wearing and may get removed after some extrusion. Alternative surfaces or coatings need to be investigated to reduce friction and improve performance for longer extrusion runs.

The studies on extrusion temperature for the PLA ADFRCs clearly showed that there was a minimal temperature for the ADFRC tape to be reshaped which was expected to be coupled to the matrix viscosity. At low temperatures (below 210 °C) the tape could not be forced through the channel. At 210 °C and above, the extrusion improved with roughly 10 mm of material successfully extruding through the channel. At these higher temperatures, the viscosity of the polymer matrix is lower, allowing the ADFRC to flow better. Using the channel temperature as an indication of the ADFRC temperature, the threshold viscosity is expected to be around 360 Pa·s. At higher temperatures (thus lower viscosities), the extrusion improved but seemed to be limited to a maximum of 10mm.

The extrusion length increased with a higher extrusion speed. With twice the extrusion speed, the extrusion length increased from 10 mm to 15 mm for PLA ADFRCs. The extrusion speed is expected to change the temperature profile of the ADFRC tape in the nozzle (a higher

speed means the tape reaches the set temperature further in the channel). A higher extrusion speed also increases the shear rate and thus lowers the viscosity of the matrix. The combined effect observed was that the extrusion length increased.

Lastly, different polymers types were investigated which showed semi-crystalline polymers extrude better than amorphous polymers. This was attributed to the sudden drop in viscosity semi-crystalline polymers exhibit when their temperature increases, and this may fit the extrusion process better as it helps to retain the compressive load carrying capability of the tape before it reaches its melt state near the channel.

A micro-buckling type failure was identified that shows local wrinkling of the ADFRC tape inside the channel as shown in Figure 4.28. An analysis of channel flow was presented in section 4.2.1 and a pressure drop Δp can be expected though the channel, effectively creating a compressive force between two points (i.e. A and B) along the length of the nozzle that can cause the micro-buckling effect observed. This pressure drop is dependent on the viscosity of the material, the extrusion speed and the channel geometry. The total compressive force is also influenced by friction in the channel. For homogenous polymers, the pressure drop is not a problem as it can be distributed through the material. For the ADFRCs, the fibres may buckle and this can cause fibre jamming and halting the flow. This buckling effect is also coupled to the viscosity of the resin that supports the fibres.

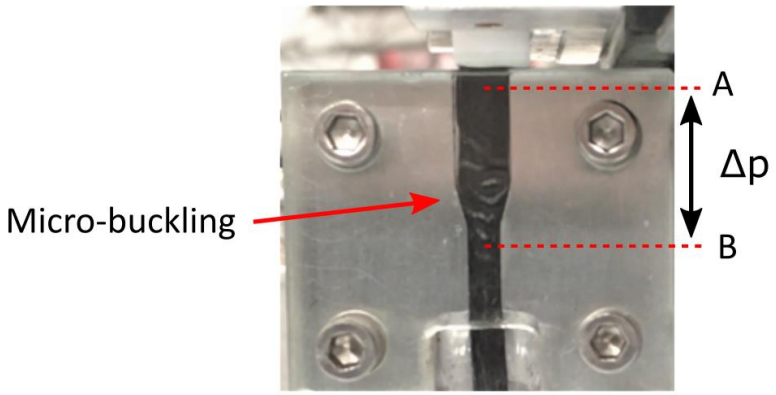

Figure 4.28: Detail of ADFRC extrusion and oberved micro-buckling effect under compressive force caused by pressure drop Δp between two points.

Figure 4.29 shows another effect that was observed when removing the ADFRC tapes after extrusion. At the channel entrance, the tape folded on itself which indicated premature heating may have occurred. This is detrimental for successful extrusion as it means no force is transmitted through the tape and the flow will halt. The tape may also have halted during extrusion and the stationary material near the inlet heats up which allows it to fold at the top as it is still being

pushing into the channel. Heating of the ADFRC tape clearly plays an important role to avoid this and therefore needs to be better understood.

Figure 4.29: Close up of the ADFRC tapes after extrusion and showing folding upon entry.

To conclude, this set of extrusion tests has yielded more information on the most suitable polymer type to extrude ADFRCs and what processing conditions work better. It was decided to focus on the PLA ADFRCs in further tests as they exhibited the best extrusion behaviour. Before the next set of extrusion tests were designed, the heating of the ADFRC tape needs to be better understood to predict the temperature profile and subsequently the viscosity profile during extrusion which is presented next.

4.5 Thermal analysis

4.5.1 Introduction

A thermal analysis was performed to improve the filament forming process by understanding and predicting the heating of the tape during extrusion. Using the predicted temperature profile, the right extrusion speed and geometric lay-out can be selected such that premature softening of the tape is prevented but that the material is soft enough to be reshaped in the constriction area.

It is expected that the dominant heat transfer mechanisms are (1) heat transfer between the nozzle and the tape and (2) heat conduction in the tape itself. Other relevant heat transfers are radiation and convection with the surrounding air, but they are expected to be secondary. When the tape enters the channel, there is direct conduction heat transfer from the channel to the tape as they are in contact with each other. The heat in the tape is distributed along the length of the tape through thermal conduction which causes the tape to begin heating up before entering the nozzle. The amount of upstream heat transfer depends on the thermal conductivity of the ADFRC tape and the extrusion speed. By changing the extrusion speed and channel temperature, the temperature profile of the tape during steady-state extrusion can be altered and matched to the geometry.

A 1-D thermal model was used to predict the temperature profile of the tape during extrusion which is detailed below. The thermal properties of the tape were estimated from the two constituent materials using the rule of mixtures, and the calculations were validated using a FLIR T650 thermal camera which monitored the temperature of the tape at the entrance. The thermal analysis was then coupled to the rheological data to map the viscosity in the channel during extrusion.

4.5.2 Thermal properties of ADFRC tapes

The thermal conductivity k of the ADFRC tape is estimated using the Halpin-Tsai equations, in a similar fashion to those used to predict the stiffness properties in the fibre direction. It is mathematically accepted to use similar calculation methods for modulus as thermal conductivity [110], [182]. Here, it must be noted that it is assumed that all fibres contribute to the conductivity. The fibres have a large aspect ratio ζ and the tapes have a high enough fibre volume content V_f such that they form a conductive network. Equation (4.15) can then be used to predict k_c based on the thermal conductivity of the matrix and fibre (k_m and k_f respectively), fibre length l and diameter D and volume fraction V_f.

$$k = k_m\left(\frac{1+\eta\zeta V_f}{1-\eta V_f}\right) \tag{4.15}$$

$$\eta = \left(\frac{k_f}{k_m}-1\right)/\left(\frac{k_f}{k_m}+\zeta\right) \tag{4.16}$$

$$\zeta = \frac{2l}{D} \tag{4.17}$$

The density and heat capacity of the ADFRC are estimated directly from the rule of mixtures using Equation (4.18) as these are bulk properties. The fibre and matrix properties are obtained from CES Edupak which document the minimal, average and maximum value of general-purpose PLA and high strength carbon fibres [111]. For carbon fibres, the heat conductivity can vary significantly with the fibre type (PAN- or pitch-based), the internal structure and the direction (radial or axial). Martin *et al.* [183] reported on the axial thermal conductivity of PAN based fibres which can range between 14-100 W/m/K. This value was used here as a better estimate as PAN-based fibres were used and the heat transfer along the fibre axis is of interest. The estimated relevant thermal properties are shown in

Table 4.3.

$$X_c = fX_f + (1-f)X_m \tag{4.18}$$

Table 4.3: Range of fibre, matrix and composite properties for a V_f of 12%.

Fibre properties	b	*min*	*avg*	*max*	**unit**
Density	ϱ	1.8	1.82	1.84	kg/m³
Heat capacity	c_p	705	710	715	J/kg/K
Heat conductivity	k	14	54.5	100	W/m/K
Matrix properties		*min*	*avg*	*max*	
Density	ϱ	1240	1255	1270	kg/m³
Heat capacity	c_p	1180	1195	1210	J/kg/K
Heat conductivity	k	0.13	0.145	0.16	W/m/K
Composite properties	Fibre content V_f = 12 %				
		min	*avg*	*max*	
Density	ϱ	1091.4	1104.6	1117.8	kg/m³
Heat capacity	c_p	1123.0	1136.8	1150.6	J/kg/K
Heat conductivity	k	0.64	2.88	4.70	W/m/K

4.5.3 Numerical model

A 1-D thermal model was created to predict the in-plane heat transfer of the ADFRC tape. The 1-D model ignores any variation in temperature through the width and thickness of the tape. To validate this approximation, the Biot number was calculated which gives an index for the heat transfer inside the body versus at the surface at the body. The Biot number is defined by Equation (4.19) below.

$$Bi = L_C \cdot h / k \tag{4.19}$$

Here, h is the heat transfer coefficient on the surface, k is the heat conductivity of the material and L_C is a characteristic length of the body. For L_C, the ratio of the volume of a unit length tape versus the surface area ($V_{body}/A_{surface}$) is taken, which was found to be 0.096 mm. By using an estimate for h = 1000 W/m² and k = 3 W/m/K gives Bi ≈ 0.03 (≪1), and therefore the main heat transfer occurs through the body (in-plane) and the 1-D model will be suitable for this purpose.

The tape was discretized into 1D elements as shown in Figure 4.30. A Lagrangian approach was used where at each timestep, the change in energy was calculated for each element and their locations were updated to reflect movement of the tape. Each element is represented by a node in its centre with associated location and temperature. The rate change of energy $\dot{E}_t$ is given by Equation (4.20) which consists of a conductive term in the material q_{cond} and the radiative and convection contributions are included in the heat exchange with the environment q_{env}.

$$\dot{E}_t = q_{cond} + q_{env} \tag{4.20}$$

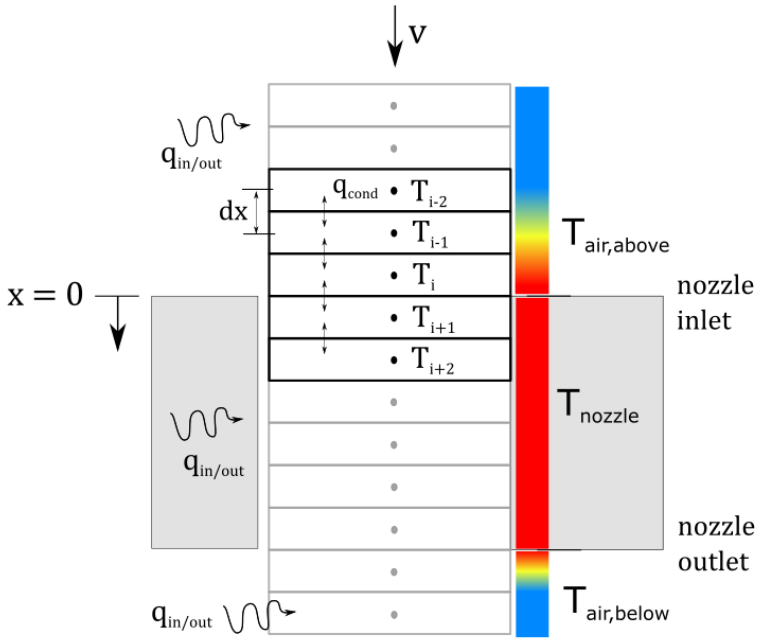

Figure 4.30: Set up of 1-D thermal model with moving elements.

Three regions can be defined which have different boundary conditions; 1) above the nozzle, 2) in the nozzle and 3) below the nozzle as shown in Figure 4.30. The conductivity term is different for the bottom node, middles nodes and top node as shown in Equation (4.21) below. Here, k is the conductivity, A is the cross-sectional area of the tape, T is the temperature and Δx is the spacing between the centres of two elements. The subscripts n and superscript p indicate the node and time step respectively.

$$q_{cond} = \begin{cases} \frac{kA}{\Delta x}\left(T_{n-1}^{p} - T_{n}^{p}\right), \text{ bottom node} \\ \frac{kA}{\Delta x}\left(T_{n-1}^{p} - T_{n}^{p}\right) + \frac{kA}{\Delta x}\left(T_{n+1}^{p} - T_{n}^{p}\right), \text{ middle nodes} \\ \frac{kA}{\Delta x}\left(T_{n-1}^{p} - T_{n}^{p}\right), \text{ top node} \end{cases} \tag{4.21}$$

The convective and radiative terms are included through heat transfer coefficients (h_{nozzle}, h_{air} and h_{rad}) as shown in Equation (4.22). Here, $A_{exposed}$ is the outer surface area of the tape and T_{nozzle} and T_{air} are the nozzle and air temperature respectively. The radiative heat transfer coefficient h_{rad} is given by Equation (4.23), with σ being the Boltzmann's constant ($5.670 \cdot 10^{-8}$ W/m^{2}K^4) and ε is the emissivity of the surface. The emissivity of ABS and PLA was studied by Morgan et al. [184] who found that ε is approximately 0.92.

$$q_{env} = \begin{cases} A_{exposed}(h_{nozzle} + h_{rad})\,(T_{nozzle} - T_n), \text{if location in the nozzle} \\ A_{exposed}(h_{air} + h_{rad})\,(T_{air} - T_n), \text{if location out of the nozzle} \end{cases} \tag{4.22}$$

$$h_{rad} = \varepsilon\sigma\left(T_n^p + T_\infty\right)\left(T_n^{p^2} + T_\infty^2\right) \tag{4.23}$$

The new temperature for each element can be calculated by Equation (4.24), equating the rate change in energy to a change in temperature for each element. Here, ϱ is the density, c_p is the heat capacity and Δt is the time step.

$$\dot{E}_t = \frac{\rho c_p A\, \Delta x}{\Delta t}(T_n^{p+1} - T_n^p) \tag{4.24}$$

The heat transfer coefficients h_{nozzle} and h_{air} are variables that influence the heating and cooling rate of the tape. The heat transfer coefficient h_{air} is expected to be around 10 - 30 W/m² and is dependent on the air velocity. The heat transfer coefficient h_{nozzle} is harder to estimate as it is dependent on the contact between the ADFRC tape and the channel. Dawson et al. [185] studied the heat transfer across a polymer-steel mould interface and highlighted the effect a small air-gap (~0.1 mm) can have on the heat transfer coefficient, which can vary between 300-2500 W/m². As the material melts during extrusion, the heat transfer coefficient can change as well. As the purpose of this study is to provide an indication of the temperature profile during extrusion, a value of 1000 W/m² is assumed initially. Later, this value was changed to better match the validation data as the exit temperature of the ADFRC tape was monitored during continuous extrusion.

4.5.4 Results

To validate the numerical model with experimental results, static tests were performed. A PLA ADFRC tape was inserted into the nozzle inlet and a FLIR T650 infrared (IR) camera was used to monitor the temperature rise in the tape at the inlet. A thermal camera measures IR radiation which the object of interest radiates and/or reflects from its environment. To obtain an accurate temperature measurement, both the emissivity ε of the material must be known and how much radiation is being reflected from the surroundings. For an opaque object, the reflection can be estimated from the emissivity. The emissivity ε relates to how efficient a material is at emitting thermal radiation and determines the relationship between radiation intensity and surface temperature, and is also dependent on the angle of radiation, wavelength and surface quality [184]. For these tests, an emissivity of 0.92 is assumed as determined for PLA by Morgan et al. [184] and an ambient temperature of 20 °C.

Two versions of this tests were done. First, the tests were performed without any active cooling above the channel. This led to an unknown and variable surrounding air temperature around the tape which had to be estimated to fit the simulation data with the experimental data. A second set of validation tests were done where the air temperature above the channel was

controlled by continuous flow of cool air along the top of the channel. This allows to better fit the simulation data with the experimental data, without assuming the air temperature above the channel as fitting parameter.

4.5.4.1 Heat-up tests without active cooling

Figure 4.31 shows the temperature rise of a PLA ADFRC tape which was fed into the inlet region (10 mm) of a heated channel (150 °C). The emissivity ε for the IR data was set at 0.92 based on the report by Morgan et al. [184] and the reflection temperature was 20 °C. A temperature rise can be seen in the tape that indicates heat is conducted upwards. The temperature is not completely constant across the width and some variation is present, mainly near the edges. Close to the heated channel, the temperature of the tape rapidly increases while further away from the nozzle entrance the tape heats up more slowly. After roughly 10 s the temperature profile reaches an equilibrium.

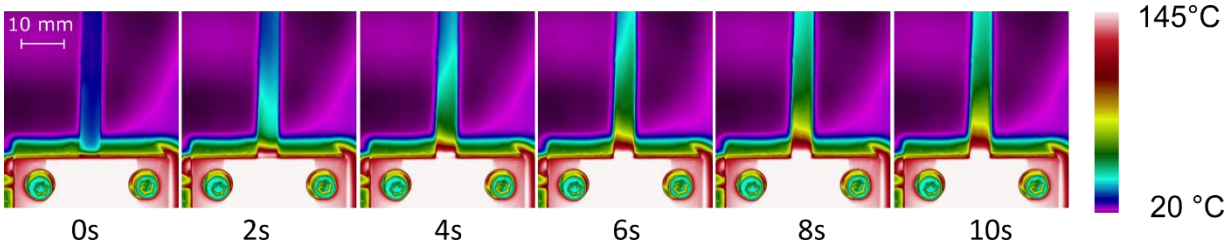

Figure 4.31: Temperature rise over time of a PLA ADFRC tape fed 10mm into a channel at a temperature of 150 °C.

The temperature of the tape was extracted from the IR data using FLIR software to obtain the time-temperature data for each pixel. The width of the nozzle was used as a reference for the mm/pixel ratio, allowing the temperature increase over time for various locations in the tape to be determined and plotted. The average resolution for the IR tests was 0.13 mm per pixel.

The method to determine the location of each pixel may be inaccurate due to an error in the mm/pixel ratio and a potential mismatch with the exact zero point (nozzle entry). To adjust for this, the numerical data is plotted not just at the estimated pixel locations, but also at the equivalent distance of one pixel above and below the derived location. This gives a temperature band in which the experimental data is expected to lie as shown in Figure 4.32 for three different nozzle set temperatures. The environment temperature above the nozzle was modelled using an exponential decay from nozzle temperature at x = 0 mm to room temperature (20 °C) at x=-100 mm (above the nozzle). This accounts for the nozzle block heating up the air. Without this assumption, the steady-state temperatures after 20 s did not converge to the experimental data and were much lower.

Overall, the steady state temperature (after 20 s) are close to the predicted values. The predicted temperature rise, however, is much faster than modelled, especially for further locations in the ADFRC away from the nozzle inlet. The sensitivity to the air temperature brings an extra variable into the analysis which has a large influence on the heating rate. To better control this, active cooling was added in the experimental set-up which is presented next.

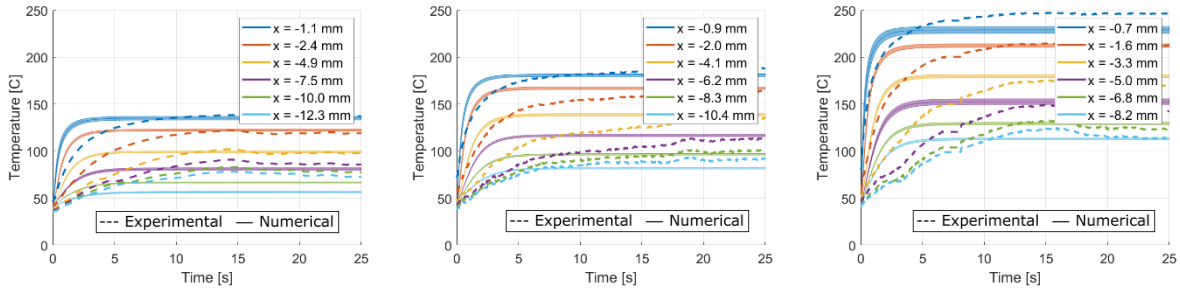

(a) 150 °C **(b)** 200 °C **(c)** 250 °C

Figure 4.32: Temperature-time curves at different locations for different nozzle set temperatures without active cooling.

4.5.4.2 Static tests with active cooling above nozzle

A second set of IR tests were done with active cooling of the tape above the nozzle to better control the environment conditions. A compressed air line was used to supply a steady flow of cool air over the top of the nozzle and past the tape. Using a K-type digital thermometer, the temperature of the compressed air was measured from the outlet and above the nozzle, which fluctuated between 17 °C to 30 °C. This value was set at 20 °C in the analysis as room temperature. The heat transfer coefficient with air h_{air} was set at 25 W/m²/K. Figure 4.33 shows the temperature increase over time with the active cooling air which shows a much smaller area of the tape that experiences a temperature increase compared to Figure 4.31.

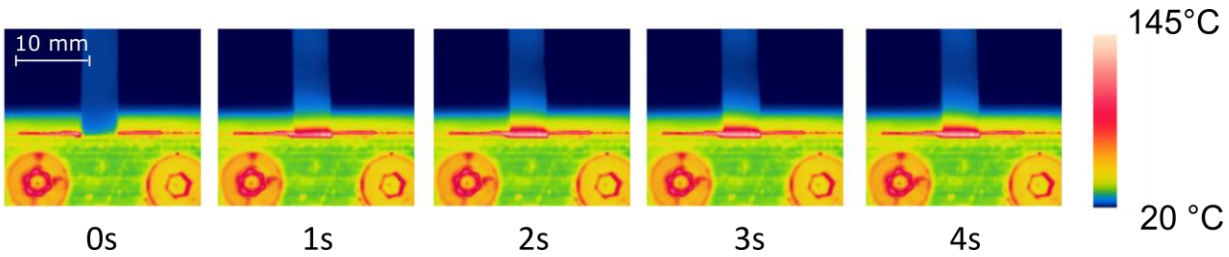

Figure 4.33: Increase in temperature over time in the ADFRC tape with the nozzle set at 150 °C and active cooling.

The temperature of the tape was extracted from the IR data in a similar fashion as sin ection 4.5.4.1 using the mm/pixel ratio and the numerical data was plotted with a temperature band to account for any location inaccuracy from the IR data as shown in Figure 4.34. The temperature rise in the ADFRC was monitored at three different temperatures (150 °C, 200 °C and 250 °C). The predicted temperature-time curves match more closely to the experimental data with the

active cooling modelled as constant air temperature (20 °C) above the nozzle. The predicted steady state temperatures show some deviation from the experimental data, especially for distances away from the nozzle inlet. The predicted temperature is consistently higher than measured which may indicate the heat transfer coefficient is lower (less heat going into the tape) or conductivity must be lower (temperature transfer in tape slower) than assumed from average values.

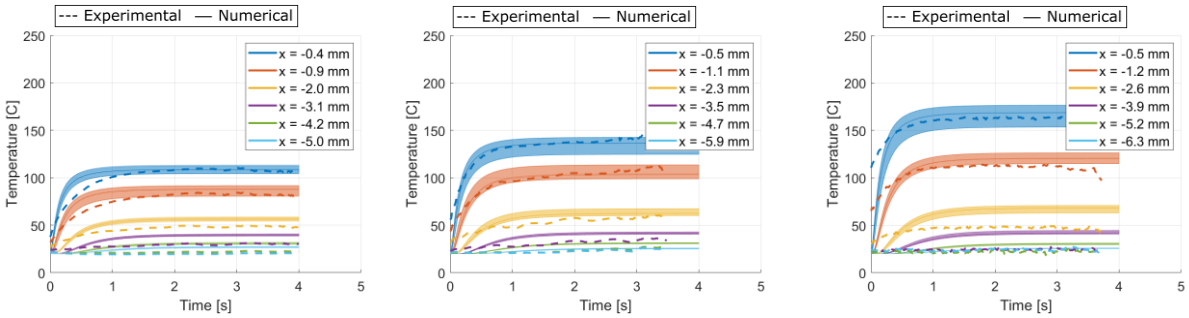

(a) 150 °C **(b)** 200 °C **(c)** 250 °C

Figure 4.34: Temperature-time curves at different locations for different nozzle set temperatures with active cooling.

To improve the temperature predictions, a parameter sweep was performed with different thermal conductivities k and heat transfer coefficient between the nozzle and ADFRC tape h_{nozzle}. The best fit is shown in Figure 4.35, where k is 2 W/m/K and h_{nozzle} is 500 W/m²/K. The predicted temperature profiles follow similar trends as measured with some mismatch between 0 s < t < 2 s. Notable deviations are the temperature mismatch for distances further away (3 mm) where the temperature is in the range of 20 – 60 °C. At lower temperatures (<100° C), the FLIR T650 is less accurate and the starting temperature from the simulation was 20 °C whilst in the experiment the tape may already have heated up as the tape was being put in the channel inlet.

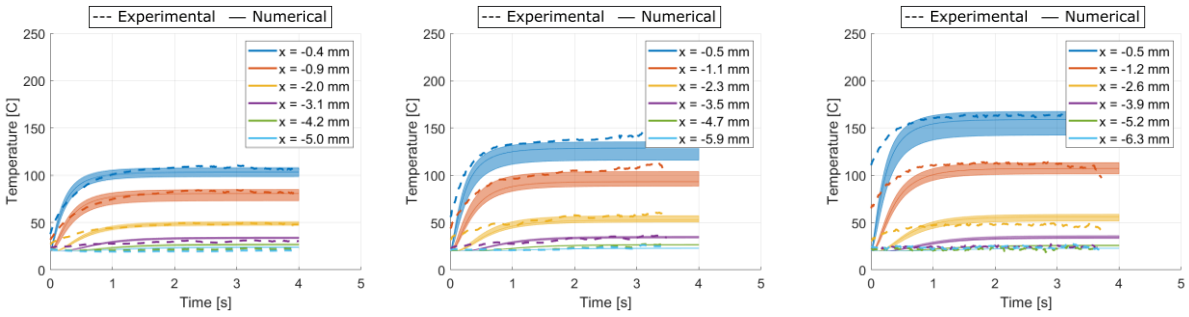

(a) 150 °C **(b)** 200 °C **(c)** 250 °C

Figure 4.35: Updated temperature-time curves at different locations for different nozzle set temperatures with active cooling

The different starting temperature and time mismatch between the numerical and experimental data is most clear for the static test at 250 °C. The predicted trends and steady state

temperature, however, are similar between the simulation and experimental data and this model can be used to give a first estimate of the temperature profile during extrusion.

4.5.5 Temperature and viscosity predictions during extrusion

The temperature and viscosity were expected to play an important role during extrusion. A thermal model was made to predict the temperature profile during extrusion. With the temperature profile, a predicted viscosity profile can be made based on the temperature prediction, the rheological data and a shear rate estimation. This section presents both the temperature profile and viscosity profile prediction.

4.5.5.1 Temperature profile prediction

The thermal model presented was validated for static cases and will now be used to give a prediction of the temperature profile during extrusion. Ideally, the model would also be validated using the exit temperature during extrusion, but continuous extrusion was not obtained yet. A best prediction of the temperature profiles is made using the current numerical model and can be used to design a second set of extrusions tests. The thermal properties used for this initial temperature profile prediction are shown in Table 4.4 for reference.

Table 4.4: Thermal properties based on static validation**.**

	Static Validation
Thermal conductivity k [W/m/K]	2
Heat capacity c_p [J/kg/C]	1137
Density ϱ [kg/m^3]	1104
Heat transfer coefficient air h_{air} [W/m^2/K]	25
Heat transfer coefficient nozzle h_{nozzle} [W/m^2/K]	500

Figure 4.36 shows the predicted temperature profiles for the temperature sweep studies performed on the PLA ADFRCs. The faster extrusion test (at 28 mm/s) is also shown for comparison. In all cases with an extrusion speed of 14 mm/s, the ADFRC tape just reaches the set temperature at the nozzle outlet. In the constriction region (denoted with "Converging" in Figure 4.36) the average temperature is typically 3 °C lower than the set temperature. It can also be seen that the tapes quickly heat up upon entry in the nozzle, with the ADFRC tape reaching a temperature above 150 °C within 2.5 mm to 5 mm for the different speed settings.

From the initial experiments, it was found that extrusion at 28 mm/s at 210 °C for PLA ADFRCs was better than 14 mm/s at 210 °C. The temperature profile of the faster extrusion test has a similar temperature profile as the 14 mm/s - 190 °C test, but with a lower temperature in the inlet region and a higher temperature in the converging section and the outlet. This shows

the combination of extrusion speed and temperature can be used to vary the temperature profile to control where in the nozzle the polymer matrix is softened.

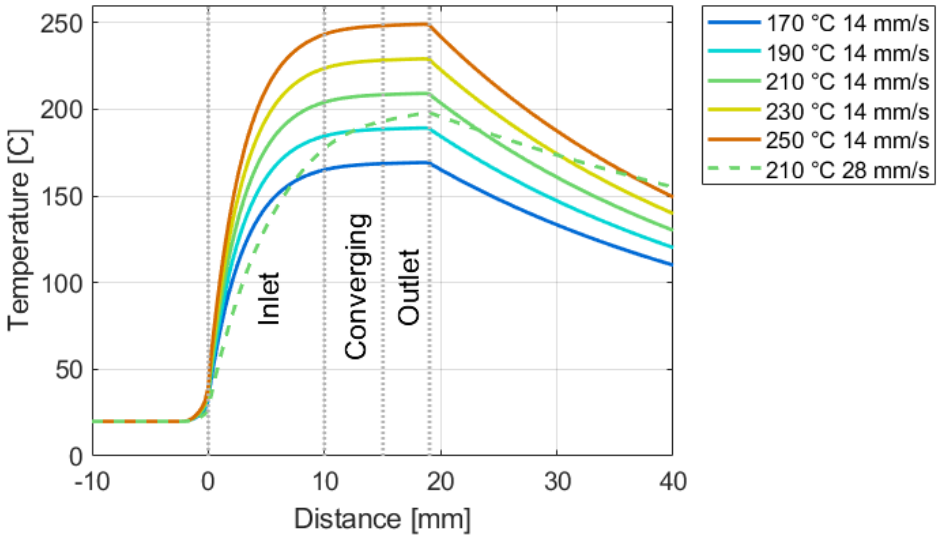

Figure 4.36: Predicted temperature profile through the channel at different processing conditions with vertical dashed lines indicating inlet, region and outlet region in the nozzle.

At this stage, the predicted temperature profiles have been validated with static cases as continuous extrusion was not yet obtained. Some conclusions can be drawn already, as they provide a first indication of the heating profile during extrusion. No excessive heating is expected to occur before the nozzle inlet which was a hypothesis from the initial extrusion studies. Instead, heating occurs gradually and can be tailored with the extrusion speed and channel temperature. The temperature in the constriction region is expected to be important as most reshaping occurs there, whilst the inlet region serves to heat up the tape but otherwise adds to the overall friction. To provide a better understanding on the extrusion process, the temperature data is used to predict the viscosity profile which is presented next.

4.5.5.2 Viscosity profile prediction

The viscosity of the polymer was expected to play an important role in how well the ADFRC can be reshaped through the channel. To predict the viscosity of the polymer, the rheological data must be known as well as the temperature and shear rate. Rheological testing was performed on the candidate polymers which was presented in section 3.2.2 and the temperature profile can be predicted using the numerical model developed. A shear rate estimation is needed to give a prediction of the viscosity which is presented here.

The shear rate was initially calculated assuming Newtonian flow in a pipe with a diameter of 1.13 mm to match the cross sectional area of the ADFRC tape (Equation (4.14). This assumption was revisited to improve the estimate of the shear rate experienced during extrusion by

accounting for the rectangular cross section. For a fixed cross-sectional area and flow rate, the shear rates experienced will be different as the flow is bounded by the side walls (channel width) and top/bottom walls (channel thickness).This changes the velocity field and shear rates [154].

The hydraulic diameter D_h can be used which considers both the cross-sectional area and wetted perimeter of the channel geometry. This value is then used as an equivalent pipe diameter for flow analysis purposes and may be used in standard equations for flows in circular channels. It depends on the ratio of the cross-sectional area A and the wetted surface area P as shown in Equation (4.25). The shear rate is calculated using Equation (4.26) where the volumetric flow rate Q is derived from the original flow velocity and the cross sectional area from D_h.

$$D_h = \frac{4A}{P} = \frac{4w_t t_t}{2(w_t + t_t)} \tag{4.25}$$

$$\dot{\gamma} = \frac{Q}{2\pi D_h} \tag{4.26}$$

Miller [186] provided another method to calculate the average wall shear stress for non-Newtonian flow in rectangular cross section. A shape factor λ was used to account for cross sectional geometry which is given in Equation (4.27) and depends on the aspect ratio of the cross section. The shear rate can then be calculated using Equation (4.28).

$$\lambda = \frac{24}{[(1 - 0.351\, t_t/w_t)(1 + t_t/w_t)]^2} \tag{4.27}$$

$$\dot{\gamma} = \frac{Q\lambda}{2AD_h} \tag{4.28}$$

A comparison of the predicted shear rates for different aspect ratios is shown in Figure 4.37, with a speed of 14 mm/s and a cross sectional area of 1 mm^2. The area equivalent diameter gives a constant shear rate as it does not account for the aspect ratio. The hydraulic diameter method shows that the shear rate during extrusion would be higher than originally predicted using the area equivalent method. The shear rate increases significantly for higher aspect ratios. The ADFRC tapes have an aspect ratio of 25, where the shear rate is expected to be roughly 300 [1/s] which is three times higher than the highest shear rate tested at for rheological testing. A similar trend is predicted by using the method presented by Miller, which estimates a shear rate of 420 [1/s] at an aspect ratio of 25 and a 14 mm/s extrusion speed.

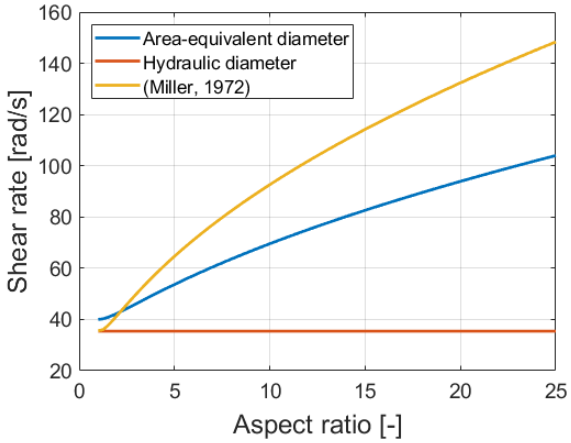

Figure 4.37: Predicted shear rate for different aspect ratio channels with a flow velocity of 14 mm/s.

The shear rate and temperature data can now be used to predict the viscosity using the rheological data. Figure 4.38 shows how the viscosity of PLA varies with increasing shear rate and temperature. The shear rate-viscosity relationship shows a shear thinning behaviour of the PLA polymer, where the viscosity reduces at higher shear rates. This effect is modelled with a power law as shown in Equation (4.29) where *K* and *n* are fitting parameters. Figure 4.38a shows the fitted curves which match the experimental data well. The temperature-viscosity relationship is modelled using an exponential fit as shown in Equation (4.30).

Figure 4.38b shows that the exponential relationship between viscosity and temperature closely fits the rheological data. The shear rate dependence of the viscosity is less pronounced than the temperature, and the viscosity is relatively constant for higher shear rates.

$$\eta = K\dot{\gamma}^n \tag{4.29}$$

$$\eta = a \cdot e^{bT} \tag{4.30}$$

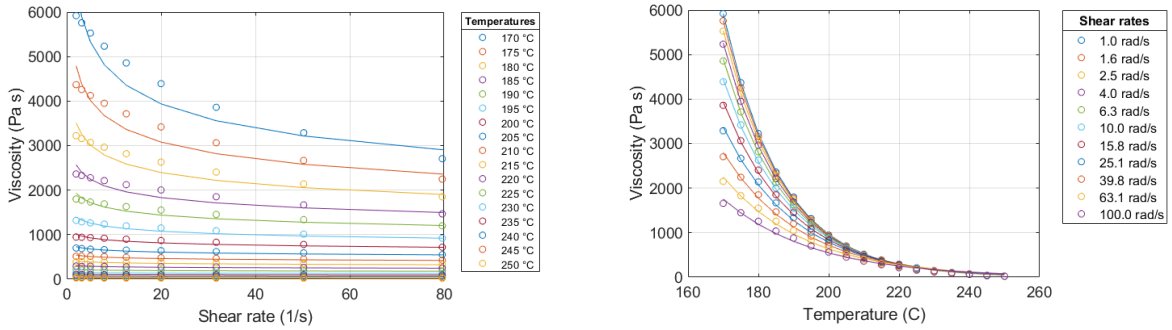

(a) **(b)**

Figure 4.38: Viscosity dependence of PLA on temperature and shear rate from rheological data

When the shear rate estimations are coupled to the rheological data, it is apparent that the process conditions used during extrusion clearly are in the shear thinning plateau ($\dot{\gamma}$ >100 [1/s]), regardless of shear rate estimation model used. In this region, changes in shear rate have relatively little influence on the viscosity, although the viscosity is still significantly different than what it

would be without shearing effects. For a temperature of 200 °C, the viscosities at a shear rate of 100 [1/s] and 300 [1/s] are 656 Pa·s and 592 Pa·s, respectively. The main factor influencing the viscosity therefore is the temperature of the material and Equation (4.30) is used fitted to the rheological data obtained with γ=100 [1/s] where $a = 1.31 \cdot 10^6$ and $b = -0.039$.

The predicted viscosity profile for the different extrusion temperatures used in the temperature sweep study are shown in Figure 4.39. These tests were performed at an extrusion speed of 14 mm/s and the viscosity profile of the faster extrusion trial (28 mm/s) is also shown. A viscosity of $6 \cdot 10^5$ Pa·s is predicted before the ADFRC tape enters the channel, however upon entry the matrix polymer is still solid. Figure 4.38b shows that the rheological data can only be interpolated between 170° - 250 °C, with some extrapolation possible using Equation (4.30). The viscosity prediction therefore only gives a representative value in the range of 0 – 6000 Pa·s and outside this range the viscosity prediction needs to be taken as a rough approximation.

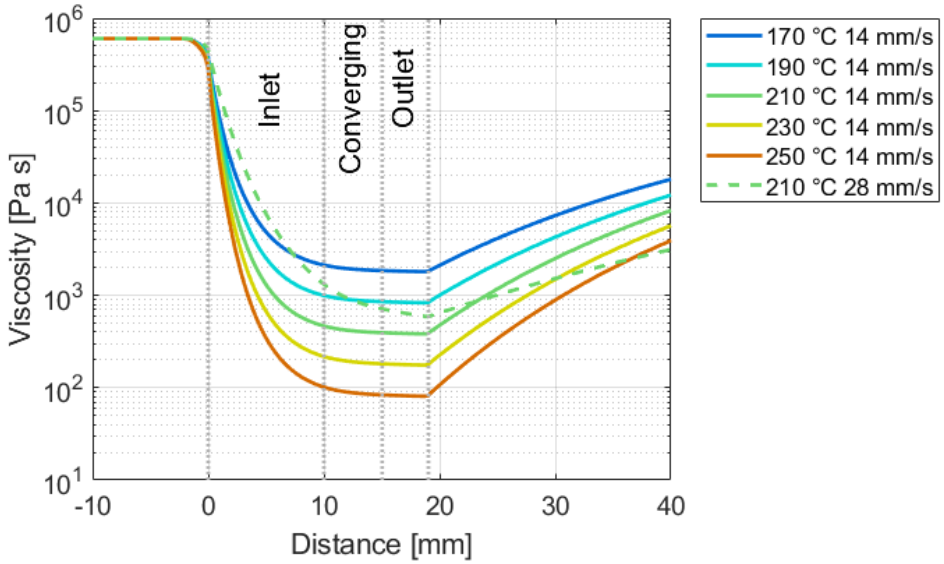

Figure 4.39: Viscosity profile predictions during extrusion at different processing conditions, with vertical dashed lines indicating inlet, region and outlet region in the nozzle.

The temperature sweep trials showed that temperatures of 170 °C and 190 °C led to poor extrusion and an improvement was obtained at higher temperatures. At 170 °C and 190 °C the average viscosity in the angle region was 1924 Pa·s and 882 Pa·s respectively. This indicates an upper boundary of matrix viscosity which is needed to successful extrude the ADFRC tape. At higher temperatures the extrusion improved but no continuous extrusion was obtained yet.

A further improvement was seen with a faster extrusion speed (210 °C-28 mm/s) and it was hypothesized that this may be due to a higher shear rate and thus lower viscosity. The viscosity prediction shows that the increase in shear rate has little influence on the viscosity of the

polymer matrix. Instead, the viscosity in the angle region is similar to the 190 °C-14 mm/s extrusion but with a higher viscosity in the inlet region. This indicates that a too high viscosity in the inlet may inhibit the extrusion process. For future extrusion trials, a shorter inlet length may be required together with higher extrusion temperatures to better control the temperature in the constriction region and prevent micro-buckling effects observed in the inlet. With the information obtained from the temperature and viscosity analysis, a new set of extrusion studies was designed which is presented next.

4.6 Final extrusion study

4.6.1 Updated nozzle design for extrusion improvements

The initial extrusion studies led to a better understanding of the flow effects involved. During extrusion, micro-buckling of the ADFRC tape was observed as well as bending of fibres in the ADFRC tape. Parameter studies showed that PLA ADFRCs had the best extrusion behaviour and that the release agent used affected the extrusion behaviour indicating surface friction should not be ignored. A thermal analysis was performed that predicted relatively fast heating of the ADFRC tape during extrusion but with the tapes reaching the set temperature of the nozzle only at the exit. The viscosity profile of the ADFRC tape was also predicted which can be used to tailor the design of the nozzles.

The new study focused around PLA ADFRCs as these had the best extrusion behaviour in the initial tests. The two main aspects which were expected to limit extrusion performance were surface coating and heating. The surface friction issue was addressed by using PTFE nozzles to reduce any potential friction to a minimum and to avoid issues with abrasive removal of the previously used surface coatings under repeated use. From the thermal analysis, a fast heat-up region was predicted, and it was hypothesized that a lower temperature, especially in the inlet region, may improve extrusion and therefore shorter inlet regions are proposed.

Based on the results of the thermal model, the tape is expected to heat up to 150 °C within 2.5 mm for an extrusion speed of 14 mm/s. Six nozzles were fabricated as shown in Table 4.5 with three different inlet lengths (1 mm, 3 mm, 5 mm) and three angles (7.5°, 10°, 15°). Different angles were added as it may reduce the pressure drop over the nozzle and prevent the micro buckling type failure.

Table 4.5: Nozzle details with varying inlet lengths and angles.

	1 mm	3mm	5mm
7.5°	PTFE	PTFE	PTFE
10°			PTFE
15°	PTFE		PTFE

The channels were machined from PTFE and an aluminium block was covered with a 0.1 mm thick PTFE tape to provide a smooth PTFE surface to close the channel (Figure 4.40). A cartridge heater was inserted into the Aluminium block for efficient heat transfer to the ADFRC tape through the 0.1 mm PTFE tape, whilst having a channel with a low friction PTFE surface on all four sides. One problem with this set-up was that bubbles may form below the PTFE tape and the tape can peel from the aluminium block when heated. This can cause a blockage in the channel which would prevent extrusion. The application the PTFE tape was done on a heated aluminium block (200 °C) as the tape expands due to its coefficient of thermal expansion. Otherwise, this may cause peeling when it is applied at room temperature and it heats up for the first time. The tape was applied carefully from one side and any air bubbles were pressed out using a squeegee like device. Before extrusion and when the channel assembly was heated it was visually checked if any blockages in the channel were present.

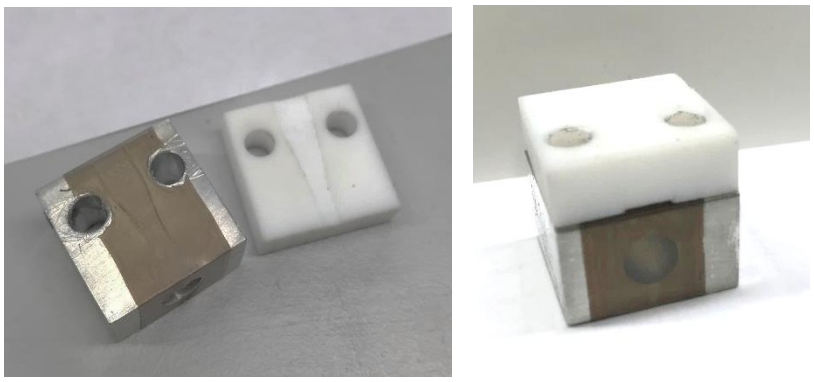

(a) (b)

Figure 4.40: Close-up of the (a) PTFE channel and aluminium hot block with PTFE tape to create a (b) closed channel with PTFE surface for lower friction

A stiff backing plate (6 mm aluminium) was used on the outside of the PTFE block to allow for the heater block and PTFE block to be bolted together tightly without local elastic deformation in the PTFE. This assembly was bolted to the aluminium frame assembly, after which the extrusion head was aligned above the channel to commence the extrusion studies.

4.6.2 Extrusion results

Extrusion tests on the new PTFE channels were performed with a speed of 14 mm/s and a temperature of 230 °C. A speed of 14 mm/s was used as it was expected the PTFE channels

would reduce the heating rate of the ADFRC tape and therefore the slower speed from the previous studies was selected. A FLIR T650 IR camera was used to monitor the outlet of the channel and the temperature of the ADFRC during extrusion. All channels from Table 4.5 showed successful continuous extrusion, each with three repeats to confirm consistent extrusion behaviour.

Figure 4.41 shows the thermal camera results of the 1 mm-7.5° nozzle where at $t = 0$ s the tape exits the channel. Once again, the emissivity was set at 0.92 for the PLA ADFRCs, with a reflection temperature of 20 °C. The emissivity coefficient of PTFE is similar to PLA and the measured temperature using the IR data matches the set temperature (230 °C). The exit temperature of the tape is around 160 °C which shows the tape does not reach the set nozzle temperature. For the 3 mm-7.5° nozzle (see Figure 4.42) the exit temperature was found to be lower (around 145 °C) which is unexpected as the total length of this channel configuration is higher. The lower temperature may be attributed to a higher pressure needed to force the tape through the 1 mm-7.5° channel which causes more intimate contact and faster heating. A close up of the thermal data during extrusion with the 5 mm-7.5° nozzle is shown in Figure 4.43, it shows successful extrusion with an average exit temperature of the ADFRC of about 160 °C, while a higher temperature than the 1 mm-7.5° configuration was expected in this case as well.

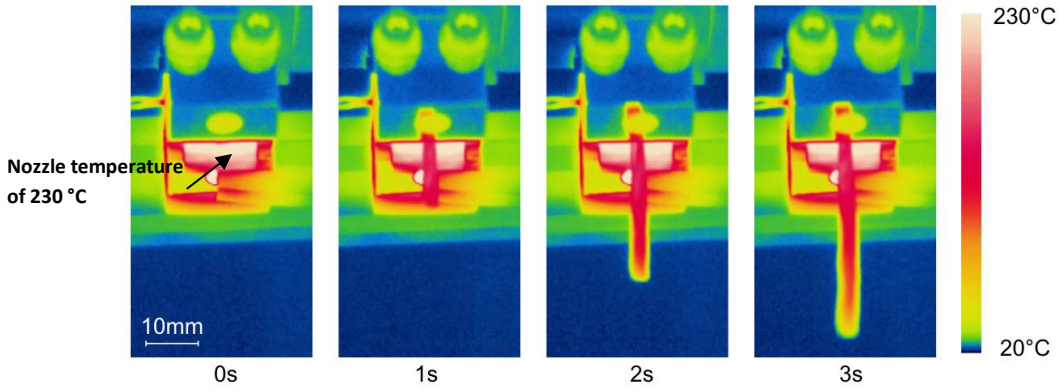

Figure 4.41: Thermal results for extrusion of ADFRC PLA tape at 230°C-14 mm/s through 1 mm-7.5° channel.

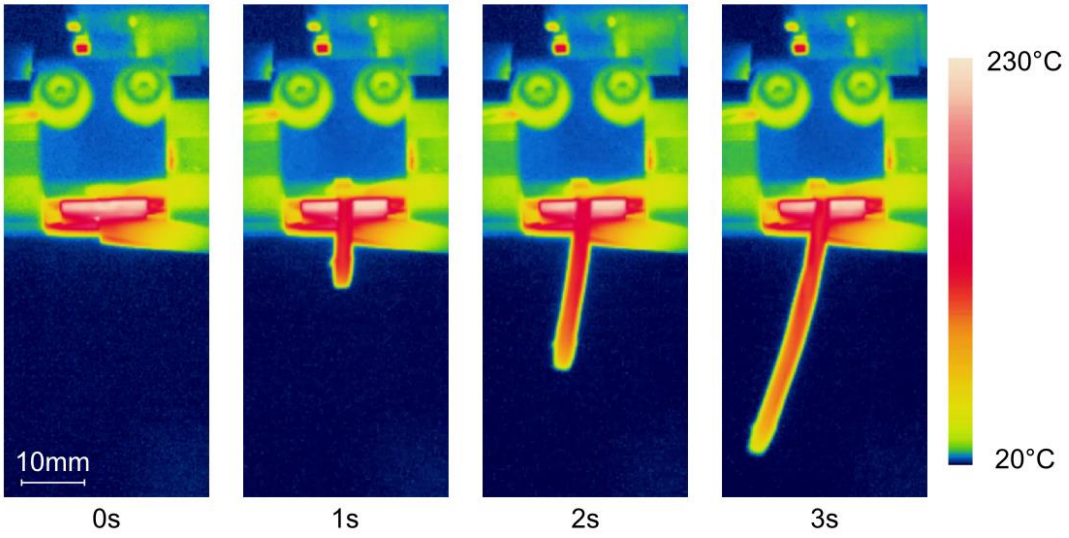

Figure 4.42: Thermal results for extrusion of ADFRC PLA tape at 230°C-14 mm/s through 3 mm-7.5° channel.

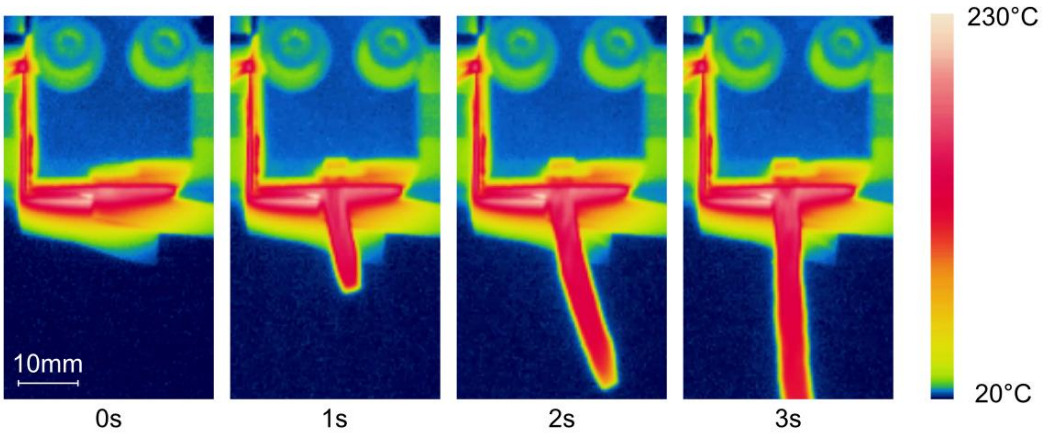

Figure 4.43: Thermal results for extrusion of ADFRC PLA tape at 230°C-14 mm/s through 5 mm-7.5° channel.

Using the FLIR software, the temperature data was extracted along the centre line of the ADFRC tape. The mm/pixel ratio was used to map the pixel location to the location on the ADFRC from the channel exit. As continuous extrusion was obtained, the steady-state temperature profile could be extracted over a certain time which allowed to plot the minimum, mean and maximum observed temperature. Therefore, Figure 4.44 shows a temperature band for the experimental data that matches the minimum, mean and maximum values of temperature observed at the given location during steady extrusion conditions.

In general, the numerical model with the thermal properties from the static validation over-predicted the exit temperatures of the tape by as much as 50-80 °C. This indicates the heat transfer coefficient between the ADFRC tape and the channel used in the simulation is too high. The predicted fast heating rate of the tape is thus unrealistic. Experimentally, it was expected that a longer inlet length channel would result in a higher exit temperature, but this trend is not present in the measured data. This indicates that the heating rate may be dependent on other variables

that are not included in the simulation, such as the quality of the ADFRC tape or the level of contact between the ADFRC tape and channel surface. The cooling rate after the ADFRC leaves the channel seems slower than predicted as the experimental data shows a near horizontal line. This may be attributed to the local air temperature being higher than room temperature and the vicinity of the heated channel, which leads to more heat going into the ADFRC tape after extrusion.

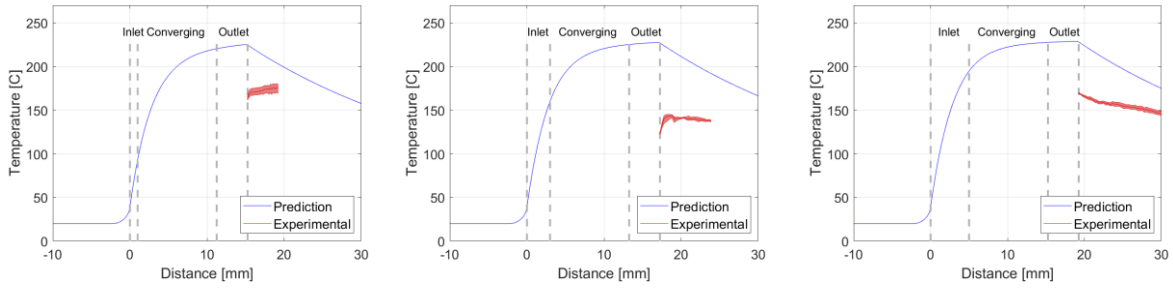

(a) 1 mm-7.5° **(b)** 3 mm-7.5° **(c)** 5 mm-7.5°

Figure 4.44: Predicted temperature profiles for 14 mm/s-230 °C extrusion for different channels with experimental data.

The numerical model was updated to better match the exit temperatures observed during extrusion. The heat transfer coefficient between the tape and channel h_{nozzle} was reduced to give a better prediction for all the extrusion cases. Figure 4.45 shows the new prediction with h_{nozzle} = 70 W/m²/K which was chosen as a compromise to provide a balance of prediction accuracy for all cases. The inconsistencies in exit temperature and inlet length mean the predicted exit temperature and actual temperature are roughly ~10 °C off as a higher exit temperature is predicted for longer inlets (opposite of what was observed). It does, however, give a good indication of the temperature profile in the channel, where clearly the tape does not reach its set temperature during extrusion.

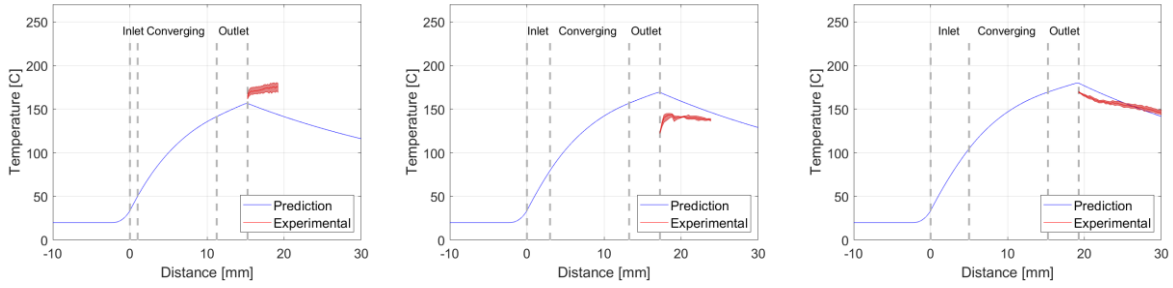

(a) 1mm-7.5° **(b)** 3mm-7.5° **(c)** 5mm-7.5°

Figure 4.45: Predicted temperature profiles for 14 mm/s-230°C extrusion for different channels with experimental data.

Extrusion experiments continued with the influence of different constriction angles, whilst keeping the inlet length constant at 5 mm. All three channel configurations (7.5°, 10° and 15°) led to continuous extrusion. The exit temperature is shown in Figure 4.46 with Figure 4.46a being

the reference extrusion (same as shown in Figure 4.45c). The nozzle with a larger angle (10 °C) has a smaller overall length but experimentally a higher exit temperature (180 °C) was observed. For the largest angle (15 °C), a lower exit temperature was observed which was closer to 150 °C. No clear trend can be seen in exit temperature versus constriction angle nor for exit temperature versus total channel length. Overall, the exit temperature of the ADFRC tapes is well below the set temperature of 230 °C and fails to reach a temperature above the melt temperature of PLA. This means the heating may not be as uniform as the tape is not in melt state through the channel but is squeezed through when the polymer matrix is above its glass transition temperature.

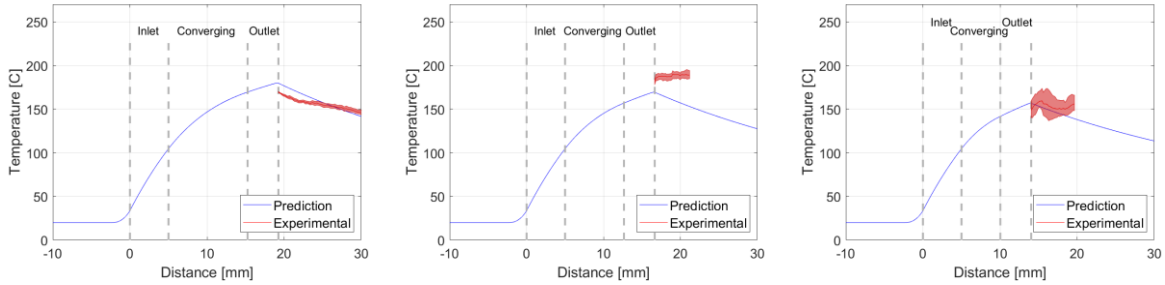

(a) 5mm-7.5° **(b)** 5mm-10° **(c)** 5mm-15°

Figure 4.46: Temperature profiles for 14mm/s-230°C extrusion for different channels with experimental data.

With continuous extrusion obtained for all PTFE channel configurations, the effect of extrusion speed and temperature was investigated. Figure 4.47 shows the temperature profile predicted and as observed for a slower speed (10 mm/s) and a higher temperature (270 °C). Both extrusions were successful and had a higher exit temperature than observed for the 14 mm/s-230°C process settings as expected (Figure 4.46a).

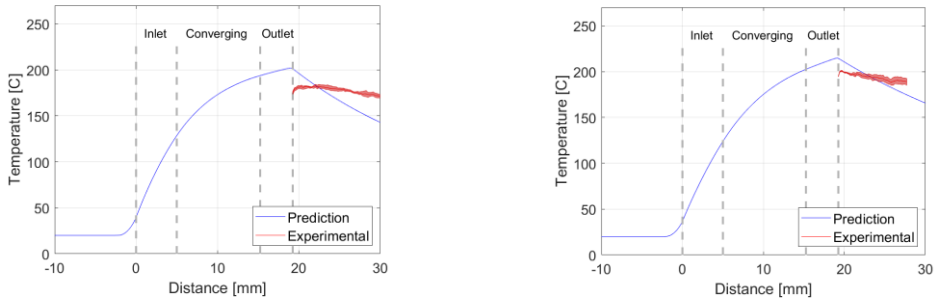

(a) 10 mm/s - 230 °C **(b)** 14 mm/s - 270 °C

Figure 4.47: Temperature profiles for 5mm-7.5° channel with different speed and temperature settings.

Lowering the extrusion speeds any further led to unsuccessful extrusions for the 5 mm/s-230 °C and 10mm/s-270°C cases. The predicted temperature profile for these conditions are shown in Figure 4.48 where there is no experimental data for the 10 mm/s-270°C case as no material was extruded. The prediction for the 5 mm/s-230 °C case is relatively close to the observed exit temperature. The temperature of the ADFRC tape seems to rise after exiting the

channel, however this is likely attributable to the flow halting and the tape heating up as it is stationary.

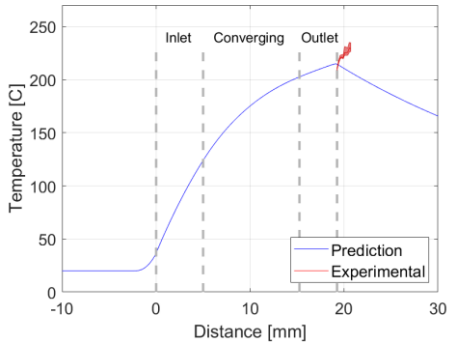

Figure 4.48: Predicted temperature profiles for unsuccessful extrusion with 7.5°-5mm channel at 5 mm/s - 230 °C.

From the thermal imaging and analysis, it can be concluded that the heating rate was lower than expected. Despite the lower temperature, successful extrusion was obtained for all nozzles using a set temperature of 230 °C and speed of 14 mm/s. Follow-up extrusion tests were done with a higher channel temperature and slower extrusion speeds to increase the temperature of the ADFRC tape, but these led to unsuccessful extrusions. This result is unexpected as a lower viscosity was expected to improve the extrusion process based on the second filament forming trials. A closer look to the viscosity profiles was performed to see if a trend could be observed.

Figure 4.49 shows the predicted viscosity profiles for all the extrusion trials done on the PTFE nozzles. The green lines show successful extrusion while the red lines show unsuccessful extrusion. The viscosity prediction for the initial trials with aluminium nozzles (Figure 4.39) showed that extrusion was best when the viscosity in the constriction area was below roughly 1000 Pa·s. The study with PTFE channels indicates that extrusion is successful for a viscosity range in the constriction area of roughly 1000 – 6000 Pa·s. When the viscosity is lower than 300 Pa·s, the extrusion halted.

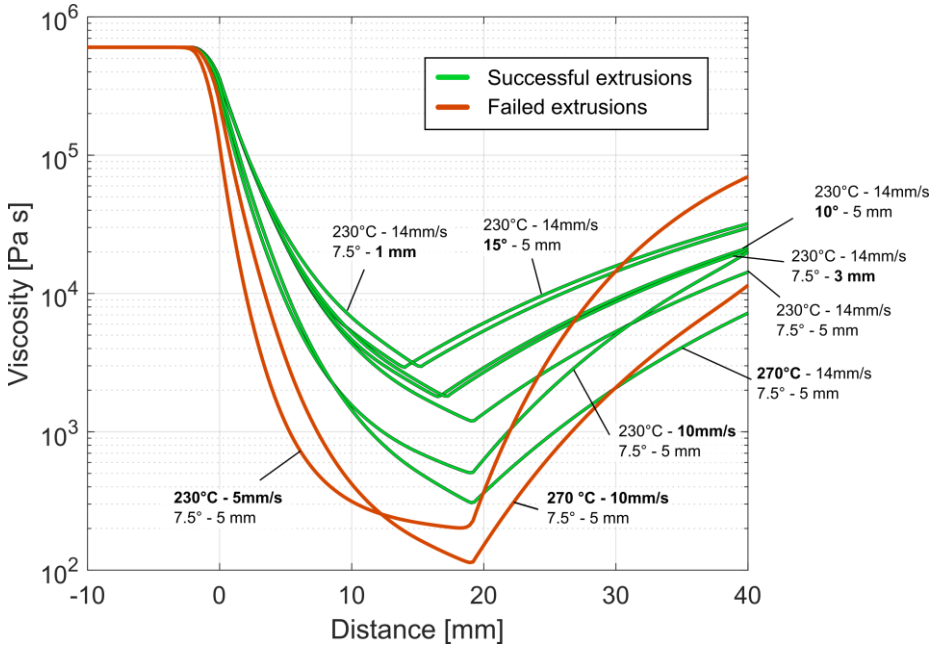

Figure 4.49: Predicted viscosity profiles for extrusion trials with PTFE nozzle with different geometries and processing conditions, showing deviations from the reference settings in bold.

4.7 Fibre orientation effects in flow

To better understand how the carbon fibres behave in the flow during extrusion, Computed Tomography (CT) scans were performed at KU Leuven university by researchers Jun Tang and Yentl Swolfs on filament forming samples. CT scanning provides a 3D image of the internal structure of an object by the computational reconstruction of a series of X-ray scans taken from different angles [187]. Internal features such as fibres, matrix and voids can be identified given a high enough resolution of the image and good contrast between the features. The contrast is caused by different attenuation of the X-rays, which is dependent on the material density, material atomic number and energy of the X-rays.

The CT-images can consequently be used to predict the fibre orientation distribution. Different methods exists such as tracing fibres through slices [188] or fibre path prediction based on cylindrical cross sections [189]. In this work, a custom CT-image analysis software (VoxTex) developed at KU Leuven was used to calculate a fibre orientation distribution of the ADFRC tape at different locations within the extrusion channel. VoxTex uses structure tensor analysis to calculate the local anisotropy, and combines that with the relative density to distinguish between fibres and matrix [190], [191]. A CT-image can be visualised as voxels with a certain grey value in 3D space. The structure tensor then becomes a 3x3 matrix with the grey value gradients in the global coordinates, and it can be used to find the principal direction of anisotropy using the eigenvalues of the structure tensor. The eigenvector with the smallest eigenvalue is the direction

in which the variation in grey value is minimal and corresponds to the local fibre direction. The structure tensor and local fibre direction is calculated for each voxel attributed to a fibre from the anisotropy and relative density threshold. With the local fibre directions known for each voxel, the fibre orientation distribution can be directly generated.

Figure 4.50 shows an example 3D image of the ADFRC tape in the inlet region with the fibres clearly visible. Dark/black regions indicate air or voids, dark gray areas are the matrix and the carbon fibres are light gray. Most fibres are orientated in the principal direction, but on the top surface misaligned fibres can be seen that lie near perpendicular to the principal direction. Some fibres appear to be curved showing fibre bending can take place in the polymer melt.

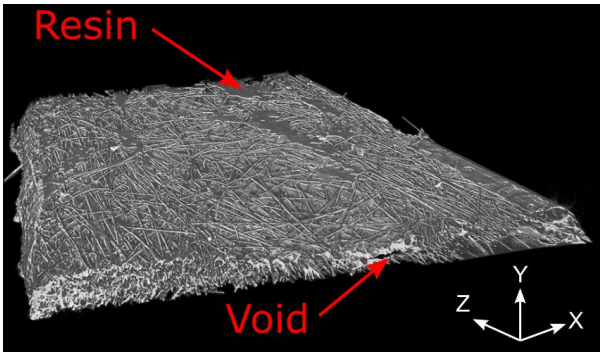

Figure 4.50: Example 3D image of ADFRC obtained using CT scanning.

The fibre orientation was extracted from CT scan data at four different regions, the inlet, contraction, outlet and die swell area as shown in Figure 4.53. This was done for three samples extruded through different nozzle angles (7.5°, 10°, 15°), all with a 5 mm inlet length. The extrusion was stopped and everything was allowed to cool in place before removing the samples, thus ensuring the fibre orientations were maintained. A comparison of the fibre orientation distributions and example cross sections are shown in Figure 4.52.

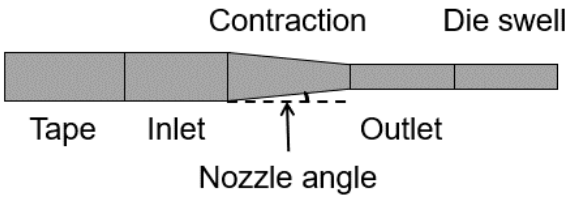

Figure 4.51: Locations where the fibre orientation is obtained from 3D CT scan data.

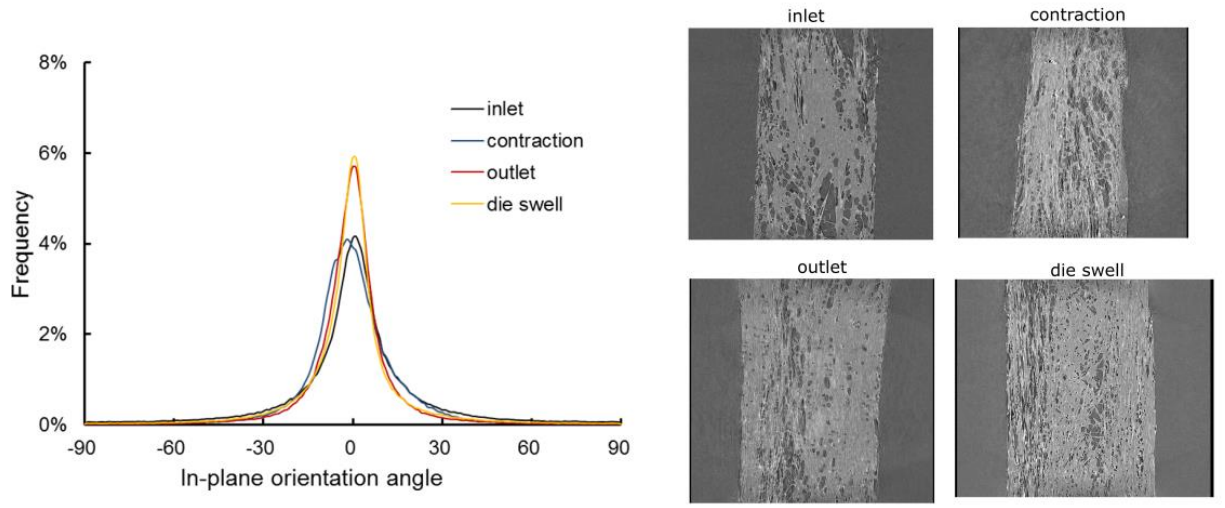

(a) 7.5°

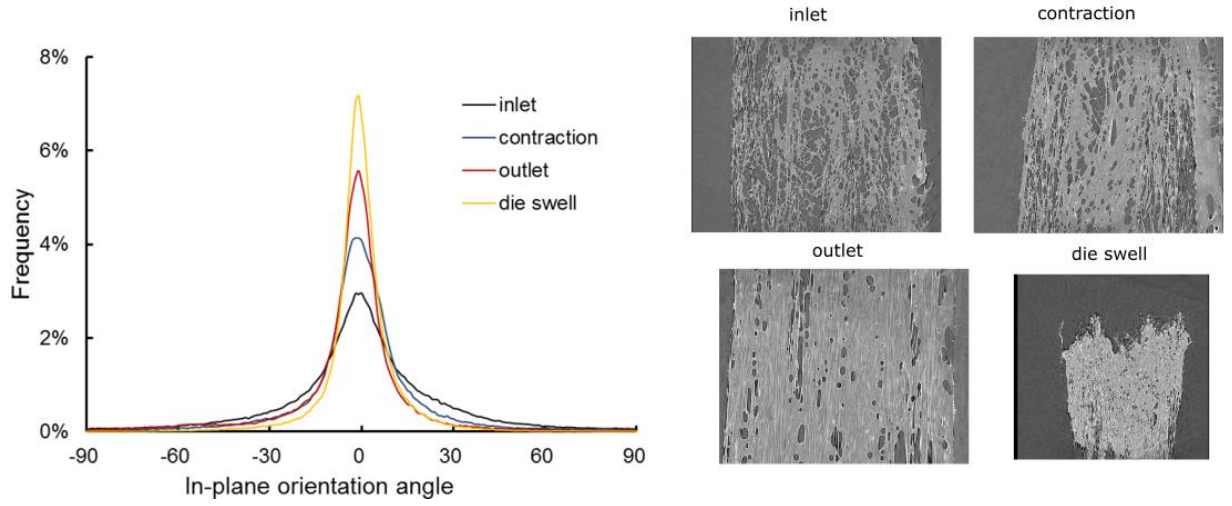

(b) 10°

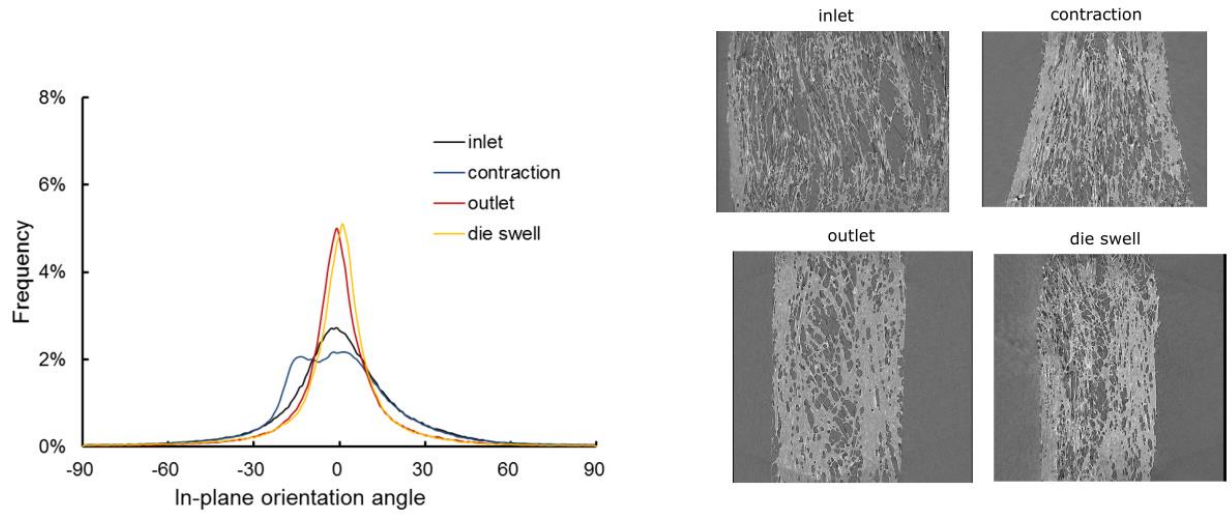

(c) 15°

Figure 4.52: In-plane fibre distributions in different locations for three different nozzle angles.

Only one sample for each nozzle configuration was scanned, so care should be taken generalising the differences between the samples. Each sample does contain thousands of fibres to

increase the statistically relevance of the dataset. In general, a trend can be seen in that the level of fibre alignment increases from the inlet to the die swell region:

- For the 7.5° sample, ~40% of fibres were aligned within ±5° in the inlet region and that increased to ~50% in the outlet and die swell region.
- For the 10° sample, ~30% of fibres were aligned within ±5° in the inlet and that increased to ~50% and ~60% in the outlet and die swell regions respectively.
- For the 15° sample, ~30% of fibres were aligned within ±5° in the inlet and that increased to ~45% in the outlet and die swell region.

A gradual increase in fibre alignment from the inlet to the contraction, outlet and die swell region can be seen for the 10° nozzle sample. For the 7.5° and 15° nozzles, the level of fibre alignment remained similar between the inlet and contraction region, with a large increase from the contraction to the outlet region. The level of fibre alignment in the outlet region remained similar again to that of the die swell. In the die swell region, the material expands and typically this is accompanied with a reduction of fibre alignment [192]. For the 10° nozzle, an increase in fibre alignment in the die swell region was observed, while for the 7.5° and 15° nozzles the fibre alignment in the die swell region stayed the same compared to the outlet region. Heller et al. [193] predicted the fibre orientation through FFF nozzles and predicted a very high level of fibre alignment through the contraction and with a small reduction in the die swell. Here, relatively long (3 mm) fibres are used which may reduce die swell as the fibres cannot freely flow outward.

The 15° sample shows a peak at an orientation angle of -15°, which can be attributed to a bundle of fibres being aligned with the side wall in the nozzle. This may be attributed due to the nature of the HiPerDiF alignment method, as fibre bundles may be present during the alignment and appear in the aligned tape. The average level of alignment in the inlet for all three samples (~32% within ±5°) is lower than originally reported for the HiPerDiF tapes (~90% within ±5°) but similar as found using optical microscopy in Chapter 3 [11]. The CT cross sections also show that the ADFRC tape had a considerable void content up to 25%. The filament forming was thus performed with a lower than expect level of fibre alignment and relatively high void content. A clear process improvement would be to increase the ADFRC tape quality and alignment to prevent premature fibre jamming and reduce the void content in the filament.

4.8 Discussions and conclusions

The aim of this chapter was to obtain a direct extrusion method for Aligned Discontinuous Fibre Reinforced Composite (ADFRC) tapes with thermoplastic matrices that allows the tapes to be progressively reshaped into a circular filament for FFF printing. A literature review was performed that highlighted the multi-physical aspects involved with flow of fibre polymer melts. For the ADFRC to be extruded into a different cross section, some flow of the polymer and fibres is required which is accompanied with a pressure drop through a channel. The fibres complicate the flow problem as they can prevent continuous flow due to fibre jamming and clogging. It was expected that the polymer viscosity (dependent on polymer type, temperature and extrusion speed), channel geometry, channel surface and fibre alignment would play an important role in this process. A set of studies were performed that resulted in continuous extrusion of the ADFRC tape and suitable processing parameters were identified to translate this into a continuous filament forming method without fibre breakage.

A set of extrusion studies were done using custom nozzles made by machining a channel in an aluminium block, which was subsequently covered with a glass plate. The channel consisted of a 10 mm long inlet section of 5 mm x 0.2 mm, a 15° angle constriction and 9 mm long outlet section of 3 mm x 0.3 mm. One of the first findings was the influence of different coatings. A lab standard Frekote release agent was first used which did not give good extrusion results. This coating was replaced with a silicone lubricant which improved the extrusion process and allowed up to 15 mm of material to be extruded. The difference in performance with different coatings shows that the surface of the channel is important for the extrusion process of ADFRCs. A potential problem with the coatings is that they wear or abrade away during extrusion, which leads to an increase in friction and may cause the flow to stop after some time. This was later addressed with different channel materials.

A glass cover plate was used to visually monitor the flow during extrusion. A micro buckling type failure was observed in the inlet region, where the ADFRC tape wrinkled inside the channel, and this was visible as a wavy pattern in the inlet region as indicated in Figure 4.53 below. The micro-buckling is expected to depend on the driving pressure required for extrusion, the softening of the polymer matrix in the inlet as well as the geometric tolerance in the channel. This effect can be detrimental to obtaining continuous extrusion and must be better understood. Some bending of fibres was also observed in the inlet region which can cause fibre jamming in the channel.

To resolve these problems, a parameter study was performed using different processing conditions, followed by modelling of the thermal and viscosity profiles and improving the nozzle design to improve extrusion.

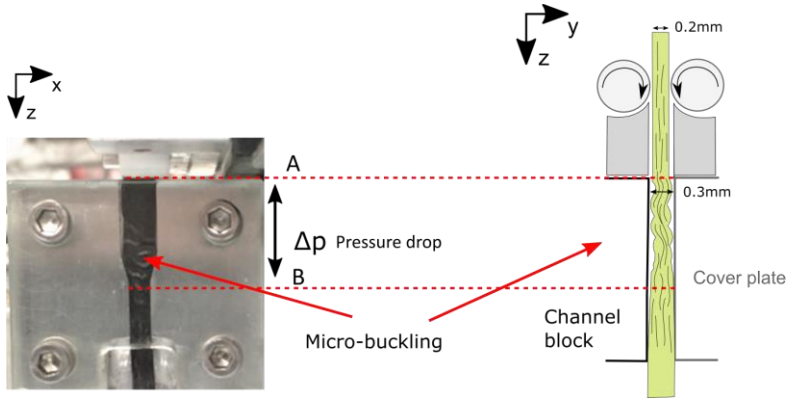

Figure 4.53: Micro-buckling observed during extrusion and a schematic side view showing channel tolerance.

A temperature sweep was performed using PLA ADFRCs that covered a wide range of matrix viscosity and a lower threshold for the temperature was identified. At 170 °C and 190 °C, no material could be extruded through the channel. At temperatures of 210 °C and above, the extrusion improved with 10 mm of extruded material. Increasing the extrusion speed led to further increase of the extruded material length (15 mm) but continuous flow was not yet achieved.

The effect of polymer type was investigated by extruding PA, ABS and PETG ADFRC tapes. The extrusion temperatures were chosen such that the polymers would have a similar viscosity as PLA at 210 °C. It was found that amorphous polymers (ABS and PETG) resulted in less good extrusion of the ADFRC tapes and that PLA gave the best performance. This was attributed to the sudden drop in viscosity that semi-crystalline polymers exhibit when they reach their melt temperature. This may help for ADFRC extrusion where a heat-up phase is needed before the reshaping takes place, but premature heating may cause micro-buckling in the inlet region as the matrix softens.

A thermal analysis was performed to better relate the extrusion behaviour to specific temperature and viscosity profiles of the ADFRC tapes. The results were validated with a static case by monitoring the temperature increase in the tape when it was inserted into the inlet region. Using the thermal analysis and static validation, a first prediction for the temperature and viscosity profiles was made during the initial extrusion tests. The predicted temperature profiles indicated that the ADFRC tapes did not reach the set temperature, which was unexpected as premature heating was identified as a limiting factor for extrusion. A comparison of all the temperature and viscosity profiles showed that the best extrusion setting (210°C-28mm/s) had a similar aver-

age temperature and viscosity in the constriction area as the unsuccessful 190°C-14mm/s extrusion. The difference was that the 210 °C-28 mm/s extrusion had a relatively lower temperature and higher viscosity in the inlet region. This indicates that a higher viscosity in the inlet region is beneficial to direct extrusion of ADFRCs as it prevents softening before the reshaping begins and this is line with the better performance of semi-crystalline polymers.

From the initial extrusion tests of ADFRCs it was seen that some stability issues are present in the form of micro-buckling and fibre bending. These phenomena were expected to be dependent on the viscosity profile of the polymer and on the required driving pressure for flow which depends on the channel geometry and coating. As continuous extrusion was not obtained yet, a final set of extrusion studies was designed to look at different channel geometries using PTFE nozzles to have a maximum reduction in surface friction.

The PTFE nozzles had different inlet lengths (1 mm, 3 mm, 5 mm) and constriction angles (7.5°, 10°, 15°C) and all showed successful continuous extrusion for PLA ADFRCs at 230°C-14mm/s. The exit temperature of the ADFRC tapes, as measured by an IR camera, was around 160 °C. Subsequently, the thermal model was updated for the PTFE nozzle configuration which indicated a much lower heat transfer coefficient than expected with the aluminium nozzles (70 $W/m^2/K$ vs. 500 $W/m^2/K$). More extrusion tests were done at slower speeds and higher set temperatures to increase the ADFRC tape temperature as this was expected to improve extrusion based on previous extrusion results. For the previous aluminium nozzle extrusions, a minimal temperature for extrusion was present which was related to an upper threshold of polymer viscosity of about 1000 Pa·s. The viscosity profile predictions for the PTFE nozzles (adjusted for the lower heat transfer coefficient and validated with the exit temperature) showed a lower threshold of polymer viscosity was present of about 300 Pa·s where at too high temperatures and low viscosities the ADFRC tape did not extrude.

From the above, an effective viscosity range for direct extrusion of ADFRC tapes can be proposed which lies between 300 Pa·s and 1000 Pa·s. The only anomaly to this finding is that some extrusion was possible for the aluminium nozzle set-up at viscosities below 300 Pa·s and for PTFE nozzles above 1000 Pa·s. This difference may lie in the different surface frictions for both nozzles. PTFE has a low coefficient of friction and as such extrusion with a higher viscosity is possible without exceeding the maximum driving pressure. For aluminium, a lower viscosity is needed as the surface friction is expected to be higher and no continuous extrusion was obtained with that configuration.

To conclude, the filament forming studies have identified a direct extrusion method for ADFRC tapes using PTFE nozzles which could be implemented with multiple stages to reshape the ADFRC tape into a circular filament with a continuous method. With a 50% width reduction demonstrated in this work, the 5 mm wide tape can be formed into a 1.25 mm square filament in two stages. The required viscosity profile has been identified and the flow of ADFRC tapes can now be better studied using this method. To continue investigating the potential use of HiPerDiF thermoplastic preforms in 3D printing application, a batch filament forming method was made and 3D printing trials were performed which are presented next.

Chapter 5

Printing performance of HiPerDiF filament

In this chapter, the fabrication of 60 cm long filament sections and the first 3D printing trials with filament made from 3 mm carbon fibre HiPerDiF preforms are presented. These HiPerDiF filament sections were made using a batch process by compression moulding of the PLA ADFRCs tapes. The goal of this work was to demonstrate that HiPerDiF filament can be used for fused filament fabrication (FFF). An introduction is first given in section 5.1, after which the methodology is presented in section 5.2. The results of the 3D printing trials are shown in section 5.3, which, to the authors knowledge, details the first deposition of a discontinuous carbon fibre reinforced thermoplastic filament with fibres above a length of 1 mm. The chapter ends with a discussion and conclusions on the 3D printing performance of HiPerDiF filament in section 5.4. The work presented in this chapter was conceptualised by the author and the experimental work was carried out in cooperation with undergraduate student Kevin Alarcon who worked under the author's supervision.

5.1 Introduction

The benefits of a carbon fibre reinforced filament for FFF have been discussed in 0 of this thesis. From a traditional 3D printing point of view, reinforced filaments have a higher stiffness and strength than unreinforced filaments. Their processing behaviour, however, may be complicated as the fibres cause extra wear, change the flow properties of the filament and a cutting mechanism must be incorporated when continuous fibre reinforcement is used in order to create separate print paths [5], [194].

Chapter 2 showed that the FFF of commercially available discontinuous fibre reinforced filaments is virtually unchanged with respect to virgin thermoplastic filaments. The performance benefit gained from the short reinforcing fibres, however, is minimal as their length is on the

order of 0.1 mm and failure in the composite is dictated by fibre pull-out instead of fibre failure. Continuous fibre reinforced filament show a much higher stiffness and strength (~10x increase) but, as demonstrated in Chapter 2, they are harder to deposit, and require dedicated and more complex printers. They are also susceptible to voids between the printed tracks (interbead voids) which reduce the performance of the resulting composite material.

Here, a novel filament is considered that may provide a better trade-off between performance and processing by using discontinuous carbon fibres with a length of 3 mm. Performance-wise, premature fibre pull-out was prevented as the fibres are above their critical length as shown in Chapter 3. Processing-wise, it is envisioned that this filament will be printable on standard FFF printers and will be able to provide benefits over continuous fibre filaments in terms of deposition and void creation.

The critical element for classical FFF using unreinforced thermoplastics is the liquefier (where the solid filament melts and is pushed through the nozzle) as defined by Turner et al. [56]. For unreinforced filaments, a melt pool is present in the liquefier and a pressure drop occurs through the nozzle. The feed rate of the filament and the temperature play an important role on the size of the melt pool and how material is extruded, and they are closely related to the viscosity and surface energy of the melt. The geometry of the liquefier and nozzle also have a large impact on the melt behaviour as they provide the boundaries through which the melt must flow.

Figure 5.1 shows a typical cross section of an FFF nozzle. The inlet diameter of the nozzle must be somewhat larger than the filament (2 mm for a 1.75 mm filament) and this gap can increase the thermal resistance. Studies have been performed to estimate the heat flux in the liquefier and predict the location of the melt front as well as estimating the pressure drop over the nozzle using momentum balance equations [56], [68], [195]. Ramanath *et al.* [195] investigated the effect of nozzle diameter and angle α through analytical modelling and FE analysis. The pressure drop increased by a factor of 1.5 from a 0.4 mm diameter nozzle to 0.25 mm nozzle. A shallower angle inside the nozzle of 70° instead of 20° reduced the pressure drop by roughly 30%.

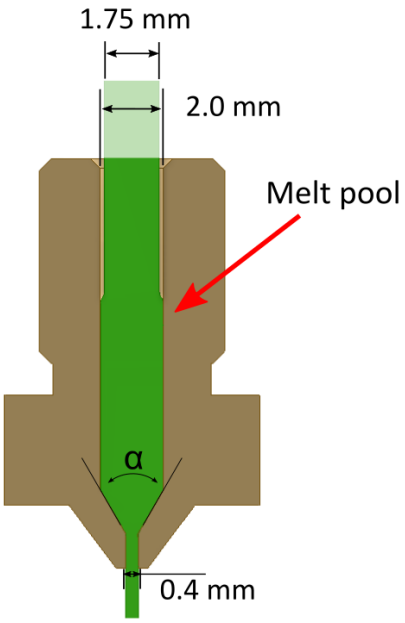

Figure 5.1: Schematic of liquefier/nozzle cross section during standard unreinforced filament printing showing melt pool.

For particle filled filaments, buckling of the filament is the most common failure during the FFF process [196]. Venkataraman et al. [196] studied the buckling behaviour of ceramic particle filled filaments, with the particles having a size up to 22 μm and a volume fraction of around 50%. The ratio between the elastic modulus of the filament E_{fil} and its apparent viscosity was used to predict whether buckling would occur. A critical ratio of $E_{fil}/\eta \sim 4 \cdot 10^5$ was found above which the filament does not buckle. This value, however, is dependent on the boundary conditions for buckling which can vary between printing set-ups; i.e. a different nozzle height, diameter or distance between the feeder and nozzle.

Nozzle clogging may be another failure mode for FFF with filled filaments, which is also relevant for fibre reinforced filaments. To date, only a few studies have been performed on nozzle clogging during FFF. It is a complex problem involving the channel geometry, hydrodynamics of the flow and physical-chemical interactions between the particles and channel boundaries [197]. Typically, clogging is explained by particle agglomeration and arch formation in the channel. Arch formation occurs when multiple particles form an arch over the cross section which leads to blockages. Beran et al. [198] recently investigated nozzle clogging in the FFF process with different spherical particle sizes, volume fractions, matrix viscosities and nozzle diameters. They found the matrix viscosity did not play a significant role and the size of the particles with respect to the nozzle diameter was the most important factor for nozzle clogging. No nozzle clogging occurred when particles were smaller than 0.16x the nozzle diameter. When the particles

are smaller, more of them are needed to form an arch in the nozzle, and this may prevent clogging.

For commercially available short fibre reinforced filament it has been shown that the 3D printing process remained essentially unchanged and can be done on standard desktop 3D printers [199]. This is typically done with carbon fibres with a length of 0.1 mm and a volume fraction of around 20%. For continuous fibre 3D printing, the 3D printing nozzle typically has the same diameter as the filament to prevent squeezing of the filament as this could lead to blockages [200], [201].

To the authors knowledge, no 3D printing trials have been performed using filaments reinforced with fibres above the critical length. Their processing behaviour is expected to lie in between that of short fibre reinforced filament and continuous fibre reinforced filament. Here, HiPerDiF filaments with 3 mm carbon fibres with a length of 60 cm were prepared using a batch manufacturing process and deposited using a desktop 3D printer. The batch manufacturing process and the 3D printing set-up are presented first in the methodology, the 3D printing results of the HiPerDiF filament are then shown.

5.2 Filament preparation and 3D printing set-up

To investigate the 3D printing behaviour of HiPerDiF feedstock reinforced with 3 mm carbon fibres, filament sections with a length of 60 cm were prepared by compression moulding the PLA ADFRC tape into a square filament. The square filament was manually extruded through different nozzles to obtain a near circular cross section and a more constant diameter along the length. 3D printing studies were subsequently performed using these 60 cm long filament sections. The preparation of the filament is first presented, followed by the printing set-up used.

5.2.1 Batch HiPerDiF filament production

PLA ADFRC tapes were used as a starting material for the batch production of HiPerDiF filament. A PLA matrix was used as they showed the best processing capability in the filament forming work (Chapter 4) and is one of the most common 3D printing filament materials. The preparation of HiPerDiF ADFRCs tapes using 3 mm carbon fibres and a PLA matrix was detailed in Chapter 3, which had a fibre volume content of roughly 12%. A custom semi-closed mould was prepared to form the thin tape into a filament with a square cross section, which was then manually extruded through a set of nozzles to give it a near circular cross section.

The aim was to obtain a HiPerDiF filament to perform proof-of concept deposition trials and investigate their 3D printing behaviour. The quality of the filament was not critical here and a simple compression moulding manufacturing method was used for this purpose. For future quality improvements and, more importantly, continuous filament manufacturing, the filament forming process presented in Chapter 4 should be further developed.

A custom semi-closed mould was prepared using three aluminium bars as shown in Figure 5.2. It consists of two top bars mounted on a bottom bar and fixed together by 6 bolts. Using this set-up, the gap width could be changed by moving the top bars to alter the filament width. A 0.1 mm thick PTFE tape was applied on the top surface of the bottom bar and on the side surfaces of the top bars to provide a non-stick and low friction surface to help the ADFRC tape flow into the square cross section. An aluminium angle section (15 mm x 15 mm x 1 mm) was used to press the ADFRC tape down. A 0.1 mm PTFE tape was used around the angle section to give it a width of 1.2 mm and the PTFE tape surfaces provided a tight fit in the semi-closed mould.

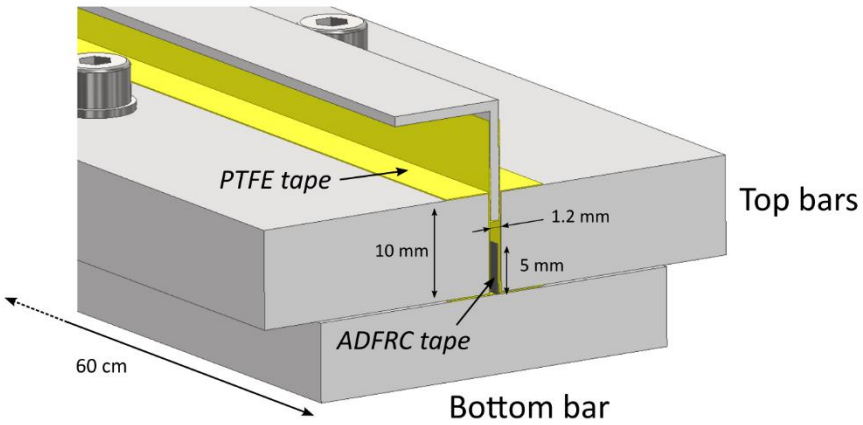

Figure 5.2: Detail of semi-closed mould set-up for manufacturing near square filament sections.

The compression moulding process consisted of pre-heating the PLA ADFRC tape in the semi-closed mould to 210 °C and holding this temperature for 1 hour. The pre-heated aluminium angle section was then manually forced down to squeeze the ADFRC tape into a square cross section and a 2 kg weight was added on top of the angle section to keep a constant pressure. The entire assembly was then allowed to naturally cool down to room temperature, after which the ADFRC filament with a square cross section was removed from the mould.

Figure 5.3 shows four moulded filament sections. The as-moulded filament contained resin flash with fibres and had a non-uniform width over its length with relatively thicker and thinner regions. The flash was cut from the filament and the thickness varied between 1.3 mm to 1.5

mm. To improve the 60 cm filament strands and give them a more consistent, and circular cross section over its length, they were manually extruded through a set of nozzles.

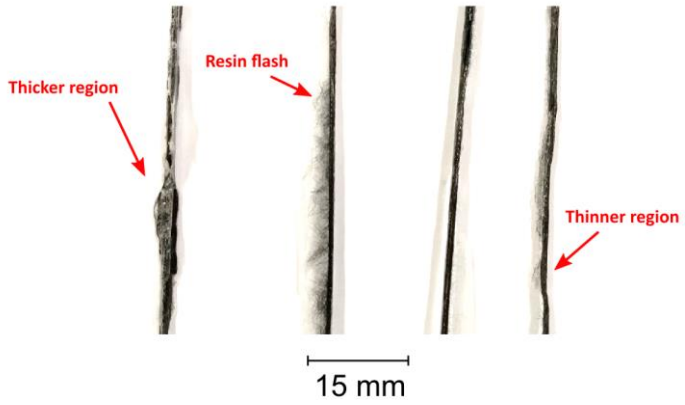

Figure 5.3: Example of moulded filament sections from semi-closed mould.

Table 5.1 shows the outlet diameters of the nozzles that were used to remove irregularities of the filament. These extrusions were performed at a temperature of 210 °C. This allowed to study which nozzle outlet diameter was most suited for extrusion and what the maximum contraction ratio for extruding the filament was. Theoretically, the ADFRC tape (5 mm x 0.2 mm) should form into a filament with a cross section of 1 mm², which is equivalent to a diameter of 1.12 mm. Table 5.1 shows the theoretical area difference with respect to the expected filament cross sectional area and the manual extrusion behaviour.

Table 5.1: Reshaping nozzles for moulded filament strands.

Nozzle	Theoretical area difference	Extrusion behaviour
1.75 mm → 1.5 mm	+ 77%	Clean pass through with little resistance
1.75 mm → 1.3 mm	+ 33%	Pass through with some resistance, push and pull required
1.75 mm → 1.2 mm	+ 13%	~10mm extruded through nozzle, pulling causes separation of filament
1.75 mm → 1.0 mm	- 21%	Blocked nozzle
1.75 mm → 0.8 mm	- 50%	Blocked nozzle

The manual extrusion of the filament strands through different nozzles shows that the ADFRC filament behaves much differently than unreinforced filament, which can be extruded through nozzles as small as 0.2 mm diameter. This is attributed to the fibres within the filament, which can cause filament buckling and nozzle clogging failures as discussed in the introduction. The studies in Chapter 4 showed that during direct extrusion of ADFRC tape, the carbon fibres can bend and micro-buckling can occur which prevents the filament from being extruded. Compared to commercially available short fibre reinforced filament, the aspect ratio of fibres in HiPerDiF filament is much higher (~400 instead of ~14) and this is expected to limit their movement, and therefore a change in cross-sectional area is harder.

The direct ADFRC extrusion studies in Chapter 4 also showed the effect of surface type on extrusion behaviour. A custom 1.3 mm PTFE nozzle was made to improve the final quality of the filament. It consisted of a 15 mm long PTFE rod with a 1.3 mm diameter channel through the centre as shown in Figure 5.4b. The filament was manually extruded through this nozzle at 270 °C which visually showed an improvement in quality. The advantage of this nozzle is that the filament fits tightly through the entire nozzle, without a wider 2 mm entry region as a standard 3D printing nozzle has as shown in Figure 5.4a. When extruded through the PTFE nozzle, the filament passes through the 1.3 mm diameter for a longer distance which improves the shaping process.

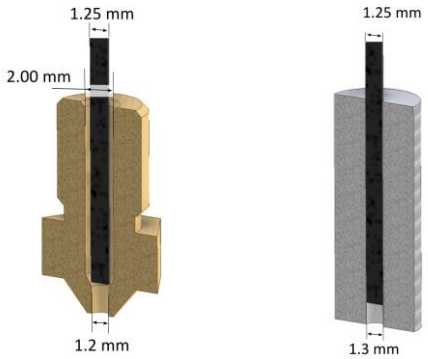

Figure 5.4: Cross section of the (a) 1.2 mm brass nozzle and (b) custom 1.3mm PTFE nozzle with a straight channel.

The final preparation of the batch filaments was done as shown in Figure 5.5. The moulded square filament was first extruded through a 1.5 mm diameter brass nozzle and then through a 1.3 mm diameter brass nozzle at 210 °C. The final step was an extrusion through the custom 1.3 mm PTFE nozzle at 270 °C. Three measurements were taken after each stage and the average cross section is shown in Figure 5.5 for each stage.

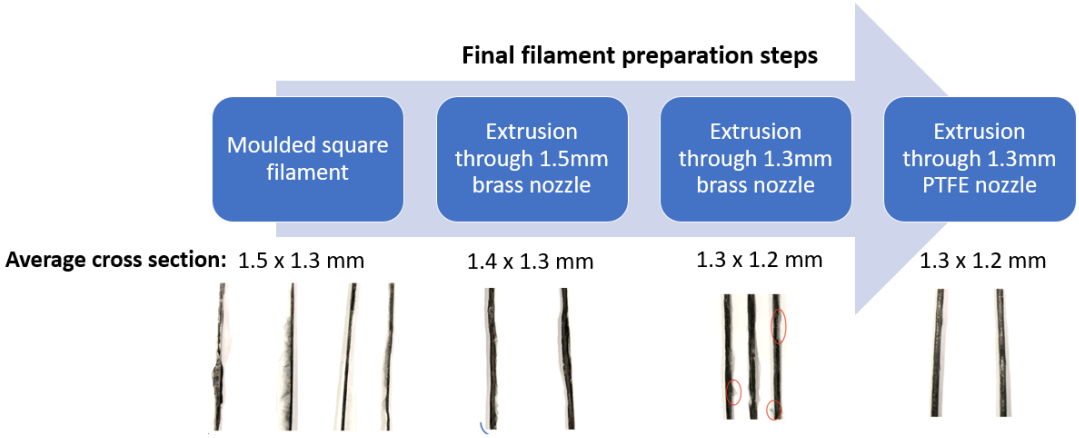

Figure 5.5: Final steps for filament preparation with manual extrusion through three nozzles.

Micrographs of the as-moulded square filament and after processing are shown in Figure 5.6. The as-moulded square filament had a large void content with both internal voids (black regions) and external voids (filled with potting resin). These voids were attributed to the entrapment of air during compression moulding of the ADFRC tape. For the as-moulded square filament, the internal void content was estimated at 10% and the external void content at 35% using grayscale analysis with ImageJ. For the circular filament, internal voids were still present with a void content estimated at 17%. The square filament has significantly higher void content than what was seen with the nozzle formed filaments in Chapter 4, implying that round filaments made from feedstocks created by the nozzle forming process would have lower void content then the filament tested here, but again the objective of this study is a proof of concept printing of aligned fibre feedstocks, and the relatively high void content should not interfere significantly with achieving the study goals.

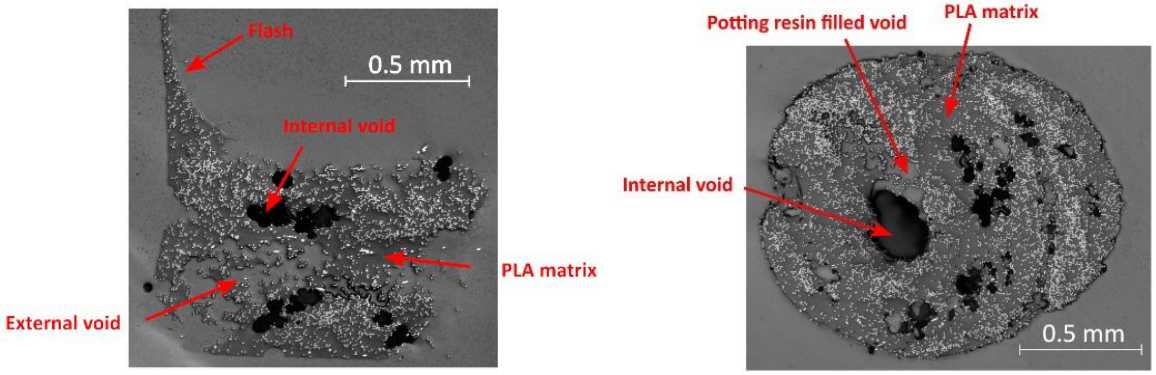

Figure 5.6: Micrographs of (a) as-moulded square filament and (b) filament after processing.

The final 60 cm HiPerDiF filament strands had an average diameter of 1.25 mm. These short filaments were then used on a desktop 3D printer to investigate their FFF processing behaviour which is presented next.

5.2.2 3D printing set-up

The previous section has detailed the preparation of short (60 cm) filament strands that can be used for fused filament fabrication. A desktop 3D printer was used with a direct extrusion head as shown in Figure 5.7. The direct extrusion head was used as this provided the best control of feed rate through the nozzle and the filament strands themselves had a limited bend radius due to their relatively high stiffness. The drive gears of the 3D printer were modified as the original drive gears had a concave section to match a traditional 1.75 mm filament, and these were replaced with straight gears to have better grip on the custom 1.25 mm diameter HiPerDiF

filament. A bed levelling sensor was added to the 3D printer to ensure the height between the printing bed and nozzle could accurately be set.

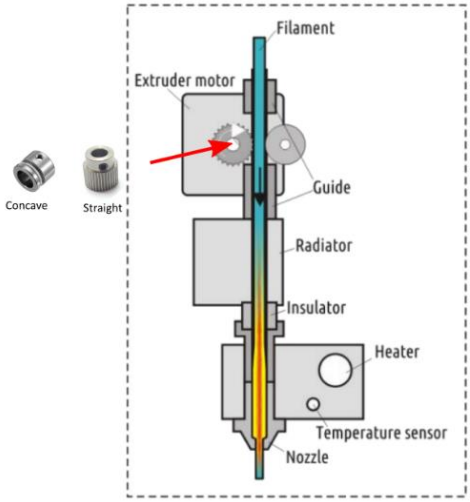

Figure 5.7: Direct extrusion set-up with extruder motor, radiator and nozzle/heater set-up [202].

An early printing trial was performed with a standard 1.75 mm to 0.4 mm nozzle used in traditional 3D printing. This print was unsuccessful as the HiPerDiF filament filled the inside of the nozzle and the inside of the PTFE tube that guides the filament into the nozzle as shown in Figure 5.8. This result was as expected as the manual extrusion tests in section 5.2.1 showed that any area constriction for the HiPerDiF filament lead to blockages. The custom PTFE 1.3 mm diameter nozzle was used for the 3D printing trials which had a straight 1.3 mm diameter channel throughout to avoid any extrusion failures such as nozzle clogging or filament buckling.

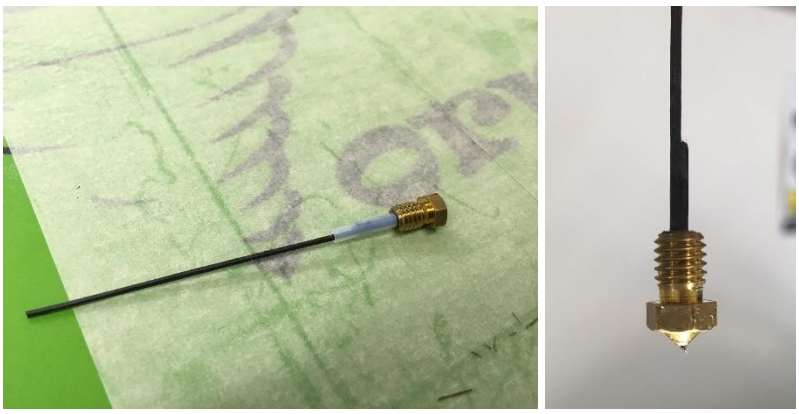

Figure 5.8: Filament jamming in initial 3D print trials with a standard 1.75 mm to 0.4 mm nozzle.

During deposition, the feed rate of the filament was matched to the speed of the extrusion head. A different feed rate than the printing speed would cause the filament to be compressed or stretched. Compression of the filament may lead to blockage similarly to what was seen with the 0.4 mm nozzle in the early print trial, while stretching of the filament can cause the filament to separate.

Three main printing parameters (temperature, speed, nozzle height) were varied to see their influence on deposition behaviour. The temperature was varied between 230 °C, 250 °C and 270 °C, the speed between 10 mm/s, 15 mm/s and 20 mm/s and the layer height between 0.5 mm, 0.65 mm and 0.8 mm. These were selected after some initial trial-and-error printing runs. The printing bed was left unheated as PLA does not require bed heating. To promote good adhesion, 3M #2090 blue masking tape was used as printing surface which is known to have good adhesion properties to PLA at room temperature.

The 3D printing path consisted of a 32 mm x 32 mm square which was printed from the outside to the inside of the printer as shown in Figure 5.9. This allowed for the investigation of both straight-line and 90° corner deposition. The path width is a variable that depends on the filament cross sectional area and the nozzle height, as this determines how much the filament is pushed down onto the printing bed. The average filament diameter was 1.25 mm (cross section area of 1.23 mm^2) and for a nozzle height of 0.5 mm, this gives a path width of 2.44 mm. A 10% overlap (negative gap size) was added to ensure the printed paths would be in contact with each other.

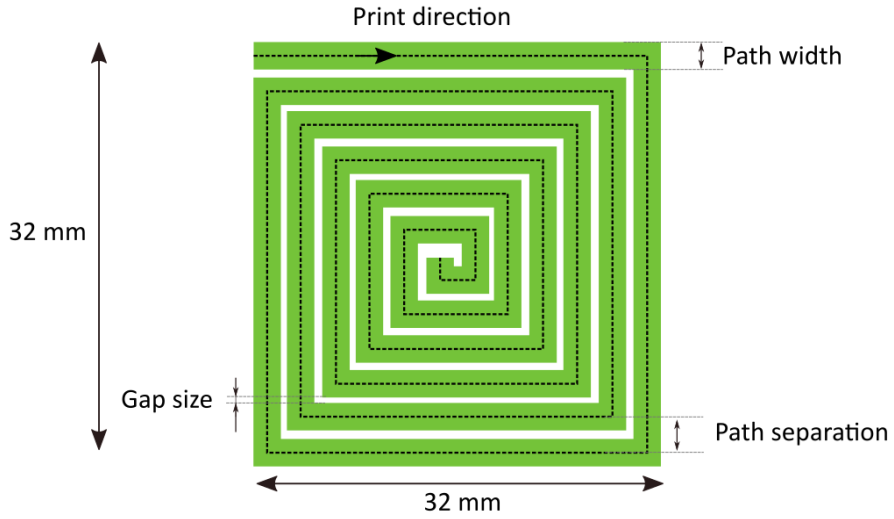

Figure 5.9: 3D printing path for HiPerDiF filament trials.

5.3 3D printing behaviour of HiPerDiF filament

The 3D printing behaviour of the HiPerDiF filament are detailed in this section. To the authors knowledge, this is the first report of 3D printing with reinforced filament containing discontinuous carbon fibres above a length of 1 mm. The HiPerDiF filament was prepared with a PLA matrix with an average fibre volume content of 12% and an average diameter of 1.25 mm.

5.3.1 Effect of nozzle temperature on deposition behaviour

Figure 5.10 shows the first study on different extrusion temperatures for the deposition behaviour of the HiPerDiF filament. These tests were performed at an extrusion speed of 10 mm/s and with a nozzle height of 0.5 mm. At 230 °C, some material was deposited onto the printing bed, but the extrusion failed and in general the quality of the print was low with localised fibre bundles. At 250 °C, the filament extrusion was better than 230 °C as more material extruded through the nozzle. The extruded material, however, did not adhere properly to the printing bed which caused some dragging of material as shown in Figure 5.10b. At 270°C, the filament extruded and adhered to the bed properly. The printed tracks can clearly be seen in Figure 5.10c with some width variation which was expected due to the intrinsic variability in the filament strands themselves. The 90° corners show that the material can be extruded through corners without major gaps forming, indicating the filament can change shape and some flow of the extruded HiPeDiF material is possible during deposition.

(a) 230 °C (b) 250 °C (c) 270 °C

Figure 5.10: 3D printed squares using HiPerDiF filament with different printing temperatures and a speed of 10 mm/s.

For all three printing temperatures, the material seems to contain dry, non-impregnated fibres which may be attributed to the quality of the filament itself and the presence of voids as was shown in section 5.2.1. Within the FFF, no external consolidation takes place and any voids present within the filament are expected to remain in the printed part.

5.3.2 Influence of printing speed

The influence of printing speed was investigated at 270 °C as it showed the best printing quality in the temperature sweep. The nozzle height was kept at 0.5 mm. Figure 5.11 shows the printed squares at three different speeds (10 mm/s, 15 mm/s and 20 mm/s). At 15 mm/s, the printing quality was less than at 10 mm/s. Some deposition at the outside regions (deposited

first) was done but fibre strands stick out of the printed tracks and at some point the extrusion failed. Similarly, at 20 mm/s some deposition occurred but printed tracks did not adhere to the bed properly and this resulted in a poorly printed square.

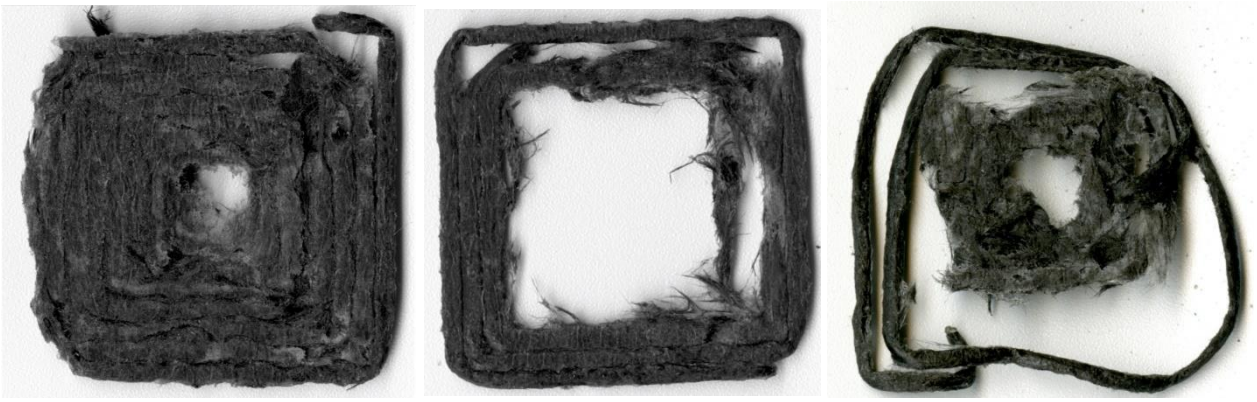

(a) 10 mm/s (b)15 mm/s (c) 20 mm/s

Figure 5.11: 3D printed squares using HiPerDiF filament with different printing speeds at 270 °C.

When printing at higher speeds, less heat is transferred from the nozzle into the filament which seems to both reduce bed adherence and make it harder to extrude the filament through the channel. The effect of faster printing speeds is similar to lowering the printing temperature which indicates this process is thermally driven.

5.3.3 Influence of printing height

Figure 5.12 shows three print trials performed at 270 °C and a printing speed of 13 mm/s at different layer heights. A printing speed of 13 mm/s was used as a potential improvement between 10 mm/s and 15 mm/s with a higher production rate. The layer height is an important parameter as it determines how much the filament is squeezed when being deposited. If the nozzle is too close to the bed, a blockage may occur during deposition while if the distance is too high it may result in poor adhesion to the bed. Three tests with different layer heights (0.5 mm, 0.65 mm and 0.8 mm) were performed as shown in Figure 5.12.

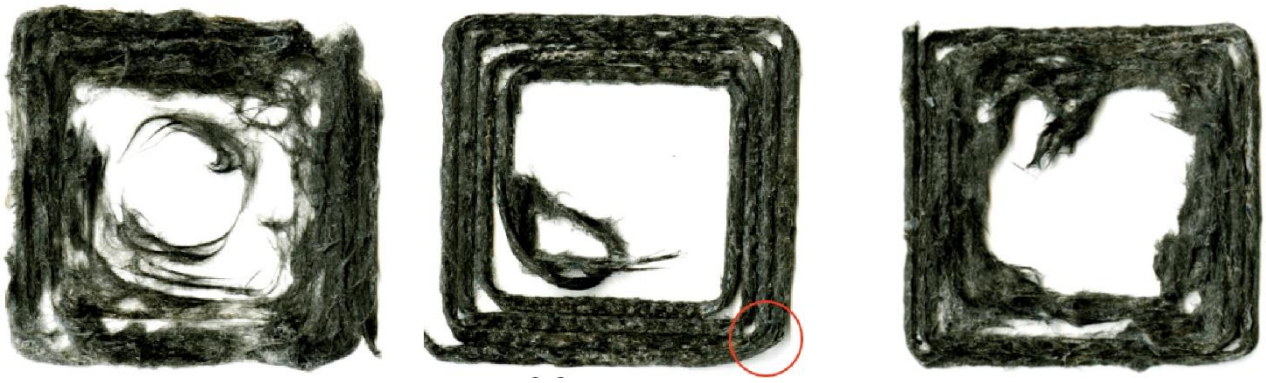

(a) 0.5mm (b) 0.65 mm (c) 0.8 mm

Figure 5.12: 3D printed squares using HiPerDiF filament with different printing speeds at 270 °C and 13 mm/s.

A layer height of 0.65 mm worked better than a layer height of 0.5 mm as the printed track shows less fibre strands deviating from the printed path in straight lines. In the corner regions, however, gaps are present which may be due to the filament being squeezed less. At a layer height of 0.8 mm, some fibre strands that stick out from the printed tracks are visible, and some area of a printed track are missing which may be due to poor adherence to the printing bed.

5.3.4 Thermal analysis of HiPerDiF filament extrusion

The exit temperature of the HiPerDiF filament was monitored with a thermal camera to provide more information on the temperature of the filament when extruded. These tests were done using a standard 1.3 mm brass nozzle, before deciding to perform the 3D printing trials with the PTFE nozzle as explained in section 5.2.2. A FLIR T650 thermal camera was used and the emissivity was set at 0.92 for the PLA matrix material. Several extrusions were performed at different temperatures (230 °C, 250 °C and 270 °C) and different extrusion speeds (6 mm/s, 14 mm/s, 22 mm/s and 30 mm/s). A cross section of a standard 1.3 mm nozzle with the 1.25 mm filament is shown in Figure 5.13 below. The nozzle has a height of 13 mm and an inlet diameter of 2 mm which results in an airgap between the nozzle and filament throughout most of the nozzle. The exit of the nozzle consists of a 1.3 mm diameter channel with a height of 1.68 mm where the filament is in closer contact to the nozzle.

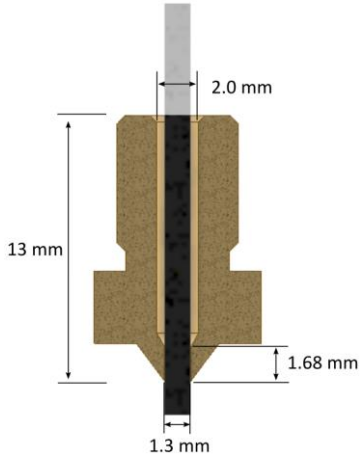

Figure 5.13: Cross section of a standard 1.3 mm nozzle with a 1.25 mm HiPerDiF filament.

Figure 5.14 shows the temperature of the filament during free extrusion at 22 m/s and 270 °C at five different time stamps. A variation in exit temperature over time can clearly be seen, and during extrusion some hot spots in the filament were present. The filament temperature was extracted from the IR data using a square box enclosing the filament (1 mm x 1 mm) just below the nozzle exit and using the minimal, mean and maximum temperature in the extraction box. The corresponding temperature vs. time profiles (minimal, mean and maximum) are shown in Figure 5.15 together with the time-averaged minimal, mean and maximum temperature. The time averaged temperatures are taken 2 seconds after the start of extrusion until 2 seconds before extrusion end. There is about a ±25 °C difference between the time-averaged mean exit temperature and minimal and maximum temperature. A significant variation of exit temperature over time is also present, which indicates that the filament is being heated unevenly during extrusion which can be due to the filament quality or the heat transfer mechanism into the filament.

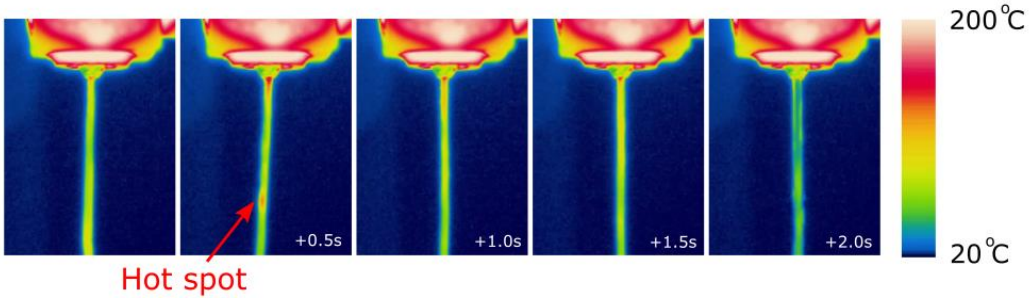

Figure 5.14: Thermal video stills from IR imaging during free extrusion of HiPerDiF filament at 22 mm/s and 270 °C.

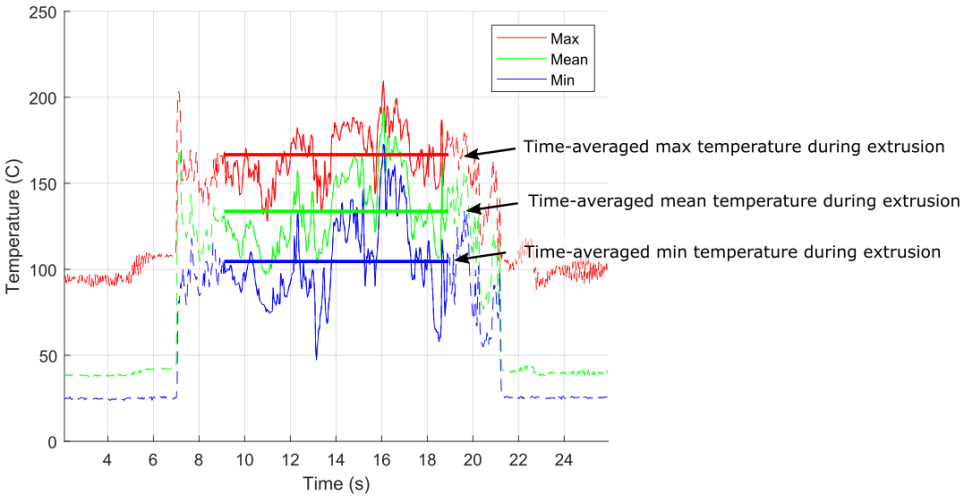

Figure 5.15: Temperature vs time during extrusion showing the max, mean and min value and the average during the extrusion.

A comparison between the observed and predicted exit temperatures for the different extrusion settings is made. For the observed temperature, the time-averaged mean temperature is used as it is statistically most relevant for the average exit temperature during extrusion. The temperature prediction for the filament extrusion was made using the 1-D numerical model presented in section 4.5. The same thermal properties were used as for the extrusion of ADFRC tapes through aluminium nozzles, which are shown again below in Table 5.2. The model was updated to include the circular cross-section of the filament as it affects the exposed area through which heat transfer occurs. The air temperature outside the nozzle was assumed to be 20 °C.

Table 5.2: Thermal properties used in thermal analysis of filament extrusion.

Thermal conductivity k [W/m/K]	2
Heat capacity c_p [J/kg/C]	1137
Density ϱ [kg/m^3]	1104
Heat transfer coefficient air h_{air} [W/m^2/K]	25
Heat transfer coefficient nozzle h_{nozzle} [W/m^2/K]	500

Three simulation cases were considered:

1. Heat transfer to filament taking place over entire length of nozzle (13 mm)
2. Heat transfer to filament taking place over a length of 1.68 mm where the filament passes through the 1.3 mm exit section
3. Heat transfer to filament taking place over a length of 1.68 mm with the nozzle exit, and assuming heat transfer with hot air at the set temperature residing in the upper part of the nozzle over a length of 11.32 mm

Figure 5.16 shows the experimental results and the predicted exit temperature from the three cases above. The error bars on the experimental results indicate the standard deviation of the time-averaged mean exit temperature. The predicted temperature for the first case is much higher than experimentally observed. As the ADFRC filament is similar as the ADFRC tape, no

significant change in the thermal conductivity, heat capacity or density is expected. This means the heat transfer is slower than expected, which can be attributed to a lower heat transfer coefficient with brass than aluminium, or less contact as the nozzle inlet is wider than the filament.

For the second simulation case, where heat transfer with the nozzle only occurs at the 1.3 mm diameter exit over a length of 1.68 mm, a much lower exit temperature is predicted than observed. This indicates that it is likely some heat transfer takes place above the nozzle exit. The third simulation case includes heat transfer via air in the nozzle inlet and direct heat transfer between the nozzle and the filament at nozzle exit. This gives the most accurate prediction to the experimental results, with a slightly lower temperature predicted than observed. During extrusion, it is unlikely the filament is completely straight and localised contact between the filament and nozzle inlet may occur in one or more places which would increase the filament temperature and can also explain the high variation in exit temperature.

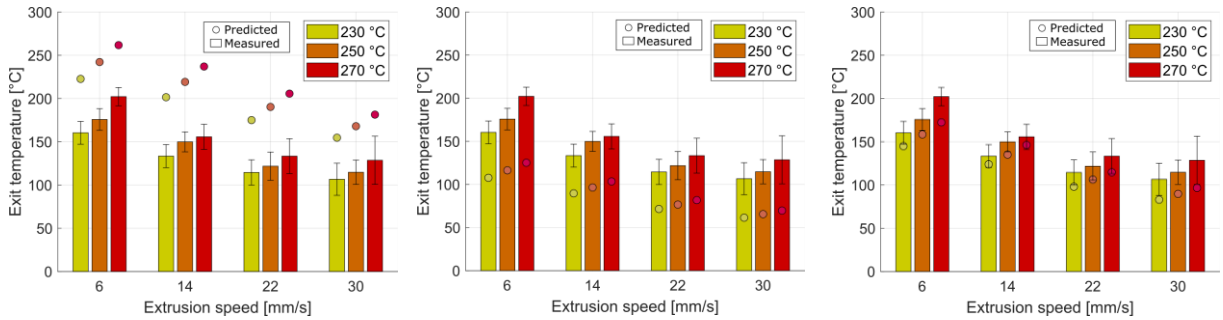

a) Case 1 **b)** Case 2 **c)** Case 3

Figure 5.16: Variation of HiPerDiF filament exit temperature observed with different extrusion speeds and temperatures and using three different nozzle lengths for the heat transfer assumption.

The experimental results show that the exit temperature is much lower than the set temperature of the nozzle. An increase in extrusion speed lowers the exit temperature as a clear drop in exit temperature can be seen from 6 mm/s to 14 mm/s for all nozzle temperatures. This effect, however, reduces at higher extrusion speeds as the exit temperatures for 22 mm/s and 30 mm/s are within 10 °C of each other. This is different than predicted by the simulations, where a larger decrease in exit temperature is expected with increasing extrusion speed. This may also be attributed to inconsistent heating of the filament during extrusion caused by the filament touching the side walls in the nozzle inlet, and this effect may be more prominent at higher extrusion speeds.

5.4 Discussion

This chapter set out to investigate the processing behaviour of a 3 mm carbon fibre reinforced thermoplastic filament (HiPerDiF filament) and demonstrate it may be used for fused filament fabrication (FFF). To the author's knowledge, this is the first report of FFF with filaments containing reinforcing carbon fibres longer than 1 mm. The filament preparation is first briefly discussed before comments are made on how the filament behaves in the 3D printing process and compares to commercially available filaments.

The HiPerDiF filament had a relatively high void content of 17% as cross-sectional analysis revealed. This was attributed to the entrapment of air during compression moulding of the AD-FRC tapes as this method did not allow air to escape. Another downside was the poor uniformity of the filament over its length, likely due to the compression moulding technique used and the difficulty to apply pressure evenly over the long, slender filament. A further development of the filament forming work in Chapter 4 is recommended to better control the filament dimensions and reduce the porosity.

Manual extrusions through different nozzles were performed to improve the quality of the as-moulded filament. These tests also showed what the smallest nozzle outlet diameter was that could be used to successfully extrude the HiPerDiF filament. Theoretically, it was expected that the ADFRC tape would form into a 1.12 mm diameter filament based on its cross-sectional area. The smallest nozzle diameter that the HiPerDiF filament could be extruded through was 1.3 mm and extrusion failed for a 1.2 mm nozzle diameter. The reason that the 1.2 mm diameter failed may be due to the entrapment of voids, which effectively increases the filament diameter. However, this result does indicate that a small area constriction causes difficulties for the HiPerDiF filament. Commercially available short fibre reinforced filaments can be extruded through nozzles with diameters around ~0.4 mm [76], [77]. The 3 mm carbon fibres in the filament have a much high aspect ratio AR (~400) than the 0.1 mm (AR~14) carbon fibres in commercially available filament. The longer fibres greatly increase the stiffness of the filament, as was shown in Chapter 3, but also limit how much movement of the fibres is possible within the matrix melt. Moreover, it is more likely to clog the nozzle as larger particles promote arch formation as shown by Beran et al. [198]. This is a fundamental difference with short fibre filament or unreinforced filaments where a melt pool is present within the nozzle during 3D printing. In that respect, the HiPerDiF filament behaves more as continuous fibre filament with limited capability for a cross-sectional area change through the nozzle.

The main 3D printing trials were done using a custom PTFE nozzle with a straight 1.3 mm diameter channel (no contraction) that did not impose any cross-sectional area change and prevented filament buckling by supporting the filament throughout. Compared to typical brass nozzles, the PTFE nozzle has a lower friction coefficient and is a softer material and this helps prevent blockages. This was found to be relevant for the filament forming of ADFRC tapes as well, as presented in Chapter 4. A downside is that PTFE also has a lower heat transfer coefficient which reduces heat transfer into the filament.

It was demonstrated that the HiPerDiF filament can be successfully deposited using FFF. The three parameters that were studied were printing temperature (230 °C, 250 °C, 270 °C), printing speed (10 mm/s, 15 mm/s, 20 mm/s) and layer height (0.5 mm, 0.65 mm, 0.8 mm). A high printing temperature (270 °C) and slow printing speed (10 mm/s) showed the best deposition behaviour. Typically, 3D printing with pure PLA filament is done with a temperature of 210 °C and a speed of ~40 mm/s. The difference is attributed to a slow heating rate of the reinforced filament using the PTFE nozzle, which therefore required higher temperatures and slower printing speeds.

During deposition, the 1.3 mm diameter HiPerDiF filament is squeezed between the nozzle and the print bed to a set layer height. This means the fibre-matrix melt must change from a circular cross section to a new shape as it is pressed down. It was discussed above that the 3 mm carbon fibres have limited movement freedom within the matrix melt as cross-sectional area changes were not possible. However, reshaping of the filament, was possible as the filament strands were successfully deposited. The matrix viscosity is expected to play an important role in how well the fibre/polymer melt can reshape and this may require higher than usual printing temperatures which further explains the relatively high printing temperature and slow printing speed.

A layer height of 0.65 mm was found to give the best printing quality. When printing at a layer height of 0.5 mm, the deposited material showed dense parts and less dense parts which indicate an uneven flow of material. As the filament cannot easily reshape, it can cause a pressure build-up in the nozzle affecting the rate at which the filament exits. At a layer height of 0.8 mm, the deposited material adhered less well to the printing bed and some corner pulling was present. As the HiPerDiF filament has a high stiffness, bed adherence is important to prevent the deposited material from moving. A heated bed may increase bed adherence and also help improve reshaping of the filament when extruded.

A comparison between the printed structure of a short fibre (0.1 mm) reinforced filament, HiPerDiF filament and continuous fibre filament is shown in Figure 5.17. The HiPerDiF filament shows dry spots which may be attributed to the low quality of the HiPerDiF filament. In the corner regions, compared to the continuous fibre filament, no clear voids can be seen in the HiPerDiF filament. This means the HiPerDiF filament allows better flow in the path width direction than the continuous fibre filament. Some smaller gaps between printed tracks can be seen in the HiPerDiF filament which are typical for 3D printed structures. The short fibre filament has the highest quality with inter-track voids only visible using microscopy.

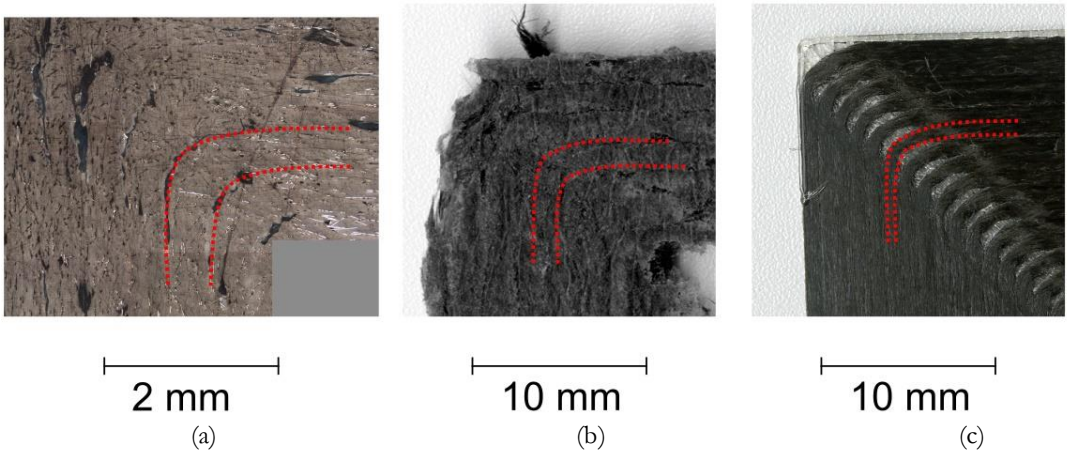

Figure 5.17: Comparison corner regions of 3D printed squares for (a) short fibre filament (b) HiPerDiF filament and (c) continuous fibre filament.

Overall, the observed quality of the 3D printed part with HiPerDiF filament was low which was attributed to several reasons. The filament itself had a low geometric tolerance with an inconsistent diameter. When printed, this causes a variable print track width and intermittent quality of bonding of the material to itself. The HiPerDiF filament had a high void content which arose from the compression moulding technique used, as voids were entrapped within the filament as confirmed by microscopy.

Lastly, flow and reshaping of the fibre-matrix melt was expected to be harder due to the high aspect ratio of the fibres. To avoid extrusion failures, unnecessary flow constrictions should be avoided. A straight PTFE nozzle was used but the nozzle exit had a 90° corner as shown in Figure 5.18a which creates a relatively sharp edge that the filament must pass. This may cause damage to or rotation of the fibres as they move pass the corner. An improved design could be made that takes into account the fibre bend radius by adding a fillet on the nozzle exit as shown in Figure 5.18b.

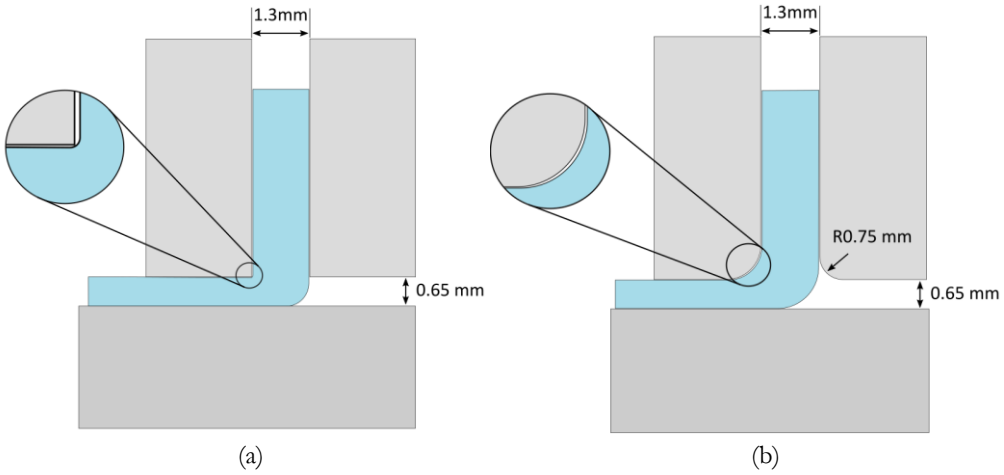

Figure 5.18: Comparison of (a) 90° nozzle exit and (b) fillet edge nozzle exit to improve filament deposition.

In general, this work has shown that the HiPerDiF filament can be extruded and used in FFF. The process is more sensitive to the nozzle configuration, temperature, print speed and layer height than pure thermoplastic filament and short fibre reinforced filament. This is as expected as the 3 mm carbon fibres have a much higher aspect ratio and are more limited in movement within the matrix when extruded. The material can be deposited into a square shape and visually a smaller gap size between printed tracks than continuous fibre filament 3D printing was seen. The basic viability of the concept has been shown, and key areas of improvement for future work have been highlighted.

5.5 Conclusions

A HiPerDiF filament with a diameter of 1.25 mm was prepared using 3 mm length carbon fibres in a PLA matrix and it was shown this filament can be used for FFF. This is the first demonstration using carbon fibres above a length of 1 mm within the FFF process, and it showed the basic viability of the concept. The processing window was determined in terms of printing temperature, speed and layer height. A custom 1.3 mm diameter PTFE nozzle was used, and the extrusion speed was set to match the printing speed to avoid compressing or stretching the filament during deposition. Higher printing temperatures (above 250 °C) than standard PLA 3D printing were required, which may be due to a lower heat transfer coefficient of the PTFE nozzle. Similarly, slower printing speeds had to be used as higher printing speed were expected to reduce the exit temperature of the filament. Square shapes were printed and the HiPerDiF filament showed good behaviour in 90° corners, avoiding gaps between the printed tracks commonly seen with continuous fibre filament.

Manual extrusion tests showed that the HiPerDiF filament could not be extruded through nozzles smaller than the filament diameter as this led to nozzle blockages. The FFF process is

therefore similar to continuous fibre filament with no cross-sectional area change imposed onto the filament. A 3D printing setup which works within these constraints is likely to be successful, as there is no intrinsic need to have a significant area change in the filament during printing. This could be achieved in many conventional FFF printers with simple changes to the nozzles and drive system, with some further consideration given to the likely larger spooled diameter of the filament.

Further work is needed to improve the quality of the filament itself as a simple compression moulding technique was used and variations in filament diameter caused a variation in print width. The deposition process itself can be improved by designing a custom nozzle that prevents jamming and improves deposition. Further refinement of printing bed temperature may also improve quality.

Chapter 6

Conclusions and future work

The aim of this thesis was *to develop a novel discontinuous carbon fibre reinforced filament using the HiPerDiF aligned fibre preforms* and investigate its 3D printing capability. The research problem was broken down into a series of stages, and a clear research path was followed as shown in Figure 6.1. Work progressed from the HiPerDiF fibre alignment method, to consolidation of ADFRC tapes, followed by reshaping of the tape into a 3D printing filament and finally 3D printing of the HiPerDiF filament. The significant progress made in all of these steps is highlighted here, and conclusions are drawn before recommendations for future work are presented.

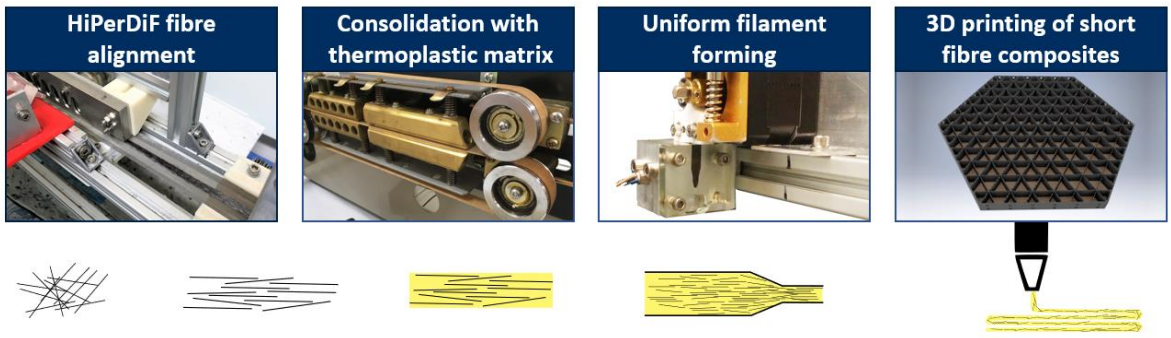

Figure 6.1: The three main parts of this thesis are the (I) design and build of filament maker, (II) numerical analysis of fibre flow and (III) material characterization.

6.1 Review of Aims and Objectives

The aim of this thesis was to create an improved fibre reinforced 3D printing feedstock using HiPerDiF aligned fibre preforms. Since the start of this work, fibre reinforced 3D printing has received considerable research interest, however, no reports have been made on a 3D printing filament with discontinuous carbon fibres above their critical fibre length to obtain their full strength yet. Here, a novel manufacturing method for the improved fibre reinforced 3D printing

method has been presented, together with the first deposition of a 3 mm carbon fibre reinforced filament using the fused filament fabrication (FFF) process.

Four objectives were identified to address the main challenges for creating an improved 3D printing feedstock:

1. Determine the current limitations of fibre reinforced 3D printing and identify important processing parameters
2. Identify suitable matrix systems to create thermoplastic carbon fibre composite preforms
3. Design a continuous manufacturing method for HiPerDiF filament
4. Investigate the 3D printing performance of the improved HiPerDiF filament

These objectives map directly to the core technical chapters of this dissertation, and the overall conclusions are drawn below together with recommendation for future work to lead to a further improvement of fibre reinforced 3D printing feedstocks.

6.2 Conclusions

6.2.1 Current state-of-the-art on composite 3D printing and existing limitations

For fibre composite materials, a trade-off between performance and processing exists with respect to fibre architecture. Aligned discontinuous fibre reinforced composites (ADFRC) are hypothesized to give an optimal trade-off between processing and performance, assuming sufficient fibre length for the fibre to reach their full strength. This work focused around the use of ADFRCs for additive manufacturing using the fused filament fabrication (FFF) process. A gap was identified in the fibre lengths of currently available fibre reinforced feedstocks for FFF, which coincides with the trade-off between performance and processing. Short fibre (up to 0.1 mm) reinforced filaments are available for standard desktop 3D printers and more recently continuous fibre reinforced filament printing techniques have been developed.

This thesis presented the first direct comparison between these two families of fibre reinforced filaments, focussing on their relative processability and mechanical performance. The processing of short fibre reinforced filaments was found to be simpler than continuous fibre reinforced filament as no modifications to a standard desktop 3D printer are needed. When extruded, short fibre filament flows similar to an unreinforced filament, filling corner regions and reducing inter-track voids as polymer sintering takes place (estimated void content of 3.5%). For continu-

ous fibre filaments, a cutter mechanism must be added to the 3D printing set-up to deposit continuous fibre filament in non-connecting regions. The continuous fibres are inextensible along their length and this created voids between printed tracks in corner regions (estimated void content of ~10%).

The mechanical performance of 3D printed parts of continuous fibre PA filament and short fibre PA filament was investigated using tensile, flexural and shear testing. The tensile modulus and strength of the continuous fibre 3D printed part were an order of magnitude higher than the short fibre filament. For the short fibre filament, the flexural modulus and strength showed a relative increase with respect to its tensile properties. The flexural modulus and strength of the continuous fibre part were lower than the tensile properties. This relative decrease with respect to its tensile properties confirms that the continuous fibre 3D printed part has a low quality, as also visually observed, because flexural properties typically are higher for high quality composites. The shear modulus and strength for 3D printed coupons with continuous fibre PA filament were determined, being 1.7 GPa and 23.4 MPa (normalised to 15% V_f). For the short fibre filament, the shear modulus and strength were 0.8 GPa and 47.5 MPa, respectively.

Short fibre filaments have better processing properties than continuous fibre filament, but with much lower tensile and flexural stiffness and strength than the continuous filament. This was attributed to the length of the fibres (0.1 mm) as they are too short to reach their full strength and provide little reinforcing effect. The continuous fibre part had a relatively low shear performance and can form a weak spot in the material, preventing useful applications. The short fibre filament parts had a relatively high shear strength and an increase in fibre length is hypothesised to improve mechanical properties whilst keeping the benefits of simpler processing.

6.2.2 Suitable materials systems for improved fibre reinforced 3D printing feedstocks

An analysis on the 3D printing process revealed important processing properties of the matrix material (including viscosity, shrinkage, coefficient thermal expansion, heat conductivity). A trade-off was performed based on the important processing properties to select the most suitable thermoplastic matrices for the novel filament development. As low costs and low processing temperatures were prioritised for this development work, the most suitable polymers were found to be ABS, PETG and PLA. Other suitable polymers included PBT and PSU, but they were not used due to their higher processing temperatures and higher shrinkage.

For the filament development, four candidate polymers were selected: ABS, PETG, PLA and PA. PA was added to provide a direct comparison with the PA continuous fibre and PA

short fibre filaments. Rheological testing was performed to compare the viscosity of the candidate polymers. PLA and PETG have a similar range in viscosity over their processing temperatures, ranging from 1000 Pa·s to ~30 Pa·s. ABS and PA had a higher viscosity ranging between 10000 Pa·s to 500 Pa·s. All polymers were stable up to an elevated temperature of 300 °C except for PA, which showed a mass reduction starting from 120°C, with a weight loss of 7% at 300 °C.

A new manufacturing method for thermoplastic ADFRCs tapes using the HiPerDiF aligned carbon fibre preforms was made consisting of a double belt press to consolidate the dry fibre preform between two polymer matrix films. Thermoplastic ADFRC tapes (100 mm x 5 mm x 0.2 mm) using 3 mm high strength carbon fibres and a V_f of 12% were prepared with the four candidate polymers. Mechanical characterisation of the ADFRCs showed that HiPerDiF PLA ADFRC had the highest performance with a modulus of 28 GPa and strength of 351 MPa. PA ADFRCs had the lowest modulus and strength (15 GPa/212 MPa) which was attributed to the low thermal stability of the matrix. The modulus and strength of PETG (27 GPa/310 MPa) was slightly higher than ABS (21 GPa/ 295 MPa).

The mechanical properties of the HiPerDiF ADFRCs were compared, after normalisation by ratio to 15% V_f, to the continuous and short fibre filament counterparts. Their modulus is similar to continuous fibre filaments (29 GPa) but continuous fibre filament has a higher strength 450 MPa. Compared to short reinforced fibre filament, the modulus and strength of the HiPerDiF ADFRCs is an order of magnitude higher.

6.2.3 Novel filament manufacturing method to maintain fibre length

To utilise the high mechanical properties of the ADFRCs tapes for FFF, a continuous manufacturing method was devised to reshape the tape into a circular filament without fibre breakage. A direct extrusion method was chosen over direct moulding or tape-twisting methods as a simpler and better to control process. The ADFRC tape was fed into a heated nozzle by two pinch rollers. Premature buckling was prevented by supporting the ADFRC tapes between two PTFE guides up to the nozzle inlet. The nozzle was made from aluminium by machining a custom channel into one face and closing it with a glass plate.

The channel inlet had a rectangular cross section of 5 mm x 0.3 mm and a length of 10 mm, leading into a 15° contraction and a 3 mm long outlet region with a 3 mm x 0.3 mm cross section. The flow behaviour was visually observed through the glass plate and the effects of coating, temperature, extrusion speed and polymer matrix type were studied. The flow of the

ADFRC melts is complicated as fibre instabilities or jamming can occur, halting extrusion. Extrusion failures were typically due to micro-buckling of the ADFRC tape in the inlet region which was attributed to too high of a backpressure for extrusion and premature heating of the ADFRC tape. Coatings had a large effect on extrusion performance of the ADFRCs, which indicated surface friction plays an important role for the extrusion of ADFRCs. Extrusion improved when a silicone mould release was used, with up to 10 mm of the tape extruding through the entire nozzle before the flow halted. Semi-crystalline polymer ADFRCs extruded better than amorphous ADFRCs, and this was attributed to the sudden drop in viscosity semi-crystalline polymers exhibit when heated which prevents premature softening before reshaping in the constriction area.

A thermal and rheological analysis was performed to predict the temperature and viscosity profiles during extrusion. For PLA ADFRCs at 170 °C and 190 °C, extrusion failed and the average matrix viscosity in the constriction was 1924 and 893 Pa·s respectively. At 210 °C, extrusion improved with an average predicted matrix viscosity in the constriction of 600 Pa·s. Extrusion improved further when the extrusion speed was doubled whilst keeping the temperature at 210 °C, for which the average matrix viscosity in the constriction was 1000 Pa·s. The difference with the lower speed 190 °C extrusion was that in the inlet region the ADFRC tape had a relatively lower temperature and higher viscosity which confirms premature softening in the nozzle can prevent extrusion.

An improved extrusion set-up was made from the two main conclusions of these extrusion tests; the importance of surface friction and premature heating. PTFE nozzles were made with shorter inlet lengths and different constriction angles to improve the extrusion. These nozzles led to continuous extrusion of the 5 mm wide ADFRC tape through the 2.5 mm wide exit sections. The exit temperature was observed which indicated a much lower heat transfer coefficient (70 $W/m^2/K$) than the original aluminium nozzles (500 $W/m^2/K$). With continuous extrusion obtained, a viscosity profile prediction was made again. The study with PTFE channels indicates that extrusion is successful for a viscosity range in the constriction area of roughly 1000 – 6000 Pa·s. When the viscosity is lower than 300 Pa·s, the extrusion halted. This work motivates a multi-stage filament forming method guided by the required viscosities to fabricate filament strand in a continuous way.

6.2.4 3D printing behaviour of HiPerDiF filament

An alternative compression moulding technique was used to fabricate 60 cm HiPerDiF filament strands with a cross section of 1.2 x 1.2 mm and perform the first extrusion and deposition studies with filaments reinforced with 3 mm carbon fibres. The extrusion studies showed that the HiPerDiF filament cannot be extruded through nozzles that require a cross-sectional area reduction of the filament. This is a processing difference to conventional unreinforced 1.75 mm filaments and short fibre reinforced filaments which typically can be extruded through nozzles with a 0.4 mm diameter exit (~20× area reduction). The carbon fibres in the HiPerDiF filament have a high aspect ratio of ~400 and little movement between the fibres is possible. In that regard, the HiPerDiF filament behaves more as a continuous fibre filament which are typically printed through straight nozzles.

A custom straight channel 1.3 mm diameter PTFE nozzle was fabricated for the 3D printing studies and the first deposition of a filament reinforced with longer (3 mm) discontinuous carbon fibres was demonstrated. For the 1.25 mm diameter filament, the optimal layer height was 0.6 mm and relatively slow extrusion speed (10 mm/s) and high print temperature (270 °C) gave the best printing quality. The slower printing speed and higher printing temperature were attributed to a slow heating rate of the filament caused by the PTFE nozzle and variations in filament diameter causing inconsistent heating. Compared to short fibre filament 3D printed parts, larger inter-track voids were observed but improvement in corner regions with respect to continuous fibre filaments were demonstrated.

This work has filled the gap between short fibre reinforced filaments and continuous fibre reinforced filaments by creating an ADFRC filament from the HiPerDiF process reinforced with 3 mm carbon fibres. It showed for the first time that HiPerDiF filament can provide an order of magnitude increase in performance over short fibre filament and can be deposited using similar techniques. The FFF processing is simpler than with continuous fibre filaments with an increase in deposition quality. It has been shown that the HiPerDiF filament has the potential to be a disruptive new technology in the additive manufactured composites industry, with applications to reusable tooling fabrication and rapid prototyping of structural composite parts.

Now, further work can commence to improve the quality of the filament itself, fabricate longer filament strands and perform more extensive material characterisation.

6.3 Future work

A pathway to an improved fibre reinforced 3D printing filament has been shown in this thesis using discontinuous carbon fibres with a length of 3 mm. A manufacturing method was developed preventing fibre breakage and it was demonstrated such a filament can offer better performance compared to short fibre filaments and better processing than continuous fibre filaments. Further work is now required to solidify the findings of this thesis and improve the filament manufacturing method, the filament quality and the deposition of the filament.

6.3.1 Custom 3D printing techniques for fibre reinforced filaments

The state-of-the-art review clearly identified a gap between short fibre filaments and continuous fibre filaments. A more detailed study on printing parameters for the different printing methods can be performed to better understand the synergy between printing temperature, printing speed and nozzle configuration. The printing analysis presented in this thesis focused mainly on the relevant material parameters for a 3D printing filament to aid the material selection, while later in the thesis it was shown that the nozzle configuration and printing parameters played an important role in how well the filament could be deposited. Moreover, the HiPerDiF filament behaved more as a continuous fibre filament and these filaments cannot cope with an area change through the nozzle. The deposition process may be improved by looking at nozzle configurations of existing continuous fibre deposition processes in more detail.

6.3.2 Alternative material systems for fibre reinforced filaments

Based on the relevant material parameters for 3D printing, a material selection was performed. This selection was done mainly around the processing temperature, the moulding pressure as equivalent to polymer viscosity, and the cost of the material. Without cost and processing temperature constraints, other polymers may be identified as suitable matrices using the same methodology presented here. Different polymers may improve the mechanical properties in the 3D printed part and the selection can be extended to include novel polymers such as vitrimers.

As reinforcement, 3 mm Toho Tenax C124 high strength carbon fibres were used for all specimens in this thesis. These fibres worked well with the HiPerDiF fibre alignment process, but different fibre length may be used to investigate how it affects the manufacture and deposition behaviour of the filament and the resulting mechanical performance. During filament forming, a micro-buckling type failure was seen which may be related to the fibre length and type and stiffer, high modulus fibres may avoid such failures. Another approach would be to hybridise the

reinforcements by using different fibres types and lengths, tailoring the mechanical properties of the filament.

Further improvements in mechanical performance may be possible by optimising the sizing of the carbon fibre. A micromechanical test campaign (i.e. fibre pull out tests or micro-droplet shear tests) is advised to provide more information on suitable polymer and fibre type/sizing fibre types. This is especially important for discontinuous fibre composite to obtain a good fibre-matrix adhesion and improve mechanical performance.

6.3.3 Improvement of the filament forming technique

Regarding the filament manufacturing method, it was opted to use pre-consolidated 5 mm wide HiPerDiF ADFRC tapes as precursor to the filament. The advantage of this process is that it allows to control the starting quality and fibre content separately, but also resulted in an extra handling step of the dry fibre preforms where fibre misalignment may occur. The fibres were consolidated with thermoplastic films in a double belt hot press and this process gave little control over fibre content. Moreover, the double belt hot press can cause fibre misalignment as the resin can flow perpendicular to the main axis along which the fibres are aligned. Both ellipse fitting using micrographs and CT scanning of the ADFRC tapes showed a lower level of fibre alignment than originally measured with the HiPerDiF process. Alternative consolidation methods could be investigated to improve the ADFRC tape quality, such as:

1. **Co-mingled fibres:** co-mingled polymer fibres and carbon fibre preforms can reduce the impregnation distance and minimise polymer flow to obtain consolidated tape.
2. **Compression roller:** A compression roller provides a more constant pressure on the fibre bed and depending of roller material or rubber hardness the side-flow of the polymer melt can be reduced.
3. **HiPerDiF in-line consolidation module**: This would allow the dry fibre preform to be directly consolidated without handling of the dry fibre preforms to a different stage.

Another manufacturing improvement could be using narrower tapes. ADFRC tapes with a width of 5 mm (standard width for HiPerDiF tapes) and thickness of 0.2 mm were prepared, and this resulted in a 1.25 mm diameter filament. The 1.25 mm diameter filament with a fibre content of 12.5% already showed a too high bending radius to be spooled for practical 3D printing application. A narrower tape (i.e. 2.5 mm x 0.2 mm) has a lower aspect ratio which makes it more

stable for the direct extrusion filament forming process and results in a thinner filament which can improve spooling capability.

For the filament forming process, a suitable processing window has been identified in terms of matrix viscosity. The early unsuccessful extrusions showed that extrusion typically failed with a micro-buckling type failure in the inlet channel. The micro-buckling type failure was attributed to too high driving pressures for extrusion through the forming channel. It was found the matrix viscosity in the inlet also plays a role as a higher matrix viscosity in the inlet region resulted in improved extrusion. A better understanding of this failure mode will help improve the filament forming process for which the following properties have been identified as relevant:

- **Matrix viscosity:** The matrix viscosity plays two roles; 1) a higher viscosity in the inlet region can prevent micro-buckling type failure as it provides a better support of the fibres and 2) a lower viscosity reduces pressure drop over the channel during extrusion
- **Pressure drop:** During filament forming, the ADFRC tape experiences a compressive force as a pressure drop is present over the channel. This is dependent on the channel geometry, extrusion speed and matrix viscosity. It was found surface friction plays an important role and can affect this pressure drop.
- **Surface friction:** Different nozzle coatings gave different extrusion results and the effect of surface friction must be considered as important parameter for filament forming
- **Fibre reinforcement:** As the failure mode looks like a buckling type failure, the fibre stiffness is expected to play an important role.

Different analyses can be developed with varying fidelity to investigate the micro-buckling type failure mode observed. A simple model may be based on a single fibre buckling on an elastic foundation to represent different matrix viscosities. However, micro-buckling was observed over the entire width of the tape and thus a better analysis can include the effective stiffness of a thermoplastic ADFRC tape at different temperatures.

During extrusion, the ADFRC tape starts as a solid tape, where the elastic forces are dominant, and changes to a melt state during extrusion where the viscous forces play an important role. More advanced models should include both the elastic and viscous effects, either representing the ADFRC as a homogeneous material or considering the fibres and polymer phase separately. Ultimately, such a model will help better understand how the fibres flow in the polymer

melt and what extrusion conditions are successful for both forming of the filament and 3D printing of the filament. Experimentally, the pressure drop may be estimated by incorporating a load cell onto the tape feeder and measuring the force needed for extrusion.

A more detailed rheological characterisation of ADFRC melts is recommended, as only the matrix viscosity was used in this thesis. The fibres increase the effective viscosity of the ADFRC and can give different shear and extensional viscosities. Better understanding of the intrinsic flow properties of ADFRC can aid the design of the reshaping nozzles and improve filament quality. An addition to this could be to study the surface friction between different moulds material treated with different release agents and the ADFRC tapes as that was found to have a significant effect on how the ADFRC extruded.

6.3.4 Processing and performance characterisation of HiPerDiF filament.

Finally, only small 3D print trials with the HiPerDiF material were done as short 60 cm filament strands were moulded and the filament had limited spooling capability. A more extensive material characterisation on both filament strands and on as 3D printed parts is recommended. This will allow a better comparison between the tensile, shear and flexural properties of the short fibre and continuous fibre filaments and as-printed parts. Finally, compression testing should be performed to get a better idea how 3D printed parts would behave in real applications. Of particular interest is how the microstructure of printed parts with structured voids influenced the different mechanical properties (i.e. flexural, tensile and compression).

In addition to this, a larger study is proposed wherein the effect of different fibre reinforcements, printing temperatures and printing strategies are investigated in order to reduce the void content and obtain higher quality parts.

With near continuous fibre performance but a discontinuous fibre architecture, this filament lends itself for recycling of high-performance fibres and can enable cheaper manufacture of composite parts for rapid prototyping or tooling. A recycling study based around the filament manufacture and 3D printing is proposed including a Life Cycle Analysis to see if such a closed-loop approach is sustainably interesting and economically viable.

References

[1] P. K. Mallick, *Fiber-Reinforced Composites: Materials, Manufacturing, and Design, Second Edition*. Taylor & Francis, 1993.

[2] A. Mouritz, *Introduction to Aerospace Materials*, First edit. Cambridge, England: Woodhead Publishing Ltd, 2012.

[3] Markforged, "High Strength 3D Printing With Continuous Fibres," 2016. [Online]. Available: https://markforged.com/. [Accessed: 01-Nov-2016].

[4] Arevo Labs, "Direct digital additive manufacturing of ultra-strong, lightweight composite parts," 2019. [Online]. Available: https://arevo.com/. [Accessed: 20-Sep-2019].

[5] A. Adumitroaie, F. Antonov, A. Khaziev, A. Azarov, M. Golubev, and V. V. Vasiliev, "Novel continuous fiber bi-matrix composite 3-D printing technology," *Materials (Basel).*, vol. 12, no. 18, pp. 1–10, 2019.

[6] Windform, "WINDFORM XT 2.0," *2015*, 2015. [Online]. Available: http://www.windform.com/windform-xt-2-0.html. [Accessed: 25-Nov-2016].

[7] V. Kunc *et al.*, "Investigation of in-autoclave additive manufacturing composite tooling," in *CAMX 2016 - Composites and Advanced Materials Expo*, 2016.

[8] G. Gardiner, "Additive manufacturing: Can you print a car?," *CompositesWorld*, 2015. [Online]. Available: https://www.compositesworld.com/articles/additive-manufacturing-can-you-print-a-car-. [Accessed: 01-Jun-2020].

[9] L. Nickels, "Carbon fiber 3D printing propels bike development," *Reinf. Plast.*, vol. 63, no. 2, pp. 93–96, 2019.

[10] L. Blok, B. Woods, H. Yu, M. Longana, and K. Potter, "3D PRINTED COMPOSITES – BENCHMARKING THE STATE-OF-THE-ART'," in *21st International Conference on Composite Materials*, 2017, pp. 1–9.

[11] H. Yu, K. D. Potter, and M. R. Wisnom, "A novel manufacturing method for aligned discontinuous fibre composites (High Performance-Discontinuous Fibre method)," *Compos. Part A Appl. Sci. Manuf.*, vol. 65, pp. 175–185, 2014.

[12] M. Such, C. Ward, and K. Potter, "Aligned Discontinuous Fibre Composites: A Short History," *J. Multifunct. Compos.*, vol. 2, no. 3, pp. 155–168, 2014.

[13] K. D. Potter, "Understanding the origins of defects and variability in composites manufacture," *ICCM Int. Conf. Compos. Mater.*, 2009.

[14] L. G. Blok, M. L. Longana, H. Yu., and B. K. S. Woods., "An investigation into 3D printing of fibre reinforced thermoplastic composites," *Addit. Manuf.*, vol. 22, pp. 176–186, 2018.

[15] R. A. Pethrick, *Polymer Science and Technology for Engineers and Scientists*. Wiley, 2010.

[16] R. J. Tapper, M. L. Longana, H. Yu, I. Hamerton, and K. D. Potter, "Development of a closed-loop recycling process for discontinuous carbon fibre polypropylene composites," *Compos. Part B*, vol. 146, no. March, pp. 222–231, 2018.

[17] R. J. Tapper, M. L. Longana, A. Norton, K. D. Potter, and I. Hamerton, "An evaluation of life cycle assessment and its application to the closed-loop recycling of carbon fibre reinforced polymers," *Compos. Part B Eng.*, vol. 184, p. 107665, 2020.

[18] L. Dong, C. Lekakou, and M. G. Bader, "Processing of composites: simulations of the draping of fabrics with updated material behaviour law," *J. Compos. Mater.*, vol. 35, no. 2, pp. 138–163, 2001.

[19] N. Hamila and P. Boisse, "Simulations of textile composite reinforcement draping using a new semi-discrete three node finite element," *Compos. Part B Eng.*, vol. 39, no. 6, pp. 999–1010, 2008.

[20] F. C. Campbell, *Manufacturing Processes for Advanced Composites*. Oxford: Elsevier, 2004.

[21] M. Connor, "Consolidation Mechanisms and Interfacial Phenomena in Thermoplastic Powder Impregnated Composites," EPF Lausanne, Lausanne, 1995.

[22] T. Köhler, T. Röding, T. Gries, and G. Seide, "An Overview of Impregnation Methods for Carbon Fibre Reinforced Thermoplastics," *Key Eng. Mater.*, vol. 742, pp. 473–481, 2017.

[23] A. Miller and A. G. Gibson, "Impregnation techniques for thermoplastic matrix composites," *Polym. Polym. Compos.*, vol. 4, no. 7, pp. 459–481, 1996.

[24] M. Sharma, S. Gao, E. Mäder, H. Sharma, L. Y. Wei, and J. Bijwe, "Carbon fiber surfaces and composite interphases," *Compos. Sci. Technol.*, vol. 102, pp. 35–50, 2014.

[25] I. Giraud, S. Franceschi-Messant, E. Perez, C. Lacabanne, and E. Dantras, "Preparation of aqueous dispersion of thermoplastic sizing agent for carbon fiber by emulsion/solvent evaporation," *Appl. Surf. Sci.*, vol. 266, pp. 94–99, 2013.

[26] Y. Huang and R. J. Young, "Interfacial micromechanics in thermoplastic and thermosetting matrix carbon fibre composites," *Compos. Part A Appl. Sci. Manuf.*, vol. 27, no. 10, pp. 973–980, 1996.

[27] D. T. Burn, "Long Discontinuous Carbon Fibre / Polypropylene Composites for High Volume Automotive Applications," University of Nottingham, 2016.

[28] L. G. Tang and J. L. Karoos, "A review of methods for improving the interfacial adhesion between carbon fiber and polymer matrix," *Polym. Compos.*, vol. 18, no. 1, pp. 100–113, 1997.

[29] S. S. Yao, F. L. Jin, K. Y. Rhee, D. Hui, and S. J. Park, "Recent advances in carbon-fiber-reinforced thermoplastic composites: A review," *Compos. Part B Eng.*, vol. 142, no. December 2017, pp. 241–250, 2018.

[30] H. L. Cox, "The elasticity and strength of paper and other fibrous materials," *Br. J. Appl. Phys.*, vol. 3, no. 72, pp. 72–79, 1952.

[31] T. Lacroix, B. Tilmans, R. Keunings, M. Desaeger, and I. Verpoest, "Modelling of critical fibre length and interfacial debonding in the fragmentation testing of polymer composites," *Compos. Sci. Technol.*, vol. 43, no. 4, pp. 379–387, 1992.

[32] M. R. Piggott, M. Ko, and H. Y. Chuang, "Aligned short-fibre reinforced thermosets: Experiments and analysis lend little support for established theory," *Compos. Sci. Technol.*, vol. 48, no. 1–4, pp. 291–299, 1993.

[33] P. D. Shipton, "The Compounding Of Short Fibre Reinforced Thermoplastic Composites," Brunel University, 1988.

[34] M. J. Folkes and W. K. Wong, "Determination of interfacial shear strength in fibre-reinforced thermoplastic composites," *Polymer (Guildf).*, vol. 28, no. 8, pp. 1309–1314, 1987.

[35] U. Gaur, G. Desio, and B. Miller, "Measuring fiber/matrix adhesion in thermoplastic composites," *Plast. Eng.*, vol. 45, no. 10, pp. 43–45, 1989.

[36] S. Y. Fu, B. Lauke, E. Mäder, C. Y. Yue, and X. Hu, "Tensile properties of short-glass-fiber- and short-carbon-fiber-reinforced polypropylene composites," *Compos. Part A Appl. Sci. Manuf.*, vol. 31, no. 10, pp. 1117–1125, 2000.

[37] Anisoprint, "Anisoprint." [Online]. Available: http://anisoprint.ru. [Accessed: 20-Jun-2011].

[38] 9T Labs, "9T Labs | Digital Composites Production," 2020. [Online]. Available: https://www.9tlabs.com/. [Accessed: 25-Jun-2020].

[39] C3DXTech, "CarbonX Carbon Fiber Reinforced Filament," 2018. [Online]. Available: https://www.3dxtech.com/brands/CarbonX™.html. [Accessed: 16-May-2018].

[40] Fiber Force Italy, "Technical Data Sheet - Nylforce Carbon Fibe." Treviso, Italy, p. 1, 2017.

[41] Proto Pasta, "Carbon Fiber PLA," *2020*. [Online]. Available: https://www.proto-pasta.com/products/carbon-fiber-pla. [Accessed: 25-Jun-2020].

[42] C. E. Duty *et al.*, "Structure and mechanical behavior of Big Area Additive Manufacturing (BAAM) materials," *Rapid Prototyp. J.*, vol. 23, no. 1, pp. 181–189, 2017.

[43] Q. Sun, C. Bellehumeur, and P. Gu, "Effect of processing conditions on the bonding quality of FDM polymer filament," *Solid Free. Fabr. Proc.*, vol. 14, no. 403, pp. 400–407, 2002.

[44] J. W. Stansbury and M. J. Idacavage, "3D printing with polymers: Challenges among expanding options and opportunities," *Dent. Mater.*, vol. 32, no. 1, pp. 54–64, 2016.

[45] C. Yan, L. Hao, L. Xu, and Y. Shi, "Preparation, characterisation and processing of carbon fibre/polyamide-12 composites for selective laser sintering," *Compos. Sci. Technol.*, vol. 71, no. 16, pp. 1834–1841, 2011.

[46] R. D. Goodridge, C. J. Tuck, and R. J. M. Hague, "Laser sintering of polyamides and other polymers," *Prog. Mater. Sci.*, vol. 57, no. 2, pp. 229–267, 2012.

[47] W. Zhu *et al.*, "A novel method based on selective laser sintering for preparing high-performance carbon fibres/polyamide12/epoxy ternary composites," *Sci. Rep.*, vol. 6, no. September, pp. 1–10, 2016.

[48] B. I. Lyons and C. S. Huskamp, "Method of reinforcement for additive manufacturing," US 20140050921 A1, 2014.

[49] S. Fischer *et al.*, "A High-performance Material for Aerospace Applications: Development of carbon fiber filled PEKK for laser sintering," *Solid Free. Fabr. 2016 Proc. 27th Annu. Int. Solid Free. Fabr. Symp. - An Addit. Manuf. Conf. SFF 2016*, pp. 808–813, 2016.

[50] B. Chen, S. Berretta, R. Davies, and O. Ghita, "Characterisation of carbon fibre (Cf) - Poly Ether Ketone (PEK) composite powders for laser sintering," *Polym. Test.*, vol. 76, no. December 2018, pp. 65–72, 2019.

[51] B. Yazdani, B. Chen, L. Benedetti, R. Davies, O. Ghita, and Y. Zhu, "A new method to prepare composite powders customized for high temperature laser sintering," *Compos. Sci. Technol.*, vol. 167, no. June, pp. 243–250, 2018.

[52] L. Benedetti, B. Brulé, N. Decreamer, K. E. Evans, and O. Ghita, "Shrinkage behaviour of semi-crystalline polymers in laser sintering: PEKK and PA12," *Mater. Des.*, vol. 181, 2019.

[53] B. N. Turner and S. A. Gold, "A review of melt extrusion additive manufacturing processes: II. Materials, dimensional accuracy, and surface roughness," *Rapid Prototyp. J.*, vol. 21, no. 3, pp. 250–261, 2015.

[54] J. T. Belter and A. M. Dollar, "Strengthening of 3D printed fused deposition manufactured parts using the fill compositing technique," *PLoS One*, vol. 10, no. 4, pp. 1–19, 2015.

[55] J. F. Rodriguez *et al.*, "Characterization of the mesostructure of fused-deposition acrylonitrile-butadiene-styrene materials," 2011.

[56] B. N. Turner, R. Strong, and S. A. Gold, "A review of melt extrusion additive manufacturing processes: I. Process design and modeling," *Rapid Prototyp. J.*, vol. 20, no. 3, pp. 192–204, 2014.

[57] S. Ahn, M. Montero, D. Odell, S. Roundy, and P. K. Wright, "Anisotropic material properties of fused deposition modeling ABS," *Rapid Prototyp. J.*, vol. 8, no. 4, pp. 248–257, 2002.

[58] L. Li, Q. Sun, C. Bellehumeur, and P. Gu, "Investigation of bond formation in FDM process," *Solid Free. Fabr. Proc.*, no. 403, pp. 400–407, 2002.

[59] W. Wu, P. Geng, G. Li, D. Zhao, H. Zhang, and J. Zhao, "Influence of layer thickness and raster angle on the mechanical properties of 3D-printed PEEK and a comparative mechanical study between PEEK and ABS," *Materials (Basel).*, vol. 8, no. 9, pp. 5834–5846, 2015.

[60] B. Huang and S. Singamneni, "Raster angle mechanics in fused deposition modelling," *J. Compos. Mater.*, vol. 0, no. January, pp. 1–21, 2014.

[61] J. Rodriguez, "Maximizing the strength of fused-deposition ABS plastic parts," *10th Solid Free. …*, pp. 335–342, 1999.

[62] L. Li, Q. Sun, C. Bellehumeur, and P. Gu, "Composite Modeling and Analysis for Fabrication of FDM Prototypes with Locally Controlled Properties," *J. Manuf. Process.*, vol. 4, no. 2, pp. 129–141, 2002.

[63] M. A. Yardimci, S. I. Guceri, M. Agarwala, and S. C. Danforth, "Part Quality Prediction Tools for Fused Deposition Processing," in *Proceedings of the Solid Freeform Fabrication Symposium*, 1996, pp. 539–548.

[64] C. Bellehumeur, L. Li, Q. Sun, and P. Gu, "Modeling of Bond Formation Between Polymer Filaments in the Fused Deposition Modeling Process," *J. Manuf. Process.*, vol. 6, no. 2, pp. 170–178, 2004.

[65] C. McIlroy and P. D. Olmsted, "Disentanglement effects on welding behaviour of polymer melts during the fused-filament-fabrication method for additive manufacturing," *Polymer (Guildf).*, vol. 123, pp. 376–391, 2017.

[66] P. G. de Gennes, "Entangled polymers," *Phys. Today*, vol. 36, no. 6, pp. 33–39, 1983.

[67] R. P. Wool, B.-L. Yuan, and O. K. McGarel, "Welding of polymer interfaces," *Polym. Eng. Sci.*, vol. 29, no. 19, pp. 1340–1367, 1989.

[68] M. A. Yardimci, T. Hattori, S. I. Guceri, and S. C. Danforth, "Thermal analysis of Fused Deposition," *Solid Free. Fabr. Proceedings, Sept. 1997*, pp. 689–698, 1997.

[69] O. Pokluda, C. T. Bellehumeur, and J. Machopoulos, "Modification of Frenkel's Model for Sintering," *AIChE J.*, vol. 43, no. 12, pp. 3253–3256, 1997.

[70] A. Bellini, "Fused Deposition of Ceramics : A Comprehensive Experimental , Analytical and

Computational Study of Material Behavior , Fabrication Process and Equipment Design," Drexel University, 2002.

[71] A. Lanzotti, M. Grasso, G. Staiano, and M. Martorelli, "The impact of process parameters on mechanical properties of parts fabricated in PLA with an open-source 3-D printer," vol. 5, pp. 604–617, 2015.

[72] K. G. J. Christiyan, U. Chandrasekhar, and K. Venkateswarlu, "A study on the influence of process parameters on the Mechanical Properties of 3D printed ABS composite," vol. 114, pp. 1–8, 2016.

[73] S. Hwang, E. I. Reyes, K. Moon, R. C. Rumpf, and N. A. M. S. O. O. Kim, "Thermo-mechanical Characterization of Metal / Polymer Composite Filaments and Printing Parameter Study for Fused Deposition Modeling in the 3D Printing Process," vol. 44, no. 3, p. 11664, 2015.

[74] U. Kalsoom, P. N. Nesterenko, and B. Paull, "Recent developments in 3D printable composite materials," *RSC Adv.*, vol. 6, no. 65, pp. 60355–60371, 2016.

[75] X. Wang, M. Jiang, Z. Zhou, J. Gou, and D. Hui, "3D printing of polymer matrix composites: A review and prospective," *Compos. Part B Eng.*, vol. 110, pp. 442–458, 2017.

[76] F. Ning, W. Cong, J. Qiu, J. Wei, and S. Wang, "Additive manufacturing of carbon fiber reinforced thermoplastic composites using fused deposition modeling," *Compos. Part B Eng.*, vol. 80, pp. 369–378, 2015.

[77] H. L. Tekinalp *et al.*, "Highly oriented carbon fiber-polymer composites via additive manufacturing," *Compos. Sci. Technol.*, vol. 105, pp. 144–150, 2014.

[78] R. Matsuzaki *et al.*, "Three-dimensional printing of continuous-fiber composites by in-nozzle impregnation.," *Sci. Rep.*, vol. 6, no. February, p. 23058, 2016.

[79] M. L. Shofner, K. Lozano, F. J. Rodríguez-Macías, and E. V. Barrera, "Nanofiber-reinforced polymers prepared by fused deposition modeling," *J. Appl. Polym. Sci.*, vol. 89, no. 11, pp. 3081–3090, 2003.

[80] C. Mahajan and D. Cormier, "3D Printing of Carbon Fiber Composites With Preferentially Aligned Fibers," *Proc. 2015 Ind. Syst. Eng. Reserach Conf.*, 2015.

[81] J. Peng, T. L. Lin, and P. Calvert, "Orientation effects in freeformed short-fiber composites," *Compos. Part A Appl. Sci. Manuf.*, vol. 30, pp. 133–138, 1999.

[82] F. Antonov, "Composites in 3D printing : trends , prospects and applications," 2015.

[83] J. P. Lewicki *et al.*, "3D-Printing of Meso-structurally Ordered Carbon Fiber/Polymer Composites with Unprecedented Orthotropic Physical Properties," *Sci. Rep.*, vol. 7, no. December 2016, p. 43401, 2017.

[84] S. Y. Fu and B. Lauke, "Effects of fiber length and fiber orientation distributions on the tensile strength of short-fiber-reinforced polymers," *Compos. Sci. Technol.*, vol. 56, no. 10, pp. 1179–1190, 1996.

[85] F. Ning, W. Cong, J. Qiu, J. Wei, and S. Wang, "Additive manufacturing of carbon fiber reinforced thermoplastic composites using fused deposition modeling," *Compos. Part B Eng.*, vol. 80, pp. 369–378, 2015.

[86] C. Yang, X. Tian, T. Liu, Y. Cao, and D. Li, "3D printing for continuous fiber reinforced thermoplastic composites: mechanism and performance," *Rapid Prototyp. J.*, vol. 23, no. 1, pp. 209–215, 2017.

[87] 3DXTech, "Updated Test Data on Carbon Fiber Filaments," 2016. [Online]. Available: https://www.3dxtech.com/blog/updated-test-data-on-carbon-fiber-filaments/. [Accessed: 18-Oct-2020].

[88] Filamentative, "Filamentative - PETG Carbon Fibre Filament Datasheet," 2019. [Online]. Available: https://www.filamentive.com/wp-content/uploads/2019/06/TDS_carbonf.pdf. [Accessed: 18-Oct-2020].

[89] 3D4Makers, "PETG Carbon Filament | 3D4Makers | 3D Printing," 2020. [Online]. Available: https://www.3d4makers.com/products/petg-carbon. [Accessed: 18-Oct-2020].

[90] Technology Outlet, "Premium PLA Carbon Fibre Filament," *2019*. [Online]. Available: https://technologyoutlet.co.uk/products/carbon-pla-3d-printer-filament. [Accessed: 07-Jan-2019].

[91] Technology Outlet, "Premium PET-G Carbon Fibre Filament," *2019*. [Online]. Available: https://technologyoutlet.co.uk/products/technology-outlet-premium-pet-g-carbon-fibre-filament. [Accessed: 07-Jan-2019].

[92] W. Zhang *et al.*, "Characterization of residual stress and deformation in additively manufactured ABS polymer and composite specimens," *Compos. Sci. Technol.*, vol. 150, pp. 102–110, 2017.

[93] MarkForged, "MarkForged - Material Data Sheet," 2019. [Online]. Available: https://static.markforged.com/markforged_composites_datasheet.pdf. [Accessed: 18-Oct-2020].

[94] Mark3D, "Printing materials for Markforged 3D printers," 2018. [Online]. Available: https://www.mark3d.com/en/printing-materials/. [Accessed: 18-Oct-2020].

[95] D. Valentin, F. Paray, and B. Guetta, "The hygrothermal behaviour of glass fibre reinforced Pa66 composites: A study of the effect of water absorption on their mechanical properties," *J. Mater. Sci.*, vol. 22, no. 1, pp. 46–56, 1987.

[96] ASTM International, "D3039/D3039M: Standard test method for tensile properties of polymer matrix composite materials." pp. 1–13, 2014.

[97] ASTM International, "D7264/D7264M-07: Standard Test Method for Flexural Properties of Polymer Matrix Composite Materials 1." pp. 1–11, 2010.

[98] C. T. Sun and I. Chung, "An oblique end-tab design for testing off-axis composite specimens," *Composites*, vol. 24, no. 8, pp. 619–623, 1993.

[99] ASTM International, "D638: Standard test method for tensile properties of plastics." pp. 1–16, 2013.

[100] M. R. Wisnom, "The Relationship between Tensile and Flexural Strength of Unidirectional Composites," *J. Compos. Mater.*, vol. 26, no. 8, pp. 1173–1180, 1992.

[101] A. Lanzotti, M. Grasso, G. Staiano, and M. Martorelli, "The impact of process parameters on mechanical properties of parts fabricated in PLA with an open-source 3-D printer," *Rapid Prototyp. J.*, vol. 21, no. 5, pp. 604–617, 2015.

[102] ASTM International, "Standard Test Method for In-Plane Shear Response of Polymer Matrix Composite Materials by Tensile Test of a 45 degree Laminate," vol. 94, no. Reapproved, pp. 1–7, 2007.

[103] F. Calignano *et al.*, "Overview on additive manufacturing technologies," *Proc. IEEE*, vol. 105, no. 4, pp. 593–612, 2017.

[104] V. V. Vasiliev and A. F. Razin, "Anisogrid composite lattice structures for spacecraft and aircraft applications," *Compos. Struct.*, 2006.

[105] D. Yang, K. Wu, L. Wan, and Y. Sheng, "A Particle Element Approach for Modelling the 3D Printing Process of Fibre Reinforced Polymer Composites," *J. Manuf. Mater. Process.*, vol. 1, no. 1, p. 10, 2017.

[106] B. G. Compton, B. K. Post, C. E. Duty, L. Love, and V. Kunc, "Thermal analysis of additive manufacturing of large-scale thermoplastic polymer composites," *Addit. Manuf.*, vol. 17, pp. 77–86, 2017.

[107] D. Pollard, C. Ward, G. Herrmann, and J. Etches, "Filament Temperature Dynamics in Fused Deposition Modelling and Outlook for Control," *Procedia Manuf.*, vol. 11, no. June, pp. 536–544, 2017.

[108] W. Pabst, E. Gregorová, and C. Berthold, "Particle shape and suspension rheology of short-fiber systems," *J. Eur. Ceram. Soc.*, vol. 26, no. 1–2, pp. 149–160, 2006.

[109] T. Mulholland, S. Goris, J. Boxleitner, T. Osswald, and N. Rudolph, "Process-Induced Fiber Orientation in Fused Filament Fabrication," *J. Compos. Sci.*, vol. 2, no. 3, p. 45, 2018.

[110] C. L. Choy, W. P. Leung, K. W. Kowk, and F. P. Lau, "Elastic moduli and thermal conductivity of injection-molded short-fiber–reinforced thermoplastics," *Polym. Compos.*, vol. 13, no. 2, pp. 69–80, 1992.

[111] Granta Design, "CES EduPack." .

[112] I. Gibson, D. Rosen, and B. Stuckers, *Additive Manufacturing Technologies: 3D Printing, Rapid Prototyping, and Direct Digital Manufacturing*. Springer, 2015.

[113] Y. Z. Wan, Y. L. Wang, X. H. Xu, and Q. Y. Li, "In Vitro Degradation Behavior of Carbon Fiber-Reinforced PLA Composites and Influence of Interfacial Adhesion," *J. Appl. Polym. Sci.*, vol. 82, pp. 150–158, 2001.

[114] J. Li and Y. F. Zhang, "The Tensile Properties of Short Carbon Fiber Reinforced ABS and ABS/PA6 Composites," *J. Reinf. Plast. Compos.*, vol. 29, no. 11, pp. 1727–1733, 2010.

[115] A. Kausar, "Design and Study of Epoxy Composites based on Polycaprolactone and Nanodiamond Functionalized Carbon Fibers," *Am. J. Polym. Sci. Eng.*, vol. 3, no. 1, pp. 50–60, 2015.

[116] L. Dányádi, J. Gulyás, and B. Pukánszky, "Coupling of carbon fibers to polycarbonate: surface chemistry and adhesion," *Compos. Interfaces*, vol. 10, no. 1, pp. 61–76, 2003.

[117] Y. Chen, X. Wang, and D. Wu, "Recycled carbon fiber reinforced poly(butylene terephthalate) thermoplastic composites: Fabrication, crystallization behaviors and performance evaluation," *Polym. Adv. Technol.*, vol. 24, no. 4, pp. 364–375, 2013.

[118] G. Tang *et al.*, "Study on the Interfacial Behavior of Clay-Coated Carbon Fiber-Reinforced PEI Composites," *Polym. - Plast. Technol. Eng.*, vol. 51, no. 8, pp. 861–865, 2012.

[119] S. L. Gao and J. K. Kim, "Cooling rate influences in carbon fibre/PEEK composites. Part 1. Crystallinity and interface adhesion," *Compos. Part A Appl. Sci. Manuf.*, vol. 31, no. 6, pp. 517–530, 2000.

[120] B. Liu, Z. Liu, X. Wang, G. Zhang, S. Long, and J. Yang, "Interfacial shear strength of carbon fiber reinforced polyphenylene sulfide measured by the microbond test," *Polym. Test.*, vol. 32, no. 4, pp. 724–730, 2013.

[121] G. Hartwig, H. Jäger, and S. Knaak, "Interlaminar Shear Strength of Carbon-Fibre Reinforced Thermoplastics Polycarbonate and Polysulfone," in *Nonmetallic Materials and Composites at Low Temperatures*, G. Hartwig and D. Evans, Eds. Boston, MA: Springer, 1986, pp. 167–175.

[122] Z. Weng, J. Wang, T. Senthil, and L. Wu, "Mechanical and thermal properties of ABS/montmorillonite nanocomposites for fused deposition modeling 3D printing," *Mater. Des.*, vol. 102, pp. 276–283, 2016.

[123] M. Biron, *Thermoplastics and Thermoplastic Composites*. Elsevier Science, 2018.

[124] S. Yumitori, Y. Arao, T. Tanaka, K. Naito, K. Tanaka, and T. Katayama, "Increasing the interfacial strength in carbon fiber/polypropylene composites by growing CNTs on the fibers," *WIT Trans. Modelling Simul.*, vol. 55, pp. 275–284, 2013.

[125] S. Chong, G. T. Pan, M. Khalid, T. C. K. Yang, S. T. Hung, and C. M. Huang, "Physical Characterization and Pre-assessment of Recycled High-Density Polyethylene as 3D Printing Material," *J. Polym. Environ.*, vol. 25, no. 2, pp. 136–145, 2017.

[126] G. Cicala *et al.*, "Comparison of Ultem 9085 used in fused deposition modelling (FDM) with polytherimide blends," *Materials (Basel).*, vol. 11, no. 2, 2018.

[127] R. J. Zaldivar, D. B. Witkin, T. McLouth, D. N. Patel, K. Schmitt, and J. P. Nokes, "Influence of processing and orientation print effects on the mechanical and thermal behavior of 3D-Printed ULTEM®9085 Material," *Addit. Manuf.*, vol. 13, pp. 71–80, 2017.

[128] R. Telford *et al.*, "Enhanced Buckling Performance of a Stiffened, Variable Angle Tow Thermoplastic Composite Panel," *2018 AIAA/ASCE/AHS/ASC Struct. Struct. Dyn. Mater. Conf.*, no. January, pp. 1–14, 2018.

[129] A. J. Comer *et al.*, "Mechanical characterisation of carbon fibre-PEEK manufactured by laser-assisted automated-tape-placement and autoclave," *Compos. Part A Appl. Sci. Manuf.*, vol. 69, pp. 10–20, 2015.

[130] D. Ray *et al.*, "Fracture toughness of carbon fiber/polyether ether ketone composites manufactured by autoclave and laser-assisted automated tape placement," *J. Appl. Polym. Sci.*, vol. 132, no. 11, pp. 1–10, 2015.

[131] S. Berretta, R. Davies, Y. T. Shyng, Y. Wang, and O. Ghita, "Fused Deposition Modelling of high temperature polymers: Exploring CNT PEEK composites," *Polym. Test.*, vol. 63, pp. 251–262, 2017.

[132] K. Stoeffler, S. Andjelic, N. Legros, J. Roberge, and S. B. Schougaard, "Polyphenylene sulfide (PPS) composites reinforced with recycled carbon fiber," *Compos. Sci. Technol.*, vol. 84, pp. 65–71, 2013.

[133] V. Kishore *et al.*, "Additive manufacturing of high performance semicrystalline thermoplastics and their composites," in *Solid Freeform Fabrication Symposium – An Additive Manufacturing Conference*, 2016.

[134] A. A. Zhansitov *et al.*, "Development of technology of polysulfone production for 3D printing," *High Perform. Polym.*, vol. 29, no. 6, pp. 724–729, 2017.

[135] 3D4Makers, "3D4Makers Filament Engineers." [Online]. Available: https://www.3d4makers.com/. [Accessed: 14-May-2018].

[136] M. L. Longana, N. Ong, H. Yu, and K. D. Potter, "Multiple Closed Loop Recycling of Carbon Fibre Composites with the HiPerDiF (High Performance Discontinuous Fibre) Method," *Compos. Struct.*, vol. 153, pp. 271–277, 2016.

[137] Teijin carbon, "Tenax ® short fiber Product Data Sheet Chopped fiber with thermoplastic sizing." pp. 1–2, 2018.

[138] B. R. Gebart, "Permeability of Unidirectional Reinforcements for RTM," *J. Compos. Mater.*, vol. 26, no. 8, pp. 1100–1133, 1992.

[139] K. Goh, *Discontinuous-Fibre Reinforced Composites*. London: Springer, 2016.

[140] H. L. Cox, "The elasticity and strength of paper and other fibrous materials," *Br. J. Appl. Phys.*, vol. 3, no. 3, pp. 72–79, 1952.

[141] C. A. Silva, J. C. Viana, F. W. J. van Hattum, and A. M. Cunha, "Fiber Orientation in Divergent/Convergent Flows in Expansion and Compression Injection Molding," *Polym. Compos.*, vol. 38(1), pp. 96–104, 2006.

[142] T. Wagner, "ParticleSizer." https://imagej.net/ParticleSizer, 2016.

[143] C. El-Mazry, M. Ben Hassine, O. Correc, and X. Colin, "Thermal oxidation kinetics of additive free polyamide 6-6," *Polym. Degrad. Stab.*, vol. 98, no. 1, pp. 22–36, 2013.

[144] R. Guo, J. Azaiez, and C. Bellehumeur, "Rheology of fiber filled polymer melts: Role of fiber-fiber interactions and polymer-fiber coupling," *Polym. Eng. Sci.*, vol. 45, no. 3, pp. 385–399, 2005.

[145] M. J. Folkes and D. A. M. Russell, "Orientation effects during the flow of short-fibre reinforced thermoplastics," *Polymer (Guildf).*, vol. 21, no. 11, pp. 1252–1258, 1980.

[146] T. D. Papthanasiou and D. C. Guell, *Flow-Induced Alignment in Composite Materials*. Cambridge, England: Elsevier Science, 1997.

[147] S. G. Advani and E. M. Sozer, *Process Modeling in Composites Manufacturing*. CRC Press - Taylor & Francis Group, 2002.

[148] A. Einstein, "Eine neue Bestimmung der Moleküldimensionen," *Ann. Phys.*, vol. 324, no. 2, pp. 289–306, 1906.

[149] G. B. Jeffery, "The Motion of Ellipsoidal Particles Immersed in a Viscous Fluid," *Proc. R. Soc. A*, vol. 102, no. 715, 1922.

[150] T. Russell, B. Heller, D. A. Jack, and D. E. Smith, "Prediction of the Fiber Orientation State and the Resulting Structural and Thermal Properties of Fiber Reinforced Additive Manufactured Composites Fabricated Using the Big Area Additive Manufacturing Process," *J. Compos. Sci.*, vol. 2, no. 26, 2018.

[151] W. C. Jackson, S. G. Advani, and C. L. Tucker, "Predicting the Orientation of Short Fibers in Thin Compression Moldings," *J. Compos. Mater.*, vol. 20, no. 6, pp. 539–557, 1986.

[152] A. Londoño-Hurtado, T. A. Osswald, and J. P. Hernandez-Ortíz, "Modeling the behavior of fiber suspensions in the molding of polymer composites," *J. Reinf. Plast. Compos.*, vol. 30, no. 9, pp. 781–790, 2011.

[153] F. Folgar and C. L. Tucker, "Orientation Behavior of Fibers in Concentrated Suspensions.," *J. Reinf. Plast. Compos.*, vol. 3, no. 2, pp. 98–119, 1984.

[154] B. R. Munson, A. P. Rothmayer, and T. H. Okiishi, *Fundamentals of Fluid Mechanics*, 7th Editio. Wiley, 2012.

[155] C. Neto, D. R. Evans, E. Bonaccurso, H. J. Butt, and V. S. J. Craig, "Boundary slip in Newtonian liquids: A review of experimental studies," *Reports Prog. Phys.*, vol. 68, no. 12, pp. 2859–2897, 2005.

[156] S. Granick, Y. Zhu, and H. Lee, "Slippery questions about complex fluids flowing past solids," *Nat. Mater.*, vol. 2, no. 4, pp. 221–227, 2003.

[157] W. R. Schowalter, "The behavior of complex fluids at solid boundaries," *J. Nonnewton. Fluid Mech.*, vol. 29, no. C, pp. 25–36, 1988.

[158] M. R. Barone and D. A. Caulk, "A model for the flow of a chopped fiber reinforced polymer compound in compression molding," *J. Appl. Mech. Trans. ASME*, vol. 53, no. 2, pp. 361–371, 1986.

[159] D. Tabor, "Friction, Adhesion, and Boundary Lubrication of Polymers.," *Am Chem Soc, Div Org Coatings Plast Chem1974*, vol. 34, no. 1, pp. 203–218, 1974.

[160] A. M. Murtagh and P. J. Mallon, "Characterisation of shearing and frictional behaviour during sheet forming," in *Composite Sheet Forming*, D. Bhattacharyya, Ed. 1997, pp. 163–216.

[161] A. M. Murtagh, J. J. Lennon, and P. J. Mallon, "Surface friction effects related to pressforming of continuous fibre thermoplastic composites," *Compos. Manuf.*, vol. 6, no. 3–4, pp. 169–175, 1995.

[162] TA Instruments, "Understanding Rheology of Thermoplastic Polymers," *AAN013*. 2013.

[163] J. shyong Wang and R. S. Porter, "On the viscosity-temperature behavior of polymer melts," *Rheol. Acta*, vol. 34, no. 5, pp. 496–503, 1995.

[164] A. B. Metzner, "Rheology of Suspensions in Polymeric Liquids," *J. Rheol. (N. Y. N. Y).*, vol. 29, no. 6, pp. 739–775, 1985.

[165] S. Mueller, E. W. Llewellin, and H. M. Mader, "The rheology of suspensions of solid particles," *Proc. R.*, vol. 39, no. 4, pp. 291–300, 2009.

[166] G. K. Batchelor, "The effect of Brownian motion on the bulk stress in a suspension of spherical particles," *J. Fluid Mech.*, vol. 83, pp. 97–117, 1977.

[167] I. M. Krieger and T. J. Dougherty, "A Mechanism for Non-Newtonian Flow in Suspensions of Rigid Spheres," *Trans. Soc. Rheol.*, vol. 3, no. 1, pp. 137–152, 1959.

[168] J. J. Stickel and R. L. Powell, "Fluid Mechanics and Rheology of Dense Suspensions," *Annu. Rev. Fluid Mech.*, vol. 37, no. 1, pp. 129–149, 2005.

[169] F. L. Yang and M. L. Hunt, "Dynamics of particle-particle collisions in a viscous liquid," *Phys. Fluids*, vol. 18, no. 12, pp. 1–11, 2006.

[170] F. Folgar and C. L. Tucker III, "Orientation behaviour of fibers in concentrated suspensions," *J. Reinf. Plast. Compos.*, vol. 3, no. April 1984, pp. 98–119, 1984.

[171] J. Wang, J. F. O'Gara, and C. L. Tucker, "An objective model for slow orientation kinetics in concentrated fiber suspensions: Theory and rheological evidence," *J. Rheol. (N. Y. N. Y).*, vol. 52, no. 5, pp. 1179–1200, 2008.

[172] H.-C. Tseng, R.-Y. Chang, and C.-H. Hsu, "Phenomenological improvements to predictive models of fiber orientation in concentrated suspensions," *J. Rheol. (N. Y. N. Y).*, vol. 57, no. 6, pp. 1597–1631, 2013.

[173] J. H. Phelps and C. L. Tucker, "An anisotropic rotary diffusion model for fiber orientation in short- and long-fiber thermoplastics," *J. Nonnewton. Fluid Mech.*, vol. 156, no. 3, pp. 165–176, 2009.

[174] C. L. Tucker, "Flow regimes for fiber suspensions in narrow gaps," *J. Nonnewton. Fluid Mech.*, vol. 39, no. 3, pp. 239–268, 1991.

[175] R. Mezher, M. Perez, A. Scheuer, E. Abisset-Chavanne, F. Chinesta, and R. Keunings, "Analysis of the Folgar & Tucker model for concentrated fibre suspensions in unconfined and confined shear flows via direct numerical simulation," *Compos. Part A Appl. Sci. Manuf.*, vol. 91, pp. 388–397, 2016.

[176] O. du Roure, A. Lindner, E. N. Nazockdast, and M. J. Shelley, "Dynamics of Flexible Fibers in Viscous Flows and Fluids," *Annu. Rev. Fluid Mech.*, vol. 51, no. 1, pp. 539–572, 2019.

[177] B. Delmotte, E. Climent, and F. Plouraboué, "A general formulation of Bead Models applied to flexible fibers and active filaments at low Reynolds number," *J. Comput. Phys.*, vol. 286, pp. 14–37, 2015.

[178] J. P. Bell, "Flow Orientation of Short Fiber Composites," *J. Compos. Mater.*, 1968.

[179] K. N. Murty and G. F. Modlen, "Experimental characterization of the alignment of short fibers during flow," *Polym. Eng. Sci.*, vol. 17, no. 12, pp. 848–853, 1977.

[180] C. Hopmann and W. Michaeli, *Extrusion Dies for Plastic and Rubber - Design and Engineering Computation*, 4th ed. Munich: Hanser Publishers, 2016.

[181] G. W. Critchlow, R. E. Litchfield, I. Sutherland, D. B. Grandy, and S. Wilson, "A review and comparative study of release coatings for optimised abhesion in resin transfer moulding applications," *Int. J. Adhes. Adhes.*, vol. 26, no. 8, pp. 577–599, 2006.

[182] S. Y. Fu and Y. W. Mai, "Thermal conductivity of misaligned short-fiber-reinforced polymer composites," *J. Appl. Polym. Sci.*, vol. 88, no. 6, pp. 1497–1505, 2003.

[183] M. Martins *et al.*, "Highly conductive carbon fiber-reinforced polymer composite electronic box: Out-of-autoclave manufacturing for space applications," *Fibers*, vol. 6, no. 4, pp. 1–23, 2018.

[184] R. V. Morgan, R. S. Reid, A. M. Baker, and D. Bernardin, John, "Emissivity Measurements of Additively Manufactured Materials," *Los Alamos Natl. Lab. (LANL), Los Alamos, NM (United States)*, no. LA-UR-17-20513, 2017.

[185] A. Dawson, M. Rides, C. R. G. Allen, and J. M. Urquhart, "Polymer-mould interface heat transfer coefficient measurements for polymer processing," *Polym. Test.*, vol. 27, no. 5, pp. 555–565, 2008.

[186] C. Miller, "Predicting Non-Newtonian Flow Behavior in Ducts of Unusual Cross Section," *Ind. Eng. Chem. Fundam.*, vol. 11, no. 4, pp. 524–528, 1972.

[187] S. C. Garcea, Y. Wang, and P. J. Withers, "X-ray computed tomography of polymer composites," *Compos. Sci. Technol.*, vol. 156, pp. 305–319, 2018.

[188] M. J. Emerson, K. M. Jespersen, A. B. Dahl, K. Conradsen, and L. P. Mikkelsen, "Individual fibre segmentation from 3D X-ray computed tomography for characterising the fibre orientation in unidirectional composite materials," *Compos. Part A Appl. Sci. Manuf.*, vol. 97, pp. 83–92, 2017.

[189] B. Weber *et al.*, "Automated tracing of microtubules in electron tomograms of plastic embedded samples of Caenorhabditis elegans embryos," *J. Struct. Biol.*, vol. 178, no. 2, pp. 129–138, 2012.

[190] I. Straumit, S. V. Lomov, and M. Wevers, "Quantification of the internal structure and automatic generation of voxel models of textile composites from X-ray computed tomography data," *Compos. Part A Appl. Sci. Manuf.*, vol. 69, pp. 150–158, 2015.

[191] R. Karamov, L. M. Martulli, M. Kerschbaum, I. Sergeichev, Y. Swolfs, and S. V. Lomov, "Micro-CT based structure tensor analysis of fibre orientation in random fibre composites versus high-fidelity fibre identification methods," *Compos. Struct.*, vol. 235, no. December 2019, p. 111818, 2020.

[192] Z. Wang and D. E. Smith, "Rheology Effects on Predicted Fiber Orientation and Elastic Properties in Large Scale Polymer Composite Additive Manufacturing," *J. Compos. Sci.*, vol. 2, no. 1, p. 10, 2018.

[193] B. P. Heller, D. E. Smith, and D. A. Jack, "Effects of extrudate swell and nozzle geometry on fiber orientation in Fused Filament Fabrication nozzle flow," *Addit. Manuf.*, vol. 12, pp. 252–264, 2016.

[194] K. Gnanasekaran *et al.*, "3D printing of CNT- and graphene-based conductive polymer nanocomposites by fused deposition modeling," *Appl. Mater. Today*, vol. 9, pp. 21–28, 2017.

[195] H. S. Ramanath, C. K. Chua, K. F. Leong, and K. D. Shah, "Melt flow behaviour of poly-ε-caprolactone in fused deposition modelling," *J. Mater. Sci. Mater. Med.*, vol. 19, no. 7, pp. 2541–2550, 2008.

[196] N. Venkataraman *et al.*, "Feedstock material property - Process relationships in fused deposition of ceramics (FDC)," *Rapid Prototyp. J.*, vol. 6, no. 4, pp. 244–252, 2000.

[197] H. M. Wyss, D. L. Blair, J. F. Morris, H. A. Stone, and D. A. Weitz, "Mechanism for clogging of microchannels," *Phys. Rev. E - Stat. Nonlinear, Soft Matter Phys.*, vol. 74, no. 6, pp. 1–4, 2006.

[198] T. Beran, T. Mulholland, F. Henning, N. Rudolph, and T. A. Osswald, "Nozzle clogging factors during fused filament fabrication of spherical particle filled polymers," *Addit. Manuf.*, vol. 23, no. May, pp. 206–214, 2018.

[199] R. T. L. Ferreira, I. C. Amatte, T. A. Dutra, and D. Bürger, "Experimental characterization and micrography of 3D printed PLA and PLA reinforced with short carbon fibers," *Compos. Part B Eng.*, vol. 124, pp. 88–100, 2017.

[200] J. Zhang, Z. Zhou, F. Zhang, Y. Tan, and R. Yi, "Molding process and properties of continuous carbon fiber three-dimensional printing," *Adv. Mech. Eng.*, vol. 11, no. 3, pp. 1–11, 2019.

[201] H. Zhang, D. Liu, T. Huang, Q. Hu, and H. Lammer, "Three-dimensional printing of continuous flax fiber-reinforced thermoplastic composites by five-axis machine," *Materials (Basel).*, vol. 13, no. 7, 2020.

[202] V. E. Kuznetsov, A. G. Tavitov, O. D. Urzhumtsev, M. V. Mikhalin, and A. I. Moiseev, "Hardware factors influencing strength of parts obtained by fused filament fabrication," *Polymers (Basel).*, vol. 11, no. 11, 2019.